Dissertation

submitted to the

Combined Faculty of Natural Sciences and Mathematics

of the Ruperto Carola University Heidelberg, Germany

for the degree of

Doctor of Natural Sciences

Presented by

Daniel Krüger, M. Sc.

born in Pasewalk

Oral examination: 11th of March 2019

Regulation of Actomyosin Contraction during Tissue Morphogenesis: Genes and Mechanics

Referees:

Dr. Anne Ephrussi

Prof. Dr. Ulrich Schwarz

Abstract

Contraction of cortical actomyosin networks drives cell shape changes and is of fundamental importance during morphogenesis of multicellular organisms. Over the course of the last decade, an increasing number of studies has demonstrated the key role played by localized myosin activation at the apical surface of epithelial cells during a wide range of tissue morphogenetic processes. However, recent *in vitro* studies and computational models suggest that the architecture of the underlying actin network is also important. Furthermore, whether apical myosin-derived forces alone are sufficient to drive cell shape changes and morphogenesis remains highly debated, as the role of the basolateral surface must also be taken into account. In this thesis, by focusing on the dynamic remodeling of a basally localized actomyosin network required for early *Drosophila* embryonic development, I provide strong evidence in support of the role of actin network organization in controlling contractility. Using a combination of genetic, biochemical, and optogenetic approaches, I identified a mechanism based on actin crosslinkers, which regulate the spatial organization of actin networks and thereby time actomyosin contraction during cellularization, the transformation of the syncytial embryo in 6000 mononucleated epithelial cells. I further demonstrate that following cellularization, myosin-II activity at the basal surface of ventral cells must be downregulated in order to allow efficient apical constriction, cell wedging and ventral furrow invagination. Collectively the results presented in this thesis provide novel insights into the underlying spatiotemporal organization of actomyosin networks and molecular principles regulating actomyosin contraction during tissue morphogenesis.

Zusammenfassung

Veränderungen der Zellgestalt im Hinblick auf ihre äußere Form basieren auf Kontraktionen kortikaler Aktomyosinnetzwerke und sind von fundamentaler Wichtigkeit für die Morphogenese multizellulärer Organismen. Während der letzten Dekaden verdeutlichte eine Vielzahl von Forschungsstudien eine entscheidende Bedeutung der lokalen Aktivierung von Myosin an der apikalen Oberfläche von Epithelzellen für die Morphogenese vieler Gewebe. Allerdings legen neuere *in vitro* Studien und Computermodelle nahe, dass die gezielte Regulation der Netzwerkarchitektur von Aktinstrukturen ebenfalls entscheidend ist. Darüberhinaus ist unklar, ob allein die durch apikales Myosin generierten Kräfte ausreichend sind, um Veränderungen der Zellform und damit Morphogenese anzutreiben oder ob auch ein Beitrag basolateraler Komponenten betrachtet werden muss. In dieser Arbeit untersuche ich dezidiert die Umordnung basaler Aktomyosinnetzwerke, welche essentiell für die frühe Entwicklung von *Drosophila melanogaster* ist, und liefere Belege für eine aktive Rolle der Organisationsstruktur von Aktinnetzwerken zur Kontrolle von Zellkontraktilität. Unter Einbeziehung von genetischen, biochemischen und optogenetischen Methoden identifizierte ich einen auf Mechanismus basierend auf aktinvernetzenden Proteinen, der die räumliche Organisation von Aktomyosinnetzwerken reguliert und dabei Netzwerkkontrationen während dem entwicklungsbiologischen Prozesses der Zellularisierung kontrolliert. Im Verlauf der Zellularisierung transformiert sich der synzytiale Fliegenembryo in 6000 einkernige Epithelzellen. Darüberhinaus zeige ich, dass im Anschluss an die Zellularisierung die Aktivität von Myosin-II in der basalen Domäne der ventralen Zellen herunterreguliert werden muss. Das ist notwendig um effiziente apikale Zellkontraktion, Transformation der Zellen in eine Keil-Form und damit die Bildung der ventralen Furche zu ermöglichen. Zusammengenommen, erlauben die in dieser Arbeit präsentierten Ergebnisse neue Einblicke in die räumlich-zeitliche Organisation von Aktomyosinnetzwerken und die der Regulation von Aktomyosinkontraktionen zugrundeliegenden molekularen Prinzipien während der Morphogenese von Geweben.

Content

Abstract v

Zusammenfassung vii

Content viii

Table of figures xii

Abbreviations and selected protein names xv

1. Introduction 1

1.1. A historical prelude 1
1.2. General concepts in morphogenesis 2
1.3. Mechanisms of morphogenesis 5
1.3.1. Cytoskeletal fundamentals 7
1.4. Morphogenesis of epithelial tissues 8
1.5. Cell polarity 10
1.6. Actin microfilament regulation 13
1.6.1. Self-organization of actin filaments 13
1.6.2. Regulation of F-actin assembly and stability 14
1.6.3. Molecular control of myosin-II activity 16
1.6.4. Contraction of actomyosin networks 18
1.6.5. Relation of actomyosin network architecture to function *in vivo* 22
1.6.6. Regulation of actomyosin network transitions 23
1.7. Actomyosin-dependent building and remodelling of epithelial tissues 26
1.7.1. Cellularization: *de novo* formation of an epithelium 26
1.7.1.1. Polarized plasma membrane remodelling during cellularization 26
1.7.1.2. Maternal-to-zygotic transition (MZT) 28
1.7.1.3. Implication for a key-regulator Bottleneck 30
1.7.2. Epithelial-specific morphogenetic movements 31
1.7.3. Tissue Invagination 32
1.7.3.1. Mammalian neural tube formation 33

1.7.3.2. Ventral furrow formation in *Drosophila* 36
1.7.3.2.1. Positioning and timing ventral furrow formation 36
1.7.3.2.2. Apical pulsing and anisotropy 38
1.7.3.3. Modelling tissue invagination 41
1.7.4. Role of the basal surface in epithelial remodelling 42
1.8. New perspectives of manipulating living organisms 44
1.8.1. Modelling morphogenesis by computers, cultures and synthetic biology 44
1.8.2. Optogenetics 45
1.8.2.1. Concepts and approaches in non-neuronal optogenetics 47
1.8.2.2. Heteromerization and photo-uncaging systems 47
1.8.2.3. Application of optogenetics to study morphogenesis 49

2. Aim of the thesis **53**

3. Results **55**

3.1. A switch in crosslinker-mediated actin network topology 55
3.1.1. Differential contractile response of actomyosin network patterns 55
3.1.2. The zygotic gene product Bottleneck functions as actin crosslinker 60
3.1.3. Cheerio and Fimbrin time actomyosin network transitions *in vivo* 64
3.1.4. Bottleneck synergizes Cheerio and antagonizes Fimbrin activity 71
3.2. Role of basal myosin-II during VF 76
3.2.1. Quantitative manipulation of basal myosin-II. 76
3.2.2. Effect on cell elongation and tissue invagination 83
3.2.3. Influence on ratcheted apical constriction. 87
3.2.4. Effect on cell shortening and furrow progression 87

4. Discussion **93**

4.1. Actin-crosslinkers time cell contractility during morphogenesis 93
4.2. Tissue invagination requires downregulation of basal myosin-II 98
4.3. Advancing optogenetics to probe morphogenesis 102
4.4. Integration into the broad theoretic framework of morphogenesis 103

5. Methods and Materials **105**

Content

5.1. Methods in cell biology 105
5.1.1. Cell culture, transfection, and live imaging 105
5.2. Methods in molecular biology 105
5.2.1. Protein expression in *E. coli* 105
5.2.1.1. Auto-induction in *E. coli* 105
5.2.1.2. IPTG-induction in *E. coli* 106
5.2.2. Protein expression in insect cells 106
5.2.2.1. Baculo virus transposition 106
5.2.2.2. Bacmid prep 106
5.2.2.3. Transfection of Sf21 or Hi5 cells 106
5.2.3. Protein expression and purification of MBP-His-Bnk deletion constructs 107
5.2.4. Recombinant expression and purification of $Bnk_{198-303}$ 107
5.2.5. Western Blot 108
5.2.6. Actin binding und bundling assay 108
5.2.7. Molecular cloning 109
5.2.7.1. Gibson assembly (One-step isothermal recombination) 109
5.2.8. Outline of cloning strategies for generated constructs 109
5.3. Methods in electron microscopy 111
5.3.1. Negative stain electron microscopy 111
5.4. Methods in light microscopy 111
5.4.1. Live imaging and optogenetics 111
5.4.2. Immunostaining. 114
5.4.3. Actin staining. 115
5.4.4. STED microscopy 115
5.5. Methods in data processing and analysis 116
5.5.1. *In silico* analysis of Bottleneck structure 116
5.5.2. Image and data analysis 116
5.5.3. Statistical analysis 120
5.6. Methods in fly genetics 120
5.6.1. Anti-GFP Nanobody-mediated protein knockdown 120
5.6.2. Verification of YFP-Cheerio and YFP-Fimbrin insertion sites 121
5.6.3. Single embryo genotyping PCR 121

5.6.4. Fly Strains and Genetics 121
5.6.4.1. Phenotypic characterization 121
5.6.4.2. Optogenetic experiments 122
5.6.5. Fly Stocks 124
5.7. Materials 126
6. Literature **133**
7. Appendix **143**
7.1. Supplementary Figures 143
7.2. Usage permissions for figures 149
Acknowledgement **153**

Table of figures

Figure 1. Mechanisms of morphogenesis 5

Figure 2. Cell polarity in an epithelial cell 11

Figure 3. Molecular regulation of actomyosin contractility.....15

Figure 4. Crosslinker-mediated network organization and effect on contractility *in vitro*.19

Figure 5. Overview of *Drosophila* cellularization 25

Figure 6. The zygotic gene *bottleneck* regulates actomyosin network transitions during cellularization 29

Figure 7. *Drosophila* ventral furrow formation as a model for tissue invagination.....35

Figure 8. Apical pulsing and anisotropy.. 39

Figure 9. Computer model recapitulating the whole process of VF.....42

Figure 10. Model system: The basal actomyosin network during early *Drosophila* development 43

Figure 11. Optogenetics enable the control of biological processes using light.....46

Figure 12. Schematic depiction of the experimental setup.....56

Figure 13. The basal actomyosin network in its hexagonal pattern is highly resistant to myosin-II activity. 57

Figure 14. Bottleneck is an intrinsically disordered and hydrophobic protein prone to aggregation 58

Figure 15. Overview of the systematic approach to produce soluble Bottleneck protein. 59

Figure 16. Analysis of the localization of Bnk deletion constructs in HeLa cells 61

Figure 17. $Bnk_{198-303}$ crosslinks actin fibers and induces actin-bundle formation.. 62

Figure 18. Map showing the position of the YFP-tag in cheerio and fimbrin and the localization 64

Figure 19. The actin crosslinkers Cheerio and Fimbrin co-localize with myosin-II at the leading edge of the cellularization furrow 65

Figure 20. Anti-GFP nanobody-mediated knock down of Cheerio and Fimbrin led to the efficient depletion of the target proteins during cellularization 66

Figure 21. Phenotypic analysis of bottleneck mutant, Cheerio and Fimbrin knockdown embryos during cellularization 67

Figure 22. Super-resolution analysis of wild type control embryos at different stages of cellularization 68

Figure 23. Super-resolution analysis of Cheerio and *bottleneck* mutant embryos reveals their critical role in actin bundling during the hexagonal phase 69

Figure 24. Localization to the leading edge of the cellularization furrow of Bottleneck does not depend on Cheerio and *vice versa* 70

Figure 25. Bottleneck and Cheerio act synergistically during hexagonal patterning..... 71

Figure 26. Depletion of Fimbrin rescues the *bottleneck* mutant phenotype 72

Figure 27. Depletion of Fimbrin rescues gastrulation in *bottleneck* mutant embryos 73

Figure 28. Model schematizing the synergistic and antagonistic effect of actin crosslinkers on the regulation of basal actomyosin remodeling during *Drosophila* morphogenesis 74

Table of figures

Figure 29. Quantitative manipulation of myosin-II levels at the cell base at the onset of gastrulation. 77

Figure 30. Increasing myosin-II at the base of ventral mesodermal cells inhibits ventral furrow formation despite normal accumulation of apical myosin-II 79

Figure 31. Increasing myosin-II at cell base of ventral mesodermal cells prevents basal shift of nuclei 80

Figure 32. Reconstruction of cell shapes in basally photo-activated embryos....81

Figure 33. Increasing myosin-II levels at the cell base prevents cell elongation and transition to conic shape. 82

Figure 34. Stabilizing basal myosin-II levels inhibits ratcheted apical contractions 84

Figure 35. Engineering a basal-specific optogenetic anchor for photo-activation in a curved tissue 86

Figure 36. Increasing basal myosin-II levels after cells constricted apically and initial tissue invagination started prevents progression of cell invagination and closure of the furrow 89

Figure 37. Myosin-II stabilization during later stages of ventral furrow formation inhibits cell shortening 91

Abbreviations and selected protein names

Abbreviation	Explanation
aa	Amino acid
AJ	Adherence junction
AP	Anterior-posterior
AR	Photo-activated region
AU	Arbitrary unit
Bnk	Bottleneck
CAAX	C-terminal motif for posttranslational prenylation
CH	Calponin homology domain
Cher	Cheerio
CIB1	Cryptochrome-interacting basic-helix-loop-helix 1
CIBN	N-terminally truncated CIB1 (aa 1–170)
CRY2	Chryptochrome 2
EDGE	Embryo development geometry explorer (Matlab sofware)
EM	Electron microscopy
F-actin	Filamentous actin
Fim	Fimbrin
G-actin	Globular actin (monomeric)
GAP43	Membrane localization signal of growth associated protein 43
GDP	Guanosine diphosphate
GEF	guanine nucleotide exchange factors
GFP	Green fluorescent protein
GTP	Guanosine triphosphate
KD	Knockdown

Abbreviations and selected protein names

Abbreviation	Explanation
MBP	Maltose binding protein
mCh	mCherry fluorescent protein
myo-II	myosin-II
MZT	Maternal to zygotic transition
NR	Non-activated region
p.	Page
PatJ	Protein associated to tight junctions (InaD-like protein)
PCR	Polymerase chain reaction
PDZ	Common structural domain
pp.	Pages
Pre A	Pre-activation
RFP	Red flourecent protein
ROI	Region of interest
SEC	Size-exclusion chromatography
Sqh	Spaghetti-squash (*Drosophila* myosin regulatory light chain)
TJ	Tight junction
Trx	Thioredoxin
UTR	Untranslated region
VF	Ventral furrow formation
YFP	Yellow fluorescent protein

1. Introduction

1.1. A historical prelude

Homo sapiens is the phylum in which human beings categorize themselves distinct from other humanoids due to the capability of discerning, reflecting and thinking (term *sapiens*). It is the ability of abstract reasoning driving the will to scrutinize nature, life and their own existence that phenotypically distinguishes a modern human from evolutionary relatives rather than differences in anatomy (perhaps with the exception of the structure of the brain). The ancient Greek philosopher Aristotle argued that humans are characterized by a 'rational soul' that provides the ability to perceive forms of other things and to compare them with one another (Amadio and Kenny, 2018). However, only the potential to transmit knowledge across generations via language and culture enabled human beings to undergo sociocultural evolution with accessible, open-source encyclopedia and world-spanning collections of scientific publications. The question of "how does life form" is one of the most fundamental interests of human culture as it aims at understanding "where we come from".

Morphogenesis is the science that studies how organisms acquire their shapes as they develop from simple fertilized eggs into complex entities. Already at the beginning of our accessible research tradition, Aristotle studied aspects of morphogenesis by describing the morphology of animals and understood that birds progressively develop organs and eventually a whole organism from a fertilized egg in a stereotypic manner (Lennox, 2017). In the 19th century German embryologists started the field of "developmental mechanics" ("*Entwicklungsmechanik"*) and tried to explore the role of mechanical forces in embryogenesis. They believed that "organ forming germ regions" ("*organbildende Keimbezirke"*) within the embryo translate invisible internal chemical differences into visible foldings through mechanical processes similar to those occurring in geology (Maienschein, 1991). In 1924, Spemann and Mangold did their key transplantation experiment and recognized the identity of organizing centers in the dorsal lip of amphibian

gastrulas that were able to induced secondary embryonic primordia regardless of the transplantation location in another embryo (Oppenheimer, 1991). However, a deeper understanding of how tissues are patterned and cells differentiate during development was achieved only in the late 1970s by Christiane Nüsslein-Volhard and Eric Wieschaus when they performed a large-scale mutagenesis screen in *Drosophila* at the EMBL in Heidelberg (Nüsslein-Volhard and Wieschaus, 1980; Wieschaus and Nüsslein-Volhard, 2016). They identified gene circuits that subdivide the embryo into discrete regions restricting morphogenetic events in space and time.

1.2. General concepts in morphogenesis

A large body of work has advanced our understanding of embryonic development especially over the last decades. Molecular biology and genetic methods have provided detailed insight into gene control, signaling cascades and cell differentiation. It became evident that morphogenesis is governed by a combination of deterministic genetically controlled mechanisms that regulate tissue patterning via cell signaling and differentiation. Long-range tissue patterning is achieved by diffusible molecules called **morphogens**, which can determine cell fate in a concentration-dependent manner (Gilmour *et al*., 2017). Morphogens do not trigger morphogenetic processes directly; instead they control gene-regulatory networks in defined domains and determine the fate of cells within them by activating transcription factors. Different morphogens often work in parallel creating complex morphogenetic fields (Gilmour *et al*., 2017). An example of how gradients of morphogens act together to trigger specific gene-regulatory circuits is explained in details for the positioning of the ventral furrow in *Drosophila* in chapter (1.7.3.2, pp. 36). Likewise, juxtacrine communication between neighboring cells (like Delta/Notch signaling) can trigger distinct pathways activating cell differentiation to manifest demarcation lines between tissue domains (Perrimon *et al*., 2012).

However, neither morphogens nor transcription factors that are downstream of them influence the shape of a cell directly. The deterministic mechanisms of tissue patterning and cell signaling rather provide the framework in which morphogenesis can happen

without encoding information on the finest scale of organization e.g. to position a single molecule of the cell-cell junction complex at a pre-defined location somewhere in the developing organism with nanoscale precision. Morphogenetic mechanisms have to be robust to compensate for different environmental conditions, which genetic blueprints cannot foresee, and have to be precise enough to construct the instrumental molecular machines properly. In this work, I will follow a definition of the term "**morphogenetic mechanism**" by Jamie A. Davies as "*a combination of the molecular interactions that directly result in shape, of other molecular interactions that control them and the principles of control that are involved*" ((Davies, 2013), p. 8).

All major molecular networks on which morphogenesis relies are based on self-assembling systems. However, as I will detail below self-assembly alone does not account for the dynamic regulation required for any living system. **Self-assembly** is the "*coming together of subunits to make a structure because their association is energetically favorable and […] reasonably probable*" ((Davies, 2013), p. 14). Therefore, self-assembly is the simplest possible mechanism for morphogenesis and inherent to many processes in biology such as protein folding, antigen–antibody recognition and actin filament assembly *in vitro* (Subramani and Ahmed, 2012). Although these molecular complexes typically are held together by energetically week non-covalent interactions, involving hydrogen bonds, hydrophobic, van der Waals and electrostatic interactions, their collective effect produces structurally and chemically stable entities (Subramani and Ahmed, 2012).

Emergence is a fundamental feature of systems composed of elements that upon interaction spawn properties that cannot just be explained by their additive contribution. It means that the interaction of a system's elements features systematic properties that go beyond the combined capacity of the system's individual components in a situation, where they do not interact ("The whole is more than the sum of the parts" (Davies, 2013)). A very complex behavior can emerge from the action of very simple operations. A prominent example of emergence is the formation of complex pattern based on a simple two-component reaction–diffusion (Turing) system comprising a factor A that acti-

vates an inhibitor I, which in turn deactivates A (Davies, 2013). Translated into the language of morphogenesis, emergence is the creation of very complex forms from the action of comparatively small and simple machines (Davies, 2013). However, self-assembly systems are limited in their degree of flexibility and exclusively depend on internal error correction based on internal association strength. This does not allow them to perceive how well the system's form is adapted to its function as there is not even a definition of function for an isolated system (Davies, 2013). It also makes self-organizing systems inflexible and prone to noise and errors that are pervasive factors of an unpredictable environment. That's why self-assembly systems are embedded in a wider context of regulation that optimizes the system for a specific function during morphogenesis. The regulatory framework incorporates external **feedback** and couples the output of a process with the production of that same output (Davies, 2013). It is important to note that the type of output produced and sensed is an external effect caused by the system without being an intrinsic component of the system. This allows a system to relate to a specific function. So called "**adaptive self-organization**" multiplies a morphogenetic system's power and accuracy and enables the formation of different structures of the body in perfect proportion and at a spatial resolution much finer than given by the deposited patterning signals in a growing embryo (Davies, 2013).

In morphogenesis, feedback happens on multiple layers ranging from the level of molecular complexes, to networks of molecules, to cells, and tissues. Different morphogenetic mechanisms share the same or overlapping sets of bottom-layer organization such as the self-assembly of actin filaments, the formation of cell-cell junctions or the production of force in an actomyosin network. Yet they achieve different outcomes depending on the upper-layer control (Davies, 2013). Thus, **modularity** is another main principle governing morphogenesis. Although each 'module' splits into sub-modules that in turn can be changed and modulated. The nature of this aspect is best captured in the term "**integron**" coined by François Jacob and promoted by Davies (Davies, 2013). At each level of organization, subunits associate and integrate to form an integron. An integron is assembled by lower level integrons and takes part in assembling an integron of the level above.

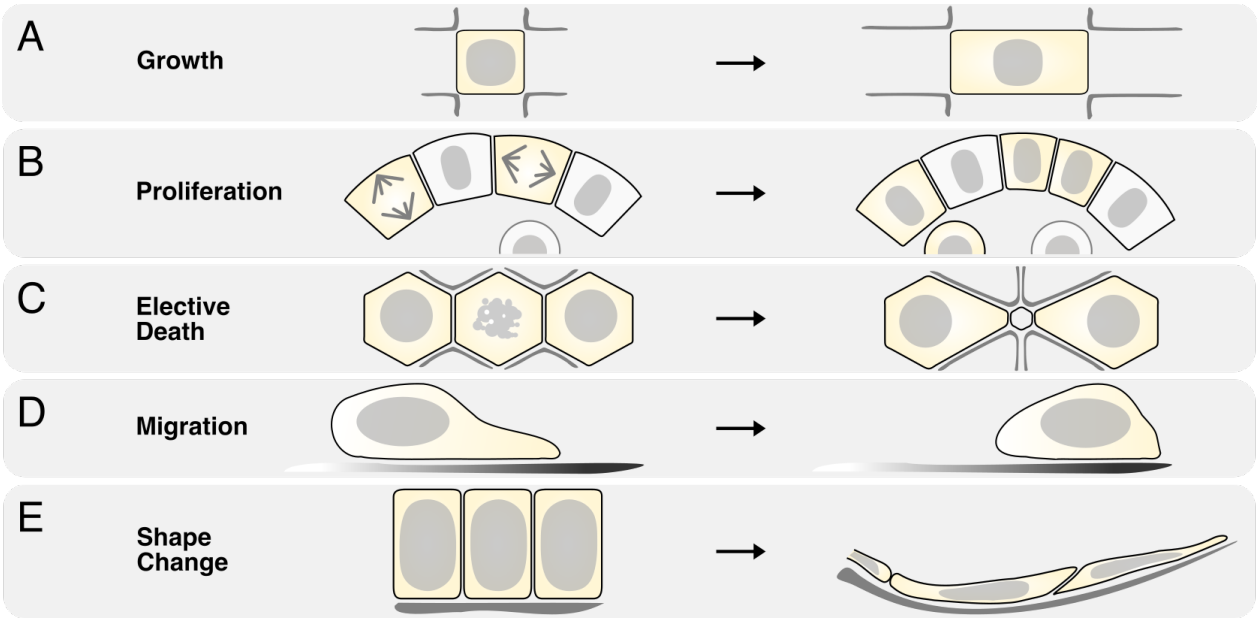

Figure 1. Mechanisms of morphogenesis. (A) Cell growth, e.g. the oriented expansion along a certain direction contributes to morphogenesis. **(B)** Proliferation e.g. by oriented cell division can impact the cell fate as seen in the mouse trophoblast, where daughter cells either contribute to inner cell mass or trophectoderm. **(C)** Elective cell death e.g. by apoptosis can contribute to create forces driving tissue folding. **(D)** Cell migration along a gradient of chemokines (and other cues) enables directed displacement of cells. **(E)** Changes in the cell shape especially of epithelia e.g. by cell flattening or apical constriction significantly drives tissue shaping.

1.3. Mechanisms of morphogenesis

The same set of integrons can be important in very different morphogenetic processes. In general, mechanisms of morphogenesis involve changes in the size, number, position or shape of cells (Heisenberg and Bellaiche, 2013). Cells can increase their size (**cell growth)** by means of fluid uptake and osmotic swelling or by metabolic growth (Figure 1A). The size of a tissue is typically determined by the size and number of resident cells (plus extracellular matrix material that can be significant in some tissues). The number of cells can change either by cell proliferation or by selective cell death in the form of apoptosis or autophagy (Davies, 2013). **Proliferation** control is essential in a developing organism and subjected to a global size sensing and regulatory systems making use of hormones (like growth hormone and insulin) and local control involving contact inhibition and paracrine signals such as Erk signaling (Davies, 2013). Oriented cell division is a morphogenetic mechanism that plays a major role in early stages of animal development determining the fate of daughter cells (Figure 1B). For example during mouse embryo-

genesis trophoblast cells divide asymmetrically to form either the placenta or the actual embryo (Morin and Bellaïche, 2011). Another striking example is represented by the snail *Lymnaea peregra*, where oriented cell division functions in defining the chirality of the body axis (Kuroda *et al*., 2009). In many other examples, oriented cell division and growth serves as a positive feedback to produce or maintain tissue shape – this is especially vital for plant morphogenesis (Davies, 2013). **Elective cell death** (Figure 1C) has three important functions during morphogenesis: to remove cells that are damaged, to adjust cell populations relative to another part of the body and to clear temporary structures (Davies, 2013).

In contrast to plants, where cells are immobile components of an assembled tissue, **cell migration** is of pivotal importance for animal morphogenesis. It fulfills important functions to bring together different cells in one location, where they might coalesce (for example blood vessel forming cells in *Xenopus laevis* (Cleaver and Krieg, 1998)), to disperse cells from a common origin (like cells of the vertebrate neural crest forming various tissues that make up the head (Le Lièvre and Le Douarin, 1975; Noden, 1983)) or to connect cells distally in a specific network (e.g neuronal growth cones forming a neuronal network (Ghashghaei *et al*., 2007)). Cell migration can be guided by different factors including chemokine gradients (chemotaxis), stiffness gradients of the substrate (durotaxis), or adhesion gradients (haptotaxis) (Figure 1D). Mesenchymal cells can undergo a special type of migratory behavior driven by protruding membranes, contractile pulling of the cell body and retraction of the cell rear (amoeboid locomotion) (Davies, 2013). This Migration behavior can be seen as a process of periodic **cell shape changes**. Cell shapes are manifold, and the shaping mechanisms include any type of isovolumetric redistribution of cytoplasm, from cell flattening and elongation, to apical constriction and basal expansion (Figure 1E). Additionally, cells can increase their surface area, undergo cell fusion and create lumens by cavitation (Davies, 2013).

1.3.1. Cytoskeletal fundamentals

All mechanisms of morphogenesis from cell growth to cell migration require the reorganization of the **cytoskeleton**, which confers shape to all animal cells (different from plant cells whose shape is predominantly determined by the cell wall). The animal cytoskeleton comprises a contractile cortical network underlying the plasma membrane and long filaments that span the entire cell body pushing and pulling the membrane. On the molecular level, it is composed of intermediate filaments, microtubules, and microfilaments consisting primarily of actin. The different cytoskeletal components contribute to different mechanical properties of the cell. Whereas actin microfilaments are tensile and provide viscoelastic properties, microtubules give the cell stability and resist compression. The distinct properties are due to structural differences. While actin microfilaments are 8 nm thick and have a high Young's modulus[1] of 2.6 GPa, which makes it perfectly suitable to bear tensional load, microtubules proto-filaments have a lower Young's modulus of 1.2 GPa, but as they are present as hollow cylinders with a diameter of 25 nm, they are 300 times more rigid than actin microfilaments and can withstand high compression loads (Davies, 2013; Gittes *et al.*, 1993).

Actin microfilaments are the primary substrate of morphogenesis and they highly dynamically re-organize during various processes including cell migration, cell shape changes and cytokinesis (Levayer and Lecuit, 2012). The adaptive self-organization of actin filaments, the cooperation with myosin-II minifilaments, other effectors and regulators of actomyosin networks will be discussed in detail in section 1.6 (pp. 13).

Microtubules are also an integral part of metazoan development, not only because of their function in assembling the mitotic spindle. During cell migration, microtubules support membrane protrusion by mechanically resisting compressive load and by enabling microtubule-dependent transport of proteins and RNAs to the leading edge of the cells

[1] The Young's modulus characterizes the tensile elasticity (resistances to stretching, or stiffness) of a solid as the ratio of stress versus strain with stress being an applied force and strain being the caused deformation.

(Etienne-Manneville, 2013). Additionally, microtubule attachment to focal adhesion sites is required to advance the cell body (Etienne-Manneville, 2013). In plant growth and morphogenesis, microtubules play fundamental roles as they are critical for anisotropic cell growth (Baskin *et al*., 1999). But also in animal cells, microtubules contribute to establishing cell polarity, an essential feature of epithelial cells discussed in (1.5, pp. 10) (Siegrist and Doe, 2007). But most importantly, microtubules, microtubule-binding proteins and the microtubule-organizing center (MTOC), from where the mitotic spindle assembles, are subject of tight developmental control to regulate proliferation and orientate cell division (Davies, 2013; Hyman and Karsenti, 1996).

In comparison, the function of **intermediate filaments** is less well understood, but it seems these biopolymers support mechanical tissue integrity and are for example needed for directed collective mesendodermal cell movements during *Xenopus* development (Sonavane *et al*., 2017).

Changes in the shape of individual cells can translate into dramatic effects at the tissue-scale – this is an apparent feature of epithelial cells, as they are connected by cell-cell adhesions allowing the transmission of forces across the cellular scale.

1.4. Morphogenesis of epithelial tissues

Epithelia separate the inside of an organism from outside. They provide an important barrier function and specialized epithelia can facilitate the exchange of substances (from air to sugar). At the same time epithelial cells are instrumental to give shape to an organism more than any other cell type.

Most newly formed epithelia arise from morphogenesis of already existing epithelia. An obvious exception is the first epithelium to be formed at the onset of embryogenesis (Davies, 2013). Although morphogenesis of the blastodermal epithelium can be remarkably different between species, the same general principles apply (Hasley *et al*., 2017). In the following paragraph, I will outline formation of the mouse blastoderm to illustrate how epithelial cells build up their unique cell architecture and how their integral molecu-

lar building blocks depend on each other. At the 8-cell stage the core molecular components of adherence junctions **E-cadherin** is activated and becomes functional (Leung *et al*., 2016). E-cadherin is a transmembrane protein whose extracellular domain builds homophilic adhesion complexes in *trans* with a neighboring epithelial cell (Hartsock and Nelson, 2008; Pinheiro and Bellaïche, 2018). The intracellular domain of E-cadherin is bound by catenin adaptor proteins (α-, β- and p120-catenin) that connect the adherence junction complex to components of the actomyosin cytoskeleton (Hartsock and Nelson, 2008). **Adherence junctions (AJ)** connect the tensile cytoskeleton to anchoring sites at the plasma membrane and link together cell neighbors allowing force transmission from one cell to the next. As cell adhesion increases, cells maximize their contact surface causing a compaction of the early embryo (Leung *et al*., 2016). During this phase, E-cadherin gets asymmetrically localized to cell-cell contacts where it delimits the basolateral domain by recruiting determinants that specify the basolateral pole including proteins of the Scribble complex (1.5, p. 10) (Kono *et al*., 2014; Vinot *et al*., 2005). On the other hand, E-cadherin is progressively removed from surfaces facing the outside of the embryo (Johnson, 2009). Mutual negative feedback mechanisms between E-cadherin and other molecules result in local modifications of the plasma membrane composition, the cytoskeleton and segregation of a set of factors anchoring in the cell-cell contact-free zone (Leung *et al*., 2016). These factors include the Par polarity complex (1.5, p. 10) and they henceforth define a structurally stable apical pole that becomes dominant in determining cell polarity (Johnson, 2009).

Between the 8- and 32-cell stages additional junctional proteins start to be expressed (Figure 2). These include **tight junction (TJ)** proteins such as occludin, zona occludens 1α-/+ (ZO1α-/+) and JAM-1, which seal the apical surface, **gap junction**-forming proteins that build pores between neighboring cells, and **desmosomal proteins**, which form cell-cell junctions connected by intermediate (cytokeratin) filaments (Collins and Fleming, 1995; Davies, 2013; De Sousa *et al*., 1993). After tight junctions have formed, sodium channels are recruited to junctions facing the inner surface and pump fluid inward to produce the blastocoel cavity leading to a spatial separation of trophectoderm and inner cell mass (Violette *et al*., 2006). At the end of trophectoderm

specification, cells are polarized biochemically and morphogenetically via a self-organization mechanism. Throughout embryonic development and also in the adult organism, epithelial polarity is maintained by the mutual antagonization of opposing protein complexes.

1.5. Cell polarity

Cell polarity can be broadly defined as a structural-functional cellular asymmetry that can be manifested as a transient state, for example the bud of a growing yeast cell, or in case of epithelial cells, which are compartmentalized in distinct basolateral and apical plasma membrane domains, as a stable condition. Cell polarization is controlled by the activity of **polarity complexes** that are highly conserved throughout evolution and their molecular components were predominantly identified in *Drosophila melanogaster*, *Caenorhabditis elegans* and yeast (Campanale *et al*., 2017). Polarity complexes comprise proteins containing protein-protein interaction domains, such as PDZ domains, that serve as scaffolds at distinct signaling centers in the apical, lateral and basal plasma membrane domains (Margolis and Borg, 2005). The apical domain is defined by the Crumbs complex, the apical/junctional domain by the Par complex, and the basolateral domain by the Scribble complex (Figure 2). At the apical plasma membrane domain, the integral membrane protein Crumbs forms a stable complex with PALS1 (*Drosophila* Stardust) and PALS1-associated tight junction homologue (PatJ) (Margolis and Borg, 2005). PatJ is a versatile scaffold protein containing multiple PDZ domains that bind to TJ proteins (Roh *et al*., 2002). The Crumbs complex physically interacts with proteins of the Par complex, which is composed of Par3 (*Drosophila* Bazooka), Par6 and the atypical protein kinase C (aPKC), a direct interactor of Par6 whose kinase function plays a pivotal role in polarity signaling (Campanale *et al*., 2017; Margolis and Borg, 2005). Both, Crumbs and Par proteins antagonize the Scribble complex, which is called complex even though there is limited support for physical interaction of its components. However, genetic analysis strongly suggests cooperative behavior in defining the basolateral domain. Besides Scribble (Scrib), the complex also comprises Discs Large (Dlg) and Lethal Giant Larva (Lgl) (Margolis and Borg, 2005). Additionally, there is emerging

evidence for another basal-specific polarity complex that includes yurt, coracle, neurexin IV and the sodium channel Na^+/K^+-ATPase (Figure 2) (Campanale *et al.*, 2017).

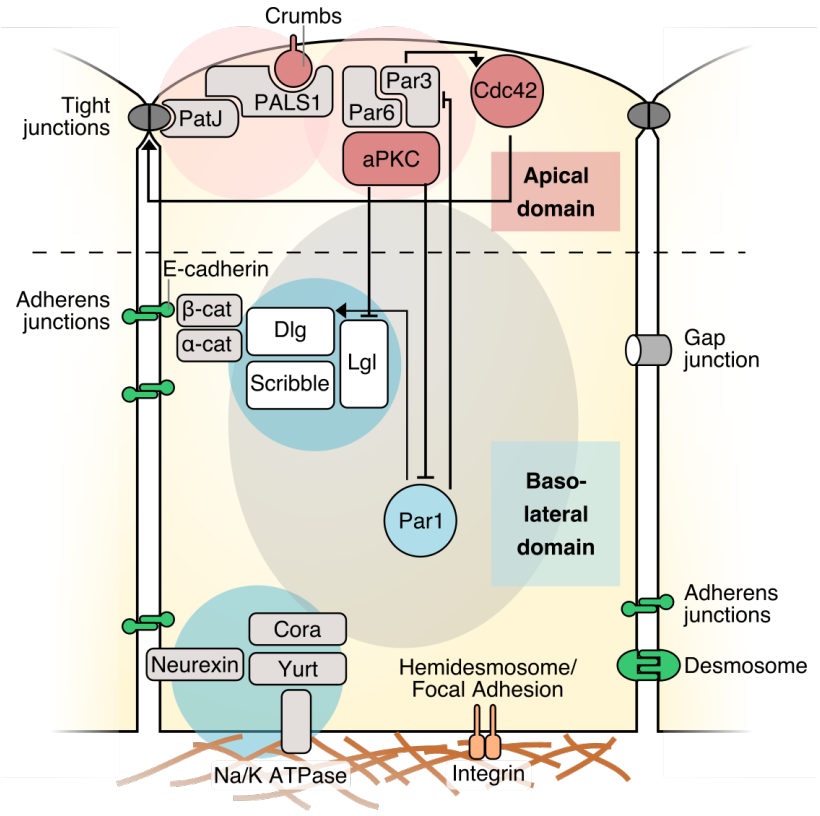

Figure 2. Cell polarity in an epithelial cell. The apical polarity complexes Crumbs (Crumbs, PALS1 (*Drosophila* Stardust), PatJ) and Par (Par3 (*Drosophila* Bazooka), Par6, aPKC) define the apical domain. Mutual negative feedback delimits the basolateral complex Scribble (Scrib, Dlg, Lgl) and a (putative) complex involving yurt, coracle, neurexin IV and the sodium channel Na^+/K^+-ATPase. The RhoGTPase Cdc42 is essential in organizing the apical domain. A signaling circuit described in the main text is depicted as an example. Epithelial cells contain different junctions like tight junctions that seal gaps, adherence junctions that connect the actin cytoskeleton to cell neighbors, gap junctions that allow molecule transport, basal junctions via Integrin (focal adhesion, hemidesmosome) that connect the cell to the ECM and desmosomes that connect intermediate filaments.

Polarity complexes scaffold **RhoGTPases** to distinct membrane domains, where they play pivotal roles in controlling cell shape by regulating the cytoskeleton, vesicle trafficking and the distribution and stability of E-cadherin-mediated adhesion complexes (Aelst and Symons, 2002). The RhoGTPase Cdc42 controls the apical complex by direct interaction with Par6 and promoting aPKC activity and TJ assembly (Figure 2) (Campanale *et al.*, 2017). The Crumbs complex protein PatJ binds TJ proteins (AJ proteins in *Drosophila*) and thus locates the apical complex. In turn, Par6 binds to Crumbs components and is associated with Bazooka, which promotes recruitment of Cdc42 providing a positive feedback loop between Crumbs, Par, Cdc42 and TJs (AJs in *Drosophila*) within the apical domain (Campanale *et al.*, 2017). In contrast, Par1 kinase, which does not belong to the Par complex, promotes the localization of the Scribble complex to basolateral AJs

or septate junctions (in *Drosophila*) and prevents basolateral localization of Bazooka (Campanale *et al*., 2017). In the apical domain aPKC directly represses Par1 kinase and components of the Scribble complex giving an example of the negative feedback between apical and basolateral domains (Figure 2). Mutual feedback mechanisms are fundamental for self-organization of cell polarity.

The correct positioning of cell junctions requires their connection to the cytoskeleton and sensation of mechanical forces (Pinheiro and Bellaïche, 2018). At AJs, E-cadherin is connected to the actin cytoskeleton via catenins, while at the cell base, transmembrane adhesion receptors such as integrins bind to components of the extracellular matrix (ECM). Integrins are also linked to intermediate filaments (forming hemidesmosomes) and to the actin cytoskeleton via adaptor proteins such as talin, vinculin and **focal adhesion** (FA) proteins like FA kinase (FAK), Src family kinases or Zyxin (Stutchbury *et al*., 2017). A number of these proteins serve as mechanosensors, converting mechanical stimuli to biochemical responses (mechanotransduction). They reinforce their interaction (catch bonds) in response to mechanical stress and activate RhoGTPases to reorganize the cytoskeleton (Ohashi *et al*., 2017). Consequently, both AJs and FAs can not only bear force but also undergo force-dependent maturation and maintenance, thus providing a self-organization mechanism to stabilize junctions that are properly connected to the cytoskeleton and functional in transmitting forces to the substrate or cell neighbors. Mechanotransduction mechanisms are important feedback mechanisms for morphogenetic processes as they coordinate cell behavior and mechanics on a short time scale and can even cause effects on longer time scale by modulating gene expression and impacting on cell fate (e.g. via YAP/Hippo signaling) (Gilmour *et al*., 2017).

From this brief overview, it is clear that the shape of a cell is governed by transmission of mechanical forces through components of the cytoskeleton, through the arrangement of its elements and their connection to the plasma membrane and the extracellular matrix via adhesion complexes. Thus, the problem of understanding cell shape regulation becomes a problem of understanding the placement of the components of the cytoskeleton (Davies, 2013). To approach this problem, it is essential to understand how the ma-

jor force-generating source in living cells, the actomyosin cytoskeleton is regulated *in vitro* and *in vivo*.

1.6. Actin microfilament regulation

The main components of microfilaments are actin fibers that are either organized in branched networks (for example at the cell cortex), or in bundles (stress fibers) that can bear tension. Minifilaments composed of myosin-II make actin fibers slide along each other and represent the primary motor of cell contractility. Other key components of microfilament organization are crosslinkers of actin fibers, and proteins that influence actin filament assembly and stability or that control myosin-II activity. The mutual interplay of these effectors will be discussed in the following chapter.

1.6.1. Self-organization of actin filaments

Globular actin monomers (**G-actin**) are 42 kDa proteins that have a binding pocket for adenosine di- and triphosphate (ADP, ATP) and possess ATP hydrolysis activity (Blanchoin *et al.*, 2014). G-actin monomers can polymerize spontaneously to form double-stranded and right-handed twisted actin filaments (**F-actin**). Each subunit makes contact with four other subunits and bivalent cations, which in physiologic conditions is typically Mg^{2+} (Blanchoin *et al.*, 2014). Self-assembly of actin filaments is thermodynamically limited by the initial nucleation step (Figure 3A). Actin dimers are highly unstable. However, upon trimerization the filament elongates rapidly as a function of monomer concentration and thermal energy (Davies, 2013). Addition of a monomer to a filament's end is followed by ATP hydrolysis. While both filament ends can grow, the (so-called) barbed end grows with 3,000 subunits/s 10 times faster than the (so-called) pointed end, giving the filament directionality (Blanchoin *et al.*, 2014). During cell and tissue morphogenesis the self-assembly of actin filaments is embedded in a wider context of regulatory proteins and mechanistically is one of the most fundamental morphogenetic integrons.

1.6.2. Regulation of F-actin assembly and stability

In vivo spontaneous (and thus uncontrolled) actin self-assembly in cellular regions with high G-actin concentration is prevented by actin **monomer-binding** proteins such as profilin (Figure 3B). Profilin also prevents nucleation at the pointed end ensuring polarized filament growth. **Nucleation** of new filaments depends on proteins that outcompete profilin for actin binding and mimic or stabilize the trimeric state, namely the Arp2/3 complex and formin family proteins (Davies, 2013). These two classes of actin polymerizing factors promote the formation of structurally different networks: whereas formins nucleate straight filaments e.g. at the inner side of adhesion complexes, Arp2/3 produces branched actin networks characteristic for cortical actin gels (Figure 3B). The Arp2/3 complex nucleates actin filaments on the side of existing filaments at a 70° angle (Goley and Welch, 2006). Branched networks generate force when they are assembled in proximity to the membrane surface, as it is the case for example at the leading edge of a migrating cell. The activity of Arp2/3 is controlled by other regulators including WASP/WAVE proteins, whose activity is tightly regulated at regions close to the plasma membrane (Blanchoin *et al.*, 2014). Branch elongation is limited by **capping proteins** such as gelsolin that block barbed end polymerization, while antagonistic proteins such as Ena/VASP, and **anti-capping proteins** present in filopodia promote branch elongation (Figure 3B) (Blanchoin *et al.*, 2014). Actin filaments can be **severed** and fragmented by ADF/cofilin. Actin bundles can originate from branched filaments liberated from their connections, by ADF/cofilin or by formin-mediated filament assembly. Straight filaments when bound and **cross-linked** by proteins such as Fascin, Fimbrin, α-actinin and Filamin can be consolidated into bundles that are tightly linked or that can slide over each other (Blanchoin *et al.*, 2014). While many proteins are able to crosslink actin fibers, myosin-II is of particular importance as the combined action of actin and myosin can generate force.

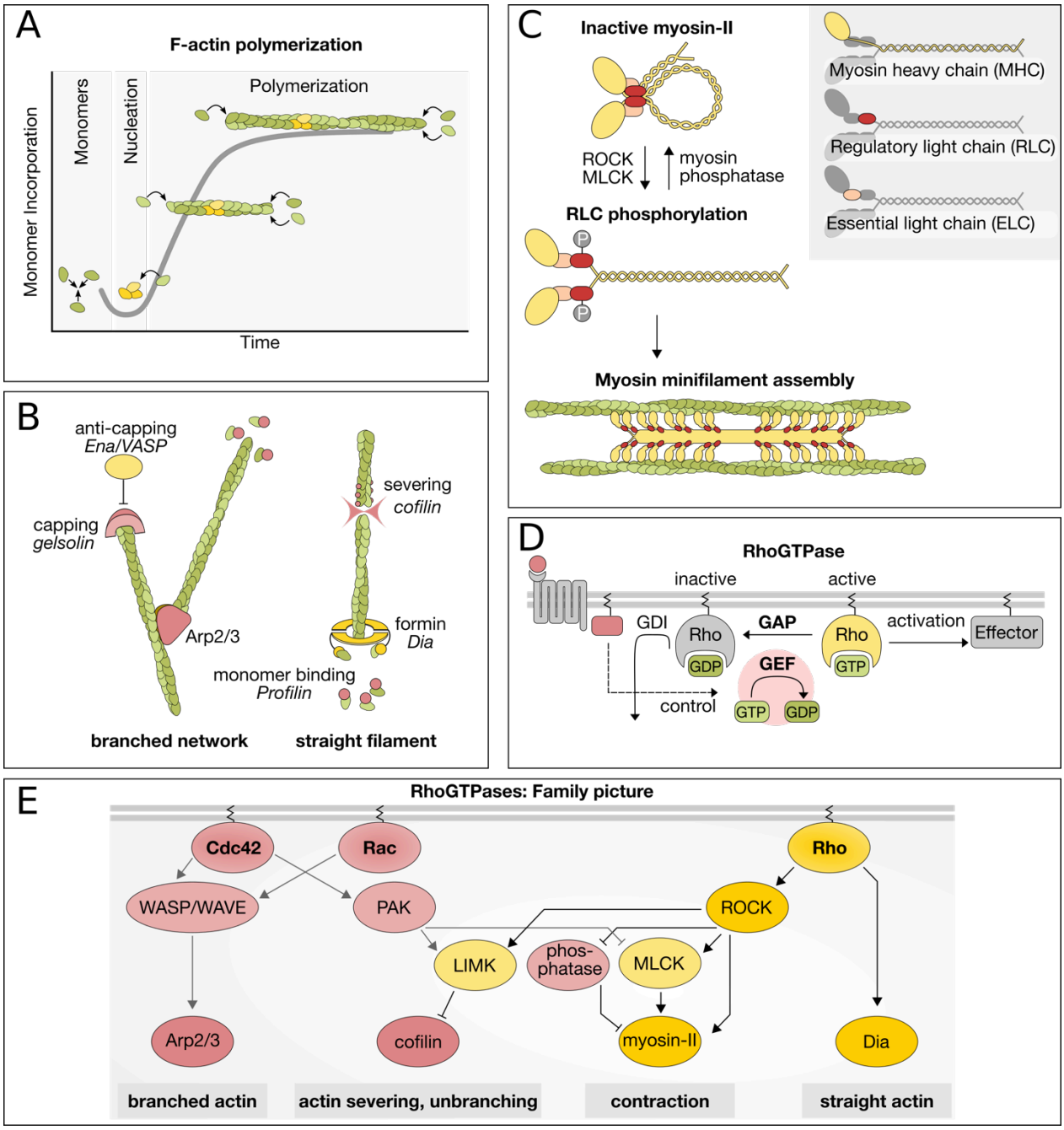

Figure 3. Molecular regulation of actomyosin contractility. (A) Actin filament self-assembly. The rate-limiting step is filament nucleation. Upon complex formation of three monomers, the probability of monomer addition increases. **(B)** Overview of actin-remodeling molecules. Actin nucleators catalyze polymerization in branched (Arp2/3) or linear structures (formin). Monomer-binding profilin prevents self-assembly. Cofilin depolymerizes and severs filaments. Capping proteins prevent filament extension. **(C)** myosin-II structure and minifilament assembly. myosin-II is a hexamer formed by MHC, RLC, ELC (two each). Phosphorylation of RLC by ROCK and MLCK triggers the assembly of myosin minifilaments and actin binding activity. **(D)** RhoGTPases are molecular switches controlling actomyosin dynamics. GDP-bound Rho is inactive. RhoGEFs triggered by upstream morphogenetic signals induce the exchange of GDP to GTP rendering Rho active. Rho-GTP activates effector proteins. RhoGAPs induce Rho-mediated hydrolysis of GTP to GDP rendering Rho inactive. Inactive Rho-GDP can be internalized and sequestered from the membrane by GDI. **(E)** The RhoGTPase family contains Cdc42 and Rac that promote branched actin networks and prevent contractility, whereas Rho stimulates linear actin fibers and cell contractility. Molecular details are described in the main text.

1.6.3. Molecular control of myosin-II activity

Myosin was first discovered in Heidelberg by Willy Kühne in 1864 (Hartman and Spudich, 2012). The superfamily of myosin motor proteins is very diverse with some isoforms having very specialized function (Hartman and Spudich, 2012). In this work myosin generally refers to **non-muscle myosin-II**, which is the pivotal motor protein organizing the cytoskeleton during morphogenesis. Myosin-II forms a hexamer of two myosin heavy chain (MHC) subunits, two essential light chains and two regulatory light chains (RLC, in *Drosophila* called Spaghetti Squash (Sqh)) (Figure 3C) (Levayer and Lecuit, 2012). Several myosin-II hexamers assemble into bipolar minifilaments that in their projecting head region can bind to actin and crosslink fibers (Figure 3C). Myosin additionally has ATPase activity and the presence of ATP/ADP influences its affinity for actin. Presence of ATP in the binding pocket impedes interaction with actin, and hydrolysis of ATP into ADP and phosphate induces a conformational change and straightening of myosin-II. Dissociation of ADP and phosphate causes a sudden increase in affinity for actin leading to actin binding followed by a restoration of the initial conformation which produces a power stroke sliding the actin filament by about 5 nm forward (Davies, 2013). By repeating this cycle in all myosin-II heads present in the minifilament, contractility is generated by pulling on actin filaments of opposite orientation in a sarcomere-like fashion.

The assembly of myosin-II hexamers, myosin binding to actin and its ATPase activity depend on the **phosphorylation state of RLC** (Figure 3C). While kinases such as Rho-associated coiled coil-containing kinase (ROCK) and myosin light chain kinase (MLCK) phosphorylate RLC and promote cell contractility, myosin phosphatase negatively regulate RLC phosphorylation and myosin-II activity (Levayer and Lecuit, 2012). Instead, phosphorylation of MHC by myosin heavy chain kinase (MHCK), casein kinase II and protein kinase C inhibits myosin-II minifilament assembly (Levayer and Lecuit, 2012). Essential signal transduction routes with input from the cell polarity machinery, mechanotransduction, cell cycle control and many other cellular processes culminate in the

spatiotemporal regulation of myosin-II activity via RhoGTPases signaling (Etienne-Manneville and Hall, 2002).

RhoGTPases are simple molecular switches that control diverse biological processes providing yet another example of the reoccurring principle of emergence in morphogenesis. The small GTPases cycle between two conformational states: an active GTP-bound and an inactive GDP-bound state (Figure 3D). In the active state RhoGTPases interact with effector proteins and initiate downstream signaling cascades. The common mechanism of effector protein activation appears to be the disruption of auto-inhibitory intramolecular interactions and the exposition of catalytic domains in case of target proteins with enzymatic activity (Bishop and Hall, 2000). The intrinsic GTP hydrolysis activity returns the protein to the GDP-bound inactive state thereby terminating signal transduction (Bishop and Hall, 2000). Rho activity is regulated by a variety of proteins. Guanosine nucleotide exchange factors (**GEF**s) facilitate the exchange of GDP to GTP. GEF proteins contain the catalytic Dbl-homology (DH) domain, a lipid-binding pleckstrin homology (PH) domain positioning the protein at the plasma membrane and protein-specific domains regulating subcellular localization and activation mechanisms (Bishop and Hall, 2000). GTPase-activating proteins (**GAP**s) catalyze the inverse functional operation by increasing the intrinsic GTPase activity rendering signal transduction inactive (Figure 3D).

RhoGTPases are peripherally anchored at the plasma membrane via a C-terminal lipidation. **RhoGDI** (guanosine nucleotide dissociation inhibitor) binds and sequesters inactive RhoGTPases away from the plasma membrane to prevent activation by GTP exchange, however the physiologic function and exact mechanism of RhoGDIs is still under debate (Boulter and Garcia-Mata, 2010). The most prominent members of the RhoGTPases family are Rho, Rac and Cdc42 (Figure 3E). Despite the common molecular mechanism of action, these three family members display distinct functions by regulating an overlapping set of integrons. Rac and Cdc42 have closely related function in promoting actin polymerization and stability, counteracting actomyosin contraction, and causing the formation of membrane ruffles, lamellipodia and filopodia (Bishop and Hall, 2000). In con-

trast, Rho signaling facilitates actomyosin contraction and stress fiber formation**. Rac and Cdc42 signaling** activates WASP/WAVE family proteins and the Arp2/3 complex to produce branched actin networks and inhibits cofilin-mediated actin severing (through LIMK). Additionally, they counteract myosin-II-mediated contraction by preventing myosin minifilament assembly through the activation of p21-activated kinase (PAK), an inhibitor of MLCK (Figure 3E). Moreover, Cdc42 has already been mentioned as an essential molecular factor regulating cell polarity (Aelst and Symons, 2002; Etienne-Manneville and Hall, 2002).

Rho signaling is based on the activation of two major effectors ROCK and the formin Diaphanous (Dia), which drive the assembly of stress fibers, focal adhesions and network contraction (Figure 3E) (Etienne-Manneville and Hall, 2002). ROCK activates myosin-II by phosphorylating and activating MLC and phosphorylating and inhibiting the antagonistic MLC phosphatase. In addition ROCK activates LIMK, which in turn inhibits cofilin. Moreover, Dia activation causes unbranched F-actin assembly. Rho signaling orchestrates the assembly of the cytokinetic furrow and contractile actomyosin rings as shown in *Xenopus* and sea urchin (Drechsel *et al.*, 1997; Mabuchi *et al.*, 1993). Many cell shape changes observed during development rely on Rho signaling (Etienne-Manneville and Hall, 2002) as discussed in (1.7.2, pp. 31).

1.6.4. Contraction of actomyosin networks

Besides the importance of regulating myosin-II activity, the contractile behavior of an actomyosin network is controlled by parameters that define the structural organization of actin fibers. These include the orientation of actin filaments in polarized or disordered patterns; the level of Arp2/3-mediated branching respective to the content of linearized actin filaments; actin polymerization and depolymerization kinetics, and importantly the type and level of actin crosslinking (Blanchoin *et al.*, 2014; Levayer and Lecuit, 2012). Cross-connections between actin filaments are mediated by actin **crosslinkers** and allow the network to achieve complex macroscopic architectures (Falzone *et al.*, 2012; Kasza *et al.*, 2010; Lieleg *et al.*, 2010; Schmoller *et al.*, 2009). Gelation, “the formation of

a three-dimensional network by […] physical cross-linking" (Mulder, 2000), provides actin networks **viscoelastic** characteristics. Due to molecular rearrangements in response to an applied stress, actin networks display elastic behavior on short time scales (less than a minute), but behave like a viscous fluid on longer time scales (Blanchoin *et al.*, 2014). In living cells crosslinked networks are heterogeneous mixtures of actin structures (co-presence of meshworks and bundles) with some network components stretching and others compressing upon force application causing non-linear stress responses (Gardel *et al.*, 2004).

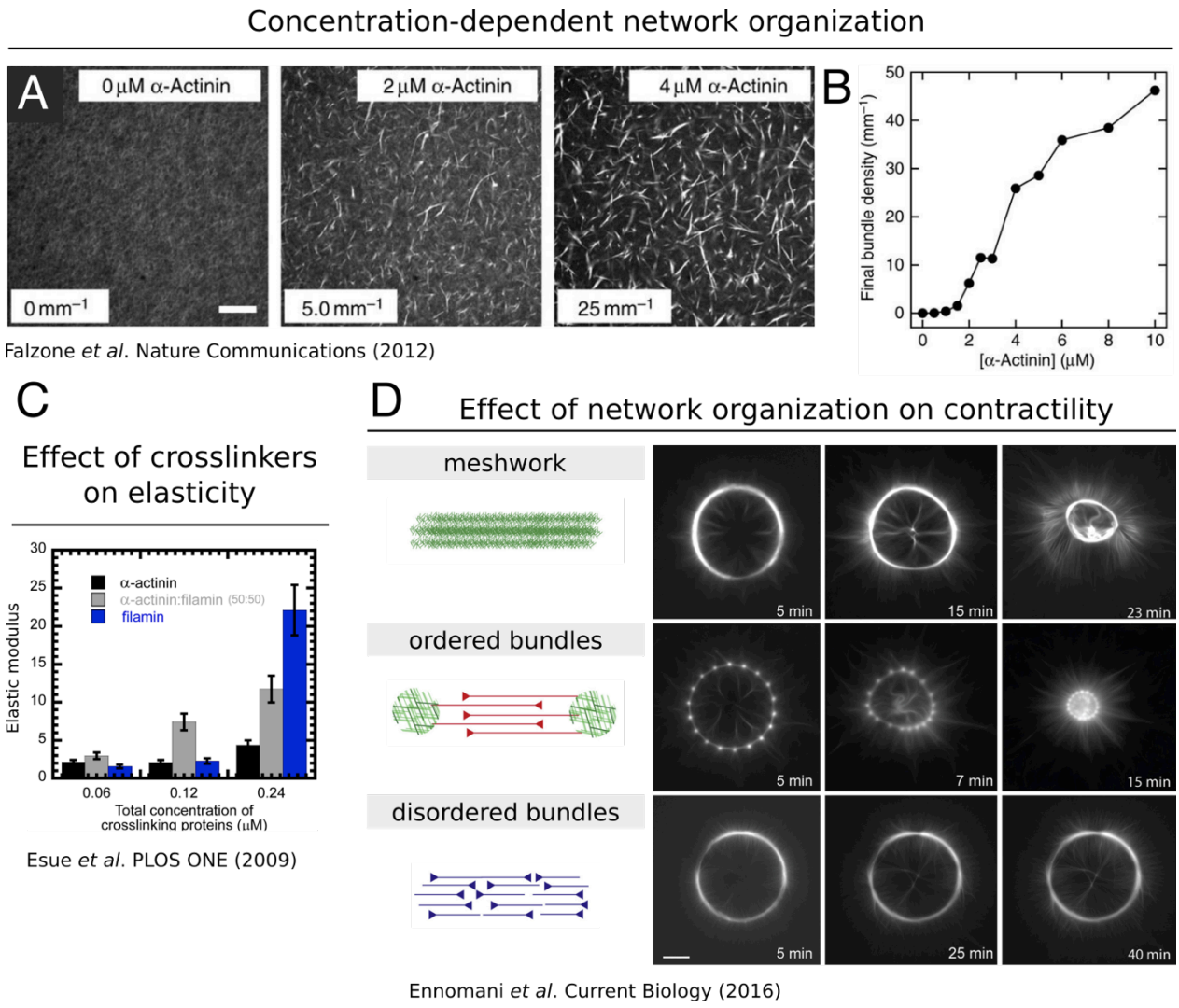

Figure 4. Crosslinker-mediated network organization and effect on contractility *in vitro*. (A) Steady state images of *in vitro* reconstituted actin networks with increasing (left to right) concentrations of the actin crosslinker α-actinin (Falzone *et al.*, 2012). At low α-actinin concentration an actin meshwork forms, whereas with increasing concentration bundles become more prevalent. **(B)** Quantification of actin bundle density over α-actinin concentration demonstrates a crosslinker concentration-dependent effect on network structuring (Falzone *et al.*, 2012). **(C)** Measured elastic

modulus of actin networks in presence of α-actinin, filamin and a combination of the two reveals a concentration-dependent increase in elastic modulus (Esue *et al*., 2009). The data show that at low equimolar concentration different actin crosslinkers can have synergistic effects in increasing network elasticity. A concentration of 0.24 *μ*M is above the crosslinking-to-bundling threshold of filamin resulting in a strong increase in elastic modulus. **(D)** Effects of network organization on contractility (Ennomani *et al*., 2016). The organization and orientation of actin filaments in either meshwork, ordered (anti-parallel) and disordered (non-polarized) bundles affect the contractile behavior of micropatterned actomyosin networks *in vitro*. (**A-D**) Figures were adapted from indicated publications with permission from the publisher (7.2, pp. 149).

Many actin-crosslinking proteins contain a tandem of dissimilar **calponin homology (CH)** domains (an N-terminal or type 1 CH domain that physically binds actin and a C-terminal or type 2 CH domain that has regulatory function) (Gimona *et al*., 2002). CH1 and CH2 cooperate in F-actin binding and are therefore sometimes referred to as actin binding domain (ABD). Proteins facilitating F-actin binding via canonical CH1/2 domains include spectrin, α-actinin and Filamin. Their affinity towards actin is very high (low *μ*M range) (Gimona *et al*., 2002). To bridge bound actin filaments, crosslinkers either contain more than one actin binding domain or they undergo dimerization. **Filamin** for example is a crosslinker bigger than 200 kDa that contains an N-terminal CH1/2 domain, 20-24 β-barrel structured Ig-like FLN repeats (IgFLN) separated into two rods by a flexible hinge region (Nakamura *et al*., 2011). The last C-terminal IgFLN mediates dimerization so that Filamin is present as a V-shaped dimer in its native state. The shape of the dimer, however, can change upon protein interaction and deforms when stressed by mechanical tension exposing cryptic binding sites, which provides Filamin mechanosensory properties and gives Filamin high freedom to organize actin structures (Ehrlicher *et al*., 2011; Gay and Baudier, 2011; Gay *et al*., 2011a; Nakamura *et al*., 2009, 2011). On the other hand, **Fimbrin** is a relative small protein that contains four CH domains (of non-canonical, distinct classes), defining two ABDs with which it can crosslink actin filaments (Gimona *et al*., 2002). In addition Fimbrin contains EF-hand modules that appear to participate in actin binding and provide regulatory function (Klein *et al*., 2004). Both Filamin and Fimbrin are evolutionary highly conserved and important components of actin network-organizing apparatus.

Based on *in vitro* experiments in reconstituted actin networks, the general notion is that depending on the size of an actin crosslinker, which limits the distance at which actin fibers can be connected, the formation of different **network architectures** can be fa-

vored: small crosslinkers such as Fimbrin or Fascin pack actin filaments into bundles, while bigger crosslinkers like Filamin or α-actinin tend to promote either formation of bundles or meshworks depending on their concentration (Figure 4A,B) (Falzone *et al*., 2012; Gardel *et al*., 2004; Lieleg *et al*., 2010; Schmoller *et al*., 2009). Due to their different molecular architecture crosslinked bundles and branched meshworks differ significantly in their contractile behavior and response to mechanical forces, with bundles revealing higher elasticity (Figure 4C) (Blanchoin *et al*., 2014; Fletcher and Mullins, 2010). However, in either network configuration, meshwork or bundle, the amount and type of crosslinking critically affects their material properties and by that their contractility depending on the degree of branching and density of packing, respectively (Figure 4C) (Esue *et al*., 2008; Pujol *et al*., 2012). For example, actin bundles can be highly contractile when filaments are crosslinked in close proximity but sufficiently separated allowing them to slide efficiently upon myosin activation. Conversely, tightly linked bundles of filaments are less accessible to myosin-II and therefore less contractile. The force that needs to be applied to bend tightly linked actin filament scales with the power of 4 of the bundle radius causing significant increase in stiffness (Blanchoin *et al*., 2014).

In addition to myosin-II accessibility, the orientation of actin filaments is critical for efficient **myosin-II-mediated contraction**. Actin bundles during cytokinesis or force-transmitting stress fibers anchored at cell adhesion complexes require anti-parallel orientation of F-actin (Blanchoin *et al*., 2014). Myosin-II activity itself seems to provide a specific mechanism for selective recognition and contraction of anti-parallel actin structures (Reymann *et al*., 2012), while specific crosslinkers such as Fimbrin and α-actinin were reported to preferentially favor the formation of anti-parallel bundles (Laporte *et al*., 2012). In a comprehensive *in vitro* study, Ennomani *et al.* tested the impact of structural organization and polarization on the contractile behavior of actomyosin networks (Figure 4D). They found that at constant crosslinking conditions, contractility depends on network architecture with ordered (anti-parallel) bundles being more contractile that non-polarized meshworks, and disordered bundles (Ennomani *et al*., 2016). In addition, the degree of connectivity (reflecting the concentration of crosslinkers) influences network contractility. At very low concentration of crosslinkers, actin structures became “too

loose" and at high concentration "too stiff" to contract. Computational models further suggest the requirement of intermediate level of network connectivity for efficient contraction (Belmonte *et al*., 2017).

1.6.5. Relation of actomyosin network architecture to function *in vivo*

Actomyosin networks of different architectures display distinct mechanical properties. **Actin bundles** organized in rings and anchored at the plasma membrane regulate cytokinesis (Pollard, 2010; Schwayer *et al*., 2016) or can be observed in cells being extruded from an epithelium (Teng *et al*., 2017). Multicellular actomyosin rings in which aligned actomyosin cables connected through AJs form to close epithelial holes upon injury or during development as for example during dorsal closure in *Drosophila* (Agarwal and Zaidel-Bar, 2018). During this process, leading edge cells of the epidermis build a supracellular actomyosin ring to facilitate apical constriction of amnioserosa cells, thereby moving dorsally to close the dorsal hole (Solon *et al*., 2009). Actomyosin bundles also contribute to the formation of tissue compartment boundaries in *Drosophila*. The asymmetric localization of myosin-II-mediated contractility at compartment boundaries straightens the demarcation line between tissues and prevents cell mixing (Heisenberg and Bellaiche, 2013). These morphogenetic mechanisms rely on mechanosensitve regulation of cytoskeletal and junctional components that facilitate AJ remodeling and reinforcement of actin stress fibers under tension with high spatial accuracy (Pinheiro and Bellaïche, 2018).

Meshwork-like actomyosin networks form the cortex of animal cells (Agarwal and Zaidel-Bar, 2018). For example, epithelial cells undergoing apical constriction during ventral furrow formation organize medioapical actin structures in a radially polarized network with medial myosin-II accumulation and actin fibers anchored at the AJs (Martin *et al*., 2009). This radial organization of the cytoskeleton is important for tissue level effects (Chanet *et al*., 2017) and will be discussed in more detail later (1.7.3.2., pp. 32). The cortical actin meshwork of the *C. elegans* zygote contracts and causes myosin-II coalescence in foci connected by actin cables (Ding *et al*., 2017). Network contraction

relaxes upon sperm entry initiating a polarized cortical flow and asymmetric cell division (Marston and Goldstein, 2006). A meshwork-like actomyosin network also dominates the neuronal growth cones of *helisoma* neurons (Welnhofer *et al*., 1997) providing it with flexibility and motile properties.

While apical cytoskeletal organization of epithelia is important for various morphogenetic processes, some systems also reveal a critical **role for basally localized networks**. The basal cell surface is in contact with the ECM, and is involved in sensing the mechanical properties of the substratum during cell migration (haptotaxis, durotaxis) via integrin-mediated FAs and other cell-matrix interactions. Connection of contractile bundles to cell-matrix junctions ensures efficient tissue-scale force transmission and is for example essential for *Drosophila* dorsal closure and *Zebrafish* retinal tissue folding (Agarwal and Zaidel-Bar, 2018; Goodwin *et al*., 2016; Nicolás-Pérez *et al*., 2016). In the *C. elegans* reproduction-related myoepithelium spermatheca, contractility is driven by basal circumferential actomyosin bundles (Wirshing and Cram, 2017). During oogenesis in *Drosophila* egg chamber elongation depends on contractions of the basal actomyosin network transmitting force to cell-matrix complexes and E-cadherin-mediated cell-cell adhesions (Qin *et al*., 2017).

1.6.6. Regulation of actomyosin network transitions

Highly dynamic morphogenetic processes require actomyosin networks to be tightly regulated in space and time. **Switches in myosin-II activity** drive network transitions for example by aligning actin filaments into anti-parallel bundles as seen during ovulation in *C. elegans* spermathecal (Wirshing and Cram, 2017). Radial polarity of the medioapical actomyosin network during *Drosophila* ventral furrow formation only forms upon activation of myosin-II (Chanet *et al*., 2017). As described in section 1.6.3 (pp. 16), myosin-II activity is controlled via its phosphorylation state by RhoGTPases signaling. Developmental signaling pathways regulate RhoGEF localization and activity to initiate Rho signaling and stimulate myosin-II. To restrict myosin-II activity spatially, GEFs and GAPs are often present within the same region to create a spatially restricted Rho “active

zone": Upon RhoGEF activation, Rho has a short-lived opportunity to bind its effectors as it will rapidly be inactivated by RhoGAP (Agarwal and Zaidel-Bar, 2018; Bement *et al*., 2006). Once activated, myosin-II can generate positive feedback as observed during cytokinetic ring constriction, where myosin-mediated contraction generates a cortical actomyosin flow towards the ring (Khaliullin *et al*., 2018). Negative feedback loops can involve effector protein recruitment to actomyosin-rich regions inhibiting further accumulation of myosin-II or active recruitment of RhoGAP in response to tension (Tan and Zaidel-Bar, 2015; West *et al*., 2017).

Other mechanisms of actomyosin network transitions are **independent of myosin-II** activity. Coordinated actin nucleation by Arp2/3 and formin proteins for instance triggers the formation of a contractile actomyosin coat around large vesicles providing the necessary force for efficient cargo release (Rousso *et al*., 2016). Likewise, coordinated destabilization of actin fibers by actin severing proteins increases F-actin turn over, which is essential for the dynamic behavior of most actomyosin networks (Belmonte *et al*., 2017). Moreover, cofilin-mediated turnover induces cytokinetic ring assembly and constriction in yeast (Chen and Pollard, 2011; Chen *et al*., 2015).

The critical function of **actin crosslinking** has already been discussed (1.6.4, p. 18). Actin crosslinking increases the length, scale and effectiveness of actomyosin contraction and connectivity has major effects on contractile behavior *in vitro* (Agarwal and Zaidel-Bar, 2018; Ennomani *et al*., 2016). *In vivo*, the Fimbrin was shown to be required for cortical rearrangements driving polarization and cytokinesis of the *C. elegans* zygote (Ding *et al*., 2017). Other studies have proposed that sequential myosin-dependent and myosin-independent mechanisms drive network transitions and contraction (Xue and Sokac, 2016). A major focus of the present thesis was to investigate the function of actin crosslinkers in governing actin network architecture and their putative role in timing network transitions and contractility. To this end, I focused on the process of cellularization during *Drosophila melanogaster* embryogenesis as it provides an ideal model system to study actomyosin network regulation in an *in vivo* context for reasons that I will discuss in the next chapter.

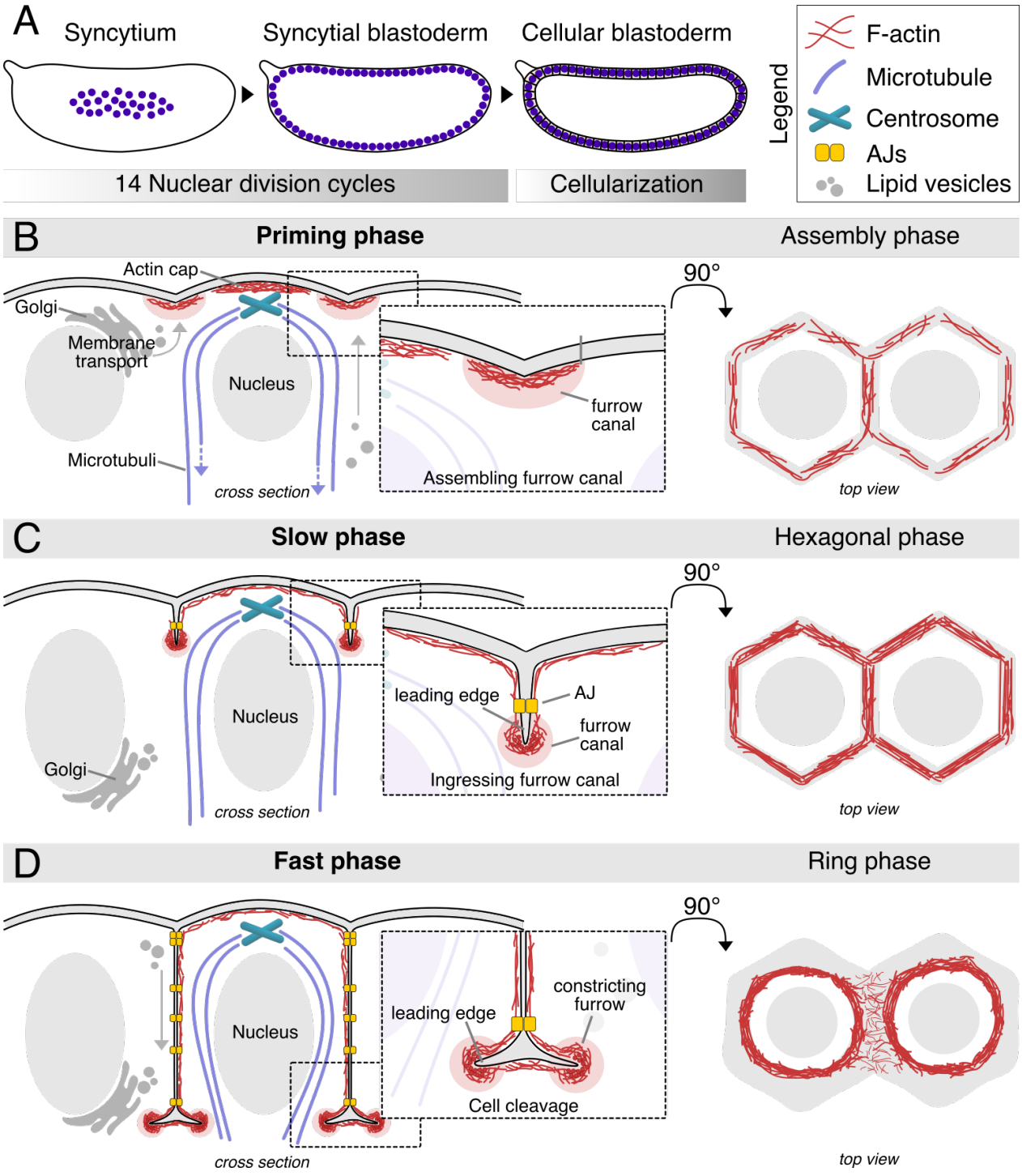

Figure 5. Overview of *Drosophila* cellularization. (A) The early *Drosophila* embryo undergoes a series of nuclear division cycles without cytokinesis. At NDC 9 the nuclei translocate giving rise to the syncytial blastoderm. During interphase of cycle 14, the plasma membrane ingresses and compartmentalizes the nuclei to form individual cells (cellularization). Cellularization integrates membrane transport, cell polarity, microtubule and actomyosin dynamics. **(B-D)** Schematic depiction of a cross section (left) showing the invaginating membrane (gray), which is pulled by the basal actomyosin network (red) at the leading edge (light red) of the cellularization furrow. Microtubule (purple) dynamics support membrane growth and subcellular distribution of cellular components. Upon further ingression of the plasma membrane, basal AJs (yellow) form; apical AJs appear at mid-cellularization. Descriptions of these processes are detailed in the main text. On the right a top view shows the basal actomyosin network at the initial assembly phase

during the priming phase (B), the stable hexagonal phase during slow phase (C) and the contractile ring phase during fast phase (D). The initial actomyosin meshwork transforms into a hexagonal array of actin bundles that does not constrict. When the cellularization furrow reaches the base of nuclei, the actomyosin network transforms into individual ring structures and constricts. Please note, that the depiction of this process was prepared during the end of my PhD time and was informed by results and insight that I gained during the whole period of my PhD.

1.7. Actomyosin-dependent building and remodelling of epithelial tissues

1.7.1. Cellularization: *de novo* formation of an epithelium

After fertilization, the *Drosophila* zygote undergoes a series of rapid mitotic nuclear divisions that are not accompanied by cytokinesis (Figure 5A). Nuclei divide initially in the interior of the embryo and move towards the surface after nuclear division cycle (NDC) 9 to form a **syncytial blastoderm** (Mazumdar and Mazumdar, 2002). After NDC 14, the embryo contains ~6000 nuclei and enters an extended interphase during which membranes ingress in between nuclei to eventually separate individual cells, to form a **cellular blastoderm** (Figure 5A) (Mazumdar and Mazumdar, 2002). This process is called cellularization, and although it is remarkably different from early mammalian zygotic divisions (1.4, pp. 8), it makes use of a common set of morphogenetic integrons including integration of cell polarity complexes, cell-cell adhesion, membrane trafficking and cell contractility.

1.7.1.1. Polarized plasma membrane remodelling during cellularization

Cellularization is a highly dynamic process starting by the end of NDC 13 when nuclei appear underneath the plasma membrane which is already partially polarized as previous metaphase pseudo-furrows establish a compartmentalization to prevent collision of mitotic spindles and to provide a basic structural framework for the emergence of the cleavage furrow (Grosshans *et al*., 2003; Mavrakis *et al*., 2009; Padash Barmchi, 2005). F-actin which is initially organized as an apical cap on top of the nuclei progressively accumulates at the tip of the ingressing membrane (Schejter and Wieschaus, 1993), leading to the formation of the **cellularization furrow** (or furrow canal) (Figure 5B). During this phase (**priming phase**), actin becomes enriched at the base of the cellulariza-

tion furrows in a process that depends on Rho1 activity (Crawford *et al*., 1998). The formin Diaphanous1 (Dia1) localizes at leading edge of the cellularization furrow throughout cellularization and both F-actin and myosin-II levels increase progressively during the first half of cellularization (Xue and Sokac, 2016). At the same time, microtubules arise from the cortically anchored centrosome pair and extend perpendicular to the apical plasma membrane plane forming an inverted basket around the nuclei. As microtubules extend towards the interior of the embryo, the shape of the nuclei changes and elongates in parallel with microtubule growth. Microtubules also control apicobasal distribution of organelles such as the Golgi apparatus and lipid droplets (Sisson *et al*., 2000; Welte *et al*., 1998). During this initial stage, called the **slow phase** of cellularization (Figure 5C), the membrane ingresses inward driven by the directed progression of the cellularization furrow. The slow phase accounts for two third of the whole duration of cellularization but only for 10 μm of the total 40 μm of membrane extension (Xue and Sokac, 2016). During the slow phase the actomyosin network is organized in an array of highly symmetric hexagons, which surround each nucleus, spanning the entire basal surface of the embryonic tissue. This hexagonal network is stable and does not constrict.

Cellularization requires incorporation of new membranes (**membrane growth**) which originates both from Golgi-derived vesicle trafficking as well as from apical microvilli and apical endocytosis (Figure 5B,C) (Fabrowski *et al*., 2013; Figard *et al*., 2016; Lecuit and Wieschaus, 2000). As the membrane ingresses, cells acquire **apicobasal polarity** by forming specialized basal AJs in close proximity of the inward-moving cellularization furrow (Figure 5C,D) and later at mid-cellularization apical AJs (Hunter and Wieschaus, 2000; Müller and Wieschaus, 1996; Tepass, 1997; Thomas and Williams, 1999). Septate junctions (SJs), which are homologous to vertebrate TJs, form basally to apical AJs later during development. Junctions and cell polarity complexes demarcate the apical, apicolateral, lateral and basal plasma membrane domains (Campanale *et al*., 2017; Izumi *et al*., 2016).

The speed of membrane ingression rapidly increases by a factor of ~2 during the **fast phase** of cellularization that takes ~20 min and accounts for ~30 *μ*m of plasma membrane growth (Figure 5D) (Xue and Sokac, 2016). During this stage, the cellularization furrow reaches the base of the nuclei and the actomyosin network undergoes a transition into ring-shaped contractile units that constrict and partition each nucleus into a single cell. As mentioned above (1.6.6, pp. 23), a recent study analyzing the constriction dynamics of cellularization furrow rings proposed two consecutive phases (Xue and Sokac, 2016). A first myosin-dependent phase and a second that is controlled by the actin depolymerization, and adaptor proteins implicated in actin bundle formation, Anillin and Septin (Xue and Sokac, 2016). Molecular characterization of Septins demonstrated that they facilitate bundling and bending of F-actin filaments into rings (Mavrakis *et al.*, 2014). Although the molecular composition of the contractile rings observed during cellularization is very similar to that of cytokinetic rings during mitosis, the assembly of the initial hexagonal network relays on the action of gene products that are unique to the process of cellularization and might employ specific mechanisms to regulate basal network contractility.

1.7.1.2. Maternal-to-zygotic transition (MZT)

Cellularization is concomitant with zygotic genome activation (De Renzis *et al.*, 2007; Müller and Wieschaus, 1996). The early *Drosophila* embryo is transcriptionally silent and both mRNA and proteins are of maternal origin. Transcription of zygotic genes starts by NDC 11 and increases towards the onset of cellularization. While most cytoskeletal components are maternally deposited with some of them being critical for cellularization, five newly expressed **zygotic genes** are critically required for cellularization. *Frühstart* (*frs*) is required for the cell cycle arrest in interphase 14 (Grosshans and Wieschaus, 2000; Grosshans *et al.*, 2003; Sung *et al.*, 2013). *nullo*, *serendipity-α* (*sry-α*), *slow-as-molasses* (*slam*) and *bottleneck* (*bnk*) directly function in organizing the cellularization furrow. The gene products of *nullo*, *serendipity-α* (*sry-α*) and *slow-as-molasses* (*slam*) are required for stabilizing the cellularization furrow. nullo and Sry-α compartmentalize the cellularization furrow by regulating microfilament assembly and myosin-II mainte-

nance and are essential for basal junctions integrity (Hunter and Wieschaus, 2000; Hunter *et al.*, 2002; Ibnsouda *et al.*, 1993; Postner and Wieschaus, 1994; Rose and Wieschaus, 1992; Schweisguth *et al.*, 1990; Sokac and Wieschaus, 2008). *nullo* and *Sry-α* mutant embryos fail to initiate the cellularization furrow causing the formation of multinucleated cells. *slam* is required for membrane growth and proper localization of RhoGEF2 at the cellularization furrow, and it is also required for the positioning of junction components including Armadillo and Discs-lost (Dlt), which in turn are needed to establish apicobasal polarity (Lecuit and Wieschaus, 2000; Lecuit *et al.*, 2002; Wenzl *et al.*, 2010).

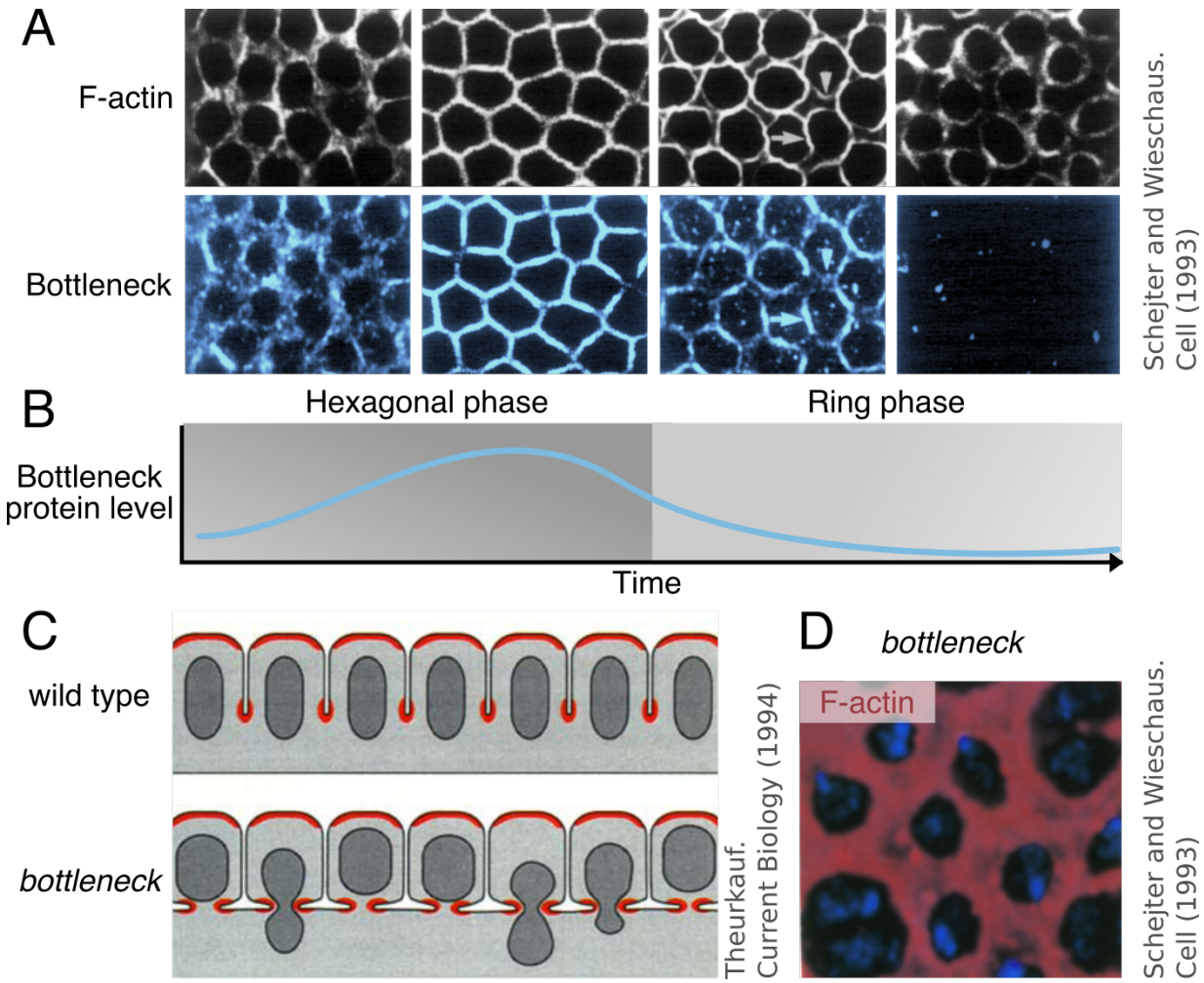

Figure 6. The zygotic gene *bottleneck* regulates actomyosin network transitions during cellularization. (A) Immunostainings showing the actin network (top) and Bottleneck (top) localization at the cellularization furrow during different stages of cellularization (left: priming phase, right: end of fast phase) (Schejter and Wieschaus, 1993). **(B)** At the protein level, Bottleneck appears at the onset of cellularization and peaks during the hexagonal phase. At the transition from hexagonal to ring phase, Bottleneck is degraded and the actomyosin network starts to constrict. **(C)**

Schematic depiction of the *bottleneck* mutant phenotype (Theurkauf, 1994). **(D)** Actin immunostainings in bottleneck mutant embryos demonstrate the lack of hexagonal organization during slow phase of cellularization (Schejter and Wieschaus, 1993). This leads to premature contractions of the basal network deforming the shape of apically anchored nuclei into bottleneck-like shapes by the contracting cellularization furrow (C). (A-D) Figures were adapted from indicated publications with permission from the publisher (7.2, pp. 149).

1.7.1.3. Implication for a key-regulator Bottleneck

The expression of the zygotic gene *Bottleneck* starts at NDC 11 and detectable protein levels appear shortly before the beginning of cellularization (Figure 6A,B) (Schejter and Wieschaus, 1993). Bottleneck protein transiently co-localizes with the hexagonally arranged actomyosin network during the slow phase before getting rapidly degraded at the transition to the fast phase (Figure 6A,B). Concomitantly with the depletion of Bottleneck, the stable actomyosin network reorganizes and transforms into contractile actomyosin rings that cleave off individual cells (Schejter and Wieschaus, 1993). The *bottleneck* mutant phenotype lacks initial hexagonal network patterning and shows pre-mature initiation of basal closure (Figure 6C,D). This leads to deformations of the apically anchored nuclei into bottleneck-like shapes with individual nuclei detaching from the cortex and getting dragged down by the constricted leading edge of the cellularization front (Figure 6C), resulting in the generation of enucleated cells and severe defects in embryonic development (Schejter and Wieschaus, 1993).

The exact mechanism by which Bottleneck functions in organizing the actomyosin network has remained elusive so far as all attempts to recombinantly express the protein did not succeed and no homolog in other species than *Drosophila* has been identified. However, when expressed in human HeLa cells, Bottleneck localized to actin stress fibers and causes a dramatic elevation of actin levels without altering myosin-II levels (Reversi *et al.*, 2014). On the other hand, *DRhoGEF2* mutants in which Rho1 fails to localize to the cellularization furrow and to activate myosin-II, result in a network with increased angularity but not if they also lack Bottleneck (Padash Barmchi, 2005). These observations suggest that Bottleneck acts directly on F-actin organization and stability rather than regulation of myosin-II activity, and that the mechanisms of action of Bottleneck might be conserved. Except for the temporal control of Bottleneck activity that is restricted by zygotic genome activation and rapid protein degradation during cellulariza-

tion (Schejter and Wieschaus, 1993), little is known about the functional regulation of Bottleneck. During cellularization, Bottleneck activity appears to depend on the lipid composition of the plasma membrane and it binds preferentially to $PI(3,4,5)P_3$ (Reversi *et al*., 2014). Cytoskeletal regulators of the Src and Tec non-receptor tyrosine kinases family antagonize bottleneck activity (Thomas and Wieschaus, 2004). Analysis of *bnk* and *src64* as well as *DRhoGEF2* and *bnk* double mutant phenotypes revealed that the basal actomyosin network does not constrict prematurely suggesting that Src-mediated and myosin-II-dependent network contractility is opposed by Bottleneck in wild type embryos (Padash Barmchi, 2005; Thomas and Wieschaus, 2004). However, the *bottleneck* mutant phenotype is dominant over loss of Anillin, which is implicated in actin bundling and actomyosin ring constriction, thus suggesting additive function for Anillin-mediated microfilament structuring and contraction regulation (Thomas and Wieschaus, 2004).

To understand how actomyosin network transformations are controlled *in vivo*, I will focus the first part of my thesis on the role of Bottleneck in controlling actomyosin network architecture during slow phase of cellularization. By studying the molecular function of this potent factor governing network organization I intend to gain insight into how its activity times actomyosin network constriction and test whether its function can be generalized in a wider mechanistic framework.

1.7.2. Epithelial-specific morphogenetic movements

Actomyosin network contractility is tightly controlled throughout all stages of development. After the first epithelium has formed, changes in shape of individual cells can cause dramatic changes in tissue shape.

Apical actomyosin constriction accompanied by dissolution of basal cell-matrix connections induces **cell ingression** and delamination. Epithelial cells transform into migratory mesenchymal cells (EMT) as seen for example during neural crest formation when cells from the dorsal neural tube delaminate to form the peripheral nervous system and vertebrate head (Acloque *et al*., 2009). **Epiboly** is the thinning and spreading of cells by apical expansion and enforcement of basal ECM connection. Epiboly movements occur

during *anamniotes* gastrulation, when the ectodermal layer spreads to cover the entire embryonic surface or during skin morphogenesis in mammals (Keller, 1978; Panousopoulou *et al*., 2016). Epithelial tissues can also **fuse,** for example tracheal cells in *Drosophila* branch out to form new E-cadherin-mediated contact sites in a process control by FGF-driven membrane protrusions (Davies, 2013). Reorganization of the apical cytoskeleton draw cells closer together and ultimately causes fusion of separated tissues (Davies, 2013). **Convergent extension** is the process in which cells rearrange to shorten the cellular array in one dimension and elongate in the orthogonal dimension. This epithelial movement is generally accompanied by **cell intercalation** and exchange of neighbors. Asymmetric accumulation of myosin-II along a row of interfaces triggers constriction and shortening of aligned cell boundaries while the orthogonal cell axis elongates. This behavior is observed for example during *Drosophila* germ band extension along the anterior-posterior (AP) axis, and is triggered by apical pulsatile actomyosin flows along the dorsoventral (DV) axis (Collinet *et al*., 2015; Rauzi *et al*., 2010). Notably, extrinsic forces associated with mesoderm internalization contribute to anisotropic cell elongation in the AP orientation, thereby promoting global germ band elongation (Butler *et al*., 2009). This mechanism provides an example of how tissue movements feed forward to other tissues and transmit forces at the level of the whole organism. *Drosophila* mesoderm internalization is an example of the epithelial movement of **tissue invagination** associated with **apical constriction** of ventral mesodermal cells (Martin and Goldstein, 2014).

1.7.3. Tissue Invagination

Invagination is the generation of a tube-like structure by local inward-pushing of a surface (Davies, 2008). Two forms of invagination exist, whereas axial invagination occurs locally at a spot when a surface pushes inward directly along the axis of tube formation, orthogonal invagination occurs along a line perpendicular to the direction of invagination. In this work, I will exclusively refer to orthogonal invagination.

Many orthologous types of tissue invaginations were suggested to be driven by coordinated apical constriction based on actomyosin network constriction of the cells in the center of the internalizing or bending tissue (Figure 7A-C) (Sawyer *et al*., 2010). However, apical constriction does not automatically induce tissue invagination. During *Xenopus laevis* gastrulation bottle cells initiate the formation of the blastopore without themselves folding inward. Instead, bottle cells undergo apical constriction to create a local hinge point and passively contribute to full extension of the archenteron (Martin and Goldstein, 2014). The changes in bottle cells' shape involve the synchronous shrinkage of the apical surface and apicobasal cell lengthening and requires apical accumulation of both F-actin and active myosin-II (Lee and Harland, 2007). Interestingly, microtubule depolymerization prevents efficient apical constriction without interfering with apical actomyosin or affecting cell lengthening (Lee and Harland, 2007). On the contrary, cells undergoing apical constriction and inward folding do not automatically require actomyosin-generated forces to drive invagination. During sea urchin development the epithelium of the vegetal plate invaginates into the blastocoel cavity to form the archenteron (Figure 7A). Although this invagination depends on RhoA activity and prominent apical F-actin accumulation is observed in the internalizing cells, actin depolymerization does not prevent the inward folding. Instead, invagination appears to be driven by matrix mechanics of secreted proteins (Lane *et al*., 1993; Linde-Medina and Marcucio, 2018).

1.7.3.1. Mammalian neural tube formation

Tissue invagination plays a major role also during vertebrate neural tube formation (Figure 7C). Improper neural tube formation causes congenital birth defects and represents one of the most frequent human birth defects such as anencephaly (Cunningham *et al*., 2002; Detrait *et al*., 2005). The inward folding of the neuroepithelium into a tube happens during primary neurulation and appears to be driven by specialized cells, so called hinge point cells (Figure 7C), that constrict apically and might cause a bending of the neuronal plate. These hinge point cells undergo stereotypic shape changes by shrinking their apical surface and becoming wedged-shaped. This cell behavior is observed in amphibians, birds and mammals (Sawyer *et al*., 2010). Several studies in dif-

ferent vertebrates revealed a polarized apicobasal distribution of actomyosin network components and regulators in hinge point cells with dense actin microfilament accumulation and an enrichment of Rho, ROCK and myosin-II in the apical domain (Sawyer *et al.*, 2010). Disruption of actin microfilaments by cytochalasin D prevents neural tube closure (Morriss-Kay and Tuckett, 1985).

The PDZ-containing and actin binding protein Shroom3 was identified to be a conserved vertebrate apical determinant required for polarized accumulation of these factors and thus essential for apical constriction in the neural tube (Gilmour *et al.*, 2017; Hildebrand, 2005; Nishimura and Takeichi, 2008; Sawyer *et al.*, 2010). Presence of Shroom3 appears to be sufficient to trigger apical constriction and cell elongation even when being misexpressed in other epithelia (Chung *et al.*, 2010). Shroom family proteins mediate communication between patterning regulators and cortical effectors of morphogenesis (Gilmour *et al.*, 2017). However, *Shroom3* expression does not determine the identity of hinge cells during neural tube formation, as it is not restricted to cells constricting apically in mouse and chicken (Sawyer *et al.*, 2010). Comprehensive signaling pathways pattering the neural tube have not been identified conclusively but Sonic Hedgehog and BMP signaling seem to be involved (Sawyer *et al.*, 2010).

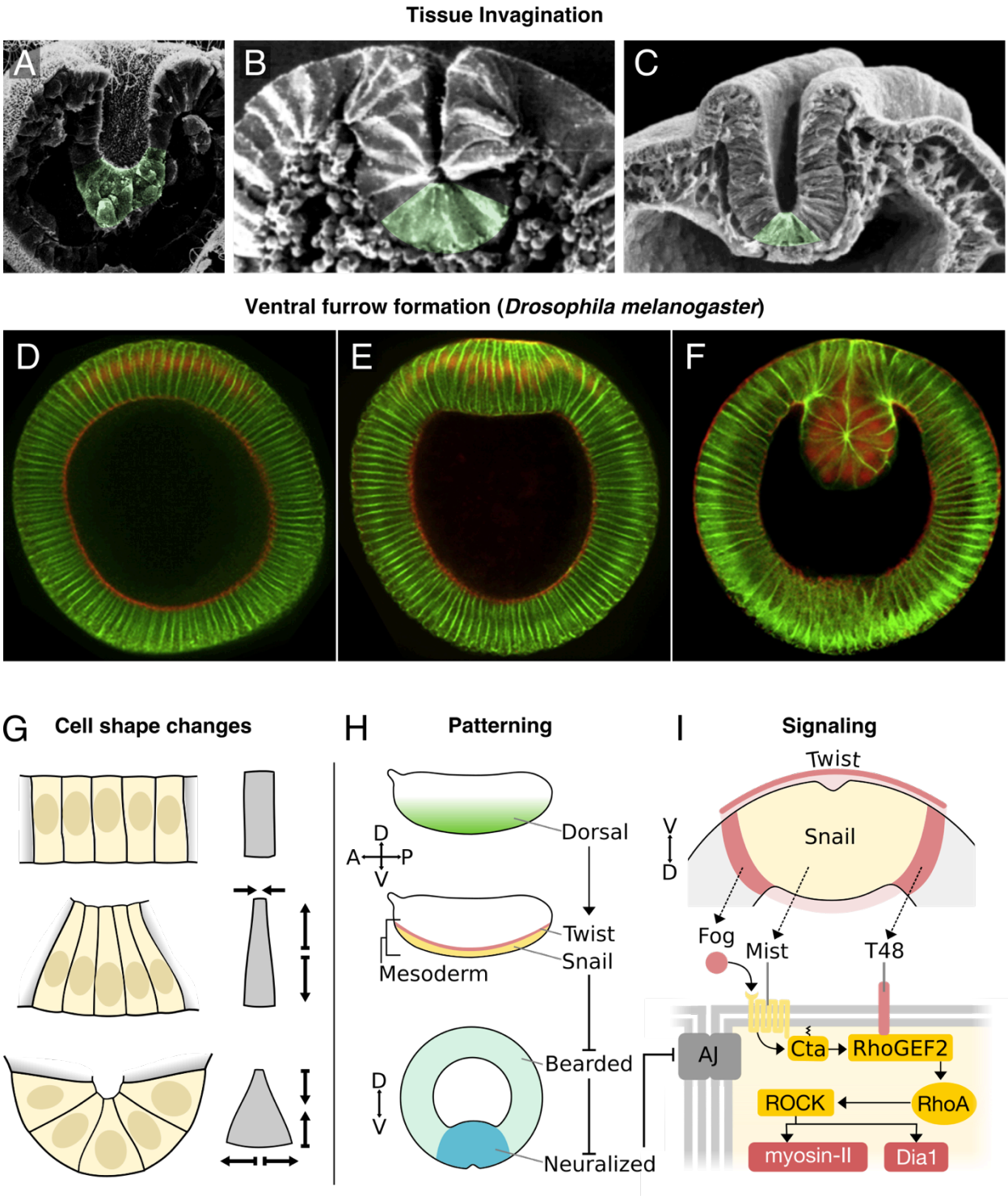

Figure 7. Drosophila ventral furrow formation as a model for tissue invagination. (A-C) Electron micrographs showing variations of tissue invagination in sea urchin gastrulation (*Anthocidaris crassispina*) (Amemiya *et al.*, 1982) (A), *Drosophila* ventral furrow formation (Sweeton *et al.*, 1991) (B), and chicken neural tube formation (Colas and Schoenwolf, 2001) (C). Cells on the tip of the invaginating archenteron (A), apically constricted and internalized cells of the ventral furrow (B) and medial hinge point cells at the neural groove stage (C) are highlighted in green. **(D-F)** Cross-sections of *Drosophila* embryos at different stages during ventral furrow formation (Polyakov *et al.*, 2014). The membrane is shown in green, myosin-II and the transcription factor Twist in red. Ventral cells (up) express Twist and the tissue progressively bends inward and folds into a tube-like structure giving rise to the mesoderm. **(G)** The stages

in tissue invagination are paralleled by characteristic cell shape changes. The columnar cells (top) constrict their apical surface while elongating along the apicobasal axis (middle) before they expand the base and shrink while keeping the apical surface constricted resulting in a wedge-shape. **(H)** The morphogen Dorsal localizes to the ventral side of the embryo, where it activates the transcription factors Twist and Snail who control apical constriction during furrow formation. Snail represses Bearded family proteins that inhibit Neuralized. Neuralized is an ubiquitin ligase that negatively regulates cell-cell junctions. **(I)** While Snail expression is confined to the presumptive mesodermal cells, Twist is expressed slightly broader. Snail expresses the G-protein coupled receptor Mist and Twist expresses its ligand Fog and the transmembrane protein T48, which recruits RhoGEF2. Transduction of Mist by Fog, via the Gα protein Concertina (Cta) activates RhoGEF2 triggering RhoA-mediated induction of actomyosin contractility. Figures were adapted from indicated publications with permission from the publisher (7.2, pp. 149).

1.7.3.2. Ventral furrow formation in *Drosophila*

A well-studied model system for tissue invagination, which is reminiscent of neural tube formation in many ways, is the formation of the ventral furrow during *Drosophila* gastrulation (Figure 7B, D-F). Ventral furrow formation follows cellularization (1.7.1) and brings the presumptive mesodermal tissue inside the embryo. The ventral furrow is formed by a 12-cell-wide stripe of cells at the ventral side of the embryo along the AP axis that will constrict apically and internalize to give rise to the mesoderm. At the same time the cells shrink their apical surface, the cells elongate along their apicobasal axis by a factor of 1.7 respective to their initial length and the cytoplasm and nuclei shift basally (Figure 7E,G) (Leptin and Grunewald, 1990; Sweeton *et al*., 1991). Having reached their maximum length, the cells shorten back to their initial size while expanding extensively at the base and maintaining a constricted apical surface (Figure 7F,G) (Leptin and Grunewald, 1990). This results in the final wedge shape of the cells and the closure of the ventral furrow (Figure 7F,G). Finally, the internalized cells disconnect from the overlying ectoderm and give rise to the mesoderm (Leptin and Grunewald, 1990). Powerful genetics and advances in live imaging techniques made it possible to study this model in great detail allowing a deep understanding of the regulative framework controlling this morphogenetic event from cell fate specification to the force-producing mechanisms driving tissue invagination.

1.7.3.2.1. Positioning and timing ventral furrow formation

In contrast to neural tube formation, the timing and positioning of the ventral furrow is genetically well characterized. The maternally provided morphogen Dorsal controls the

expression of two zygotic transcription factors, **Twist and Snail** (Figure 7H) (Leptin and Grunewald, 1990; Nüsslein-Volhard *et al*., 1984; Simpson, 1983; Sweeton *et al*., 1991). Dorsal directly activates Twist and these two in collaboration trigger Snail expression. Twist and Snail control mesodermal specification by activating the expression of a wide set of genes (Gilmour *et al*., 2017). Snail acts as an EMT promoting transcriptional repressors for ectodermal genes including those encoding for E-cadherin and the apical polarity complex Crumbs that eventually leads to the disassembly of AJs (Leptin, 1991). Yet, the earliest role of Twist and Snail start is to regulate the expression of genes that induce tissue folding. Snail activity indirectly causes AJ turnover by promoting the ubiquitin ligase Neuralized trough the repression of its inhibitors from the Bearded family (Figure 7H) (Chanet *et al*., 2017; De Renzis *et al*., 2006). Twist also activates expression of TNF-receptor-associated factor 4 (Traf4), which physically interacts with β-catenin and supports efficient relocalization of AJs at the apical surface (Mathew *et al*., 2011).

Furthermore, Twist and Snail cause a remodeling of the cortical actomyosin meshwork by activating the transcription of three regulators that cooperate in recruiting RhoGEF2 to the apical domain (Barrett *et al*., 1997; Hacker and Perrimon, 1998): the G-protein-coupled receptor Mist (Mesoderm- invagination signal transducer), its ligand Fog (Folded gastrulation) and the transmembrane protein T48 (Figure 7I) (Costa *et al*., 1994; Dawes-Hoang *et al*., 2005; Kolsch *et al*., 2007; Manning *et al*., 2013; Sweeton *et al*., 1991). The latter of which directly binds the PDZ domains of RhoGEF2 (Kolsch *et al*., 2007), while Mist binds to the secreted signal Fog and signals via the associated downstream Gα protein Concertina (Cta) to induce **Rho1-mediated signaling** via GTP exchange facilitated by RhoGEF2 (Figure 7I) (Kerridge *et al*., 2016; Manning *et al*., 2013; Morize *et al*., 1998). GTP-bound Rho1 activates its substrates ROCK inducing myosin-II activity and Dia1 promoting F-actin assembly (Fox and Peifer, 2007; Kerridge *et al*., 2016). Furthermore, a non-receptor tyrosine kinase called Abelson (Abl) controls F-actin distribution in the ventral mesodermal cells via the actin regulator Enabled (Ena) (Fox and Peifer, 2007). Interestingly, Huckebein and Tailless control the invagination of the posterior midgut by inducing expression of essentially the same Twist and Snail targets regulating Rho signaling (Costa *et al*., 1994; Gilmour *et al*., 2017). This is a compelling

example of how morphogenetic integrons are structured, how they reoccur in other circumstances and how they are generally intervened with cell signaling within a wide deterministic genetic framework.

1.7.3.2.2. Apical pulsing and anisotropy

Apical constriction is driven by pulsed coalescences of a medial actomyosin meshwork connected with junctional actin at apical cell-cell boundaries (Martin *et al*., 2009; Sawyer *et al*., 2010). Taking up the thread that an actomyosin network conceptually behaves as self-organizing system, it will adapt to transduced forces resulting from the combined action of cell cortical tension, adhesion and compression load. Actomyosin networks as well as mechanoresponsive junctional components will always tend to approach the state of minimal free energy and redistribute their constituents according to the laws of thermodynamics (Heisenberg and Bellaiche, 2013). **Periodic network pulsation** may be an intrinsic feature of actomyosin networks that (from a teleonomic perspective) need to oscillate between assembly and disassembly to find the preferred state of minimal energy and maximize fitness of the system to not get trapped in a suboptimal local fitness maximum (Davies, 2013). In other words, organization and cellular anchor points of an actomyosin network constantly need to be reassessed in order to respond to a changing environment. In fact, *in vitro* observations that myosin activity alone can lead to rupture and disassembly of F-actin and thus F-actin turn-over in combination with computer simulations of 2-D actin networks support the idea that pulsation is an intrinsic property of actomyosin systems which depends on the extent of crosslinking and F-actin turnover (Banerjee *et al*., 2017; Belmonte *et al*., 2017; Blanchoin *et al*., 2014).

The subcellular distribution of cytoskeletal and adhesive complexes dictates cell shape and thus drives morphogenesis. Intracellular redistribution of actomyosin (or **actomyosin flow**) for instance is essential for amoeboid cells to extent their leading edge forward and move (Heisenberg and Bellaiche, 2013). To understand how inner-cell flows impact on cell shape transitions in a multicellular context several aspects of the flow dynamics need to be taken into account: the frequency and amplitude of contractions, which is de-

fined by mechanical properties of the actomyosin network (1.6.4, pp. 18) and its anchors at the plasma membrane, the direction of actomyosin flows, the coupling strength to junctional structures and the efficiency of mechanisms stabilizing periodic shape changes (Heisenberg and Bellaiche, 2013).

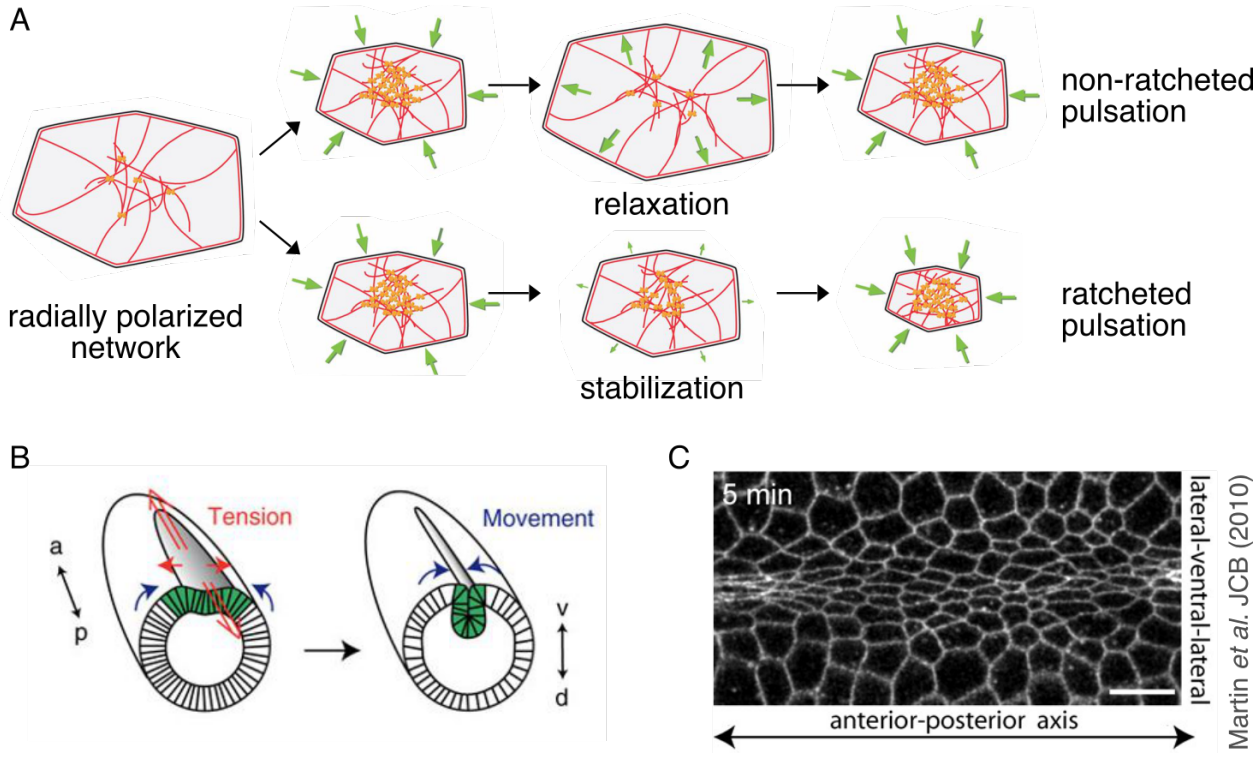

Figure 8. Apical pulsing and anisotropy. (A) Schematic depiction of different modes of pulsation (Martin and Goldstein, 2014). A radially polarized network, as present in the apical domain in constricting cells during ventral furrow formation, can show pulsatile behavior caused by the periodic assembly and disassembly of actomyosin networks. If upon contraction the network is not maintained and relaxes back into the initial size, the pulsation is non-ratcheted and does not cause net-constriction. If, on the contrary, network relaxation is limited by means of a molecular ratchet, the network undergoes progressive decrease in surface area (ratcheted pulsation). **(B)** Anisotropy is result of unequal tension along the anterior-posterior (A-P) axis, where many cells contract and thus produce high tension, compared to tension along the dorsal-ventral (D-V) axis, where only 12 cells contract und thus produce relatively low tension (Chanet *et al.*, 2017). (C) Confocal image showing the cell membrane of an apically constricting *Drosophila* embryo during VF (Martin *et al.*, 2010). The ventral cells constrict more in D-V than in A-P orientation casing an anisotropic surface geometry. Figures were adapted from indicated publications with permission from the publisher (7.2, pp. 149).

During ventral furrow formation the apical actomyosin meshwork of the invaginating cells is organized in a radially polarized manner (Figure 8A) (Chanet *et al.*, 2017). Apical constriction is initiated by medial coalescence of myosin-II from where fibers extend to the junctional actomyosin circumferential belts (Martin *et al.*, 2009). These actomyosin structures are highly dynamic. Myosin-II levels periodically increase, move to the center of

the cell apex and disassemble producing a centripetal actomyosin flow (Martin *et al.*, 2009). The pulsatile actomyosin flow translates into periodic apical constriction and inward pulling of cell-cell junctions-containing cell boundary. Importantly, the pulsing alone is not sufficient to drive constriction. During dorsal closure amnioserosa cells undergo **non-ratcheted pulsation**, where constricted apical surfaces relax back to the initial size without net constriction (Figure 8A), until external forces provided by neighboring epidermal cells contain the constricted state (Solon *et al.*, 2009). To manifest cell shape changes, the constricted state has to be stabilized by means of a **molecular ratchet** (Figure 8A). Apical constriction during ventral furrow formation displays ratcheted pulsatile behavior with a period of ~90 s, as the expansion of the apical cytoskeleton is limited after each constriction cycle causing the cell area to get incrementally smaller (Xie and Martin, 2015). The identity of the machinery serving the function of a molecular ratchet has yet to be identified – given their role in other contractile systems, actin crosslinkers are likely playing an important role in this regulation. At least partly, Snail and Twist targets are involved in this regulation (Martin *et al.*, 2009; Mason *et al.*, 2013). While Snail targets promote actomyosin contractility *per se*, Twist targets are required to prevent network relaxation. Interestingly, Twist activity is required for core components of the myosin-II regulatory apparatus to be radially polarized (Mason *et al.*, 2013).

The strengthening of force-bearing cell-cell apical junctions, to which the actomyosin network is coupled, leads to the assembly of an supracellular apical actomyosin network structure transmitting forces across the whole tissue (Martin *et al.*, 2010). It is the tissue-wide force transmission that also causes **anisotropic surface constriction** of the ventral mesodermal cells (Figure 8B) (Guglielmi *et al.*, 2015). Since more cells constrict along the AP axis compared to the 12 cells in DV orientation, pulling forces originating from cells along the AP axis are higher, preventing cell constriction in this dimension, whereas in DV orientation cells can constrict more efficiently (Figure 8B) (Doubrovinski *et al.*, 2018). Single cell anisotropy schematically resembles the shape of the entire ventral furrow. Following this hypothesis, anisotropy is an indication for mechanical feedback between cell neighbors within a tissue undergoing coordinated morphogenetic movements. In line with this interpretation, distortion of apical junction integrity by inter-

fering with junctional components such as β-catenin (Arm) or the adaptor protein afadin (Canone) does not stop apical pulsation but prevents coordinated constriction and furrow formation, and the ventral mesodermal cells fail to acquire anisotropy (Martin *et al.*, 2010; Sawyer *et al.*, 2009; Sweeton *et al.*, 1991).

Although the current level of insight into the regulation of apical constriction during *Drosophila* ventral furrow formation is not reached in other systems so far, the general concept of network pulsation contributing to coordinated cell behavior also seems to apply for example for ingression of endodermal precursors during *C. elegans* gastrulation (Roh-Johnson *et al.*, 2012). In this case, pulsations originate from actively induced oscillation myosin-II activity mediated by feedback loops of activator and inhibitor systems based on RhoGEFs and RhoGAPs (Agarwal and Zaidel-Bar, 2018). To what extent oscillating myosin-II activity contributes to pulsation of the invaginating cells during *Drosophila* ventral furrow formation is still under debate.

1.7.3.3. Modelling tissue invagination

Myosin-II-dependent apical constriction has been shown to be both necessary and sufficient to initiate cell internalization in *Drosophila* (Guglielmi *et al.*, 2015; Izquierdo *et al.*, 2018). However, it is still unclear if apical constriction is the only driving force causing the whole series of cell shape changes described earlier (1.7.3.2, p. 36) and how forces transmit throughout the apicobasal axis of constricting cells. Other topics under debate include the role of lateral cells, and the function of microtubules during invagination.

A recent computational study based on a 2D vertex model suggests that the cell shape changes occurring during ventral furrow formation represent simply a well-controlled repositioning of the cytoplasm in response to apical constriction (Figure 9) (Polyakov *et al.*, 2014). According to this model, the entire set of morphogenetic events following apical constriction relies on the passive mechanical properties of ventral cells. Precise volumetric measurements confirmed that during invagination the volume of the cells remains constant (Polyakov *et al.*, 2014). This model is based on region-specific elasticities of different plasma membrane domains that differentially change over time (Figure 9). Be-

sides the constricting and force-generating apical plasma membrane domain, the model implies a critical role for the material properties of the lateral and basal plasma membrane surface. More specifically, progressive decrease of basal rigidity as apical tension increases seems to accommodate for all the cell shape changes observed *in vivo*. Consistently, disassembly of basal actomyosin has been observed during ventral furrow formation (Dawes-Hoang *et al.*, 2005; Sweeton *et al.*, 1991).

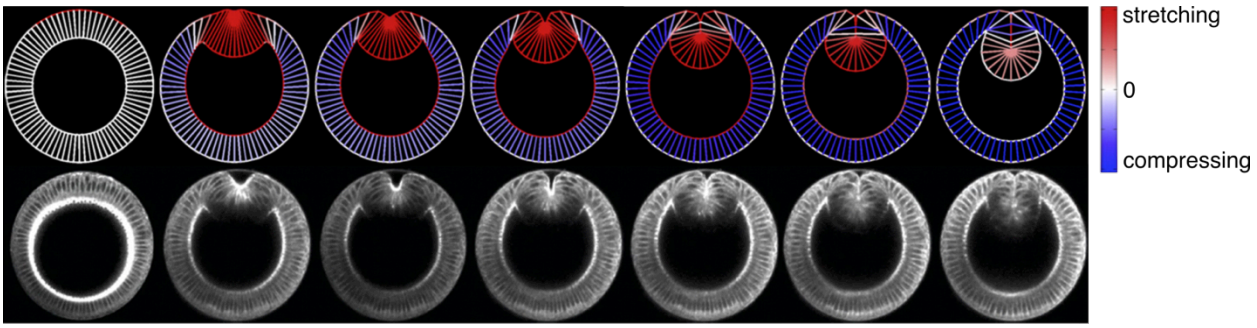

Figure 9. Computer model recapitulating the whole process of VF. Polyakov *et al.* proposed a model, in which actomyosin-driven apical constriction is the only driving force required for the entire folding process if basal rigidity decreases progressively (Polyakov *et al.*, 2014). The result of a computer simulation is shown in the top row with blue color indicating compression forces and red color indicating stretching forces. Cross sections in the lower row show myosin-II in a *Drosophila* embryo during ventral furrow formation. Figures were adapted from indicated publications with permission from the publisher (7.2, pp. 149).

1.7.4. Role of the basal surface in epithelial remodelling

In this thesis, I will investigate specifically the role of the basal surface during epithelial morphogenesis focusing on cellularization and ventral furrow formation (Figure 10). During the process of cellularization, the basal actomyosin network is organized in a stable non-contractile hexagonal pattern before transforming into individualized ring-shaped structures that becomes contractile and constricts (Figure 10). At the end of cellularization, the basal actomyosin network of mesodermal cells on the ventral side of the embryo changes from a contractile to an expansible configuration – a transition (Figure 10) that might be important for the concomitant cell shape changes happening during ventral furrow formation as discussed above (Figure 7G).

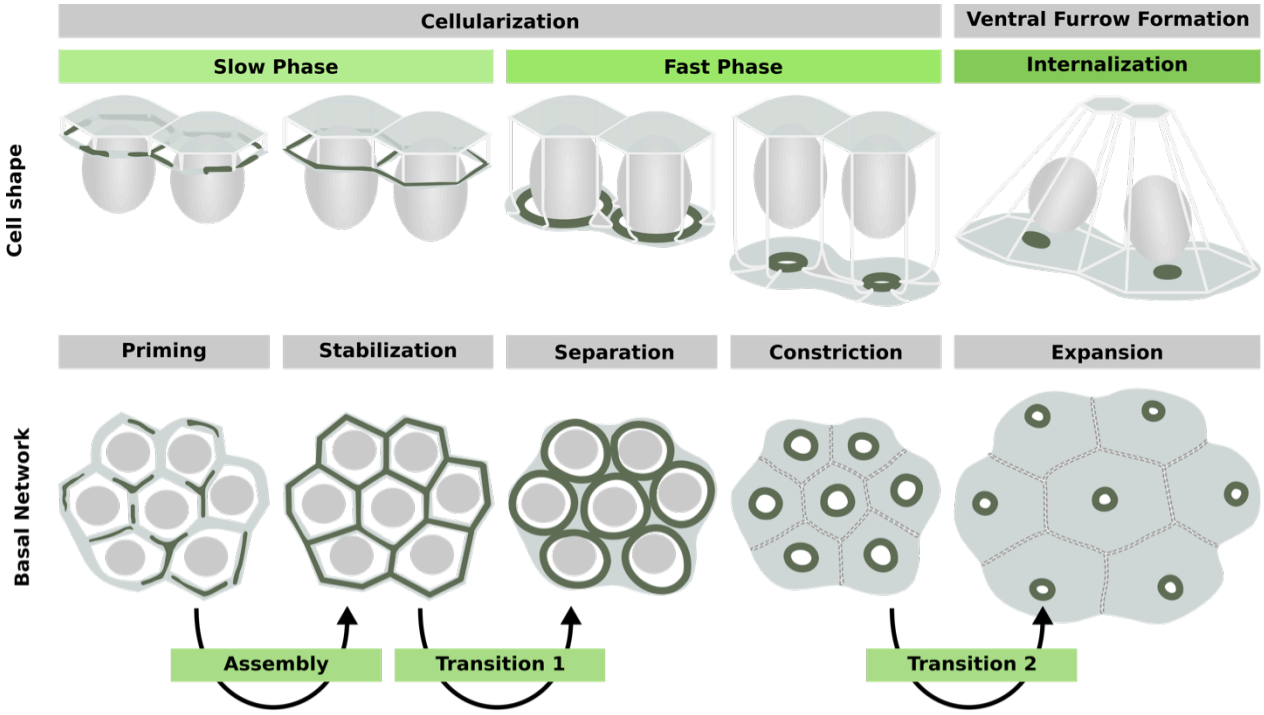

Figure 10. Model system: The basal actomyosin network during early *Drosophila* development. The early *Drosophila* embryo is an advantageous model system to study actomyosin network transitions *in vivo*. At different stages of tissue morphogenesis (upper row) distinct actomyosin network configurations, which fulfill specific functions (gray boxes), are prevalent. During cellularization, a basally localized actomyosin network assembles at the cellularization furrow (lower row). The initial network does not constrict and is organized into regular hexagonal structures. When the cellularization furrow has reached the base of the nuclei, the network transforms into separated ring structures that become contractile and constrict (tansition 1). At the end of cellularization, the basal actomyosin network of ventral mesodermal cells changes from a contractile to an expansible configuration (transition 2). This transition might be of relevance for the cell shape changes during VF.

An active function of the basal actomyosin network in promoting epithelial movements has been described in a number of systems. During *Drosophila* oogenesis basal myosin-II periodically oscillates in follicular cells to drive basal network pulsations and ECM deposition (Haigo and Bilder, 2011; He *et al*., 2010). The resulting forces cause global anisotropic elongation of the egg chamber. Ascidian endoderm invagination relies on sequential cell shape changes that depend on coordinated apical and basolateral contraction which likely generates differential cortical tensions (Sherrard *et al*., 2010). *Drosophila* posterior spiracle cell invagination involves apical constriction and basolateral membrane elongation (Simões *et al*., 2006). Besides myosin-II activation mediated by RhoGEFs at the apical domain, the RhoGAP Crossveinless, a suppressor of Rho and

thus myosin-II activity, is recruited to the basolateral surface generating membrane compartments with differential mechanical properties, (Simões *et al*., 2006).

Interestingly, during cranial neural tube formation in mouse and chick embryos, F-actin and active myosin-II enrich basally before accumulating at the apical domain of hinge point cells (Sadler *et al*., 1982; Sai and Ladher, 2008; Zolessi and Arruti, 2001). This remarkable similarity to *Drosophila* ventral furrow formation prompted me to further investigate force transmission in three dimensions and the role of the basal surface during tissue morphogenesis. Lack of genetic mutants that specifically interfere with the basal pool of myosin-II and of techniques to precisely manipulate and observe cell shapes in 3D over time have so far limited our understanding of basal surface dynamics. Recent advances in 3D image acquisition and reconstruction as well as optogenetics make it now possible to circumvent these limitations (Gelbart *et al*., 2012; Guglielmi *et al*., 2015; Izquierdo *et al*., 2018).

1.8. New perspectives of manipulating living organisms

1.8.1. Modelling morphogenesis by computers, cultures and synthetic biology

Genetic screens in model organisms have been instrumental to identify the general framework governing many developmental processes. This led us to understand the basic structure of regulatory circuits and molecular components of the machineries driving morphogenesis allowing the building of predictive models. A model has to represent all interesting parts of a system while omitting its irrelevant features (Davies, 2013). Thereby, it can not only help discriminating between conflicting experimental data, but also establish if the level of available information is sufficient to recapitulate an observed morphogenetic behavior. Modern models are based on computer-based **mathematical simulations** and offer a powerful complementary approach to investigate biological systems.

Tissue engineering strategies are of interest to both the field of developmental biology and regenerative medicine. Cells and tissues *in vivo* are complex entities that experi-

ence versatile signaling inputs. Removing cells or tissues from their native environment and forcing them to run their program in a simplified and controlled environment, can help learning about tissue-intrinsic behaviors (Sonnen *et al*., 2018). Growing 3D organ models (organoids) from (induced) stem cells has high potential to increase our understanding of coordinated cell behavior and tissue homeostasis and diseases mechanism (Nature Cell Biology, 2018). Organoids provide powerful modeling platforms to test aspects of morphogenesis and mechanisms like self-organization and differentiation.

Another way of modeling morphogenesis is to apply synthetic biology techniques to manipulate developing organisms. The term **synthetic morphogenesis** goes back to a definition by J. A. Davies as the application of "emerging techniques of synthetic biology to the field of anatomy, with the aim of programming cells to organize themselves into specific, novel arrangements, structures and tissues" (Davies, 2008). The (bio-orthogonal) construction of a morphogenetic mechanism in cells that do not already make use of it allows us to test if this mechanism can stimulate the expected morphogenetic behavior (Davies, 2013). Synthetic morphogenesis approaches aim to create in order to test whether we understand in line with a famous quote from Richard Feynman, who said: "What I cannot create, I do not understand". Some of the most powerful and useful synthetic methodologies to control cell behavior are based on non-neuronal optogenetics.

1.8.2. Optogenetics

Optogenetics is a technique that couples genetics with light stimulation (Miller, 2006). Together with Richard Grandison, I have established an e-Learning platform introducing non-neuronal optogenetics to a broad audience (URL: https://www.embl.de/training/e-learning/optogenetics/). Optogenetic techniques have been successfully applied in cell and developmental biology to control basic biological processes with light (Guglielmi *et al*., 2016). It is for example possible to control cell contractility and motility, or to perturb cell-signaling pathways by triggering the activity of membrane receptors and direct cell fate decisions (Figure 11A).

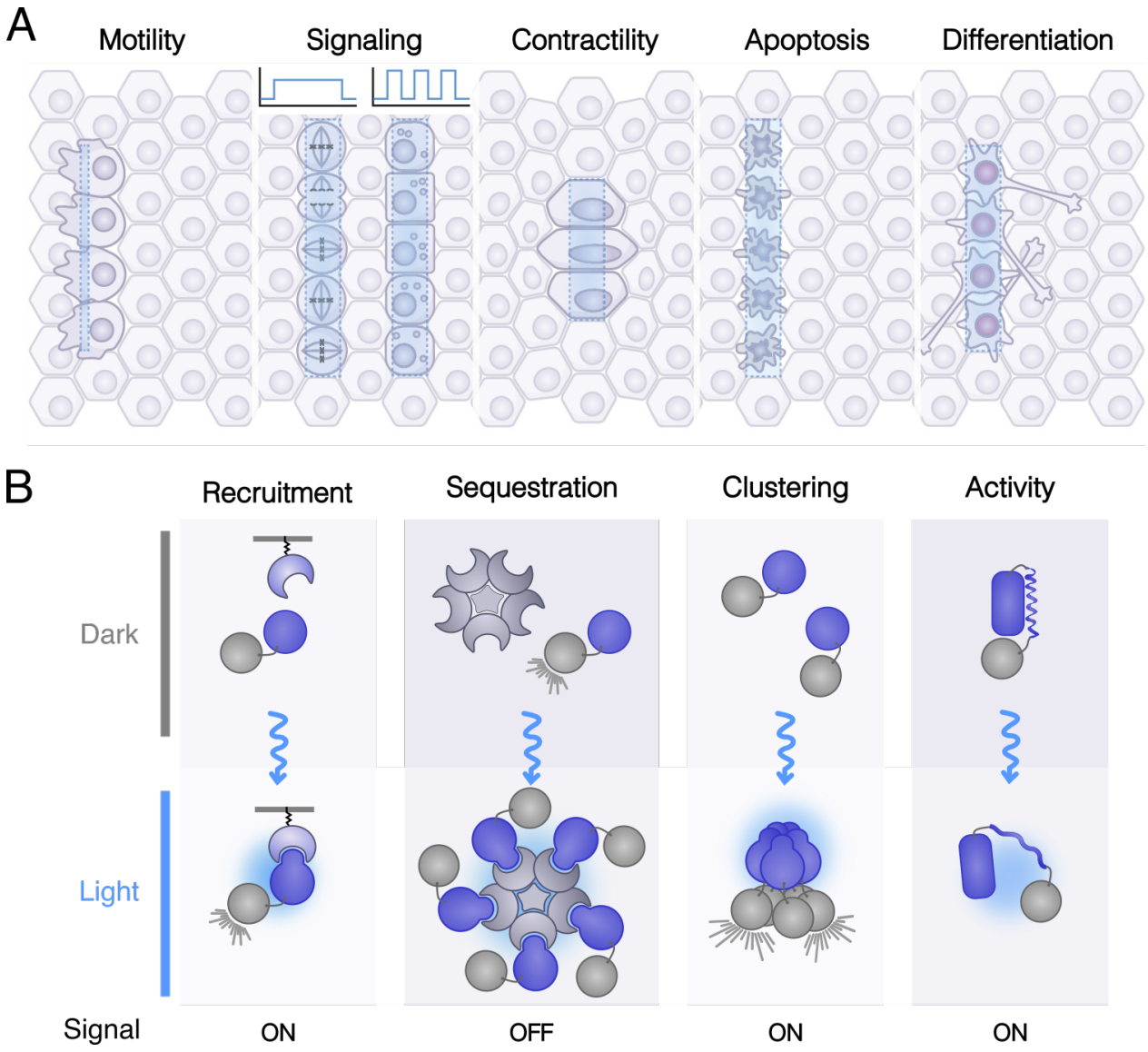

Figure 11. Optogenetics enable the control of biological processes using light. (A) Optogenetic techniques make it possible to selectively interfere with various biological processes using light with high spatiotemporal precision (Guglielmi *et al.*, 2016). It is possible to control cell motility, to manipulate signaling pathways, to change the contractile behavior or to trigger cell fate decisions such as apoptosis or differentiation. **(B)** Optogenetics make use of a limited set of molecular approaches. Light-induced dimerization can be used to recruit a protein of interest to a specific location, where it can pursue its function, or to sequester away the protein from its native localization inhibiting its function. Clustering based on light-dependent oligomerization can induce active functional signaling hubs (or the opposite depending on the target protein). Photouncaging based on LOV domains can be used to directly trigger protein activity with light. Panel (A) was adapted from Guglielmi *et al.*, 2016.

Classic perturbations used to interfere with gene activities in developing organisms are limited in their spatiotemporal precision (Guglielmi *et al.*, 2016). For instance, standard genetic approaches, involving loss- or gain-of-function, have pleiotropic effects on multiple cell types or tissues and act on long time scales. Chemical perturbations do not allow

precise spatial precision and often compounds cannot be delivered to the site of interest due to limitations regarding permeability and diffusion. Optical perturbations, such as laser cutting techniques, are advantageous as they allow full temporal control, but lack substrate specificity as they ablate cytoskeletal components unspecifically.

Optogenetics combine the power of genetic perturbations with the spatiotemporal precision of advanced optical microscopy systems (Figure 11A). Since light is the trigger to stimulate an optogenetic system, the relayed synthetic mechanisms can be activated at a defined time point with the precision of laser light on the *μ*m-scale. Moreover, by changing the frequency, amplitude and duration of the light-stimulation pattern it is possible to dynamically interfere with developing biological systems.

1.8.2.1. Concepts and approaches in non-neuronal optogenetics

Optogenetic techniques make use of a defined set of molecular approaches to control cellular processes with light (Toettcher *et al.*, 2011). The most common approach is based on light-induced recruitment of a photosensitive protein to an anchor protein (Figure 11B). Re-localization of a target protein to a specific site of the cell can positively regulate its function by enabling it to interact with its downstream binding partners or can inhibit its function by sequestering it away from its site of action. Protein clustering is another approach based on photosensitive protein domains that oligomerize upon light-activation (Figure 11B). Depending on the target protein, clustering can either induce active signaling or prevent activity due to steric hindrance. It is also possible to directly control the enzymatic activity of a target protein by light. A photosensitive module bioengineered into the target protein can expose a hidden signaling motif or relieve the protein from allosteric autoinhibition upon light-dependent change in protein conformation (Figure 11B).

1.8.2.2. Heteromerization and photo-uncaging systems

While the first optogenetic systems employed channelrhodopsin-like photosensitive ion channels to stimulate neuronal activity by light (Boyden *et al.*, 2005; Zemelman *et al.*,

2002), systems in non-neuronal optogenetics are based on molecules that undergo light-induced dimerization or unfold upon light activation (photo-uncaging). The majority of these light-sensitive protein domains derives from plants or cyoanobacteria and do not have functional homologues in animal systems. Therefore, they function in a bio-orthogonal manner when employed in synthetic morphogenetic systems studying animals.

Photo-uncaging strategies make most commonly use of LOV (Light, Oxygen or Voltage) domains (Pudasaini *et al*., 2015). Upon blue light illumination, a covalent bond forms between an α-helical connector and adjacent PAS domain (adduct formation) leading to unfolding of the α-helix. This unfolding can expose a recognition motif for posttranslational protein modification, protein trafficking, or protein-protein interaction which was masked in the dark (Niopek *et al*., 2014, 2016). When placed into a sensitive location within a target protein, LOV domains can also be used to control enzymatic activity and protein-protein interaction directly. LOV domain modules have also been engineered to efficiently induce protein dimerization (Guntas *et al*., 2015; Kawano *et al*., 2015).

The class of molecules undergoing **photo-dimerization** is more versatile but employ coherent molecular mechanisms. Two component heterodimerization systems comprise a photosensitive protein domain that upon light exposure changes its conformation and an interactor that exclusively binds the photosensitive protein in its excited state (Zhang and Cui, 2015). In the dark the two proteins remain unbound. Photo-dimerization systems differ in their molecular properties and reaction parameters including the requirement of different co-factors, the wavelength of light activation, binding affinity, sensitivity and efficiency of light activation, reversibility and disassembly parameters. The most prominent optogenetic dimerization systems are the chryptochrome and phytochrome systems in addition to engineered LOV domain-based systems such as magnets and iLID.

Phytochrome B of the **phytochrome** system is activated by red light (650 nm) and binds in its active state to the Phytochrome Interacting Factor (Levskaya *et al*., 2009). The

phytochrome system has the advantage that dissociation can be triggered specifically by far-red light illumination (750 nm) and that the dissociation time of the complex in the dark is slow (18 hours) (Tischer and Weiner, 2014). Its limitation is the requirement for the phyco-cyanobilin co-factor that is not present in animals and needs to be delivered ectopically.

Instead, the **chryptochrome** system is based on the photosensitive domain of Cry2 that depends on the cofactor FAD, which is abundant in most living organisms (Kennedy *et al*., 2010). Cry2 can be activated by a range of blue light (405 – 488 nm) or using multiphoton laser light of 950 nm wavelength. **Two-photon excitation** has significant advantages when employed to thick specimens as it enables the experimentalist to locally restrict light illumination and activation deep inside tissues. Visible light is subject to significantly stronger light scattering and has the disadvantage that an undefined volume is activated when deeper focal planes are excited. Hence, single photon excitation cannot be employed to specifically activate focal planes deeper insight tissues. Upon blue-light exposure, Cry2 undergoes photo-isomerization and binds to the N-terminal domain of Cryptochrome-interacting basic-helix-loop-helix 1 (CIB1), usually referred to as CIBN (Kennedy *et al*., 2010). Anchoring CIBN to the plasma membrane enables the relocalization of a target protein fused to Cry2 to the plasma membrane upon photo-activation. The dissociation time of the Cry2-CIBN complex is between 5 and 10 min (Tischer and Weiner, 2014). Cry2 in absence of CIBN can also form homo-oligomers upon blue light illumination (Taslimi *et al*., 2014).

1.8.2.3. Application of optogenetics to study morphogenesis

The feasibility of implementing optogenetics to modulate cell contractility and signaling has been demonstrated using different optogenetic modules, however, in a still small number of publications. For instance, light-inducible receptor tyrosine kinases (RTKs) have been successfully engineered using LOV domains to bypass endogenous ligand binding and activate downstream signaling upon light illumination (Grusch *et al*., 2014). Optogenetic control of RTKs offers the opportunity to quantitatively manipulate growth

factor signaling pathways, such as EGF or FGF to further elucidate their impact on tissue shaping. In *Drosophila* an optogenetic system for activating extracellular signal regulated kinase (Erk) signaling via Ras was implemented to achieve high spatiotemporal control over this important developmental patterning pathway (Johnson *et al.*, 2017). Perturbing the spatial extent of Erk pathway activity during early *Drosophila* development caused patterning defects and distorted morphogenesis (Johnson *et al.*, 2017). Buckley *et al.* succeeded in putting a component of the apical cell polarity system in *Zebrafish*, Pard3, under optogenetic control by employing the phytochrome system (Buckley *et al.*, 2016). Using this optogenetic module it was possible to manipulate the localization of the Pard3 apical polarity protein with subcellular precision and high temporal control in the developing neural tube and to study cell fate decisions (Buckley *et al.*, 2016). As elucidated in great detail, understanding morphogenesis requires an understanding of cell shape transitions as well as the concomitant dynamic remodeling of the cytoskeletal architecture. As actomyosin contractility is the pivotal force-generating source driving shape transitions, studying morphogenesis using synthetic biology by means of optogenetics requires the control of cell contractility. The first photo-caged enzyme created was the GTPase Rac1 that promotes membrane ruffling and leading edge formation via its effector PAK (Wu *et al.*, 2009). When expressed in single cells it was possible to direct cell movement via light-induced activation of Rac1, which provided a clear demonstration of the power of optogenetics. *In vivo* optogenetic activation of Rac resulted in the formation of cell protrusions and guided movement of border cell clusters in *Drosophila* and individual neutrophils in zebrafish (Wu *et al.*, 2009, 2011). Another important contribution from our lab at EMBL was the establishment of an optogenetic tool to negatively interfere with cell contractility in *Drosophila* embryos. The Cry2/CIBN-based optogenetic module enabled the light-controlled recruitment of the catalytic domain of the phosphatase OCRL to the plasma membrane where it catalyzes the hydrolytic breakdown of $PI(4,5)P_2$ that is required for cortical attachment of many actin-binding proteins (Guglielmi *et al.*, 2015). Acute depletion of $PI(4,5)P_2$ led to the collapse of F-actin anchor points at the plasma membrane and subsequent F-actin depolymerization. By employing this OCRL optogenetic tool, it was shown that local inhibition of apical

constriction during ventral furrow formation was shown to prevent mesoderm invagination (Guglielmi *et al*., 2015). Hence, this study demonstrates conclusively that apical constriction is necessary for tissue invagination. Moreover, using different patterns of light activation it was shown that the contractile behavior of individual cells responded to local geometrical constraints of the surrounding tissue.

Only very recently, effort in our lab succeeded in the implementation of another optogenetic module with which it is possible to specifically activate myosin-mediated actomyosin contraction via Rho signaling (Izquierdo *et al*., 2018). Light-induced recruitment of RhoGEF2 fused to the photosensitive Cry2 to the plasma membrane-anchored CIBN led to the activation the GTPase Rho1 during early *Drosophila* development triggering a downstream signaling cascade culminating in myosin-II activation. The precise spatial and temporal activation of Rho signaling at the apical surface of epithelial cells on the dorsal side of the *Drosophila* blastoderm was sufficient to induce apical constriction and tissue internalization independently of any pre-determined condition or differentiation program (Izquierdo *et al*., 2018). This study is a beautiful example of how synthetic morphogenesis can serve as a stringent modeling approach to test a morphogenetic mechanism. In fact, this study revealed that apical constriction alone can induce tissue invagination. However, the invagination does not recapitulate the whole series of cell shape changes observed during endogenous ventral furrow formation resulting in an incomplete invagination. Therefore, these experiments suggest an involvement of at least a second factor required for full tissue invagination.

In this thesis, I will specifically focus on the role of the basal cell surface dynamics during epithelial morphogenesis and tissue folding using optogenetic tools to perturb actomyosin contractility in the developing *Drosophila* embryo in combination with cutting-edge microscopy systems, genetic approaches, *in vitro* assays and automated data processing.

2. Aim of the thesis

Tissue morphogenesis is driven by cell shape changes in individual cells requiring cytoskeletal rearrangements and generation of inter-cellular and intra-cellular forces produced by precisely controlled actomyosin contractions.

The contractile behavior of actomyosin networks is regulated by myosin-II activity and localization, and by the molecular architecture of actin networks sculptured by actin-remodeling enzymes and crosslinking proteins. *In vitro* studies have shown that actin filament organization governs contractility and *in vivo* the structure of different types of actomyosin networks correlates with specific cell contractile behavior. A broad motivation for my thesis was first to investigate of how different configurations of actomyosin networks regulate cell contractility *in vivo* and second to study how transitions between different network topologies are regulated on a molecular level in time and space during tissue morphogenesis. To study network transitions *in vivo* I will characterize the remodeling of a basally localized actomyosin network during the process of cellularization. I will focus on investigating the mechanisms of action of Bottleneck, which is specifically expressed during cellularization and is required for hexagonal patterning and timing of actomyosin fiber contractility at the basal surface of the forming cells. By studying its mechanism of action, I could shed light on some of the general principles governing the spatiotemporal organization of actomyosin contractility *in vivo*.

A second aim of my thesis was to study the contribution of basal actomyosin dynamics to tissue invagination during ventral furrow formation. To this end, I employed optogenetics to specifically interfere with the basal pool of myosin-II in combination with quantitative imaging to study the influence of this perturbation on cell shape changes and tissue invagination.

3. Results

3.1. A switch in crosslinker-mediated actin network topology

3.1.1. Differential contractile response of actomyosin network patterns

During cellularization the syncytial *Drosophila* embryo is transformed in 6000 mononucleated epithelial cells (1.7.1, p. 26). Cellularization starts with assembly of a basally localized actomyosin network at the leading edge of the ingressing plasma membrane (cellularization furrow) during the priming phase (Figure 12A). Initially this network is organized in interconnected hexagonal arrays of actin fibers and does not constrict (Figure 12B). As the membrane further ingresses, the actomyosin network is transformed into individual rings (Figure 12C) and constricts when the cellularization furrow has reached the base of the nuclei to eventually close off the cells basally. As discussed in the introduction, this dynamic transition in actomyosin organization is tightly controlled in space and time and is of vital importance for the subsequent developmental stages.

In order to test whether an upregulation of myosin-II activity is sufficient to drive cell contractility when actin filaments are organized in the hexagonal conformation, I employed the CRY2/CIB1 optogenetic module to control membrane localization of the *Drosophila* RhoGTPase-activating factor RhoGEF2 using blue light (Figure 12D). The catalytic domain of the RhoGEF2 was fused to the photosensitive domain of CRY2 and co-expressed with an N-terminally truncated version of CIB1 (CIBN) anchored at the plasma membrane (Izquierdo *et al*., 2018). While in the dark RhoGEF2-CYR2 is present in the cytoplasm, blue light illumination triggers the translocation of RhoGEF2-CYR2 to the plasma membrane via the induced interaction with the membrane-anchored CIBN. At the cell membrane RhoGEF2-CYR2 activates Rho1, which starts a downstream signaling cascade to activate myosin-II (Figure 12D) (1.6.3, p. 16). This optogenetic system was established recently in our lab and used to stimulate myosin-II activity at the apical plasma membrane to induce apical cell constriction (Izquierdo *et al*., 2018). I tuned the

experimental conditions to specifically stimulate myosin-II activity at the base of epithelial cells using two-photon microscopy (Figure 12E).

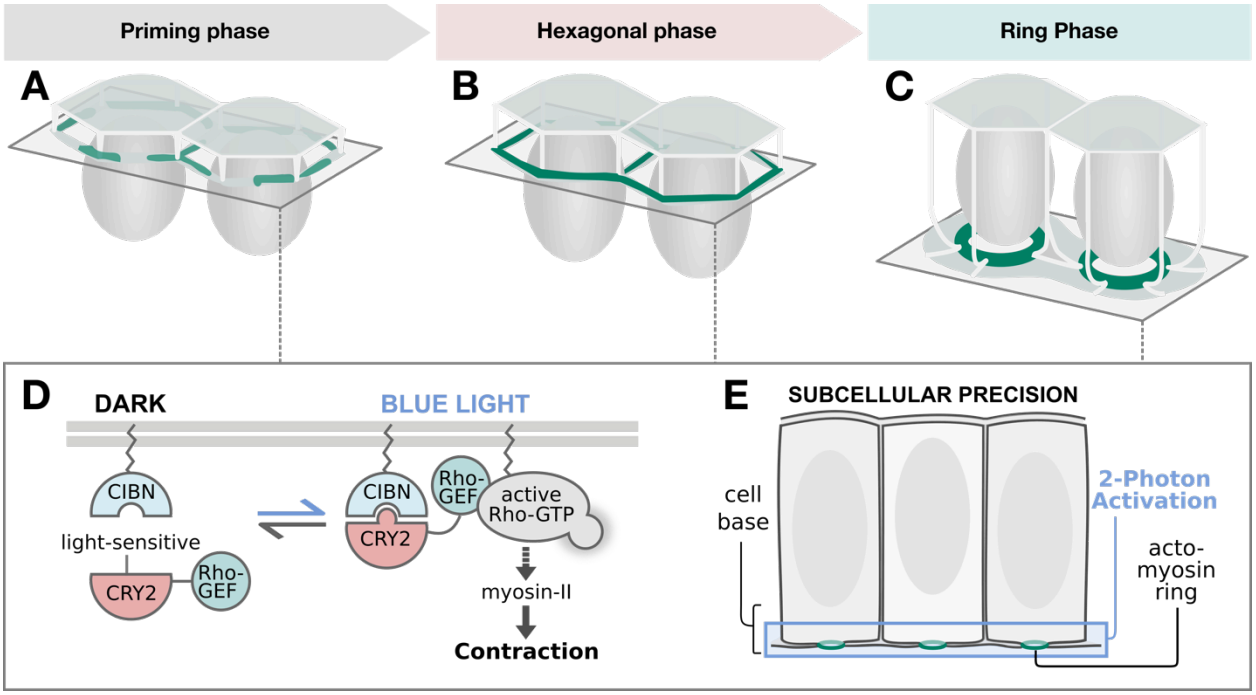

Figure 12. Schematic depiction of the experimental setup. (A-C) Schematic depiction showing the shape of the basal actomyosin network (green) during different stages of cellularization. The actomyosin network assembles at the basal membrane (light green) during the priming phase (A) into a hexagonal pattern (B). At the same time the membrane (light gray lines) ingresses. When the cell membrane reaches the base of the nuclei (gray ellipses), the actomyosin network rounds up into rings (C), constricts and eventually cleaves off individual cells. Myosin-II was photo-activated at the plane of the cellularization furrow (gray box). **(D)** Scheme outlining the RhoGEF2-CRY2/CIBN optogenetic system. The photosensitive domain of CRY2 is fused to the *Drosophila* RhoGTPase exchange factor RhoGEF2 and an N-terminally truncated version of CIB1, CIBN, is fused to the plasma membrane via a CAAX box. In the dark RhoGEF2-CRY2 shows cytoplasmic localization. Upon blue light illumination, CRY2 undergoes a conformational change triggering the interaction with CIBN and the recruitment of RhoGEF2-CRY2 to the plasma membrane, where it activates Rho1 signaling to stimulate myosin-II activation. **(D)** Schematic representation illustrating the experimental setup. A region of interest (blue box) was defined at the cell base and illuminated using two-photon microscopy to restrict photo-activation to the cell base at the level of the basal actomyosin network.

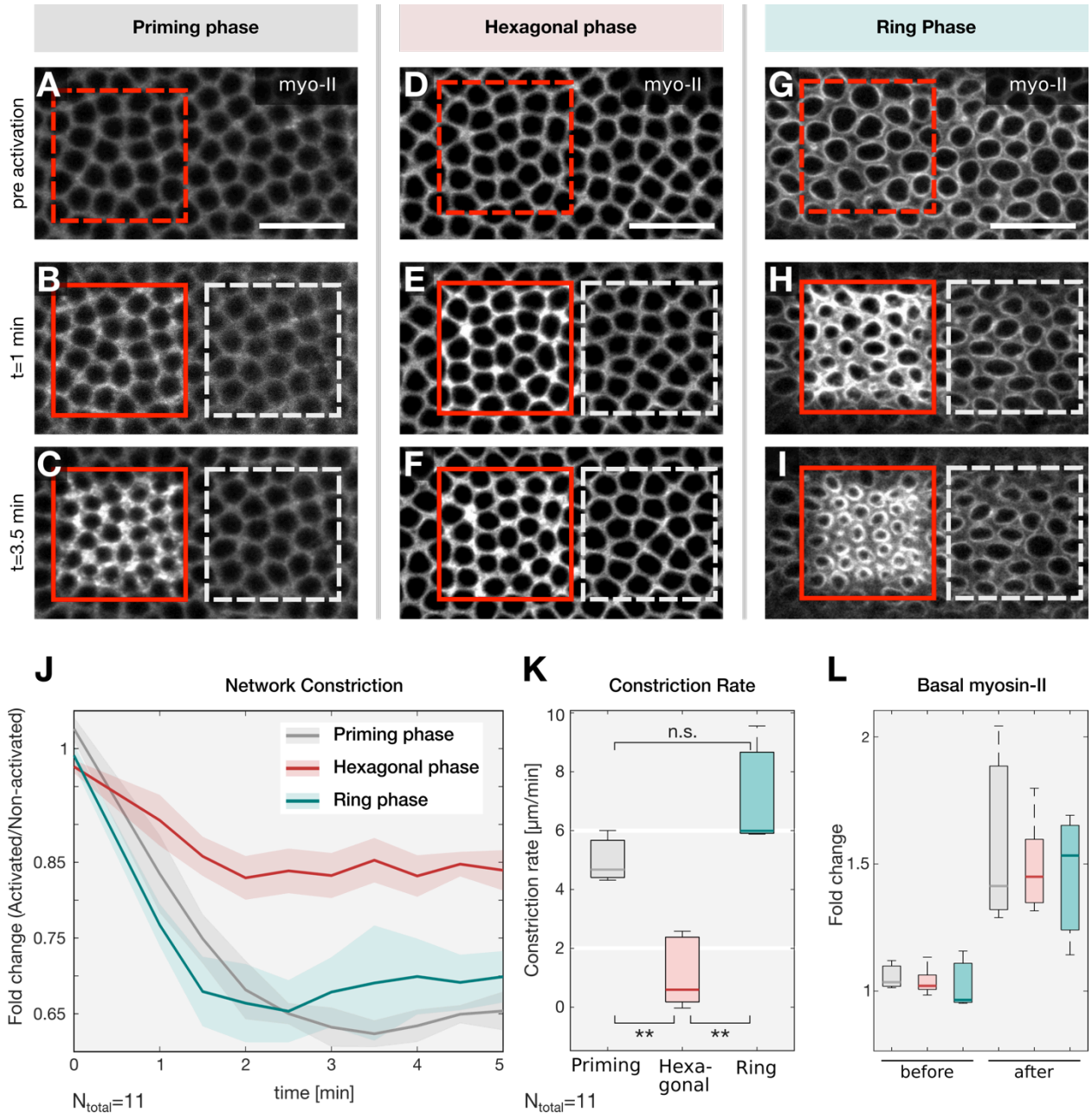

Figure 13. The basal actomyosin network in its hexagonal pattern is highly resistant to myosin-II activity. (A-I) Confocal sections of *Drosophila* embryos co-expressing RhoGEF2-CRY2, CIBN::GFP-pm and the myosin-II probe Sqh::mCh were imaged using a 561 nm excitation to visualize the actomyosin network either before (A,D,G), or after photo-activation at the cell base (B,C,E,F,H,I). Local photo-activation was achieved using two-photon illumination (950 nm) in a subset of cells (red square/dashed line: pre-activation region; red square/solid line: photo-activated region) during the priming phase (D-F), the hexagonal phase (G-I), or the ring phase (J-L). Basal myosin-II in (B, E, H) was recorded 1 min and in (C, F, I) 3.5 min after photo-activation. The white dashed boxes indicate a region of the same size as of the photo-activation region in the non-activated part of the embryo. (A-I) Scale bars indicate 20 μm. **(J)** Quantification of the extent to which the actomyosin network constricted over time upon optogenetic activation of myosin-II during the priming phase (gray, N=3), the hexagonal phase (red, N=5) and the ring phase (green, N=3). The mean area of the individual contractile units within the photo-activated region was measured and normalized to the non-activated region at the respective time point. The solid line indicates the mean fold change (area of the contractile units in the non-activated region/activated region) and the semi-transparent area represents the standard deviation. **(N)** Network constriction rate calculated during the first minute after photo-activation. When myosin-II was activated

during the priming (gray) or the ring (green) phase, the network constricted with a rate >5 μm/min, compared to a constriction rate of about 1 μm/min when myosin-II was activated during the hexagonal phase (red). Significances were estimated using non-paired Student's T-test with **: p<0.01. **(O)** Quantification of myosin-II levels in the photo-activated region before and after photo-activation. Irrespective of the network configuration (gray: priming phase; red: hexagonal phase; green: ring phase), myosin-II levels increased by a factor of about 1.5 upon light stimulation.

Using this experimental setup, I tested the response of different actomyosin network configurations to optogenetic stimulation of myosin-II. *Drosophila* embryos co-expressing the optogenetic module and the myosin-II probe Sqh::mCh were imaged using 561 nm light to visualize the actomyosin network in the whole tissue and photo-activated only in a restricted region (red box in Figure 13A-I) at the basal plane of the cellularization furrow using two-photon (950 nm) illumination. At different stages of cellularization (either during the priming, hexagonal or ring phase) myosin-II was stimulated by a single pulse of light focused on a defined region and the response of the actomyosin network was recorded over time. The non-activated cells (white box in Figure 13A-I) served as internal controls as they were only imaged using 561 nm laser excitation. In embryos photo-activated during the priming phase, when the network displayed a meshwork-like configuration or during the ring phase, the photo-activated region constricted to 65 % of the non-activated area with a rate >5 μm/min (Figure 13A-C, G-L). In contrast, during the hexagonal phase the photo-activated region constricted only to 85% with a rate of <2 μm/min (Figure 13D-F, J-L). These results show that hexagonally organized actomyosin fibers during slow phase of cellularization are more resistant to myosin-II motor activity as compared to when they are organized in a meshwork or ring-like

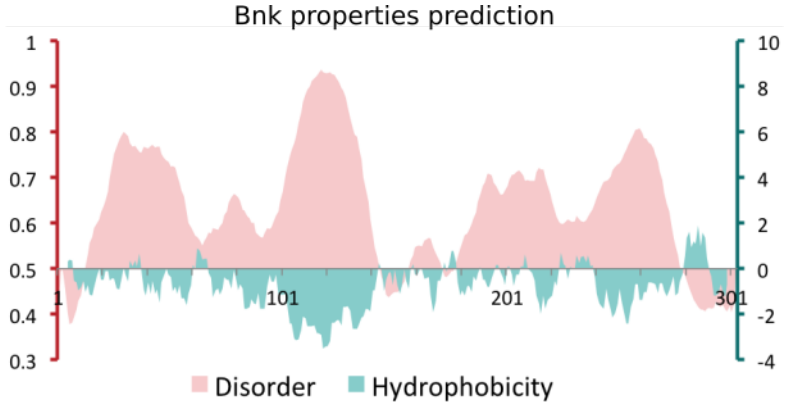

Figure 14. Bottleneck is an intrinsically disordered and hydrophobic protein prone to aggregation. Graph showing a per-residue disorder prediction (red, left y-axis, RONN v3.2) and a Kyte-Doolittle hydrophobicity plot (green, right y-axis, ExPASy ProtScale) of the 303 amino acid spanning Bottleneck protein. Bottleneck is highly unstructured (score >0.5 indicates disorder) and hydrophobic (high Kyte-Doolittle score indicates high hydrophobicity).

shape. This result supports the hypothesis that the architecture of the actomyosin network critically impacts on its contractile behavior *in vivo*.

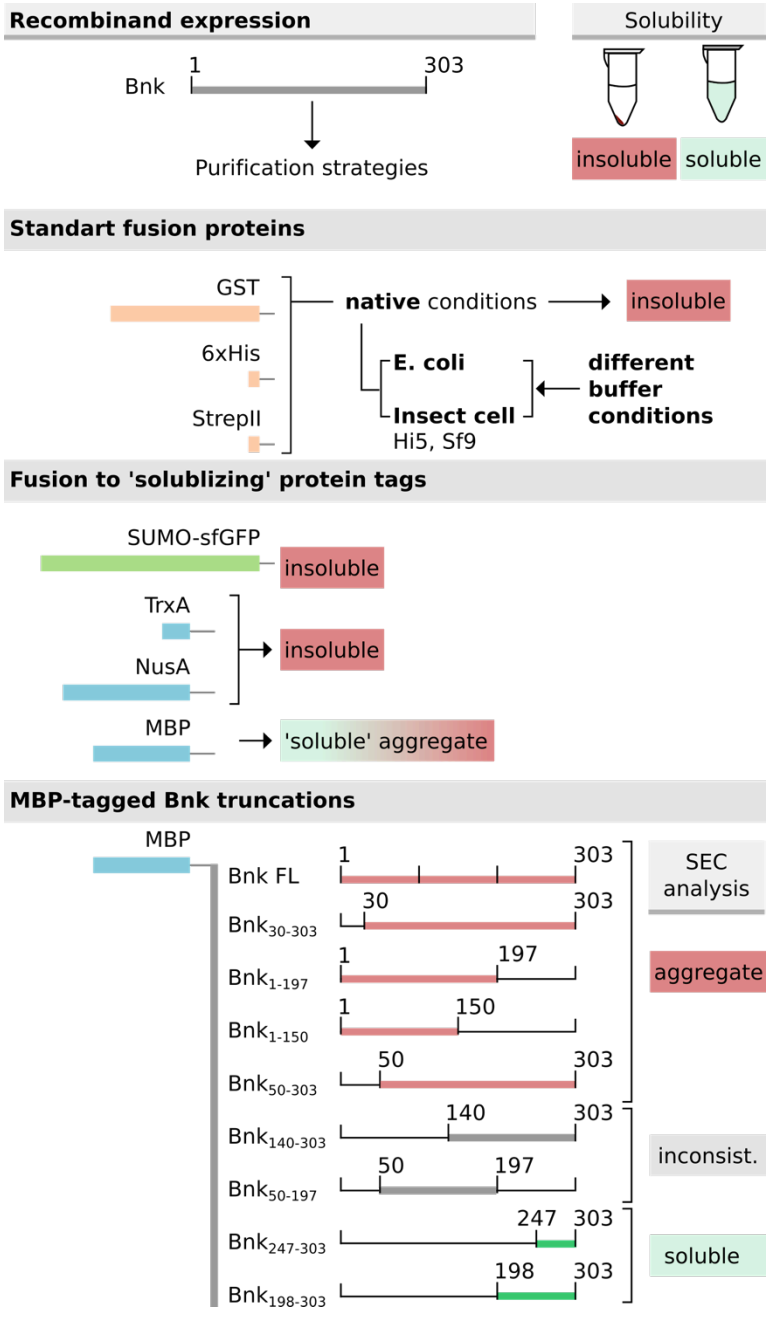

Figure 15. Overview of the systematic approach to produce soluble Bottleneck protein. Bottleneck is spanning 303 amino acids but due to high disorder and hydrophobicity it is prone to aggregate. The solubility was assessed by measuring the pelleting behavior upton centrifugqation. Full-length Bottleneck was first expressed as GST-, His-fusion proteins in *E. coli* and His-, StrepII-tagged Bottleneck was expressed in insect cells (Sf9 and Hi5 cells) . Irrespective of the expression and native lysis conditions tested, the protein was insoluble. Bottleneck was fused to solubilizing tags like SUMO-sf-GFP, TrxA, NusA and MBP. Only MBP-Bottleneck showed increased solubility and the purified protein did not pellet upon tabletop centrifugation, however it formed big molecular structures assessed by size exclusion chromatography (SEC) and pelleted upon ultracentrifugation. Afterwards, multiple Bnk truncations were expressed and purified as MBP fusion proteins. While most sample proteins aggregated or showed inconsistent results, MBP-$Bnk_{247-303}$ and $Bnk_{198-303}$ could be purified as soluble proteins.

3.1.2. The zygotic gene product Bottleneck functions as actin crosslinker

The higher resistance of the hexagonal actomyosin network to myosin-II motor force suggests specific mechanisms restricting network contractility. To gain insight into the molecular machinery controlling actomyosin organization during slow phase of cellularization, I sought of investigating the molecular function of Bottleneck, a key regulator of network transitions during cellularization that was found to be required for the assembly of the hexagonal actomyosin network and prevent premature constriction (Schejter and Wieschaus, 1993). Although the *bottleneck* mutant phenotype was identified already few decades ago, the mechanisms of action of Bottleneck protein have remained elusive so far. All attempts to characterize its function *in vitro* have been unsuccessful due to its high degree of predicted disorder and hydrophobicity which make Bottleneck to be very prone to aggregation (Figure 14).

For that reason, in collaboration with Theresa Quinkler I systematically optimized expression and purification conditions to produce recombinant Bottleneck (Figure 15). I expressed full-length Bottleneck fused to either GST, His or StrepII using different expression protocols (auto-induction, IPTG induction at 24°C, 30°C, 37°C) and tested various lysis buffers differing in the buffer system, pH, salt concentration, etc. (Appendix 1A) in *E. coli* and in insect cells (Figure 15). Since the fusion proteins were insoluble in all tested conditions, I expressed full-length Bottleneck fused to solubility-enhancing protein tags including SUMO-sf-GFP, TrxA, NusA and MBP. Only MBP-tagged Bottleneck showed increased solubility among the tested conditions (Appendix 1B). Although I was able to purify MBP(-His-)Bottleneck using affinity chromatography (Appendix 1C), the protein formed high-molecular aggregates that pelleted upon ultracentrifugation (Appendix 1D). This led me to the conclusion that the purification of full-length Bottleneck was not possible under native conditions – most likely due its intrinsic physicochemical characteristics (Figure 14).

Instead, I took advantage of the observation that exogenous expression of Bottleneck in HeLa cells recapitulated the protein's native localization to actin-rich structures like stress fibers (Reversi *et al.*, 2014). Therefore, I expressed multiple Bottleneck trunca-

tions in HeLa cells with the aim to identify truncations that resembled the localization of the full-length protein and presumably retained functionality (Figure 16). At the same time a series of Bottleneck deletion constructs fused to a cleavable MBP-tag and a His-tag (Appendix 3) were expressed in *E. coli* (Appendix 1E). The purified MBP-His-Bnk fusion proteins were analyzed using size exclusion chromatography (SEC) to test whether or not the protein aggregated (Figure 15). Using this dual approach, I identified an N-terminal deletion construct, MBP-His-Bnk$_{198-303}$ that retained solubility (Appendix 1F-H, Appendix 2A) and localized like the full-length protein (Figure 16B,F).

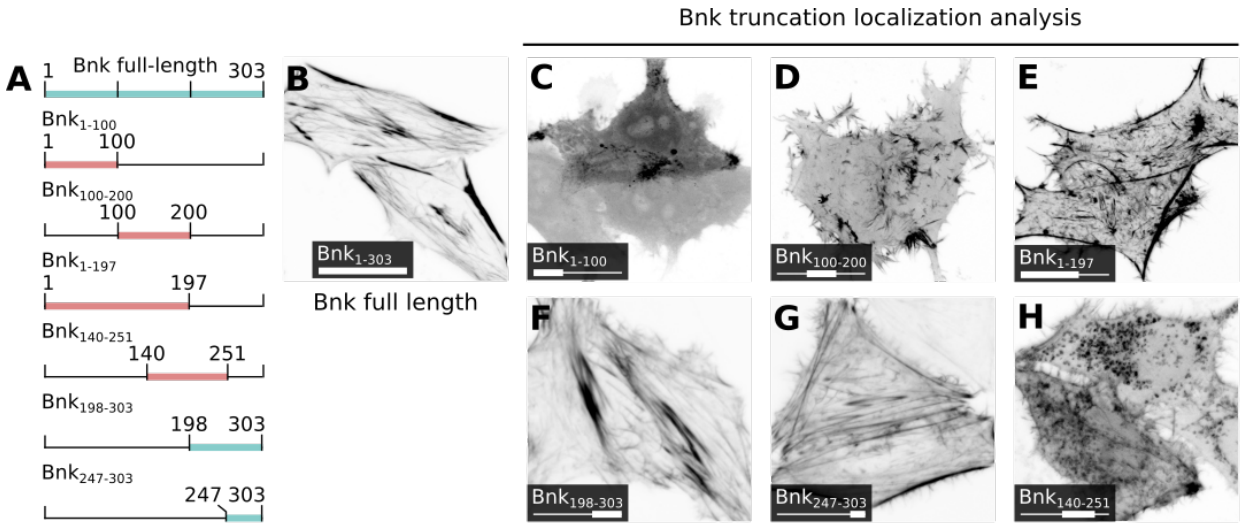

Figure 16. Analysis of the localization of Bnk deletion constructs in HeLa cells. (A) Schematic overview of the different Bottleneck deletion constructs tested. **(B-H)** Confocal images showing the localization of Bottleneck deletion constructs fused to GFP (B: Bnk$_{1-303}$, C: Bnk$_{1-100}$, D: Bnk$_{100-200}$, E: Bnk$_{1-197}$, F: Bnk$_{198-303}$, G: Bnk$_{247-303}$, H: Bnk$_{140-251}$) expressed in HeLa cells.

Having obtained enough purified recombinant MBP-His-Bnk$_{198-303}$, I tested whether it could bind actin directly using an actin co-sedimentation assay. While MBP-His-Bnk$_{198-303}$ alone remained in the supernatant fraction upon ultracentrifugation, in presence of *in vitro* polymerized filamentous actin (F-actin) a portion of the protein shifted to the pellet fraction (Appendix 2B) suggesting actin-binding activity. To test whether MBP-His-Bnk$_{198-303}$ was able to organize actin filaments, I visualized actin filaments in the presence of MBP-His-Bnk$_{198-303}$ using negative staining electron microscopy with the help of Simon Mortensen form Carsten Sachse's lab at EMBL, Heidelberg. MBP-His-Bnk$_{198-303}$ was incubated with F-actin and 5 nm Ni-NTA-Nanogold to directly visualize

MBP-His-Bnk$_{198-303}$, via the intramolecular His-tag. The EM micrograph revealed that although a number of MBP-His-Bnk$_{198-303}$ molecules aligned with F-actin filaments, the majority of MBP-His-Bnk$_{198-303}$ did not bind F-actin and appeared as dispersed mono-

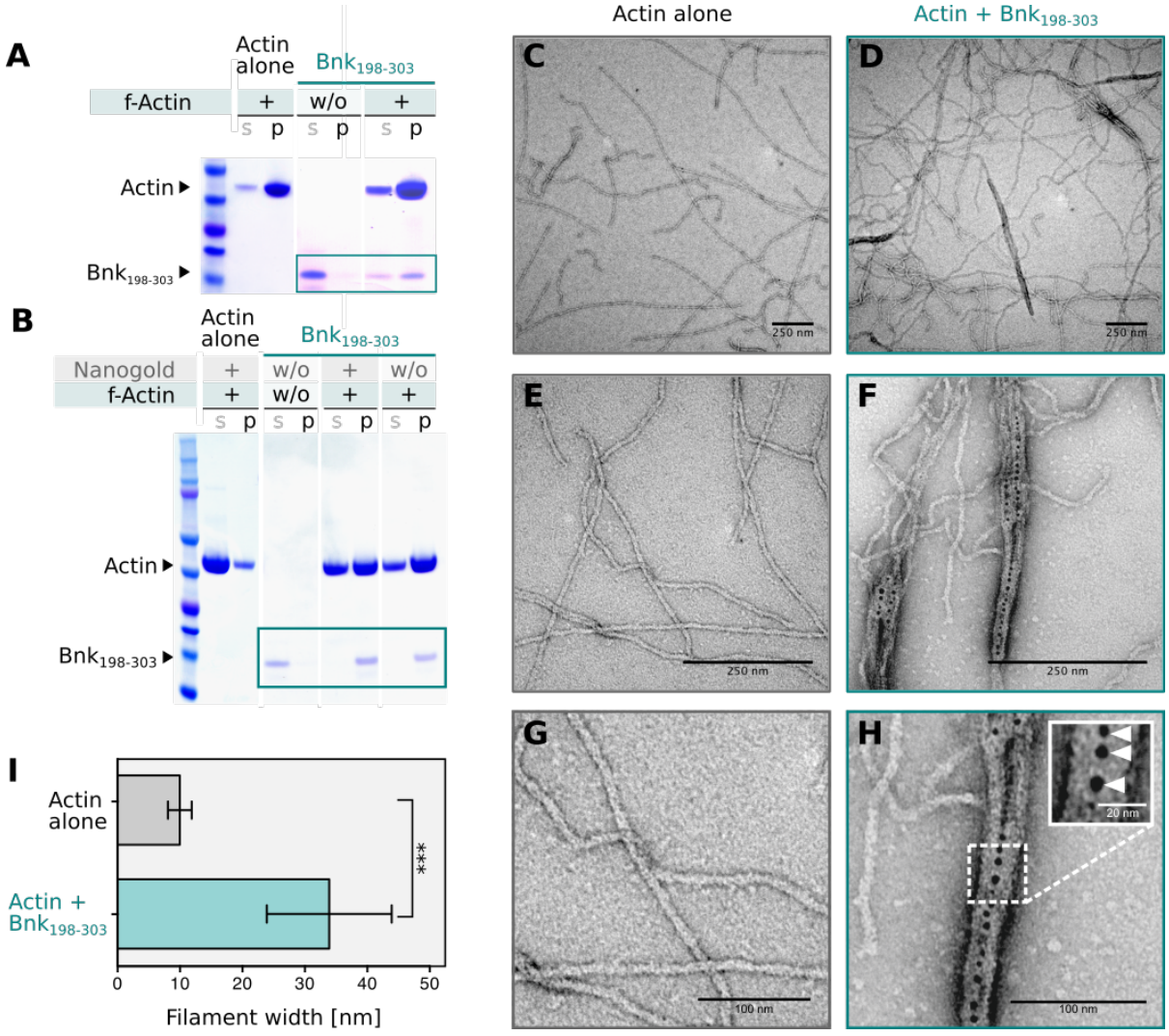

Figure 17. Bnk$_{198-303}$ crosslinks actin fibers and induces actin-bundle formation. (A) Coomassie stained gel showing the results of an actin-binding assay. While in the absence of actin, purified Bnk$_{198-303}$ remained in the supernatant fraction (s), in presence of F-actin, the majority of Bnk$_{198-303}$ protein co-pelleted with actin filaments (p: pellet fraction). The green box highlights Bnk$_{198-303}$ protein bands. **(B)** Coomassie stained gel showing the results of an actin bundling assay. In the presence of F-actin, Bnk$_{198-303}$ moved from the supernatant fraction (s) to the pellet fraction (p). The ratio of F-actin in the pellet to that in the supernatant increased in presence of Bnk$_{198-303}$. The presence of 5 nm Ni-NTA Nanogold particles did not alter actin or Bnk behavior. The green box highlights Bnk$_{198-303}$ protein bands. **(C-H)** Electron micrographs showing actin fibers alone (C, E, G) or bound by Bnk$_{198-303}$ (D, F, H) at low magnification (C, D), high magnification (E, F) and a further zoom in (G, H). Note that the samples were supplemented with 5 nm Ni-NTA Nanogold particles to directly visualize Bnk$_{198-303}$ in negative stain micrographs. Inset in (H) shows a zoom of an actin bundle. Arrowheads highlight the localization of Bnk$_{198-303}$ in the center of the bundle. **(I)** Quantification of the width of actin filaments in absence (gray) or presence (green) of Bnk$_{198-303}$. Bnk$_{198-303}$ induced actin bundles resulting in an increased filament width. Significances were estimated using non-paired Student's T-test with ***: p<0.001.

meric structures suggesting low actin-binding activity (Appendix 2C). I suspected that the MBP-tag interfered with the comparably small Bottleneck construct and thus I decided to optimize a purification procedure that allowed me to cleave off the MBP tag and to produce His-$Bnk_{198-303}$, hereafter referred to as $Bnk_{198-303}$.

Using an actin co-sedimentation assay, I found that $Bnk_{198-303}$ alone remained in the supernatant upon ultracentrifugation, but shifted to the pellet fraction in the presence of F-actin suggesting direct actin binding activity (Figure 17A, green box). To test if $Bnk_{198-303}$ alone could organize actin filaments *in vitro*, I performed an actin-bundling assay, which differs from the actin-binding assay in that pelleting is done at a lower centrifugation speed. At low speed centrifugation, polymerized actin filaments do not pellet unless they are bundled together by actin crosslinking proteins. The result of this experiment showed that in presence of $Bnk_{198-303}$, F-actin was enriched in the pellet fraction, supporting the hypothesis that Bottleneck acts as an actin bundling/crosslinking protein (Figure 17B). Hence, I repeated the electron microscopy experiment to visualize actin filaments in the presence or absence of $Bnk_{198-303}$ together with 5 nm Ni-NTA-Nanogold to directly visualize $Bnk_{198-303}$ (Figure 17C-H). While in absence of $Bnk_{198-303}$, F-actin appeared as individual fibers with an average width of ~10 nm (Figure 17C, E, G, I), $Bnk_{198-303}$ induced filament bundles with an average width of ~30 nm (Figure 17D, F, H, I). The visualized actin bundles were decorated by Nano gold particles (inset Figure 17H) at the bundles' center demonstrating that purified $Bnk_{198-303}$ directly crosslinks actin fibers and induces actin bundling *in vitro*.

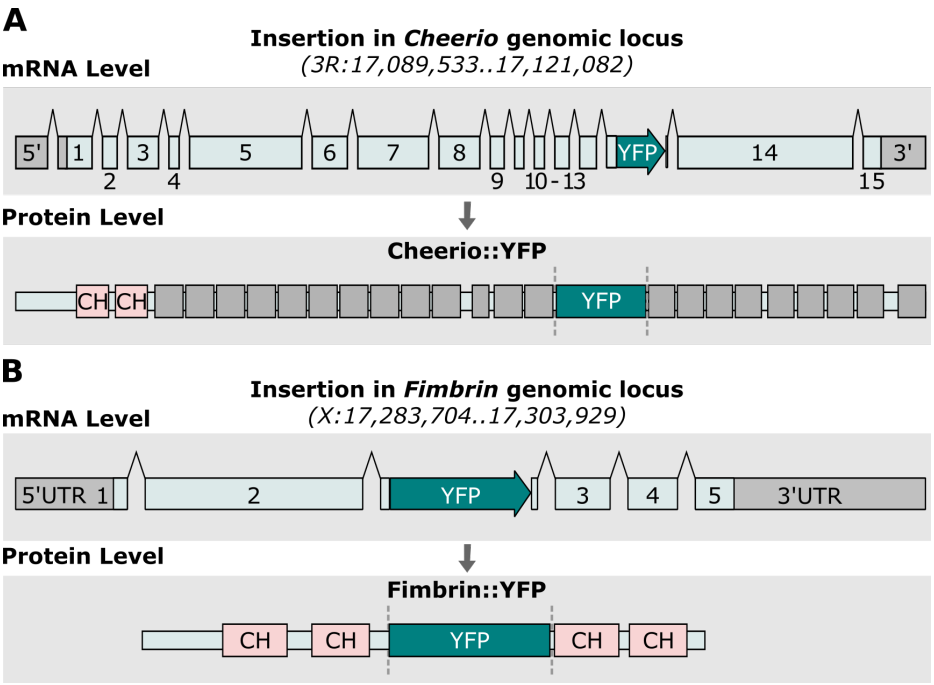

Figure 18. Map showing the position of the YFP-tag in cheerio and fimbrin and the localization. (A, B) Schematic representation of the YFP gene trap, comprising the YFP/Venus gene flanked by a splice donor and splice acceptor site, inserted into the genomic locus of cheerio (A) and fimbrin (B) at the mRNA level (upper panel) and protein level (lower panel). mRNA architecture of the tagged genes. Exons are numbered and shown in light green, untranslated regions (UTRs) are shown in gray, the YFP gene is shown in dark green and introns are shown as lines connecting the exons (upper panels in A, B). Protein architecture coded by the tagged genes. The actin-binding Calponin homology (CH) domains are shown in light red and the fluorescent protein YFP is shown in dark green. Ig-like FLN repeats are shown in dark gray (lower panels in A, B). Dashed lines indicate the splice sites flanking the YFP-insertion. The YFP-tagged fly lines cher[CPTI001399] and fim[CPTI100066] were obtained from the Cambridge Protein Trap Insertion (CPTI) collection. The insertion sites for fim[CPTI100066] were characterized here for the first time.

3.1.3. Cheerio and Fimbrin time actomyosin network transitions *in vivo*

The increased resilience of the hexagonal actin network to myosin-II activity, the dependence of this network configuration on Bottleneck and the molecular function of Bottleneck as an actin-bundling protein, are consistent with a model in which Bottleneck antagonizes myosin-II mediated network contraction by tightly crosslinking actin filaments together during the slow phase of cellularization. This prompted me to test whether this conclusion could be generalizable to other actin crosslinkers.

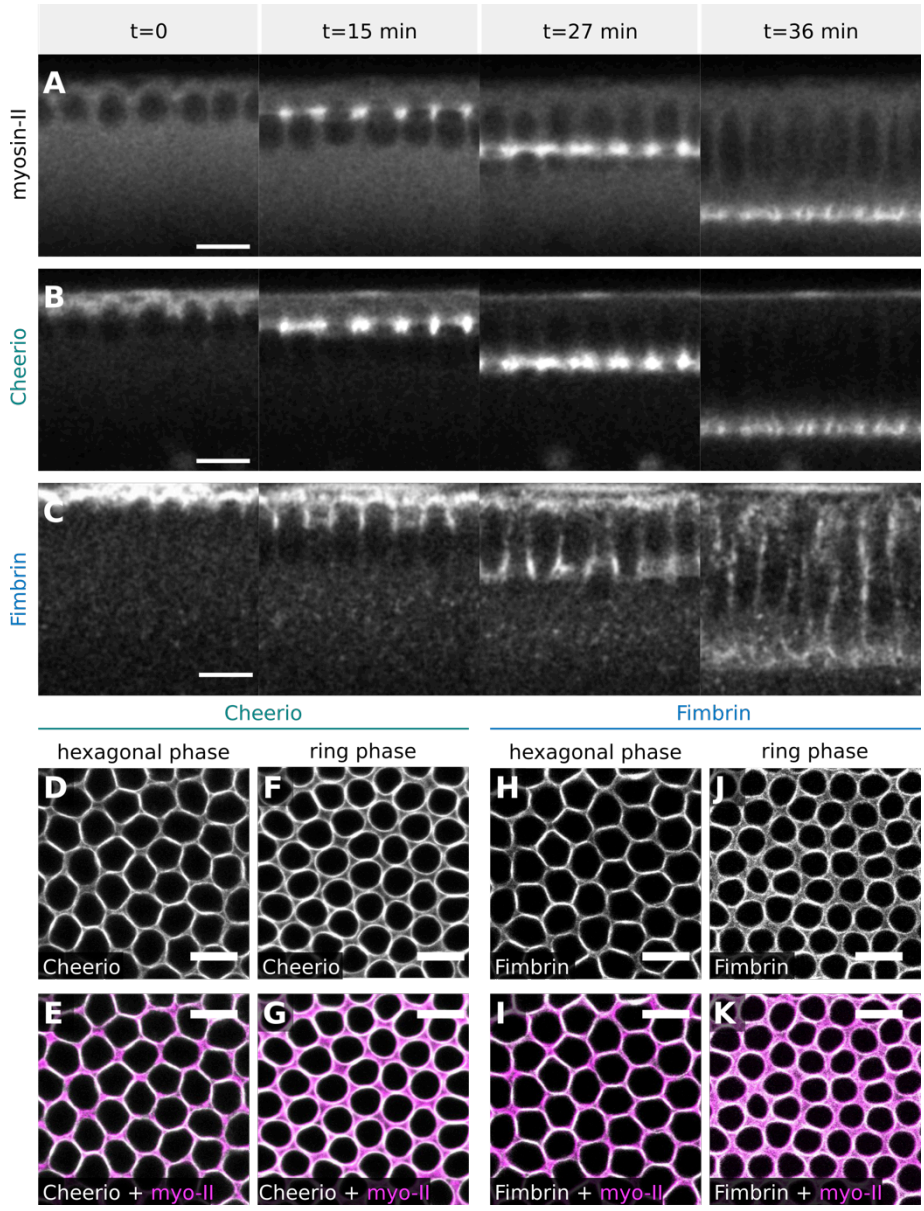

Figure 19. The actin crosslinkers Cheerio and Fimbrin co-localize with myosin-II at the leading edge of the cellularization furrow. (A-C) Confocal (A,B) and two-photon (C) microscopy images of cellularizing embryos expressing the myosin-II probe Sqh::mCh (A), Cheerio::YFP (B) or Fimbrin::YFP (C). Still frames showing the sagittal cross sections (from left to right) at the onset of cellularization (t=0), after 15 min, 27 min and 36 min. Similar to myosin-II (C), Cheerio localized predominantly to the cellularization front (D) throughout cellularization. Fimbrin was enriched at the cell base throughout cellularization but also localized to other sites of the cell (E). Scale bars, 20 μm. **(D-K)** Confocal images of cellularizing embryos co-expressing the myosin-II probe Sqh::mCh (magenta) and Cheerio::YFP (gray) (D-G) or Fimbrin::YFP (gray) (H-K), showing the basal network during the hexagonal phase (D-E, H-I) and ring phase (F-G, J-K) of cellularization. Both, Cheerio and Fimbrin, co-localized with myosin-II at the leading edge of the cellularization furrow during the hexagonal and the ring phase. Scale bars, 10 μm.

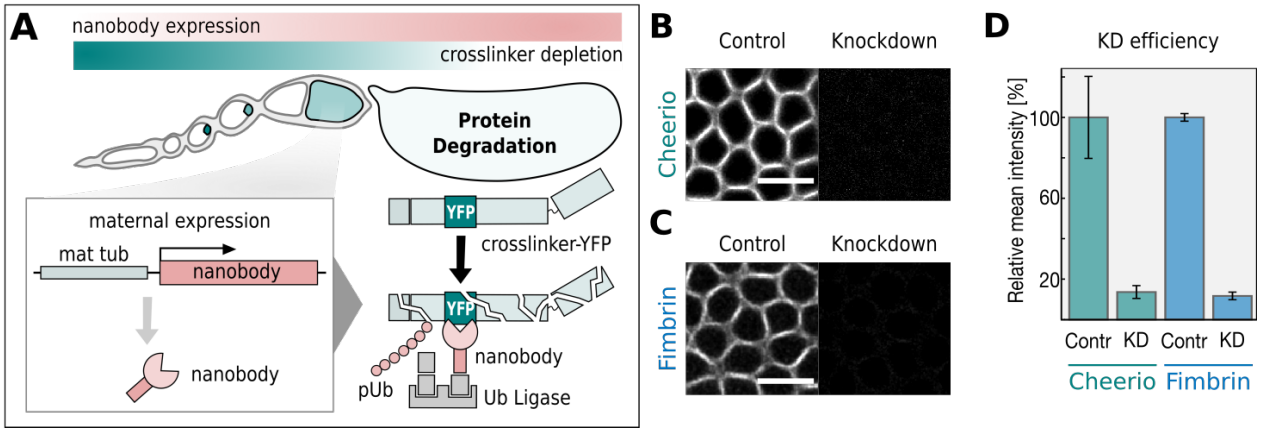

Figure 20. Anti-GFP nanobody-mediated knock down of Cheerio and Fimbrin led to the efficient depletion of the target proteins during cellularization. (A) Schematic depiction showing the anti-GFP nanobody expression driven by the maternal tubulin promoter in the ovaries leading to a progressive depletion of the YFP-tagged crosslinker during early embryogenesis. The YFP-tagged crosslinker is bound by anti-GFP nanobody fused to an F-box protein priming the crosslinker for proteasomal degradation. **(B,C)** Confocal images showing the YFP fluorescence of Cheerio (A) and Fimbrin (B) in the absence (Control) or presence (Knockdown) of the nanobody. **(D)** Quantification of the knockdown efficiency based on the YFP-signal of Cheerio and Fimbrin upon nanobody expression (KD) normalized to the average of the control (Contr).

I investigated the localization of a series of endogenously YFP-tagged actin crosslinkers in fly lines homozygous for the YFP insertion during early *Drosophila* development (Figure 18). Cheerio and Fimbrin, the *Drosophila* orthologues of Filamin and plastin, were identified to co-localize with myosin-II to the basal actomyosin network both during the hexagonal phase and during the ring phase (Figure 19).

To analyze the role of Cheerio and Fimbrin during cellularization, I depleted the proteins using the anti-GFP nanobody system. The nanobody was expressed maternally in flies homozygous for either Cheerio::YFP or Fimbrin::YFP and the actomyosin network was visualized by a co-expressed myosin-II probe (Sqh::mCherry) (Figure 20A). Upon nanobody-mediated protein knockdown, on average more than 85% of the YFP-tagged crosslinkers was depleted (Figure 20B-C).

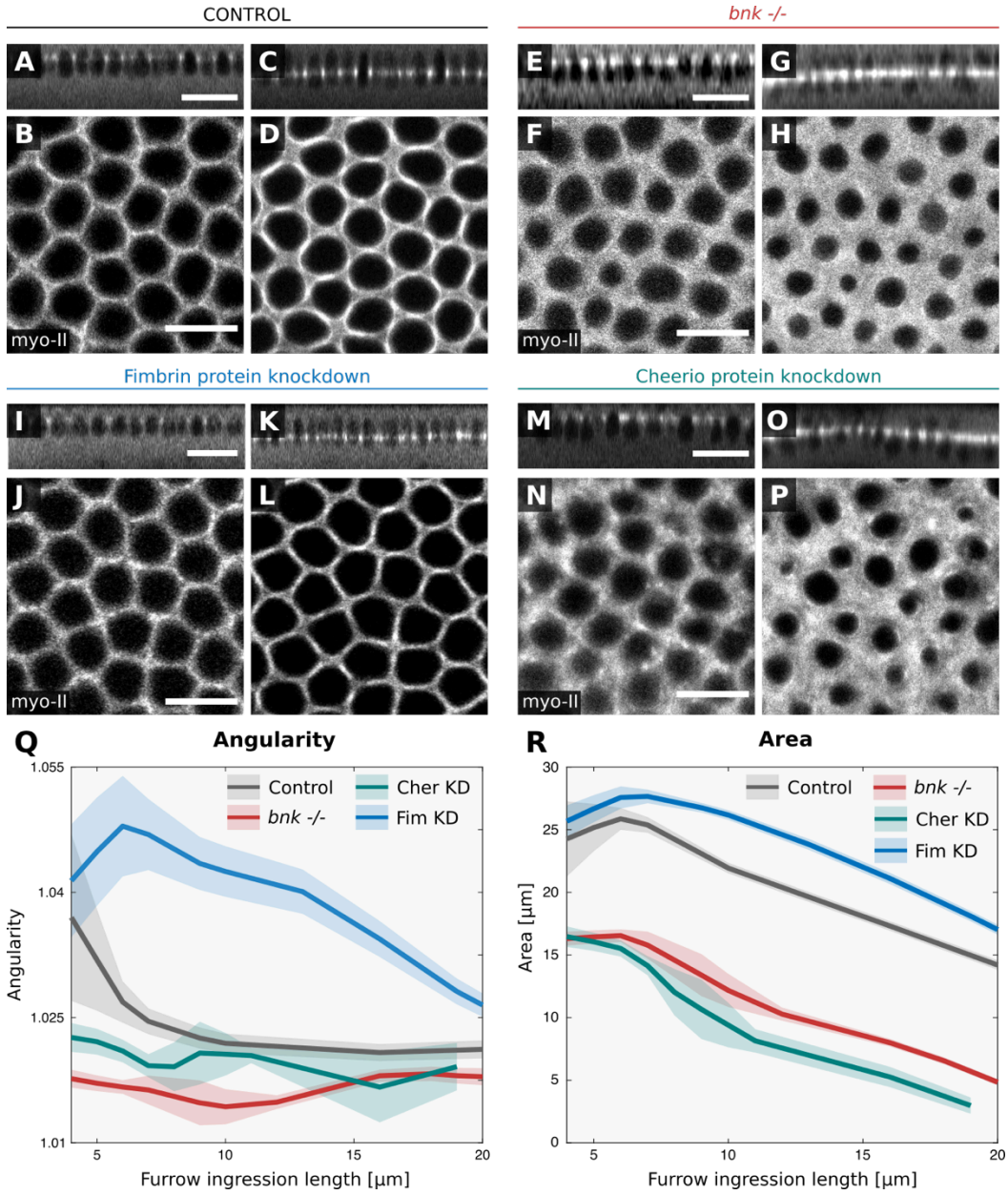

Figure 21. Phenotypic analysis of bottleneck mutant, Cheerio and Fimbrin knockdown embryos during cellularization. (A-P) Confocal images illustrating the actomyosin network in cellularizing embryos expressing the myosin-II marker Sqh::mCh in control embryos (A-D), in *bnk -/-* embryos (E-H), and in embryos expressing the nanobody knockdown module targeting Fimbrin (I-L)) or Cheerio (M-P). The upper panels show sagittal cross sections (scale bar: 20 μm) and the lower panels the basal myosin-II signal. Scale bars: 10 μm. Images represent two sequential stages of cellularization: (A-B, E-F, I-J, M-N) furrow is at 5 μm from the apical surface, and (C-D, G-H, K-L, O-P) furrow is at 10 μm from the apical surface. (Q-R) Quantification of the average angularity (Q) and area (R) of the contractile units present in the network relative to the ingression depth of the cellularization furrow in either control (black), bnk -/- (red), Cheerio knockdown (green), or Fimbrin knockdown (blue) embryos. Solid lines indicate the average value and the semi-transparent area the SEM.

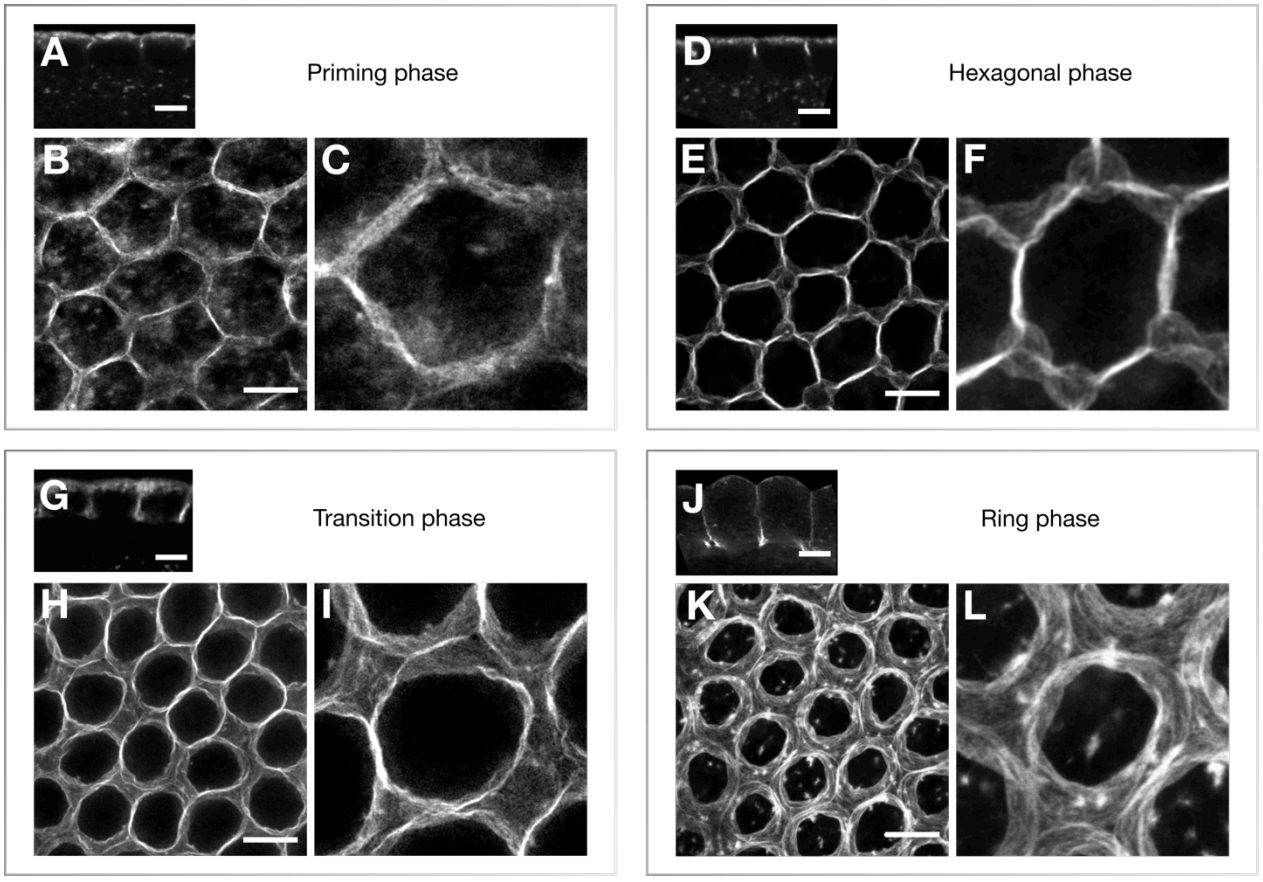

Figure 22. Super-resolution analysis of wild type control embryos at different stages of cellularization. (A-R) STED images showing the actin signal in sagittal cross sections (A, D, G, J) and the basal actin network from the top-view in an overview image (B, E, H, K) and close up (10 μm x 10 μm) of a single contractile unit in (C, F, I, L). The *Drosophila* embryos were fixed at different stages of cellularization as indicated in the panels, stained using phalloidin–Atto 647N and imaged using 2D-STED microscopy at a resolution of ~15 nm. During the priming phase (B, C) actin filaments assembled into fibers to form a hexagonal array. During the hexagonal phase (E, F) actin structures were bundled in fibers, which appeared to be shared by two adjacent contractile units rather than forming two parallel structures in close proximity. During the transition phase (H, I) the hexagonal organization disassembles, actin cables bend to individualize contractile rings. During the ring phase (K, L) each contractile unit was composed of individualized ring structures and a meshwork at the interspace. Scale bars: 5 μm.

The phenotypic analysis of Cheerio and Fimbrin knockdowns revealed two complementary phenotypes (Figure 21A-R). Similar to the *bottleneck* mutant phenotype (Figure 21E-H), knockdown of Cheerio (Figure 21M-P) impaired hexagonal network assembly, giving rise to a meshwork-like network pattern that constricted prematurely and in an uncoordinated manner (Figure 21R). On the contrary, knockdown of Fimbrin prolonged the duration of the hexagonal phase (Figure 21 I-L). The geometry of the different mutant phenotypes was diametrically different, as *bottleneck* mutants and Cheerio knockdown embryos assembled into round contractile units that constricted prematurely,

whereas Fimbrin knockdown embryos showed increased angularity throughout cellularization with reduced constriction kinetics (Figure 21Q-R).

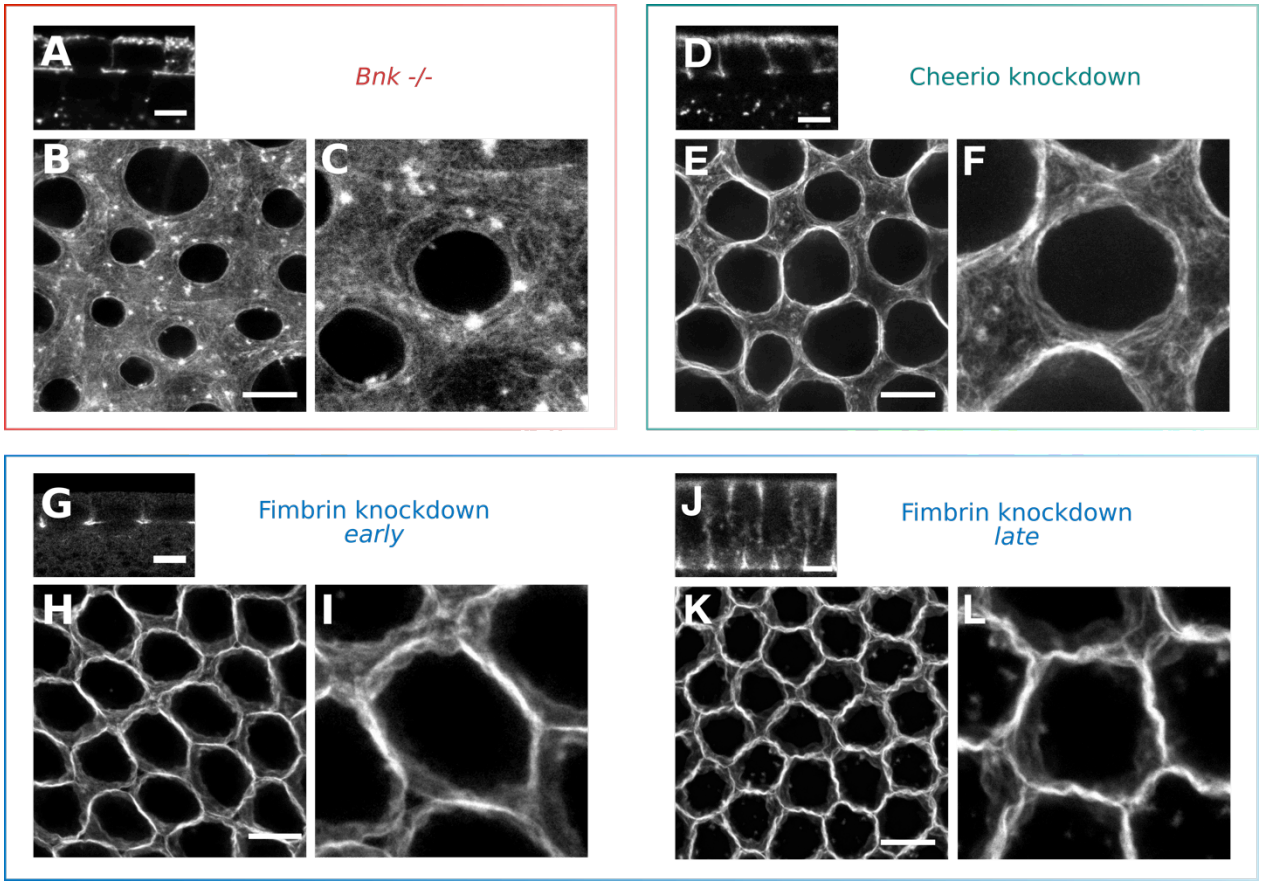

Figure 23. Super-resolution analysis of Cheerio and *bottleneck* mutant embryos reveals their critical role in actin bundling during the hexagonal phase. (A-L) STED images showing the actin signal in sagittal cross sections (A, D, G, J) and the basal actin network from the top-view in an overview image (B, E, H, K) and close up (10 μm x 10 μm) of a single contractile unit in (C, F, I, L). The *Drosophila* embryos were fixed at different stages of cellularization as indicated in the panels, stained using phalloidin–Atto 647N and imaged using 2D-STED microscopy at a resolution of ~15 nm. Upon loss of Bnk (B-C) actin fiber formation was severely impaired and actin was disorganized forming a meshwork of filaments and thin bundles. Knockdown of Cheerio (E-F) resulted in reduced actin fiber formation, network disorganization and desynchronized ring constriction. Knockdown of Fimbrin did not affect actin fiber formation during the hexagonal phase (H, I), but rather caused persistence of actin fibers organized in a hexagonal pattern and shared by adjacent units (K, L) also at later stages of cellularization. Scale bars: 5 μm.

The defects in actomyosin network organization described above are suggestive of impaired actin crosslinking. Therefore, I used STED microscopy to visualize actin organization at single filament-resolution. Embryos were fixed and stained with fluorescently labeled phalloidin and imaged by STED super-resolution microscopy. In control embryos, during the hexagonal phase actin fibers appeared as an array of individual filaments that were tightly bundled together and interconnected across the entire basal surface of the

embryo (Figure 22A-F). At later stages, the hexagonal network disassembled and actin cables bended to form individualized units (Figure 22G-I) that during the ring stage appeared as individual actin ring structures, interconnected by an actin meshwork at the interspace between contractile units (Figure 22J-L).

In *bottleneck* deficient or Cheerio knockdown embryos, actin bundling was severely impaired and actin filaments localized diffusely in a disordered meshwork covering the basal membrane (Figure 23A-F). In contrast, in Fimbrin knockdown embryos hexagonal assembly was normal but the transition to contractile rings was impaired and the network remained interconnected in a hexagonal array of actin bundles (Figure 23G-L). Collectively, these results demonstrate that correct spatial actin network organization and timing of contractility depends on two crosslinkers that play a distinct role in either promoting actin bundling and hexagonal patterning (Cheerio), or in promoting network remodeling into contractile actin rings (Fimbrin).

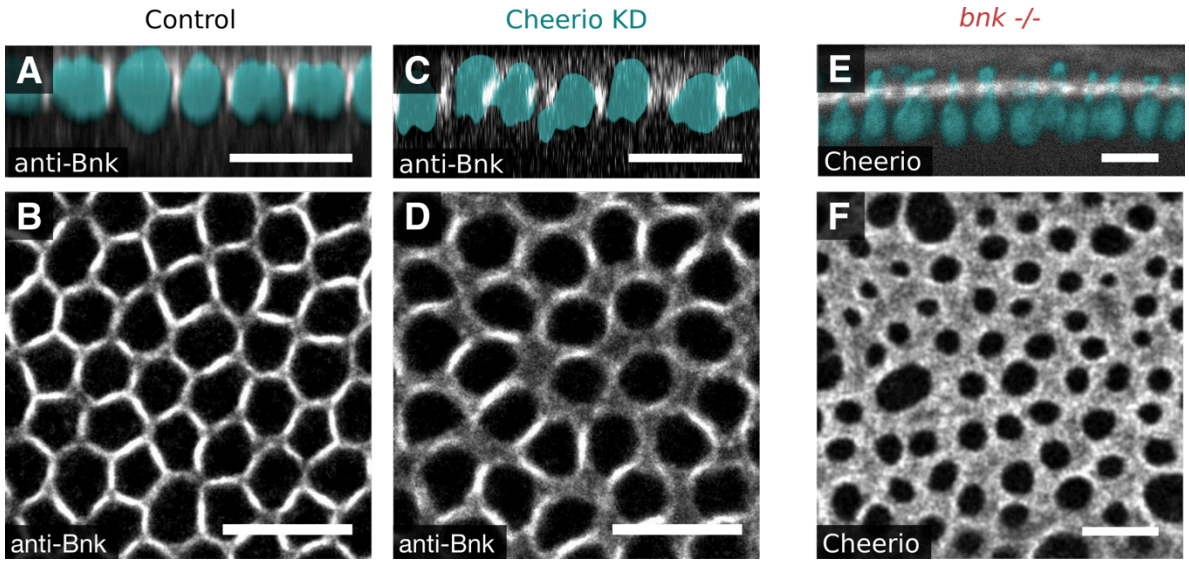

Figure 24. Localization to the leading edge of the cellularization furrow of Bottleneck does not depend on Cheerio and *vice versa*. (A-D) Confocal images of *Drosophila* embryos fixed and immunostained for Bottleneck (grayscale) and DAPI (cyan) in a control (A,B) and upon Cheerio knockdown (C,D). **(A-E)** Confocal images of *bnk -/- Drosophila* embryos expressing Cheerio::YFP (grayscale) and Histone::RFP (cyan). Sagittal sections are shown in (A, C, E) and top-views of the basal network are shown in (B, D, F).

3.1.4. Bottleneck synergizes Cheerio and antagonizes Fimbrin activity

The Cheerio and Fimbrin knockdown phenotypes suggest that while Cheerio and Bottleneck act in a cooperative fashion to control actin bundling at the plasma membrane, Fimbrin and Bottleneck act antagonistically in timing actomyosin ring conversion.

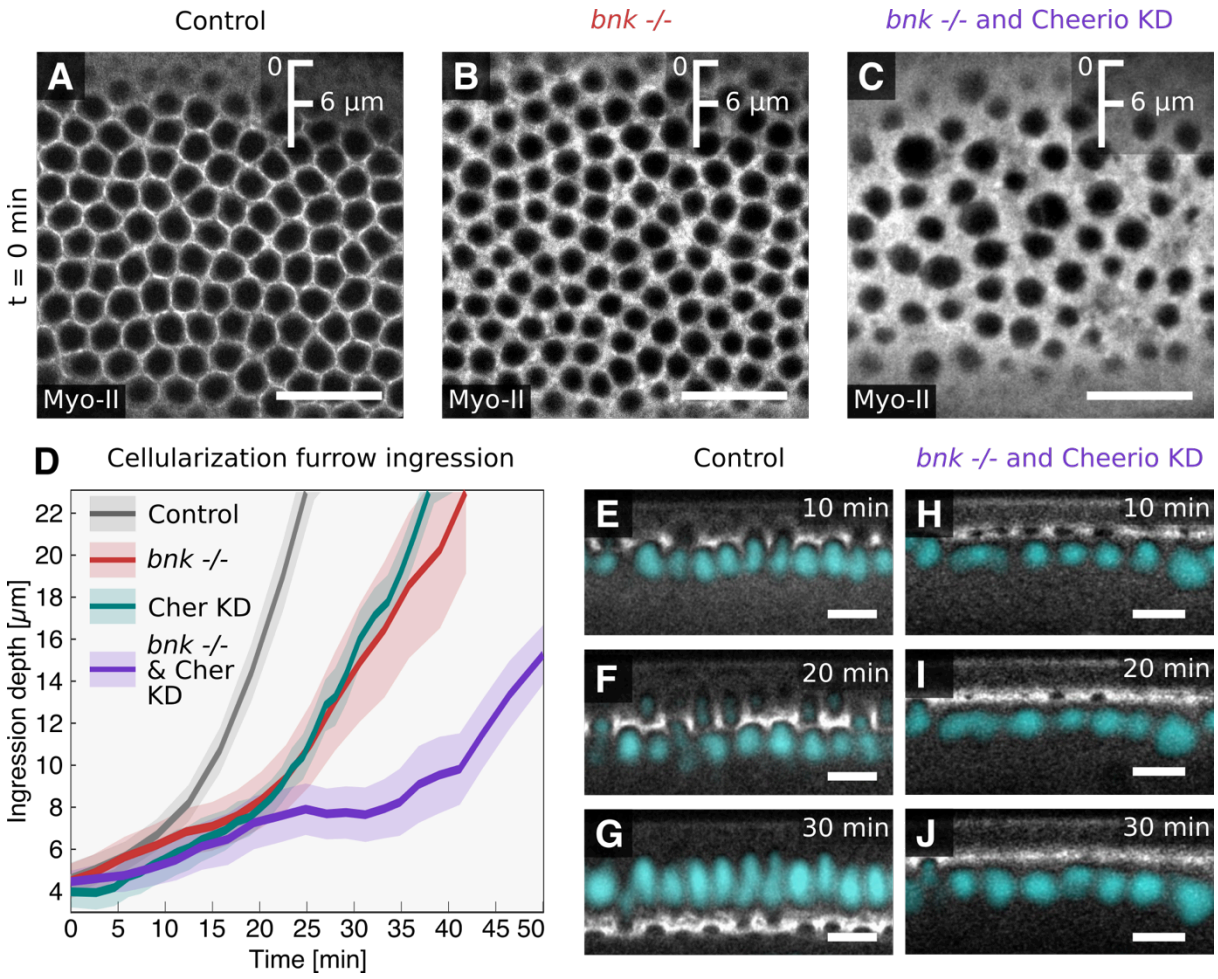

Figure 25. Bottleneck and Cheerio act synergistically during hexagonal patterning. (A-C, E-J) Confocal images of *Drosophila* embryos expressing the myosin-II marker Sqh::mCh in controls (A, E-G), in *bnk -/-* (B), or in *bnk -/-* and Cheerio KD double mutant embryos (C, H-J). Top views showing the basal actomyosin network at an ingression depth of 6 *µ*m in a control (G), in a bnk -/- (H), and in a bnk -/- and Cheerio KD double mutant embryo (I). The bottleneck mutant phenotype characterized by the lack of the hexagonal phase and hyper-contractility worsen in embryos in which Cheerio was also knocked down. Scale bars: 20 *µ*m. **(D)** Graph showing the ingression kinetics of cellularization (ingression depth of the furrow over time) in controls (black), *bnk -/-* (red), Cheerio KD (green), and in bnk -/- Cheerio KD double mutant embryos (purple). The ingression kinetics slows down in *bnk -/-* and Cherrio KD embryos. In *bnk -/-* and Cheerio KD double mutant embryos the phenotype gets synergistically worse resulting in a final ingression depth of no more than 10 *µ*m. Solid lines indicate the average ingression depth over time and the semi-transparent area indicates the standard deviation. **(E-J)** Sagittal sections showing myosin-II (grayscale) in a control embryo (E-G) or in a *bnk -/-* Cheerio KD double mutant embryo (H-J) 10 min (E, H), 20 min (F, I) and 30 min (G, J) after the cellularization furrow reached an ingression depth of 4 *µ*m. The position of the nuclei was inferred from lack of myosin-II signal and colored in cyan. Scale bars: 10 *µ*m.

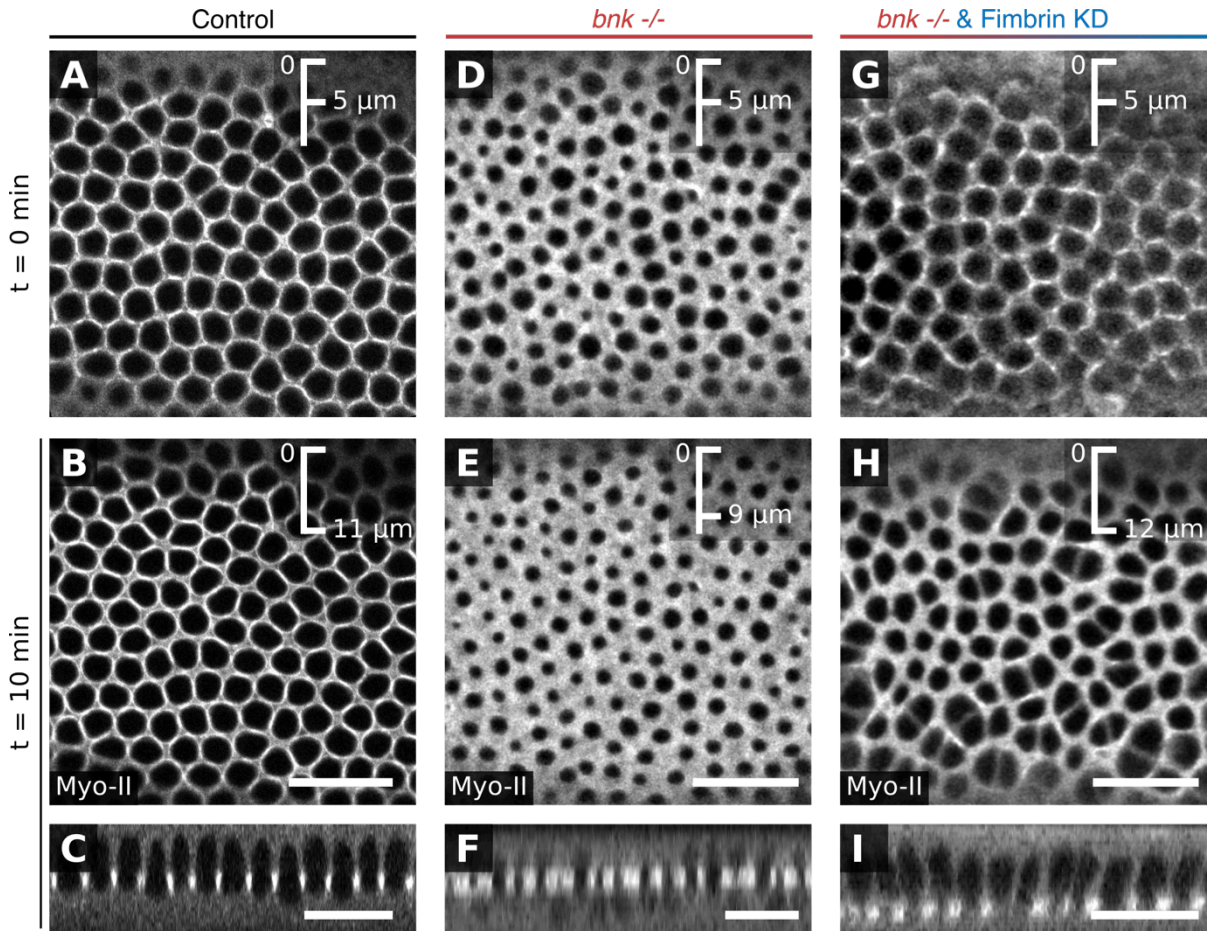

Figure 26. Depletion of Fimbrin rescues the *bottleneck* mutant phenotype. (A-I) Confocal images of *Drosophila* embryos expressing the myosin-II marker Sqh::mCh in control (A-C, M-P), in *bnk -/-* (D-F, Q-T) or in *bnk -/-* Fimbrin KD double mutant embryos (G-I, U-X). Images show cross-section views of the basal actomyosin network at a furrow ingression depth of 5 μm (A, D, G) and 10 min later (B, E, H). Images in (C, F, I) show sagittal sections of (B, E, H). Depletion of Fimbrin, partially rescued the *Bnk* mutant phenotype in terms of hypercontractility and defects in network organization. Scale bars: 20 μm.

Given the similarities between the *bottleneck* -/- and Cheerio KD phenotypes, I tested whether there was a mutual dependence of the two proteins in terms of localization to the basal actomyosin network. I immunostained Bottleneck in Cheerio KD embryos and analyzed endogenously YFP-tagged Cheerio in *bottleneck -/-* embryos and found that although the basal actomyosin network showed the described disorganized patterns, the predominant localization of the proteins to the leading edge of the cellularization furrow did not change compared to the control (Figure 24). This suggests that rather than being required for each other's localization in a linear signaling route, Bottleneck and Cheerio function in a parallel pathway. In fact, when I analyzed the mutant phenotype of Cheerio

KD *bottleneck* -/- double mutants, the defects in network organization severely worsen with actomyosin constrictions from the very beginning of cellularization (Figure 25A-C). causing an arrest of membrane invagination and improperly formed cells (Figure 25D-J). Thus, Bottleneck and Cheerio function synergistically to promote actin bundling and hexagonal patterning.

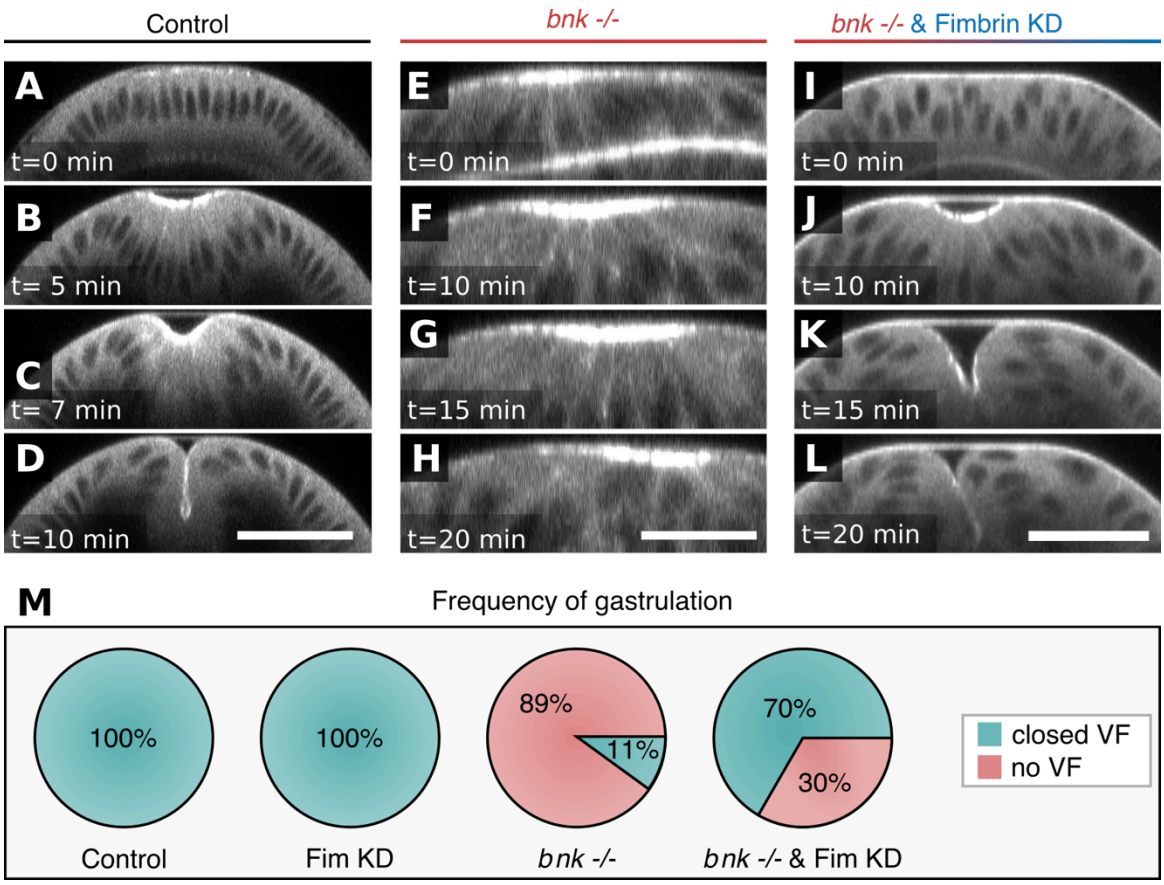

Figure 27. Depletion of Fimbrin rescues gastrulation in *bottleneck* mutant embryos. (A-L) Confocal cross sections of a control embryo expressing the myosin-II marker Sqh::mCherry at the onset of ventral furrow formation (A), after 5 min (B), 7 min (C), or 10 min (D). Confocal cross sections of a *bnk -/-* mutant embryo expressing the myosin-II marker Sqh::mCherry at the onset of ventral furrow formation (E), after 10 min (F), 15 min (G) or 20 min (H). Confocal cross sections of a *bnk -/-* Fimbrin KD double mutant embryo expressing the myosin-II marker Sqh::mCherry showing rescue of ventral furrow invagination at the onset of ventral furrow formation (I), after 10 min (J), 15 min (K) or 20 min (L). Scale bars: 10 μm. (M) Frequency of normal gastrulation (ventral furrow formation) in control, Fimbrin knockdown, bnk -/-, and *bnk -/-* Fimbrin double mutant embryos. Green color indicates the fraction of embryos with normal ventral furrow and red color indicates the fraction of embryos that initiated but did not complete ventral furrow invagination.

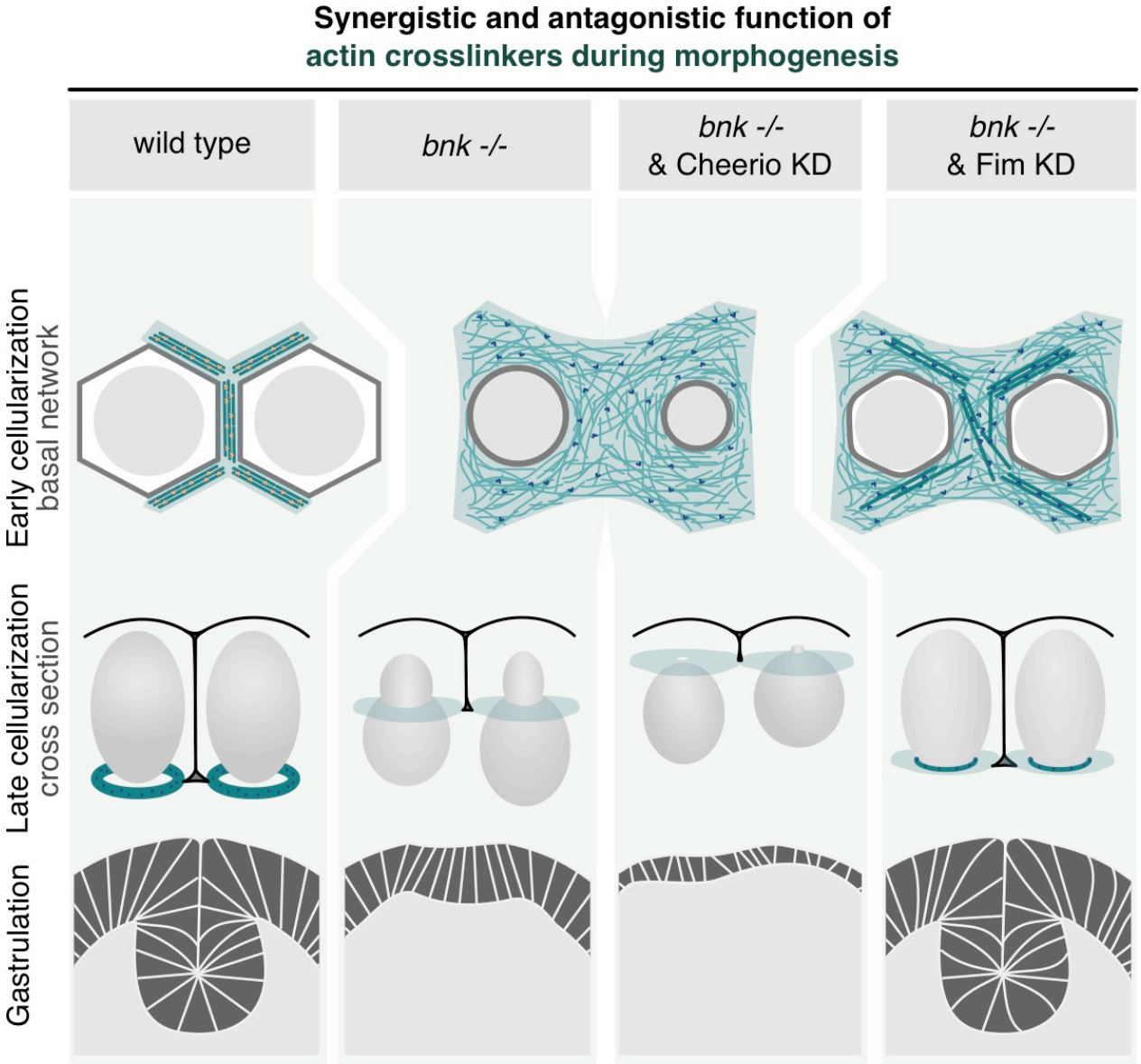

Figure 28. Model schematizing the synergistic and antagonistic effect of actin crosslinkers on the regulation of basal actomyosin remodeling during Drosophila morphogenesis. In wild type embryos during the process of cellularization the basal actomyosin network is composed of parallel actin bundles formed by the crosslinkers Bottleneck and Cheerio (yellow) organized in regular hexagonal arrays that do not constrict. The crosslinkers might connect actin bundles to the plasma membrane (gray lines) surrounding the nuclei (light gray circle). Later during cellularization Bottleneck is degraded and the hexagonal network transforms into individualized cellularization rings. This transition depends on the activity of the crosslinker Fimbrin (blue) that allows for efficient myosin-II contraction and force transmission along actin structures driving ring assembly and constriction. The precise timing of the series of network transition is required to ensure the proper progression of gastrulation and ventral furrow formation. In *bottleneck* mutants (*bnk -/-*) or upon Cheerio knockdown, actin bundle formation is severely impaired giving rise to a disordered actomyosin meshwork that constricts prematurely and deforms apically anchored nuclei into bottleneck-like shapes. The distorted timing of actomyosin contraction causes cellular defects that prevent the formation of the ventral furrow. *Bottleneck* and Cheerio double mutants display severe worsening of the individual phenotypes and a collapse of actomyosin networks causing an arrest of morphogenesis revealing synergistic action of Bottleneck and Cheerio. On the contrary, depletion of Fimbrin in bottleneck mutant embryos partially restores spatial organization of the actomyosin network preventing premature constriction and a rescue of morphogenesis arguing for a role of Fimbrin to facilitate network contraction.

In contrast, Fimbrin KD *bnk* -/- double mutant embryos partially rescued the hexagonal organization of the early basal network and restored regular network constriction behavior and cellularization proceeded normally (Figure 26). However, not only cellularization but also the subsequent morphogenetic process of ventral furrow invagination occurred normally. While the majority of *bottleneck -/-* embryos (~90%) failed to internalize the ventral cells, upon deletion of Fimbrin the series of cell shape changes characteristic for ventral furrow formation occurred normally resulting in tissue internalization in 67% of the embryos.

Taken together these results support a model in which a switch in antagonist crosslinking activity regulates transitions in actin network organization and contractility during morphogenesis (Figure 28).

3.2. Role of basal myosin-II during VF

Morphogenesis represents a continuous process of developmental events that need to be well orchestrated in order to form an organism. As previously shown, *bottleneck* mutant embryos are characterized by severe disorganization of the basal actomyosin network during cellularization that also prevent the subsequent morphogenetic event of ventral furrow formation. This arrest of morphogenesis can be rescued by depleting Fimbrin, which I showed is required for actomyosin contraction and acts by antagonizing Bottleneck activity during cellularization. These findings demonstrate that miss-regulation of basal actomyosin contractility network at the end of cellularization affects the subsequent cell shape changes required for tissue invagination during gastrulation. In the second part of this thesis, I focused on the regulation of basal contractility during ventral furrow formation. This part of my thesis was peer-reviewed and published in the EMBO Journal (Krueger *et al*., 2018). The optogenetic experiments presented in the second part of my thesis were conducted in collaboration with Pietro Tardivo and Congtin Nguyen, two students who I trained and supervised during the second half of my PhD.

3.2.1. Quantitative manipulation of basal myosin-II.

Central to the second part of this thesis is a model that passive mechanical force distribution upon accumulation of myosin-II at the apical surface of the ventral cells can drive the complete series of cell shape changes observed during ventral furrow formation by taking into account changing elastic properties of the basolateral cortex over time (1.7.3.3, p. 41) (Polyakov *et al*., 2014).

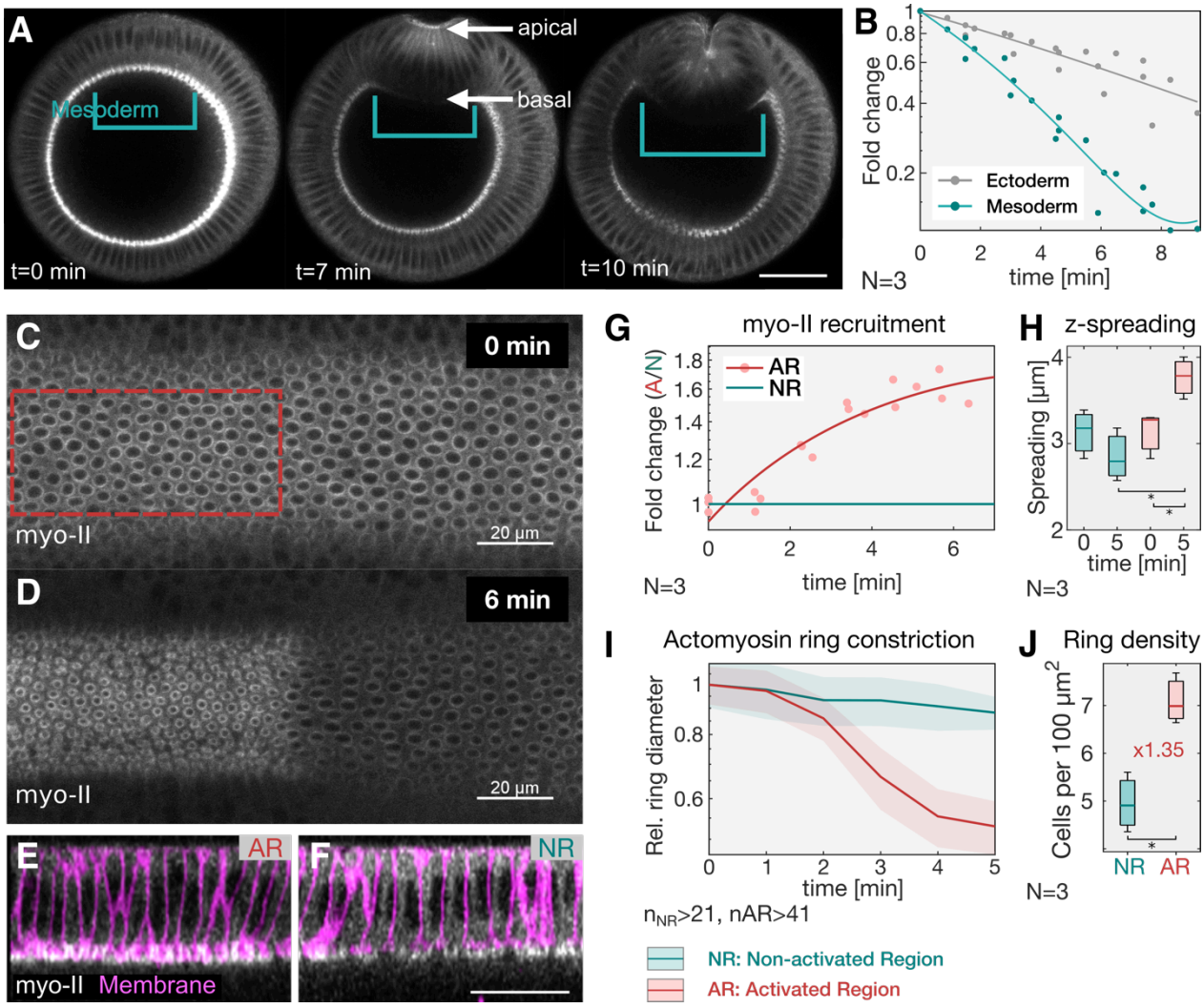

Figure 29. Quantitative manipulation of myosin-II levels at the cell base at the onset of gastrulation. (A) Confocal sections at different time points of a *Drosophila* embryo expressing the myosin-II probe (Sqh::GFP) mounted vertically to image the cross-section using two-photon microscopy. Open rectangles highlight the ventral mesodermal cells. At the end of cellularization myosin-II is present at the cell base (lower arrow). During ventral furrow formation basal myosin-II was depleted at the same time myosin-II accumulated at the apical cell surface (upper arrow). Scale bar, 40 μm. **(B)** Quantification of basal myosin-II levels (N=3 embryos) in ectodermal (gray) and mesodermal (green) cells. A polynomial function 3rd degree was fitted to the data ($r^2_{Ectoderm}$: 0.98 and $r^2_{Mesoderm}$: 0.87). Note the logarithmic y-axis. **(C-F)** Confocal images showing the basal actomyosin network of the dorsal tissue of embryos co-expressing RhoGEF2-CRY2/CIBN::pmGFP, and Sqh::mCherry at the initial stage (C) at the end of cellularization and 6 min after photo-activation (D). Photo-activation of the cell base was restricted to a region of interest (red dashed line) using two-photon microscopy. Z-projection of the same embryo showing the cross section of the activated region (AR) (E) and non-activated region (NR) (F) with the superimposed plasma membrane signal (CIBN::GFPpm in magenta) recorded immediately after the final Sqh::mCherry acquisition (displayed in white). Scale bars, 20 μm. **(G)** Quantification of basal myosin-II (N=3) within the region of activation (AR, red) relative to the non-activated region (NR, green) over the course of 6 min. A polynomial function (2nd degree, r^2_{AR} = 0.88) was fitted to the data (straight line). **(H)** Quantification of the z-spreading along the apico-basal axis. The width of a Gaussian function fitted to the z-profile was used as an estimate for myosin-II spreading. In each box plot, the central mark, the bottom, and the top edge of each box indicates the median, the 25th and 75th percentile, respectively. Whiskers extent to the most extreme data point. **(I)** Quantification of the diameter of basal actomyosin rings in the non-activated region (NR, green) and activated region (AR, red). The ring diameter was normalized to the mean value of the first time point. The constriction speed was estimated by the slope of a linear function fitted to the data. **(J)** Quantification of actomyosin ring density in the activated (AR) compared to the non-activated region (NR) revealed a 1.35-fold increase (N = 3 embryos; nNR: 431, nAR:

302). In each box plot, the central mark, the bottom, and the top edge of each box indicates the median, the 25th and 75th percentile, respectively. Whiskers extent to the most extreme data point. When present, * indicates $p \leq 0.05$, n.s. indicates no statistically significant differences according to two-sample t-Test. Figure and legend adapted from (Krueger *et al.*, 2018).

In support of this hypothesis, myosin-II, which predominantly localizes to the cell base at the end of cellularization and onset of gastrulation, is depleted from the basal surface of the invaginating cells at the same time myosin-II accumulates at the apex (Figure 29A). Quantification of basal myosin-II revealed decreasing protein levels, both in lateral ectodermal and ventral mesodermal cells. However, at the time point of the half-maximal decrease, 5 min after the onset of ventral furrow initiation, there was a ~2-fold reduction of basal myosin-II in the mesodermal cells compared to the lateral ectodermal cells (Figure 29B).

To investigate the role of basal myosin-II downregulation for tissue invagination, I adopted the same optogenetic system described earlier (Figure 12D,E) to induce a 2-fold increase in myosin-II levels at the basal surface of ventral cells which corresponds to the amount that is lost during invagination. In order to facilitate calibration of the optogenetic system, I focused on the dorsal tissue at the end of cellularization because this part of the embryo does not undergo any morphogenetic movements at this stage and reflects well a naïve epithelium. Embryos co-expressing the optogenetic module RhoGEF2-CRY2/CIBN::pmGFP and the myosin-II probe Sqh::mCherry were photo-activated in a subset of cells using two-photon illumination (λ=950 nm) at the basal surface, about 27 μm from the apical cortex, in a focal volume of 5 μm (Figure 29C-F). I used two-photon illumination at a power of 13 mW and a scanning time of 60 s at 95 s intervals. Between the photo-activation cycles the myosin-II confocal signal was recorded using 561 nm laser excitation.

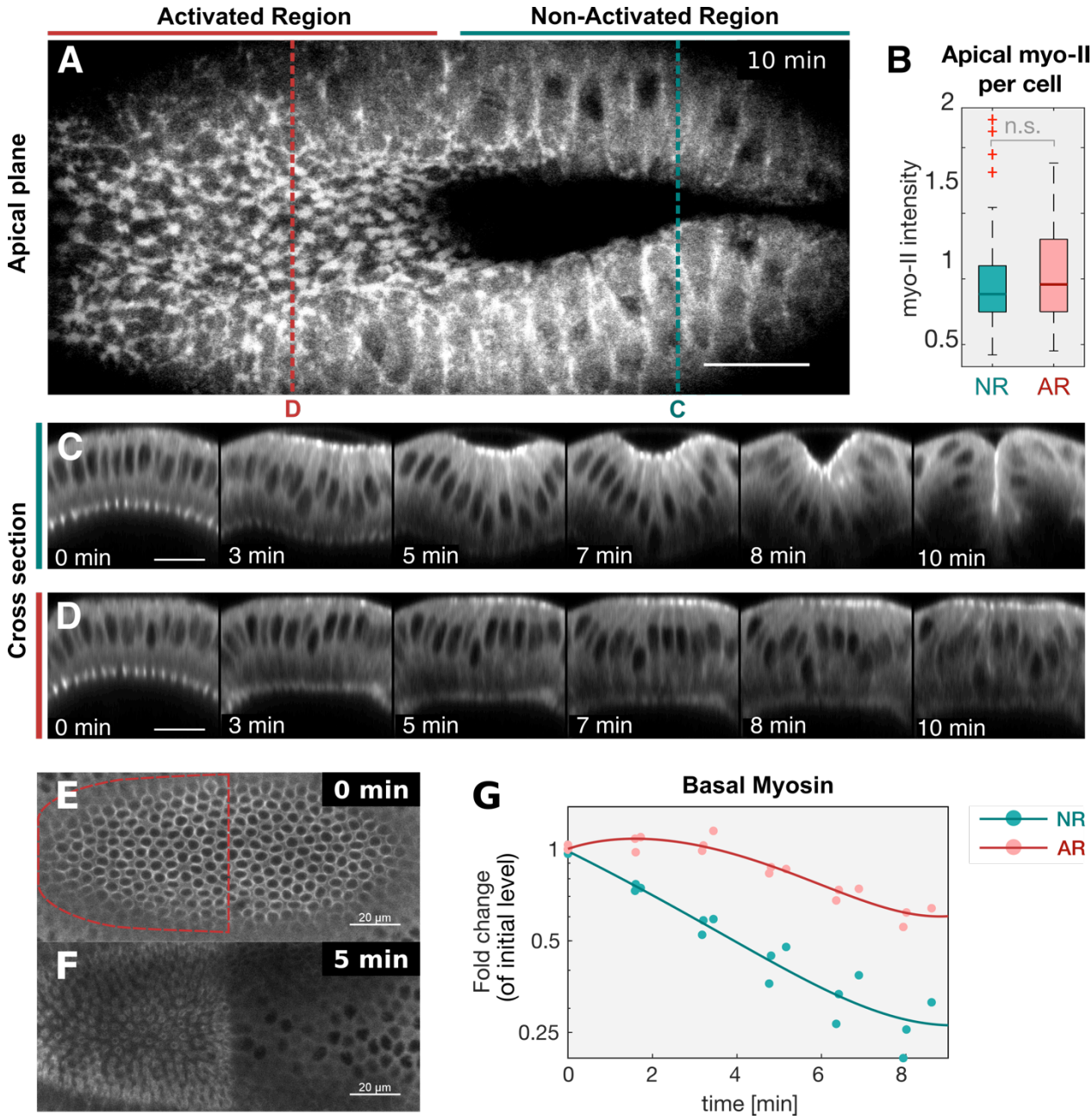

Figure 30. Increasing myosin-II at the base of ventral mesodermal cells inhibits ventral furrow formation despite normal accumulation of apical myosin-II. (A, C-F) Confocal images showing a *Drosophila* embryo co-expressing the optogenetic module and the myosin-II probe Sqh::mCh 10 min after the initial activation photo-activation of the cell base. The cell base of the anterior half of the embryo was photo-activated (two-photon λ=950 nm), and whole-cell myosin-II signal was recorded (λ=561 nm) in an alternating fashion. **(A)** Top view showing the apical cell surface 10 min after initial photo-activation. Red and Blue dotted lines indicate the location of the cross-section panels displayed in (C) and (D). **(B)** Quantification of apical myosin-II per cell in the non-activated (NR) and activated region (AR) normalized to the median of the combined cell population in the NR and AR (N = 3 embryos; n_{NR}: 94, n_{AR}: 78). Significances (by two-sample t-Test): n.s. indicates no statistically significant differences. In each box plot, the central mark, the bottom, and the top edge of each box indicates the median, the 25th and 75th percentile, respectively. Whiskers extent to the most extreme data point and the '+' symbol indicates an outlier. **(E, F)** Confocal images showing top views of the basal actomyosin network with the semi-elliptical region of photo-activation (red dashed line) at the beginning of the experiment (E) and 5 min after initial activation (F). Quantification of basal myosin-II levels (N=3) in the activated region (red) and non-activated region (green). The straight line represents a polynomial

fit (3rd degree) to the respective data (r^2=0.91 for the activated region and r^2=0.97 for the non-activated region). Note the logarithmic y-axis scale. All scale bars, 20 μm. Figure and legend adapted from (Krueger *et al.*, 2018).

Under these conditions I achieved a ~1.6-fold increase of basal myosin-II levels over the course of 6 min (Figure 29G). Importantly, the up-regulation of myosin-II was confined in the z-dimension (along the apico-basal axis) with a maximum z-spreading of ~4 μm from the most basal plane which is only slightly bigger than the z-spreading in non-activated control cells (Figure 29H). In line with the findings presented in section 3.1.1 (p. 55) the selective optogenetic activation of the basal actomyosin network resulted in a ~5-fold

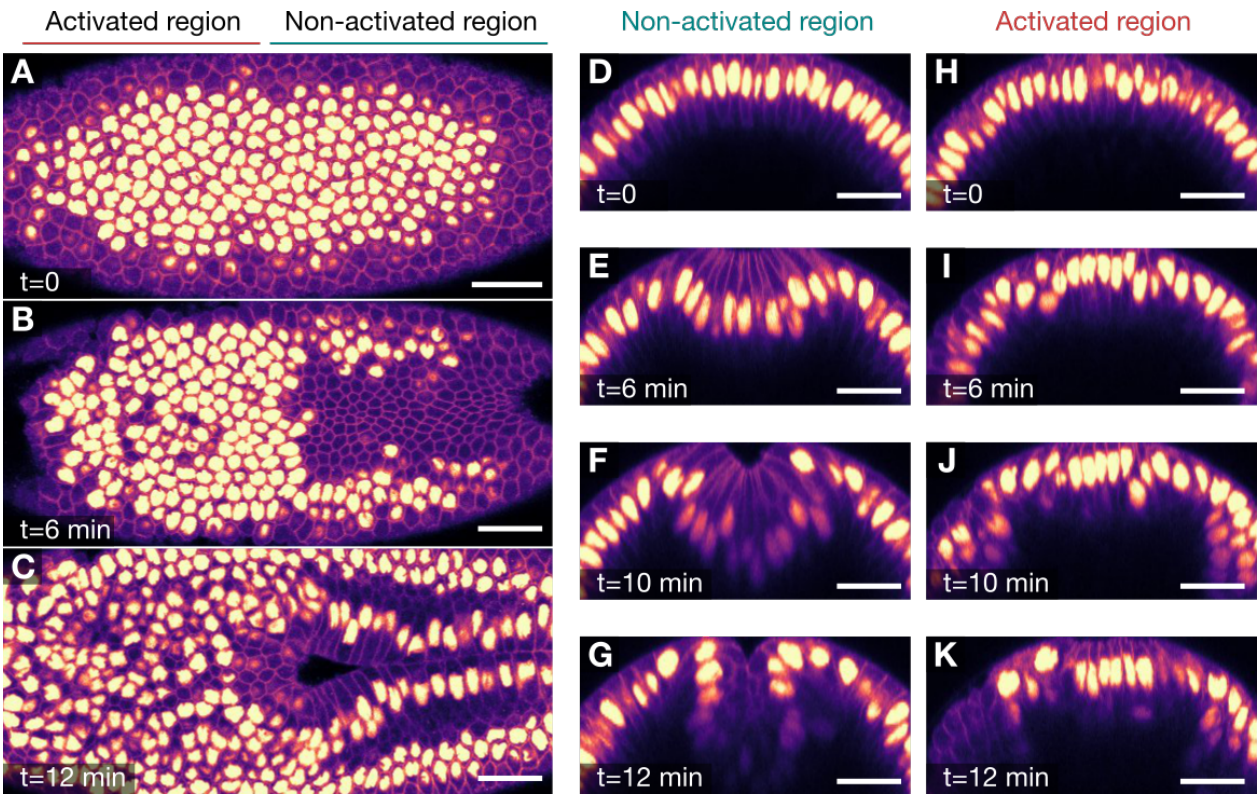

Figure 31. Increasing myosin-II at the cell base of ventral mesodermal cells prevents basal shift of nuclei. (A-K) Confocal still frames showing the nuclei in combination with the cell boundaries. *Drosophila* embryos co-expressing the optogenetic module, RFP-nls (nuclear localization sequence) labeling the nulei and the membrane marker GAP43::mCh. The cell bases of the left (anterior) half of the embryo were photo-activated and the whole embryo imaged using 561 nm excitation. Images are shown using 'mpl-magma' lookup table coloring the high-intensity values in yellow (nuclei) and low intensity values in violet (membrane). **(A-C)** Top views showing the apical surface before photo-activation (A) and 6 min (B) and 12 min (C) after photo-activation. The corresponding cross section showing the non-activated region (D-G) and the photo-activated region (H-K) pre-activation (D,H) and at different time points after photo-activation as indicated in each panel (E-G, I-K). While in the non-activated region the nuclei shift basally upon constriction of the apical surface and cells internalize during the course of the experiment, the nuclei in the non-activated region remain close to the apical surface. Scale bars: 25 μm.

increase in the constriction rate of actomyosin rings compared to the non-activated region (Figure 29I). To exclude the possibility that the optogenetic perturbation caused defects in basal tissue integrity, I compared the density of actomyosin rings inside and outside the photo-activation area. The measured increase in ring density upon photo-activation of ~1.3 fold, argues that cells were still interconnected at the base and thus tissue integrity remained intact (Figure 29J). To summarize, I established conditions to quantitatively control myosin-II levels selectively at the basal cell surface in a subset of the tissue and in an adequate time-scale for applications during ventral furrow formation.

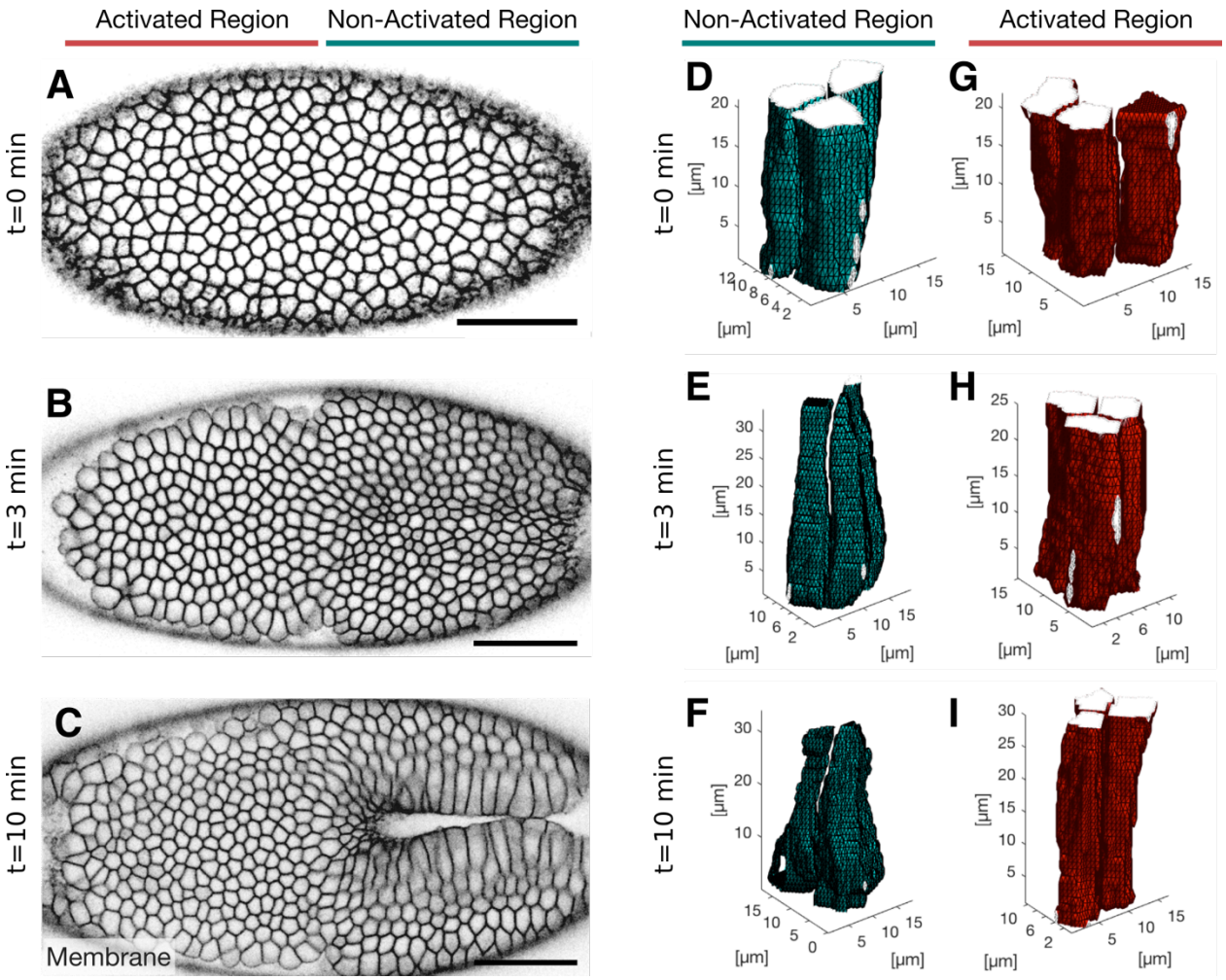

Figure 32. Reconstruction of cell shapes in basally photo-activated embryos. (A-C) Confocal images showing the ventral apical plasma membrane signal (CIBNpm::GFP) in embryos co-expressing the optogenetic module and Sqh::mCherry. The anterior (left) half of the embryo was photo-activated at the cell base and Sqh::mCherry was recorded in the whole embryo. The experiment was started when apical accumulation of myosin-II was detected and terminated at different time points to record the CIBNpm::GFP in the whole embryo using two-photon illumination. Still frames acquired at the initial time point (A), 3 min (B) and 10 min (C) after initial photo-activation. **(D-I)** Representative examples ($18 \leq n \leq 136$) of reconstructed cells in the non-activated region at the initial time point (D), 3 min (E) and 10

min (F) after photo-activation change from a columnar to a conic shape. In contrast, representative examples (83 ≤ n ≤ 133) of cells in the activated region at the initial time point (G), 3 min (H) and 10 min (I) remain columnar. Figure and legend adapted from (Krueger *et al.*, 2018).

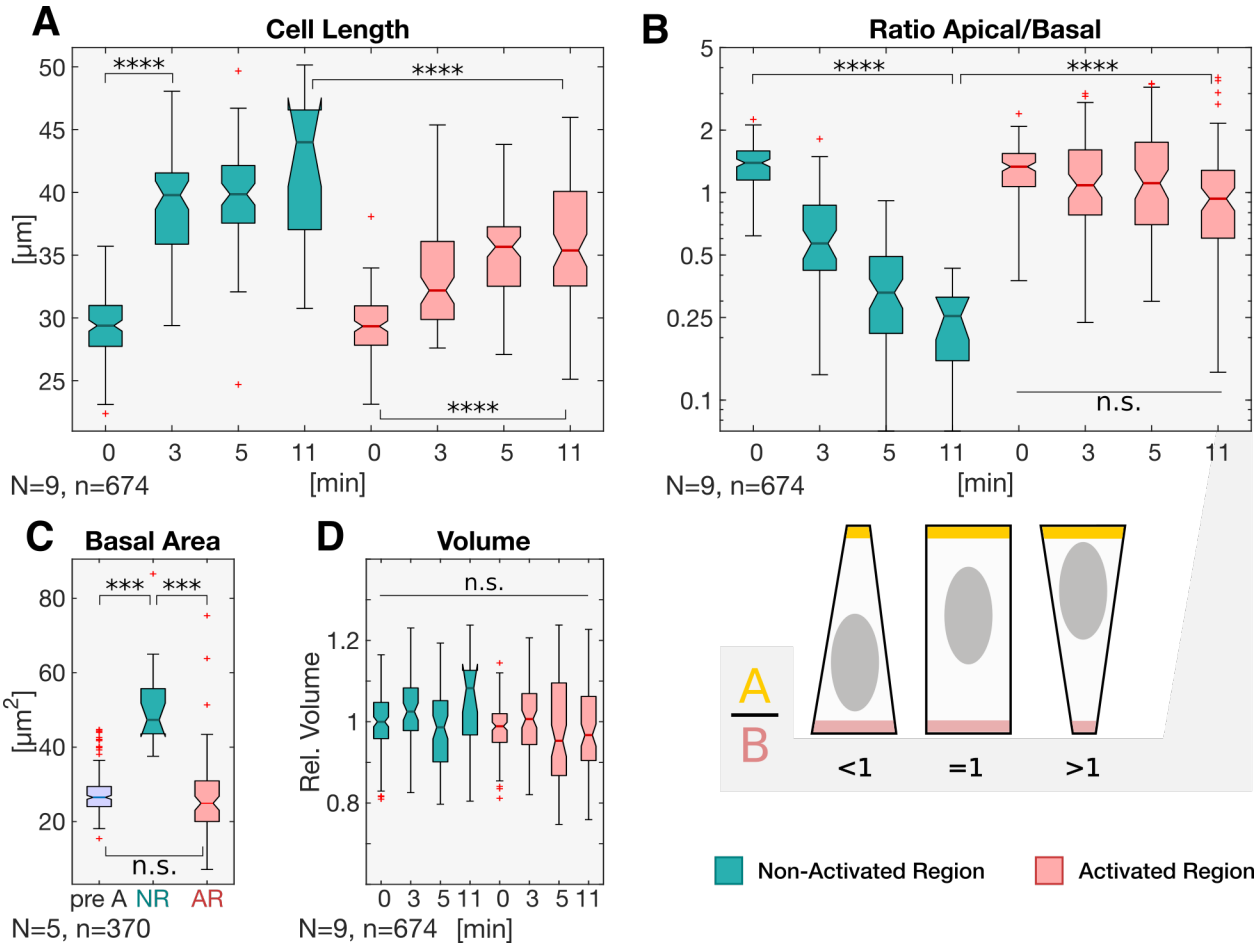

Figure 33. Increasing myosin-II levels at the cell base prevents cell elongation and transition to conic shape. (A-D) Quantification of reconstructed cell shapes in the non-activated (green) and activated region (red) analyzing cell length (A), apical/basal ratio (B), basal area (C) and volume (D) at different time points after initial photo-activation of the cell base. (A) Cells in the non-activated region elongated almost 2-fold, while cells in the photo-activated region showed impaired cell elongation. ANOVA result: $F(7,666)=117.9$, $p=3.8e\text{-}112$. Cohen's $D > 0.87$ between NR and AR (excluding t = 0 min). (B) The apical/basal (A/B) ratio describing the cell shape represents the most apical divided by the most basal volume with a ratio of 1 indicating a columnar shape, a ratio < 1 a conic shape and a high ratio > 1 indicates an inverted conic shape. The cartoon illustrates the cell shapes represented by different A/B ratios. While the non-activated cells showed a progressive decrease of the A/B ratio, the photo-activated cells did not undergo shape transitions and remained constant at an A/B ratio of ~ 1 (ANOVA ($F(3,384)=1.617$, $p=0.18$) revealed no statistically significant differences). ANOVA result (all datapoints): $F(7,666)=44.95$, $p=4e\text{-}52$. Cohen's $D > 0.73$ between NR and AR (excluding t = 0 min). (C) Quantification of the basal cell area pre-activation (pre A; t = 0 min) in the non-activated region (NR) and in the activated region (AR) after 11 min. (D) Quantification of the cell volume in the non-activated and activated region normalized to the mean of all samples. A one-way ANOVA test was performed ($F(7,666)=3.34$, $p=0.0017$) followed by a post-hoc Tukey test and Cohen's D test ($d<0.5$) both revealing no significant differences. (A-D) The central mark, the bottom, and the top edge of each box indicates the median, the 25th and 75th percentile, respectively. Whiskers extent to the most extreme data point and the '+' symbol indicates an outlier. Notches indicate comparison intervals. Between $n_{NR(11\ min)} = 18$ and $n_{NR(0\ min)} = 136$ cells per sample with a total number of $n_{total} = 674$ cells from at least two embryos per sample and altogether 9 embryos were analyzed. In all panels,

**** indicates p ≤ 0.0001, *** indicates p ≤ 0.001, and n.s. indicates no statistically significant differences according to two-sample t-Test. Figure and legend adapted from (Krueger *et al.*, 2018).

3.2.2. Effect on cell elongation and tissue invagination.

With the conditions established, I aimed to quantitatively increase the level of myosin-II at the basal surface of ventral mesodermal cells to pre-invagination levels over time, corresponding to a desired increase in myosin-II levels of ~2-fold. Embryos co-expressing the optogenetic module RhoGEF2-CRY2/CIBNpm::GFP and the myosin-II probe Sqh::mCherry were photo-activated at the cell base of the ventral tissue in a semi-elliptical region, reflecting the shape of the ventral basal surface, prior to the beginning of invagination. In alternating cycles of optogenetic activation within the defined region and 561 nm laser excitation in the whole embryonic tissue, the Sqh::mCherry signal was recorded over time to visualize and quantify myosin-II (Figure 30A,B). The result of this experiment showed that while the non-activated part of the embryo underwent normal cell internalization and tissue folding, photo-activated cells did not internalize (Figure 30A,C,D) although myosin-II accumulated normally at their apical surface (Figure 30B). By quantifying basal myosin-II levels, I confirmed a ~2-fold up-regulation in the photo-activated compared to the non-activated region (Figure 30E-G). To better understand cell movements and the behavior of the nuclei, embryos co-expressing the optogenetic module together with a nuclear marker (RFP-nls) and the plasma membrane (GAP43::mCh) were photo-activated at the cell base of the embryo's anterior part (Figure 31). I observed that as cells constrict their apical surface and start to internalize, the nuclei shift from an apical position to the cell base in the non-activated region (Figure 31D-G). Instead in the photo-activated cells a basal translocation of nuclei was not observed (Figure 31H-K). This suggests that nuclei movement is subject to cytoplasmic flows and hydrostatic pressure rather than actively regulated during tissue invagination.

Having seen severe defects in tissue invagination, I wanted to analyze the effect of basal myosin-II stabilization on the cell shapes. To do so, photo-activation was terminated at consecutive time points to record the CIBNpm::GFP membrane signal in a image stack covering the entire tissue depth (Figure 32A-C). Using automated image segmen-

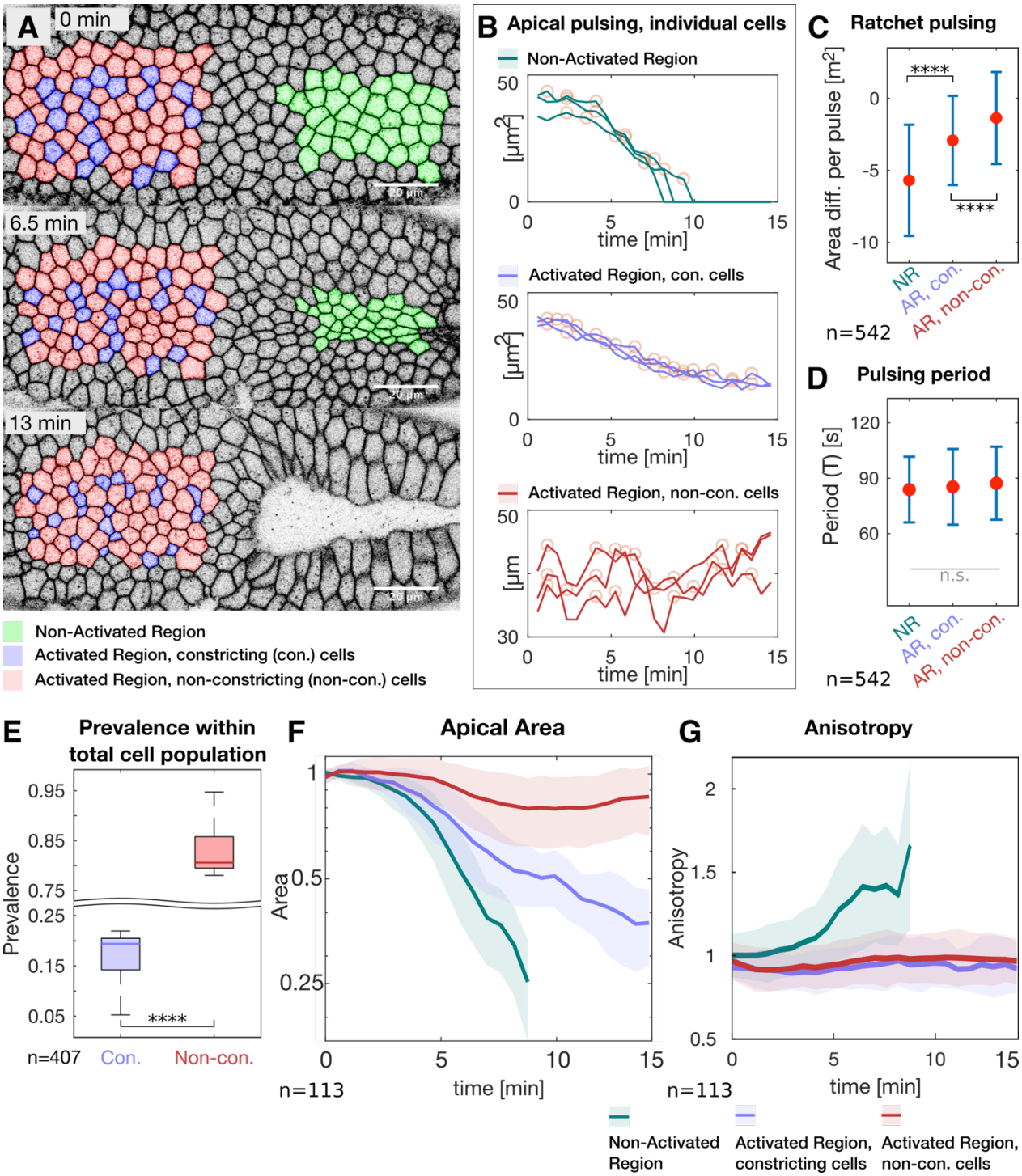

Figure 34. Stabilizing basal myosin-II levels inhibits ratcheted apical contractions. (A) Confocal images showing the apical membrane (GAP43::mCherry) of the ventral tissue of embryos expressing RhoGEF2-CRY2/CIBN::GFPpm and the membrane marker GAP43::mCherry at different time points after photo-activation of the basal surface of cells in the anterior (left) half of the embryo. Sequentially and with a time interval of 35 s an apical GAP43::mCherry stack was recorded and the cell base was photo-activated for ~20 s. Cells in the non-activated region (green) underwent normal apical constriction. In the activated region, two populations of cells were observed, one that constricted (purple) and one that did not constrict (red). Scale bar 20 μm. **(B)** Graphs showing the apical area of three individual cells in the non-activated region (top), constricting in the activated region (middle) and non-constricting

(bottom) over the course of one experiment. Yellow circles indicate the position of automatically identified local maxima used for further analyses. **(C)** Diagram showing the extent of ratcheted constrictions defined by the mean difference in apical area between adjacent peaks. Cells in the non-activated region (NR) showed ratcheted constrictions stabilizing the constricted state between two pulses, non-constricting cells in the activated region (AR, non-con.) showed a value close to 0 (no difference in size between two pulses) reflecting non-ratchet pulsation behavior, and constricting cells in the activated region (AR, con.) showed an intermediate behavior with impaired ratcheted constriction. Data points are significantly different as determined by ANOVA ($F(2,539)=72.04$, $p=1.9e-28$) and post-hoc Tukey test. **(D)** Quantification of the pulsation period (T) revealed a period of about 90 s for all categories. No statistically significant differences between group means were determined by one-way ANOVA ($F(2,540)=1.438$, $p=0.24$). (C and D) Red dots indicate the mean values and the error bars represent the standard deviation. More than 500 pulses (n_{NR} = 119, $n_{AR,\ non\text{-}con.}$ = 128, $n_{AR,\ con}$ = 295) of more than 100 cells were analyzed. **(E)** Diagram showing the prevalence of constricted (con.) and non-constricted (Non-con.) cells in the photo-activated region. (N = 5 embryos; n: 407 cells; Cohen's D: d = 10). In each box plot, the central mark, the bottom, and the top edge of each box indicates the median, the 25th and 75th percentile, respectively. Whiskers extent to the most extreme data point. **(F,G)** Quantification of the apical area (F) and anisotropy (G) of cells in the non-activated region (green), constricted (purple) and non-constricted cells (red) in the photo-activated region. The straight line indicates the mean value, the semi-transparent colored area the standard deviation. Different from non-activated cells, cells in the photo-activated region did not acquire anisotropy (irrespective of their constriction behavior). n_{NR} = 34, $n_{AR,\ non\text{-}con.}$ = 20, $_{nAR,\ con}$ = 59). In all panels, **** indicates $p \leq 0.0001$, and n.s. indicates no statistically significant differences according to two-sample t-Test. Figure and legend adapted from (Krueger *et al.*, 2018).

tation and tracking, I reconstructed the cell shape and quantitatively analyzed the geo metric characteristics of the segmented cells with the help of a custom-made MATLAB script (Figure 32D-I). The results of this analysis demonstrate that while non-activated cells showed cell lengthening (Figure 33A) and cell shape changes stereotypic for the first phase of cellularization, the photo-activated cells maintained a columnar shape. The cell shape was quantified by the simple apical to basal surface area ratio (A/B), that decreased in the non-activated cells from 1.4 to 0.25 (Figure 33B), whereas in photo-activated cells the average A/B ratio did not change as their basal surface did not expand (Figure 33C). The change of the A/B ratio in the non-activated cells was accompanied by cell elongation from 25 μm to 35 μm (Figure 33A). Instead, the lack of this cell shape transition is paralleled by impaired cell elongation in photo-activated cells (Figure 33A). Notably, the total cell volume in both, non-activated and photo-activated region, did not change over time demonstrating that the principle of volume conservation was still fulfilled (Figure 33D).

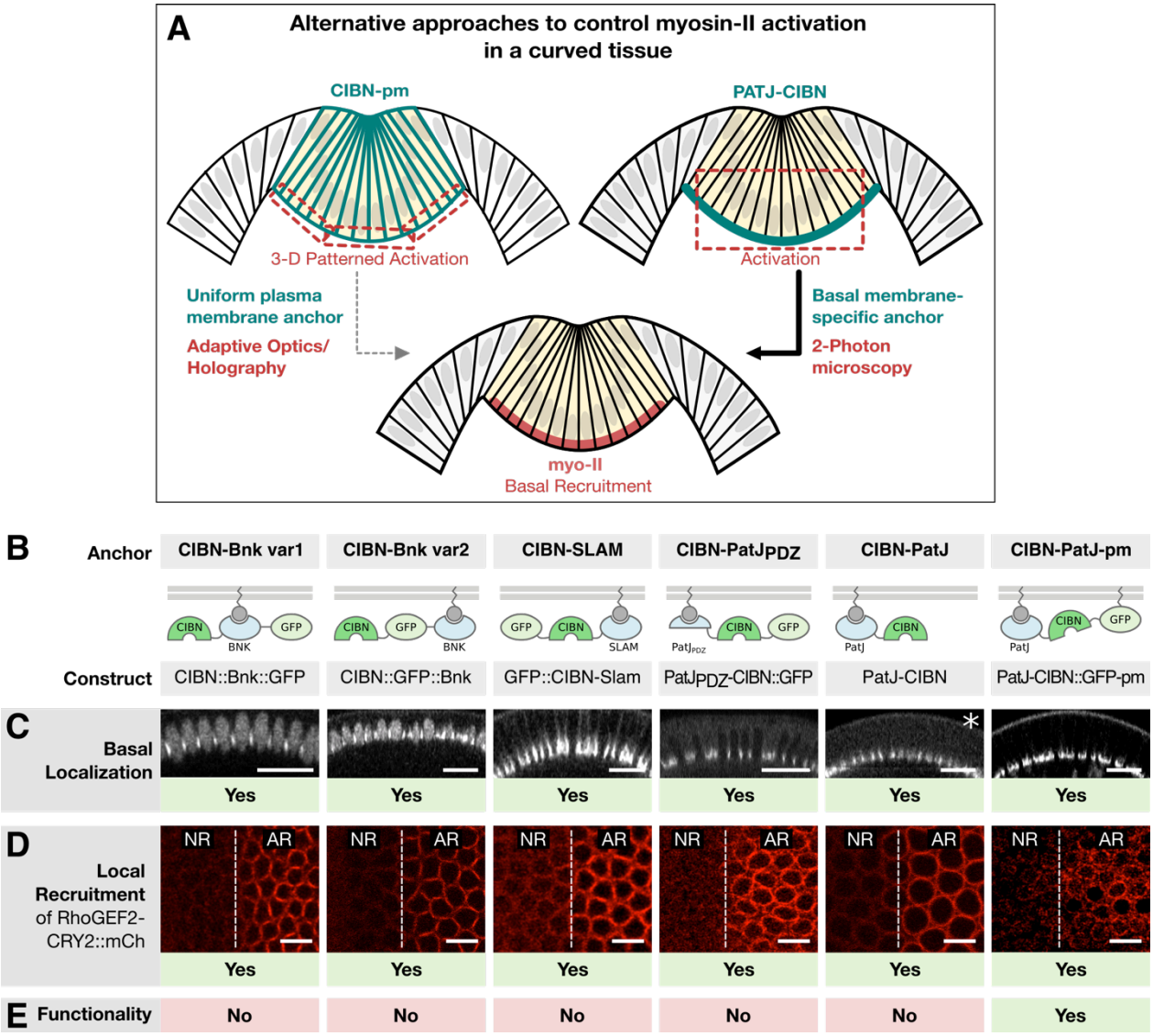

Figure 35. Engineering a basal-specific optogenetic anchor for photo-activation in a curved tissue. (A) Schematic illustration of two alternative approaches to specifically control myosin-II activation in a curved tissue using either a uniformly distributed optogenetic anchor (like CIBN-pm) in combination with 3-D patterned light delivery by adaptive optics and holography (left), or an optogenetic anchor that specifically localizes to the cell base. In the latter scenario RhoGEF2-CRY2 can be still recruited specifically to the cell base even though a bigger focal volume is photo-activated. **(B)** Schematic depiction of CIBN fused to Bottleneck (CIBN::Bnk::GFP, CIBN::GFP::Bnk), Slam (GFP-CIBN-Slam) and PatJ (PatJPDZ-CIBN::GFP, PatJ::CIBN, PatJ-CIBN::GFP-CAAX) in different configurations. **(C–E)** Confocal images of embryos co-expressing one of the designed optogenetic anchors and RhoGEF2-CRY2::mCherry were imaged during late cellularization. (C) Cross sections show the localization of the GFP-tagged optogenetic anchor. Please note that the construct PatJ-CIBN (indicated by asterisk) lacks a fluorescent marker and its localization was thus inferred from the recruited RhoGEF2-CRY2::mCh. Scale bars, 20 µm. **(D)** The cell base was locally photo-activated (right side of the dashed line (AR)) using two-photon illumination and afterwards the RhoGEF2-CRY2::mCherry signal acquired using confocal microscopy. NR indicates the non-activated region. Scale bars, 10 µm. **(E)** Summary of the functionality of the tested optogenetic anchors. (C-E) Although all anchors tested localized to the cell base and efficiently recruited RhoGEF2-CRY2::mCherry, only PatJ-CIBN::GFP-pm was effective in inducing myosin-II-mediated actomyosin ring constriction. Figure and legend adapted from (Krueger *et al.*, 2018).

3.2.3. Influence on ratcheted apical constriction.

The cell shape analysis showed that photo-activated cells maintained their columnar shape. However, over time the A/B ratio became highly variable with some cells acquiring an inverted conic shape with an apical surface being bigger than the basal surface and other cells acquiring the opposite conformation (Figure 33B, Appendix 4). For that reason, I decided to study the impact of increasing basal myosin-II on apical surface dynamics in photo-activated embryos co-expressing CIBNpm::GFP, RhoGEF2-CRY2 and the plasma membrane marker GAP43::mCherry (Figure 34A). I found that in contrast to wild-type embryos or to cells in the non-activated region, the photo-activated cells did not form apical anisotropy suggesting defects in the distribution of tissue tension (Figure 34A). Moreover, two populations of cells were found in the photo-activated region, cells that constricted and cells that did not constrict or expand their apical surface (Figure 34A). Analysis of the pulsatile behavior of the apical cell surface (Figure 34B) in the non-activated region revealed the characteristic cycles of constriction and stabilization known as ratcheted contractions (Figure 34C) with a mean period of ~90 s (Figure 34D). Although cells in the photo-activated region likewise pulsed with an average period of ~90 s (Figure 34D), more than 80% of the photo-activated cells displayed non-ratcheted pulsation behavior as they did not stabilize the constricted state but relaxed back to their initial size (Figure 34C,E). The remaining 20% of the cells did undergo net contraction, however with slower kinetics revealing inhibited ratcheted contractile behavior (Figure 34E,F) and without acquiring an anisotropic shape (Figure 34G). To conclude, preventing down-regulation of basal myosin-II interferes with the capability of cells to constrict their apical surface, despite normal apical accumulation of myosin-II (Appendix 5).

3.2.4. Effect on cell shortening and furrow progression

Having tested the effect of increasing myosin-II levels at the first stages of ventral furrow formation, I also wanted to test the effect on later stages after the cells have undergone apical constriction and cell elongation already. To still be able to achieve precise optogenetic activation, I had to account for the increasing curvature of the internalizing tissue

(Figure 35A). On possibility was to make use of adaptive optics and holography microscopy to tune the activation pattern according to the curved basal cell surface. An alternative approach, that I decided to follow, was to keep the general experimental setup but re-engineer the optogenetic module by replacing CIBN::GFP-pm with an optogenetic anchor that selectively localizes to the basal surface. A basal-specific optogenetic anchor would allow for restricted recruitment of RhoGEF2-CRY2 to the cell base irrespective of the tissue curvature and illumination volume (Figure 35A).

To engineer an optogenetic anchor, I generated a series of fusion proteins composed of CIBN and proteins, which were reported to localize to the cell base at the end of cellularization including Bottleneck, Slam (1.7.1.2, pp. 28) and PatJ (1.5, pp. 10). An overview of the tested proteins is shown in Figure 35B. Live-imaging of embryos expressing either of the anchor proteins revealed predominant basal localization (Figure 35C) and localized recruitment of RhoGEF2-CRY2::mCherry for all candidates (Figure 35D). However, only a PatJ-based anchor composed of full-length PatJ N-terminally fused to CIBN and an additional membrane-tethering CAAX box signal was effective in inducing contractility (Figure 35E). Even when the embryos were photo-activated using single photon illumination of 488 nm at the beginning of cellularization when the basal surface is close to the objective, only CIBN-PatJ-GFP-CAAX, hereafter referred to as CIBN-PatJ::GFPpm, allowed for activation of myosin-II and actomyosin constriction (Appendix 6). As all other anchors including two that were also based on PatJ did not support optogenetic activation of myosin-II, I hypothesized that RhoGEF2-CRY2 needs to be very close to the plasma membrane and in a proper orientation to activate the membrane-bound Rho1 and start a signaling cascade to stimulate myosin-II (1.6.3, pp. 16) which was only achieved by tethering the anchor protein directly to the membrane via the CAAX box signal (Figure 35B).

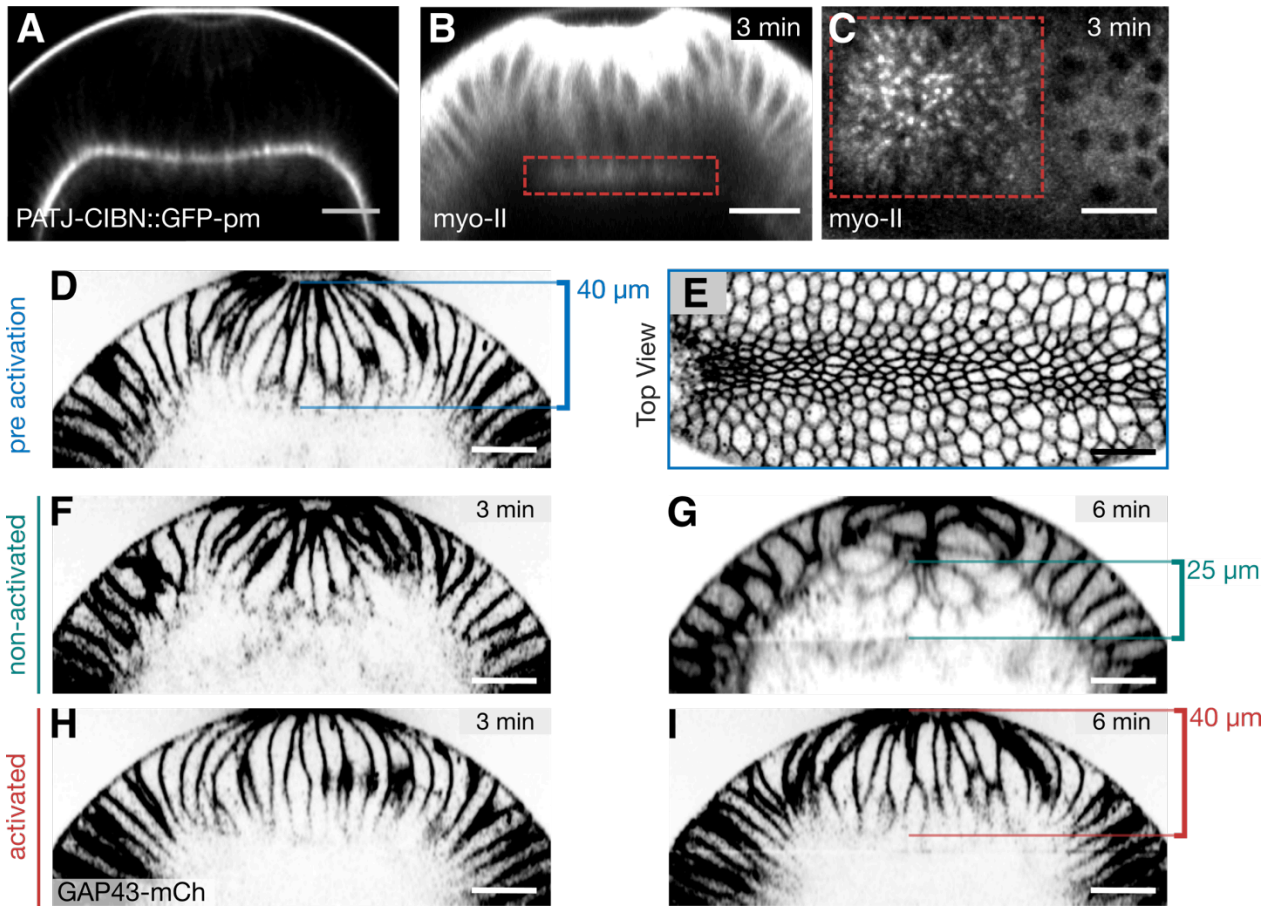

Figure 36. Increasing basal myosin-II levels after cells constricted apically and initial tissue invagination started prevents progression of cell invagination and closure of the furrow. (A) Confocal cross section showing the localization of the basal-specific optogenetic anchor CIBN-PatJ::GFP-pm expressed in an embryo during ventral furrow formation. **(B-I)** Confocal images of the ventral tissue of embryos co-expressing CIBN-PatJ::GFP-pm, RhoGEF2-CRY2 and Sqh::mCherry (B,C) or the membrane marker GAP43::mCherry (D-I). The embryos were allowed to undergo apical constriction and tissue internalization of 3-5 *µ*m before the anterior (left) half of the embryos was photo-activated (in basal stacks) for 100 s. Afterwards, photo-activation and mCherry signal acquisition was done alternatingly. (B) Cross section showing the myosin-II distribution 3 min after photo-activation. Red dashed box highlights myosin-II locally recruited to the base. (C) Top view showing increase of basal myosin-II in the photo-activated region (red dashed box). (D) Cross section and (E) top view of the apical surface showing the plasma membrane at the initial time point before photo-activation. The ventral mesodermal cell constricted apically and started to internalize. (F,G) Cross sections of the non-activated region 3 min (F) and 6 min (G) after initial photo-activation show the closure of the ventral furrow in that region. (H,I) Cross sections of the activated region 3 min (H) and 6 min (I) after initial photo-activation show that the photo-activated cells did not further internalize. While the width of the central tissue forming the ventral furrow initially is 40 *µ*m (D), the tissue shrank to about 25 *µ*m in the non-activated region (G) but remained constant in the activated region (I). Scale bars, 20 *µ*m. Figure and legend adapted from (Krueger *et al.*, 2018).

The newly engineered optogenetic module allowed me to maintain the general experimental setup. In fact, photo-activation in embryos co-expressing RhoGEF2-CRY2/CIBN-PatJ::GFPpm and Sqh::mCh resulted in localized two-fold increase of myosin-II to the cell base in the ventral mesodermal cells (Figure 36A-C, Appendix 7). To investigate the

effect of increasing basal contractility at later stages of the invagination process, RhoGEF2-CRY2/CIBN-PatJ::GFPpm and the plasma membrane probe Gap43::mCherry were co-expressed in embryos and imaged using 561 nm excitation to visualize the cell shape. After cells had constricted apically and an initial indentation of the tissue was observed, an image stack covering the whole tissue depth was recorded to visualize the Gap43::mCherry membrane before activation (Figure 36D,E). Afterwards, one half of the embryo was activated at the cell base using two-photon illumination and in turn the membrane signal was recorded in the whole embryo. While the non-activated half of the embryo completed cell internalization and the tissue formed a tube-like shape, the photo-activated tissue did not further invaginate (Figure 36F-I).

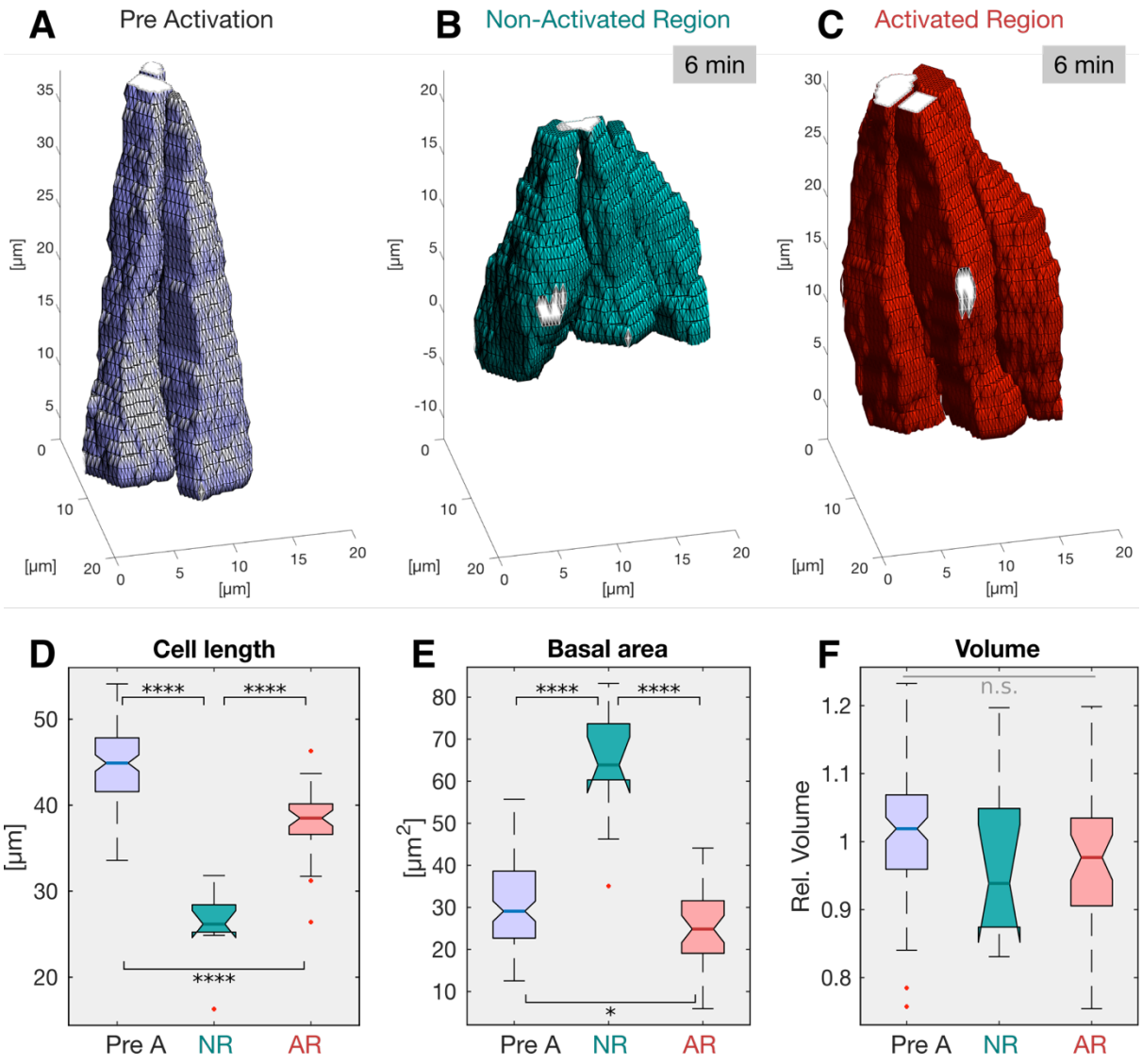

Figure 37. Myosin-II stabilization during later stages of ventral furrow formation inhibits cell shortening. (A-C) Reconstructed cell shapes from membrane signal of embryos co-expressing CIBN-PatJ::GFPpm, RhoGEF2-CRY2::mCherry and the membrane marker GAP43::mCherry photo-activated at the cell base at later stages of ventral furrow formation. (A) Reconstructed cell shapes before first photo-activation (pre activation) shows that the cells were apically constricted and elongated. (B,C) After 6 min, cells in the non-activated region expanded the base and shortened, whereas photo-activated cells did not undergo this shape transition. **(D-F)** Quantification of the length (D), basal area (E) and volume (F) from reconstructed cells (pre A: pre activation ($n_{pre\ A}$ = 107), initial time point; NR: non-activated region (n_{NR} = 10); AR: activated region (n_{AR} = 37)). The central mark, bottom and top edges of each box indicate the median, 25th and 75th percentile, respectively. Whiskers extent to the most extreme data point and the '+' symbol indicates an outlier. Notches indicate comparison intervals. (D) Photo-activated cells showed impaired cell shortening seen in the non-activated cells. ANOVA result: F(2,151)=110.2, p=3e-30; Cohen's D: d > 1.5. (E) The basal area did not expand in the photo-activated region, while it increased significantly in the non-activated cells. ANOVA result: F(2,151)=52.02, p=6.5e-18; Cohen's D: $d_{preA:NR}$, $d_{AR:NR}$ > 2, $d_{preA:AR}$ < 0.5. (F) The cell volume did not show statistically significant differences between group means as determined by one-way ANOVA (F(2,151)=2.227, p=0.11). In all panels, **** indicates p ≤ 0.0001, and n.s. indicates no statistically significant differences according to two-sample t-Test. Figure and legend adapted from (Krueger *et al.*, 2018).

Detailed analysis of the reconstructed cell shape (Figure 37A-C) demonstrated that initially the cells underwent apical constriction and elongated to an average length of ~45 μm (Figure 37D). Within 6 min the non-activated cells expanded their basal surface by a factor of ~2 (Figure 37E) and simultaneously shortened to a length of 26 μm (Figure 37D), while photo-activated cells did not expand their basal area and shortened significantly less to 38 μm (Figure 37D,E). The cell volume did not significantly change over time or upon optogenetic activation (Figure 37F). I concluded "that myosin-II downregulation is required for basal expansion and cell shortening allowing the completion of tissue invagination and closure of the ventral furrow" (Krueger *et al.*, 2018).

4. Discussion

As documented in this thesis, I have identified a mechanism that regulates the spatio-temporal organization of actomyosin contraction during tissue morphogenesis. This mechanism is based on developmentally controlled actin crosslinker activity and its correct functioning is required for development of the *Drosophila melanogaster* embryo. I further demonstrate that following blastoderm formation, myosin-II activity must be downregulated at the basal surface of ventral cells in order to permit basal surface expansion and tissue invagination.

4.1. Actin-crosslinkers time cell contractility during morphogenesis

Cellularization during early *Drosophila* embryogenesis provides a suitable model system to study dynamic actin network remodeling *in vivo*. The results presented in this thesis demonstrate that distinct actomyosin network architectures correlate with different contractile behaviors in response to optogenetic stimulation of myosin-II activity. During the slow phase of cellularization, the basal actomyosin network is organized in a symmetric hexagonal array of actin fibers and is more resilient to myosin-II motor force compared to when it is organized in a meshwork-like configuration or in individualized ring during the fast phase of cellularization. These observations are consistent with *in vitro* studies and computer models showing that network contraction depends on the structural organization of actin fibers (Belmonte *et al*., 2017; Ennomani *et al*., 2016; Reymann *et al*., 2012).

The results presented in the first part of my thesis suggest, that the timely regulated action of different actin crosslinkers modulate network topology and contractility. A key element controlling the transition between different network configurations is provided by the zygotic expression of the *bottleneck* gene. Using actin co-sedimentation assays and electron microscopy I could show that Bottleneck crosslinks and bundles actin fibers in tightly connected cables. In agreement with these results, STED nanoscopy demonstrated that *bottleneck* mutant embryos display severely impaired actin bundle formation,

lack of hexagonal patterning and premature constriction. In addition, I identified two maternally deposited actin crosslinkers, Cheerio and Fimbrin, that differentially regulate actomyosin network transitions during cellularization. While Cheerio acts synergistically with Bottleneck to facilitate actin bundling and is required for hexagonal network assembly and maintenance, Fimbrin antagonizes Bottleneck activity and is required for hexagonal-to-ring transition and efficient constriction during the fast phase. Double mutant analysis of Bottleneck and Cheerio revealed a severe disorganization of the actin network and an arrest of morphogenesis, whereas depletion of Fimbrin in a *bottleneck* mutant rescued premature constriction and embryogenesis. Collectively, these findings lead me to propose that the spatiotemporal organization of actomyosin networks governed by the action of actin crosslinkers serves as a morphogenetic mechanism to time actomyosin contraction during tissue development. From a teleonomic point of view a switch in the response of actin network structures to myosin-II motor force appears favorable over a mechanism directly regulating myosin-II, since myosin activity might be required to facilitate inward-progression of the plasma membrane during cellularization and maintain the developing tissue under systemic tension to synchronize cell movements at the organismal-scale.

As discussed in the introduction (1.6.6, pp. 23), it is commonly thought that actomyosin network transitions *in vivo* are triggered by activation of myosin-II or by changes in actin filament stability and turnover. My results highlight the importance of actin crosslinkers and are consistent with previous reports. The Fimbrin homologue plastin has been shown to control cortical rearrangements driving polarization and cytokinesis of the *C. elegans* zygote (Ding *et al.*, 2017). Likewise, in mice plastin regulates the organization of a basal actomyosin network required for epidermal morphogenesis (Dor-On *et al.*, 2017). During cellularization the function of Fimbrin might be to crosslink actin filaments in such a way that myosin-II can efficiently bind and contract actin fibers. Hereby, it might allow the transmission of forces along actin structures promoting the disruption of interconnected hexagonal arrays into contractile rings once fibers are released from Bottleneck-mediated filament condensation, due to progressive depletion of Bottleneck. This interpretation is substantiated by a study that finds Fimbrin favoring actin bundling in

anti-parallel configuration to promote myosin-dependent contractility and cytokinetic ring constriction in fission yeast (Laporte *et al*., 2012). Additionally, knockdown of Fimbrin rescues hyper-contractility of the *bottleneck* mutant phenotype including the subsequent morphogenetic process of ventral furrow formation suggesting that Fimbrin is required for network contraction *per se* and that Bottleneck and Fimbrin antagonize each other's activity in wild-type embryos. Although, these studies clearly demonstrate a requirement for Fimbrin-type of actin crosslinking to produce a defined network structure at the right time and space, the function of Fimbrin-type crosslinkers might mainly be to prepare a network configuration for efficient myosin-mediated contraction supposedly by governing network connectivity, which was found to be an essential parameter regulating contractile behaviors (Belmonte *et al*., 2017; Ennomani *et al*., 2016). In this context, Fimbrin-type actin crosslinkers rather pursue a supportive role of for myosin-dependent network transitions. This proposed mode of action is compatible with a recent study analyzing the dynamics of actomyosin ring constriction during cellularization, which argues that the transition from the hexagonal to the ring phase requires myosin-II activity (Xue and Sokac, 2016). Ring constriction during the fast phase requires F-actin turnover and the action of the actin-bundling proteins Septin, and the adaptor protein Anillin (Xue and Sokac, 2016). In fact, mutant phenotypes for Septin and Anillin partially resemble the Fimbrin knockdown phenotype displaying a prolonged hexagonal phase, increased angularity and impaired ring constrictions (Figure 21) (Mavrakis *et al*., 2014; Thomas and Wieschaus, 2004). Therefore, Fimbrin might contribute to myosin-independent cellularization ring constriction similar to the mode of yeast cytokinetic ring constriction (Laporte *et al*., 2012; Skau *et al*., 2011).

Different from Fimbrin, Cheerio is not required for network contraction *per se*; instead loss of Cheerio impairs spatial organization of actin structures during cellularization resulting in a *bottleneck*-like mutant phenotype. Proteins of the Filamin family, to which Cheerio belongs, are relatively large and provide scaffold function due to interactions with multiple proteins including RhoGTPases and receptors that link Filamins to the plasma membrane (Feng and Walsh, 2004; Ohta *et al*., 1999; Stossel *et al*., 2001; Zhou *et al*., 2010). While small actin crosslinkers such as Fimbrin predominantly promote actin

bundling, Filamins have the potential to bundle or to crosslink actin filaments in a meshwork-configuration depending on their concentration (Tseng *et al*., 2004). Based on the knockdown phenotypes I have described during cellularization, Cheerio likely promotes actin bundling at the plasma membrane similar to its proposed function in ring canal assembly during *Drosophila* oogenesis (Li *et al*., 1999; Sokol and Cooley, 1999). Ring canals share similarities to the non-contractile actin network during cellularization as they represent structures that originate from stalled cytokinetic rings, whose function is to allow communication between the oocyte and follicular cells (Li *et al*., 1999).

Interestingly, Cheerio possesses mechanosensitive properties due to physical separation of protein domains revealing cryptic interaction interfaces upon tension and this mechanosensitivity appears to be required during ring canal maturation (Huelsmann *et al*., 2013). A force-dependent mechanism based on Filamin A was described, where strain increases β-integrin binding and causes FilGAP to dissociate from Filamin A (Ehrlicher *et al*., 2011; Nakamura *et al*., 2009). Such a mechanism could provide additional regulation also during cellularization to locally different tension trajectories or global changes in tissue tension during different stages of cellularization. Investigation of mechanosensitive responses of Cheerio and of other components of the cytoskeleton might facilitate our understanding of self-organizing structures during tissue morphogenesis and reveal novel insights into feedback mechanisms running in response to network transitions. The ability of Filamins to organize actomyosin networks in different conformations suggests the presence of regulative mechanisms to direct its crosslinking activity to favor different network configurations. Refilin A, a protein involved in perinuclear actin bundle formation, has been shown to bind to Filamin A and cause a change in its v-shaped conformation to promote actin bundle formation (Gay and Baudier, 2011; Gay *et al*., 2011a, 2011b; Huelsmann *et al*., 2013). While Cheerio and Fimbrin are present throughout cellularization, Bottleneck is only transiently present during the hexagonal phase (Schejter and Wieschaus, 1993). Given Cheerio's nature of undergoing versatile protein interaction and the synergistic function of Cheerio and Bottleneck, it would be interesting to test to what extent the proteins directly interact to cooperatively organize actin networks *in vivo*. Of further interest would be to investigate whether Bottleneck

contributes to direct Cheerio's actin structuring activity towards actin bundle formation or whether the action of the two proteins is strictly parallel. Both Cheerio and Bottleneck can associate with plasma membrane components (van der Flier and Sonnenberg, 2001; Reversi *et al*., 2014) and it is therefore likely that their synergistic function can be explained by a cooperative control of actin bundling, membrane tethering, and thus interconnection of adjacent hexagonal units to prevent myosin-mediated network constriction.

The function of Cheerio and Bottleneck during cellularization is mechanistically different from the role of Fimbrin. While Fimbrin is a required component of the contractile machinery, its function might be to connect actin fibers to allow myosin-mediated contraction or actin depolymerization-based ring constriction. In contrast to that, Cheerio and Bottleneck actively govern network architecture to withstand myosin-mediated force to prevent a collapse of the early actomyosin network. In fact, myosin-II stimulation is sufficient to enhance actomyosin constriction only during the initial priming or during the later ring phase, when Bnk is not present.

The mechanisms through which Cheerio- and Bottleneck-mediated actin organization prevent network contractility could be versatile. Actin bundles aligned with the internalizing plasma membrane in a regular symmetric pattern might compensate opposing forces of neighboring units and thus neutralize local inward-directed forces preventing local constrictions. However, this mechanism would be very sensitive to local or external (from the environment) mechanical disturbances. Alternatively, the alignment of actin bundles induced by Bottleneck and Cheerio might be so tight that they outcompete myosin minifilaments or the particular orientation of bundled fibers might prevent productive myosin-mediated contraction (1.6.4, pp. 18). The function of Cheerio and Bottleneck on the molecular level could be additive and not identical. Filamin was reported to increase the elasticity more than the viscosity of actin networks enhancing the network stiffness (Esue *et al*., 2008; Ito *et al*., 1992) and I show that Bottleneck tightly connects actin filaments increasing their width of 3-fold (Figure 17I). According to the material properties of actin fibers, the force required to bend tightly linked filaments scales with the power of 4

of the bundle radius causing a significant increase in stiffness (1.6.4, pp. 18) (Blanchoin *et al*., 2014). Thus, the combined effect of Bottleneck and Cheerio might ultimately cause an increase in rigidity that counteracts the effect of myosin-mediated contraction. However, the key agent controlling network architecture seems to be Bottleneck since the presence of Cheerio alone during the fast phase of cellularization does not prevent network constriction. After Bottleneck is lost from the network, actin filaments are more accessible for myosin-II and Fimbrin supports myosin-dependent remodeling of the actin network by connecting actin fibers in structures compatible with and favorable to the action of myosin-II.

Bottleneck might have evolved to exclusively regulate contractility during the process of cellularization in the early *Drosophila* embryo, since *bottleneck* does not seem to be expressed in other tissues or developmental stages and no orthologous protein has been identified in other organisms. However, the results presented in the first part of my thesis do not only reveal a 'gene-centric' framework for the developmental control of *Drosophila* cellularization regulated by the zygotic expression of Bottleneck, but also represents a specific morphogenetic integron (1.2, pp. 2) in a more general term. Bottleneck's mode of action demonstrates that the spatial organization of actin networks governed by the activity of actin crosslinkers can control contractile processes during tissue morphogenesis. The activity of other genes might have evolved to fulfill the same function bottleneck provides to control cellularization in other morphogenetic processes. Furthermore, my results demonstrate how the functional diversification of actin crosslinkers impact actomyosin network transitions *in vivo*.

4.2. Tissue invagination requires downregulation of basal myosin-II

The process of ventral furrow formation is severely defective in bottleneck mutant embryos although myosin-II accumulates at the apical surface of ventral cells. One possible explanation of why apical myosin accumulation does not result in tissue invagination in *bottleneck* mutant embryos is that the increased contractility of the basal actomyosin network interferes with the normal intracellular dynamics required for cell shape chang-

es. Consistent with this hypothesis, decreasing basal network contractility by depletion of Fimbrin in *bottleneck* mutant embryos rescued defects in ventral furrow formation. In the second part of this thesis I directly tested the role of basal relaxation for tissue invagination using precise optogenetic stimulation of myosin-II at the basal surface of invaginating cells.

Following cellularization, the naïve *Drosophila* blastoderm undergoes tissue folding at the ventral side of the embryo. Although the importance of apical actomyosin contractions in initiating tissue invagination has been clearly demonstrated by the work of Emiliano Izquierdo in the lab (Izquierdo *et al*., 2018), computer models suggested that there is an additional requirement for relaxation of the basolateral surface (Polyakov *et al*., 2014). Indeed, I confirmed that myosin-II is progressively downregulated from the basal surface of internalizing cells during ventral furrow formation. To test whether this downregulation is functionally relevant, I precisely modulated myosin-II levels at the basal surface of invaginating cells using optogenetics to maintain pre-invagination levels of myosin-II over time, essentially transforming the base of ventral mesodermal cells into an ectoderm-like constitution. Using this approach, I unraveled a role for basal myosin-II downregulation in supporting the whole series of cell shape changes observed during ventral furrow formation. Depending on the time point of photo-activation, stabilizing basal myosin-II either prevents the entire internalization process or stops the folding of the ventral furrow into a tube-like structure. Quantitative live imaging and reconstruction of cell shape changes revealed that prior to the beginning of invagination, down-regulation of basal myosin-II is required to allow efficient apical constriction and cell lengthening, while after initial tissue internalization has occurred, it is necessary for cell shortening and closure of the furrow. These results demonstrate the requirement of basal myosin-II downregulation and basal relaxation throughout the entire invagination process.

Apical constriction is thought to cause a redistribution of cytoplasm generating a hydrodynamic flow towards the basal side of the cells causing cell elongation (He *et al*., 2014). The inhibitory effect on cell lengthening that I observed upon increasing basal myosin-II levels, can be explained by a secondary inhibitory effect on apical constriction (Krueger

et al., 2018). Indeed, while nuclei shift basally in non-activated cells, they remain at the apical surface upon basal photo-activation. This suggests that nuclei passively move in response to apical constriction and hydrodynamic flows and disproves models proposing an active function for microtubule in controlling nuclear positioning during ventral furrow formation. In this regard ventral furrow formation seems to be different from constriction of bottle cells during *Xenopus* gastrulation, where apical constriction and tissue invagination do not seem linked as closely (Gong *et al*., 2004; Lee and Harland, 2007).

Importantly, inhibition of apical constriction upon basal stabilization of myosin-II is not due to a decrease of apical myosin-II accumulation but it is rather caused by intracellular events that do not allow ratcheted contractions. Although a recent study revealed a competitive mechanism for actomyosin accumulation at different subcellular locations (Lomakin *et al*., 2015), the optogenetic activation of Rho signaling that I have employed lead to a two-fold increase of basal myosin-II and did not interfere with apical myosin-II levels. Photo-activated cells underwent non-ratcheted pulsation at the apical surface with cycles of constriction and relaxation without net-decrease in surface area (Figure 34). Basal contractility might elastically withstand hydrodynamic pressure caused by apical contractions, which then cannot be mechanically stabilized by means of a molecular ratchet. Over time some cells constricted apically, shifted their nuclei basally and expanded the cell base, while other cells displayed the opposite behavior. This uncoordinated cell behavior might be due to local stochastic differences between cells that allow some cells to constrict either the apical or basal surface while the opposite side expands. Therefore, uncoordinated apical constriction might result from imbalanced force transmission across the tissue that also manifests itself in the lack of anisotropy. It is interesting to note that the frequency of pulsation did not change upon basal photo-activation, arguing for the pulsatile behavior as an intrinsic feature of the apical actomyosin system rather than a consequence of coordinated periodic contractions of neighboring cells (1.7.3.2.2, pp. 38). By reconstructing the shapes of cells in the photo-activated region, I observed that cells that constricted their apical surface and expanded their base also had different numbers of cell neighbors in their basal and apical surface (Appendix 4, p. 146). A recent study revealed the existence of a novel cell shape called

scutoid that exactly possesses this characteristic (Gómez-Gálvez *et al*., 2018). Scutoid shapes appear to be present in many epithelia to minimize tissue energy and stabilize three-dimensional packing as well as to achieve epithelial bending. Adaptation of this non-canonical cell shape upon optogenetic perturbation of tissue invagination might be a mechanism to balance forces across the tissue or a measure of morphogenetic robustness aiming to proceed embryonic development on an alternative strategy.

During *Drosophila* posterior spiracles formation, induction of apical constriction by RhoGEF- myosin-II activation is accompanied by deactivation of Rho signaling at the basal cell surface (1.7.4, pp. 42) (Simões *et al*., 2006). During ventral furrow formation no gene has been identified that specifically regulate basal myosin-II levels. However, the fact that upon basal increase of myosin-II, no decrease of apical myosin-II is observed argues against a competitive mechanism between cell apex and base suggesting the presence of an active mechanism controlling basal myosin-II levels.

The effect of basal photo-activation on cell shortening is consistent with a theoretical model arguing that apical constriction is the only active force driving invagination and the whole series of cell shape changes observed during ventral furrow formation can be explained as passive mechanical responses of the cells (Polyakov *et al*., 2014). This model makes two assumptions: first that the cell volume is conserved throughout the invagination process (which was confirmed) and second that different plasma membrane domains can be deformed elastically. In particular, according to this model elastic energy stored in the cortex of the lateral plasma membrane is released upon basal surface expansion resulting in a shortening of cells that acquire a wedge-shape and internalize. However, as the process of cell elongation lasts for about 10 minutes it is unclear whether elastic responses can operate on this long-time scale. In favor of this idea, it was demonstrated that actin stress fibers can display elastic-like properties on a time scale beyond the turnover of constituent components (over 60 min) facilitated by mechanosensitive proteins such as zyxin (Oakes *et al*., 2017). In the future, a rigorous subcellular measurement of cell material properties could help clarifying this point. While it is difficult to disprove any possible effect of basal myosin-II upregulation on other cell-

internal processes, the dual outcome of the same experimental procedure preventing cell elongation first and cell shortening afterwards is consistent with a major role of cell mechanical responses.

My results are consistent with a recent study from our lab by Izquierdo *et al.* that has reconstructed epithelial folding on the dorsal side of the embryo by the optogenetic induction of myosin-mediated apical constriction (1.8.2.3, pp. 49) (Izquierdo *et al.*, 2018). While apical constriction was sufficient to initiate tissue invagination, it was not sufficient to drive a complete tube-like folding and closure of the ectopic furrow. A more detailed inspection of 3D cell shape changes during apical optogenetic activation could clarify the extent to which cell elongation and basal extension occur. A lack of basal myosin-II downregulation could be a factor limiting tissue folding in this experimental scheme. Possibly, the ratio of apical versus basal myosin-II needs to be well controlled to promote the whole series of shape changes driving a full invagination. Together, these experiments reveal the power of optogenetics to persue experiments with high precision and test hypotheses that could not have been addressed by other approaches.

4.3. Advancing optogenetics to probe morphogenesis

Over the last years optogenetics has been proven to provide a powerful new method to test morphogenetic mechanisms and perturb living biological systems (1.8.2.3, pp. 49). In this thesis, I showed that optogenetics can be used to quantitatively modulate intracellular signaling pathways with subcellular precision. In the first part I showed, that optogenetic stimulation of myosin-II can be used to probe the contractile properties of actomyosin networks in living *Drosophila* embryos, while in the second part I used optogenetics to modulate the level of myosin-II quantitatively in internalizing ventral cells to match the myosin-II content of non-internalizing ectodermal cells. The analytic testing of input/output relationships helps understanding minimal requirements for morphogenetic processes and provide measures towards quantitative biology (Shekhar *et al.*, 2014).

The further development of optogenetic tools is important when established techniques face technical limitations. Here, I have developed a (to my knowledge) first optogenetic

module that allows subcellular restricted activation patterns based on a polarized membrane anchor. By adding a membrane-localization tag I turned a correctly (basally) localized but non-functional anchor protein (PatJ-CIBN) into an effective optogenetic anchor that could support stimulation of Rho signaling and myosin-II activation. The strategy I developed could represent a general strategy for the activation of membrane-bound interaction partners. Domain-specific optogenetic recruitment provides a significant advancement in the synthetic molecular toolbox (Karunarathne *et al*., 2015) and represents a useful strategy to study the role of specific surface domains during morphogenesis of tissues and organs with complex anatomy. The refinement of optogenetic methods will in the future allow the simultaneous application of multiple synthetic modules to study morphogenesis. In this regard, domain-specific recruitment will be essential as many optogenetic systems share the same activation wavelength (Zhang and Cui, 2015). The possibility to synthetically build the shape of an organ or of an organism will open the opportunity to investigate the extent to which shape *per se* can generate functionality and influence for example cell differentiation.

4.4. Integration into the broad theoretic framework of morphogenesis

In my thesis, I have identified a morphogenetic mechanism that regulates the spatiotemporal organization of actomyosin contraction during the process of cellularization. The developmentally controlled expression of a single actin crosslinker, Bottleneck, influences significantly the fate of the entire organism. However, additional actin crosslinker activities are required to correctly control actomyosin network transitions in time and space. They integrate into a regulative morphogenetic framework, an integron, which might also be employed to fulfill the same function in other morphogenetic contexts. Similar mechanisms to withstand mechanical forces could for example function to regulate actomyosin networks undergoing ratchet-like contractions and prevent network relaxation. In the second part of my thesis I further showed that the contractile properties of the basal actomyosin network present at the end of cellularization need to be remodeled to accommodate tensile load and expand during the folding process of the ventral furrow. My results argue that hydrodynamic pressure resulting from apical constriction needs to

be released by basal surface expansion for which down-regulation of basal myosin-II is the molecular requirement. The polarized distribution of myosin-II that is required for many cellular processes including cell migration and cell division (Conti and Adelstein, 2008) thus is a morphogenetic mechanism also controlling inward folding of cells during tissue invagination.

5. Methods and Materials

Experimental procedures concerning the second part of my thesis (3.2, pp. 76), methods were adapted from Krueger *et al*., 2018.

5.1. Methods in cell biology

5.1.1. Cell culture, transfection, and live imaging

Hela cells were cultured in DMEM (Gibco) supplemented with 2 mM l-glutamine (Gibco), 10% fetal calf serum (PAA) at 37°C and 5% CO2. The cells were seeded at a cell number of 10.000 cells in 2 ml culture medium on 35 mm tissue culture-ready glass-bottom dishes (MatTek corporation). After 16 h plasmid transfection was done using Fugene HD (Roche) according to the manufacturer's instruction. Cells were live imaged 12-24 h after transfection using a Zeiss LSM 780 confocal microscope with a Plan Apochromat 63×/NA 1.2 water immersion objective (Carl Zeiss).

5.2. Methods in molecular biology

Buffer compositions, kits, reagents and chemicals used are specified in 5.7 (pp. 126).

5.2.1. Protein expression in *E. coli*

Plasmids were transformed into chemically competent *E. coli* Rosetta 2(DE3) cells (Novagen) using standard heat-shock procedure. LB supplemented with antibiotics was inoculated with a single *E. coli* colony and grown over night at 37°C.

5.2.1.1. Auto-induction in *E. coli*

TBL medium supplemented with antibiotics was inoculated with 5% (v/v) of over night culture and incubated shaking for 24-26 h at 22°C. The cells were harvested by centrifu-

gation, the cell pellet snap-frozen and stored at -80°C or further processed directly afterwards.

5.2.1.2. IPTG-induction in *E. coli*

LB medium supplemented with antibiotics was inoculated with 5% (v/v) of overnight culture and grown to an OD_{600nm} of 0.6-0.8 and induced with 0.5 mM IPTG. After induction the cultures were growth at 18°C, 22°C or 37°C for 8 h, 16 or 24 **Protein expression in insect cells**

5.2.2.1. Baculo virus transposition

The pFastBac vector (Thermo Fisher Scientific) containing the gene of interest was transformed into *E. coli* DH10MultiBac by electroporation and plated on an YTE agar plate containing Ampicillin (100 g/ml), Kanamycin (30 μg/ml), Gentamycin (7 μg/ml), Tetracycline (10 μg/ml), X-gal (400 μg/ml) and IPTG (5 mM) and incubated over night at 37°C. White colonies were re-streaked on a fresh plate and again incubated over night at 37°C.

5.2.2.2. Bacmid prep

Overnight cultures were grown in 2xTY medium supplemented with antibiotics were lysed using the QIAprep Spin Miniprep Kit (Qiagen), DNA was precipitated using isopropanol, washed in 70 % ethanol and pelleted using table top centrifugation. The DNA was resuspended in sterile ddH_2O. Using routine PCR and M13 primers the presence of the insert was controlled.

5.2.2.3. Transfection of Sf21 or Hi5 cells

A total number of $0.6x10^6$ of Sf21 cells were seeded per well in a 6-well plate and transfected with the purified Bacmid using FuGene according to the manufacturer's instructions. Cells were incubated at 27°C for 48-60h to produce the V_0 titer.

A suspension culture (20 ml, 0.6x10^6 cells/ml) of Sf21 or Hi5 cells was infected with 2 ml of V_0 suspension. Cultures were split every day to maintain a cell concentration of 0.6x10^6 cells/ml till the cells stopped growing. Every day samples were taken, pelleted, washed, resuspended and lysed LB and analyzed by Coomassie gel to analyze the expressed protein.

Two days after proliferation arrest were lysed under native conditions using SLB and centrifuged at 40,000 rcf. Soluble protein remained in the supernatant.

5.2.3. Protein expression and purification of MBP-His-Bnk deletion constructs

To test the solubility of the different Bottleneck truncations, MBP fusion constructs containing also a His-tag were expressed in *E. coli* Rosetta 2(DE3) cells using an auto-induction system. Buffers are listed in Table 5 (pp. 128) and Table 6 (pp.130). The bacteria culture was harvested by centrifugation and lysed in SLB using a microfluidizer. Proteins were batch-purified using a Ni-NTA (His affinity purification) or amylose resin (MBP affinity purification) according to the manufacturer's procedure with a 2 h incubation at 4°C. The standard wash buffer WB and elution buffer EB were used for MBP affinity purification. The wash buffer His-WB and elution buffer His-EB was used for His affinity purification. To assess the solubility and aggregation behavior of the purified proteins, size exclusion chromatography was performed using a Superdex 200 Increase 10/300 GL (GE Healthcare) in His-WB. The protein peak at the molecular size of ~75 to 50 kDa was compared to the void peak at ~8.5 ml elution volume.

5.2.4. Recombinant expression and purification of Bnk$_{198-303}$

Recombinant MBP-Bnk$_{198-303}$ was expressed and purified (His affinity purification) as described above, except purification was done on a cOmplete His-tag purification column (Roche). Buffers are listed in Table 6 (pp.130). The MBP tag was cut from MBP-Bnk$_{198-303}$ using a GST-3C protease expressed in-house (by the protein expression and purification facility) over night at 4°C, and at the same time the buffer was changed to His-WB, followed by a second cOmplete column His-purification (the His-tag remained

attached to $Bnk_{198-303}$). Afterwards, a size exclusion chromatography was done using a Superdex 200 16/600 column in bottleneck buffer. The protein was concentrated to 20 μM using an Amicon Ultra 4 mL Centrifugal Filters (3,000 NMWL).

5.2.5. Western Blot

An SDS-PAGE was performed and the sample blotted on a methanol-activated Immobilon-P PVDF membrane (Millipore) using a Trans-Blot® SD semi-dry transfer cell (Bio-Rad) in transfer buffer for 50 min at constant voltage of 15 V. A PonceauS staining was done to control efficient blotting. The membrane was incubated in 5% milk/PBST shaking for 1 h at room temperature and in primary antibody shaking over night at 4°C. The membrane was washed in PBST, incubated in HRP-conjugated secondary antibody diluted in 5% milk/PBST shaking for 1 h at room temperature and washed again in PBST. Substrate (SuperSignal West Pico, Thermo Fisher Scientific) was added, chemiluminescence detected using Amersham hyperfilm ECL (GE Healthcare) and the film developed after different exposure times.

5.2.6. Actin binding und bundling assay

The actin binding and bundling assays were done using the *Actin Binding Protein Biochem Kit – Non-Muscle Actin* (Cytoskeleton, Cat. # BK013) kit following the manufacturer's instruction. In brief, the sample protein (Bottleneck was used at a concentration of 20 μM) was incubated in presence or absence of F-actin for 1 h at room temperature. Afterwards, the samples were spun at 100,000 rcf (actin binding assay) or 14.000 rcf (actin bundling assay) for 1 h at 24°C. The supernatant fraction was removed and the pellet resuspended in water. 4x Laemmli buffer was added and the samples were run on a NuPAGE 4-12% Bis-Tris Gel SDS PAGE (Invitrogen/Thermo Fisher Scientific) and stained with Coomassie brilliant blue.

5.2.7. Molecular cloning

All plasmids were cloned using Gibson assembly, the Gateway cloning system and standard molecular biology procedures. Except for the Gibson assembly, all methods including mRNA purification, reverse transcription, PCR, DNA purification, *E. coli* transformation and gateway cloning were done using commercialized procedures with kits and reagents listed in Table 2 (pp. 126), chemicals listed in Table 3 (p. 126) and buffers listed in Table 5 (pp. 128).

5.2.7.1. Gibson assembly (One-step isothermal recombination)

Using SnapGene (GSL Biotech LLC) software DNA fragments to join were designed to have overhangs at either ends and were PCR-amplified by gene-specific primers comprising 5' extensions. The Gibson assembly reaction was performed using a custom-made Gibson assembly master mix (Table 5) according to (Gibson *et al.*, 2009). On ice a 15 µl aliquot of Gibson assembly master mix was mixed with 5 µl of DNA fragment mixture containing 60 fmol of linearized (by PCR amplification or enzymatic restriction) plasmid backbone and 20 fmol of each additional DNA fragment. The assembly mix was incubated for 60 min at 50°C and transformed into TOP10 *E. coli* cells.

5.2.8. Outline of cloning strategies for generated constructs

The *bottleneck* (P40794; reference sequence: AAC46467.1) coding sequence was amplified from a *Drosophila melanogaster* embryo (0-12 h) cDNA library. Full-length *bottleneck* was cloned into pGEX-6P-1, pET-24a, pFastBac-HTa, pETM11-SUMO-sfGFP, pETM-22, pETM-66 and pETM-44 using Gibson assembly, classical cloning approaches or Gateway cloning.

Truncations of *bottleneck* (1-303, 1-100, 100-200, 1-197, 140-251, 198-303, 247-303) were cloned into pENTR/D-TOPO (Thermo Fisher Scientific) and then sub-cloned into a mammalian expression vector comprising a C-terminal GFP tag (pcDNA6.2/C-EmGFP-Dest; Thermo Fisher Scientific) using the Gateway system. A custom-made destination

vector (pDEST-MBP-3C-His, Appendix 3) containing a T7 promoter, the MBP gene, an HRV 3C site cleavage site, a hexa-His-tag and chloramphenicol resistance together with a ccdB death cassette flanked by attachment R sites (attR) was derived from a pDEST17 (Thermo Fisher Scientific) vector. Bottleneck fragments (1-303, 1-150, 50-197, 1-197, 50-197, 140-303, 198-303, 247-303, 50-303) were sub-cloned into pDEST-MBP-3C-His to produce MBP-His-Bnk truncations.

To generate transgenic fly lines maternally expressing the nanobody, the gene for the F-box protein Slimb fused to nanobody gene were amplified from a pUAST-attB-nanobody vector (kind gift from Emmanuel Caussinus) and cloned into a modified pCatub67Mat-polyA *Drosophila* expression vector.

To engineer novel basal-specific optogenetic anchors, full-length $PatJ_{1-871}$ (Q9NB04-1; reference sequence: AAN11498.1), $PatJ_{PDZ}$ (L27 and first PDZ domain comprising aa 1 – 244 from reference sequence Q9NB04-1), full-length $Slam_{1-1173}$ (Q9VME5-1; reference sequence: AAF52374.3) were amplified from a *Drosophila melanogaster* embryo (0-12 h) cDNA library. Full-length Bnk (P40794; reference sequence: AAC46467.1) was amplified from existing plasmids. All other fragments including CIBN (CIB1 N-terminal domain), EGFP, and the plasma membrane (pm) anchor (CAAX box) were amplified from existing plasmids (Guglielmi *et al*., 2015) to finally assemble (3' to 5') PatJ-$Linker_{(GAGA)}$-CIBN::GFP-pm, PatJ-$Linker_{(GAGA)}$-CIBN, $PatJ_{PDZ}$-$Linker_{(LAAPFT)}$-CIBN::GFP, GFP::CIBN-Slam, CIBN::GFP::Bnk and CIBN-Bnk::GFP using Gibson assembly. The constructs were initially cloned into a pENTR/D-TOPO-derived entry vector (Thermo Fisher Scientific) linearized by restriction enzymes or split and amplified by PCR. The resulting pENTR constructs were sub-cloned into the pPW vector (*Drosophila* Genomics Resource Center, Bloomington, IN) using the Gateway cloning system (Thermo Fisher Scientific) following the manufacturer's instructions.

5.3. Methods in electron microscopy

5.3.1. Negative stain electron microscopy

The samples were prepared as described in the actin bundling protocol (5.2.6, p. 108), except after 45 min of incubation of f-actin and Bottleneck$_{198-303}$, the samples were incubated with 5 nm Ni-NTA-Nanogold (Nanoprobes) for 15 min. Excess nanogold was removed by ultracentrifugation at 49,000 rcf for 45 min at 4°C and the pellet fraction was resuspended in bottleneck buffer. The sample was further diluted (1:5) in bottleneck buffer and 3.6 µl was applied to a glow-discharged carbon-coated EM grid and blotted according to the side blotting method (Ohi *et al.*, 2004). Grids were imaged using a Morgagni 268 transmission electron microscope (FEI) operated at 100 kV with a side-mounted 1K CCD camera. Filament width was measured using Fiji and statistical analysis was done using GraphPad Prism 6.0. The filament width for f-actin in presence of Bottleneck was only measured when 5 nm Ni-NTA-Nanogold was present in the bundles.

5.4. Methods in light microscopy

5.4.1. Live imaging and optogenetics

Flies were kept in a cage with a removable agar plate at the bottom. The agar plate was collected and halocarbon oil was added to select cellularizing embryos under a standard stereomicroscope. Embryos were dechorionated using 100% sodium hypochlorite for 2 min, rinsed with ddH_2O and mounted onto a 35 mm glass-bottom dish (MatTek corporation) in PBS. For the optogenetics experiments, parental crosses, fly cages and embryos were kept in the dark and the sample preparation was done under a red-light emitting LED lamp.

Live-imaging experiments were performed at 20°C using a Zeiss LSM 780 NLO confocal microscope (Carl Zeiss) equipped with a tunable (690-1040nm) femtosecond (140 fs) pulsed laser (Chameleon; Coherent, Inc.) with a repetition rate of 80 MHz and a 40x C-

Apochromat (NA 1.20) water immersion objective (Carl Zeiss) unless stated differently. Deep Amber lighting filter (Cabledelight, Ltd) was used to filter bright field illumination to prevent pre-activation of photosensitive embryos. Live imaging of YFP- and GFP-tagged proteins was conducted using 488 nm or 950 nm two-photon excitation and mCherry-tagged proteins were imaged using 564 nm excitation. The microscope was operated using Zen Black software (Carl Zeiss) and the Pipeline Constructor Macro (Politi, Cai *et al*., 2017).

For the optogenetics experiments in 3.1.1 (pp. 55), a pre-activation Sqh::mCherry image stack using 561nm excitation was acquired initially. A region of interest was defined within a subset of cells in which RhoGEF2-CRY2 was photo-activated specifically at the cell base using two-photon (950 nm) excitation. The cell base was activated in a focal volume of max 2 μm height in a bi-directional scanning mode with a total dwell time of 1 μs, a pixel size of 300 nm and 10 mW laser power. Afterwards, the Sqh::mCherry signal was recorded for 5 min to visualize the effect of photo-activation. Embryos were photo-activated at different stages of cellularization (priming phase, hexagonal phase and ring phase). The complete data set was produced in one day to ensure stable expression levels. When the same embryo was photo-activated two consecutive times, a new region of activation was set and the position of the cell base was redefined to activate the cell base using the same parameters as for the first activation. Before and after the second photo-activation, the embryo was imaged using 561nm excitation laser.

For the optogenetic experiments of the second part of this thesis (3.2, pp. 75) the samples were prepared as described above and embryos were mounted with their ventral epithelium facing the coverslip, unless described differently. Two imaging settings were used in an alternating fashion to record mCherry fluorescent signal and to photo-activate RhoGEF2-CRY2. The mCherry fluorophore was excited using 561nm excitation laser in confocal microscope configuration. The sample was aligned, the spatial range of z-stacks and the position of the cell base was defined in the mCherry configuration. For whole-cell recordings, the standard mCherry z-stack size was ~55 μm with 0.94 μm interval.

An initial mCherry (pre-activation) z-stack was acquired, followed by cycles of photo-activation and mCherry recording with a varying number of iterations. Local photo-activation in the non-descanned/two photon microscopy mode was achieved with 13 mW laser power and a wavelength of 950 nm. Frames were scanned bi-directionally with a total dwell time of 3.15 μs. A region of interest (ROI) was defined to locally restrict the photo-activation to one half of the embryo or a defined subset of cells. Due to the curvature of the tissue, a semi-elliptical ROI was designed to specifically restrict basal activation to the ventral cells and exclude the lateral tissue. The cell base was photo-activated within a focal volume of 5 μm for 80 frames (60 s) per activation cycle. As the cell base further ingressed during the course of the experiment, the focus was adapted by sequentially increasing the focal offset at the macro interface and by manually changing the focus during activation. The time to complete one photo-activation cycle was about 95 s. At the end of each experiment, a whole-cell two-photon z-stack was acquired with a standard size of 80 μm with a 1.00 μm interval and 22 mW laser power.

For assessing apical myosin-II levels, the Sqh::mCherry signal was recorded in a 15 μm z-stack with a laser (561 nm) power that ensures non-saturating signal acquisition. Otherwise, the previously described photo-activation protocol was maintained. The experiment was terminated after apical constriction and an initial indentation of the non-activated tissue (3 – 5 μm) had been observed. The final Sqh::mCherry recording was immediately followed by a whole-embryo two-photon acquisition to visualize the cell membrane and reconstruct the cell outlines.

The imaging protocol was modified to analyze apical pulsatile contractions, as a higher temporal resolution for GAP43::mCherry acquisition was required. The photo-activation time was reduced to 20 s and GAP43::mCherry was recorded in a 5 μm-spanning apical z-stack. The final time resolution amounted to 35 s.

Sample preparation and the general microscopy/photo-activation protocol remained constant for the PatJ-CIBN::GFP/RhoGEF2-CRY2 experiments. However, the activation time, laser power and the illuminated volume was increased to 100 s, 20 mW and 8 μm, respectively. All laser powers were measured 1 cm from the objective.

To test the effects on myosin-II recruitment during early cellularization, when the basal actomyosin network is very close to the apical surface thus diminishing any possible light penetration constraints both for the efficiency of photo-activation and visualization of myosin-II, embryos of the appropriate genotype were photo-activated within a region of interest using a pulse of 488 nm light ensuring an efficient activation of RhoGEF2-Cry2 at the onset of cellularization. The effects on myosin-II were assessed by recording the Sqh::mCherry signal using 561 nm excitation pre- and post-photo-activation. To test the functionality of the newly engineered basal optogenetic anchors, embryos expressing RhoGEF2-CRY2 and the respective anchor were continuously activated using 488 nm single photon excitation while simultaneously recording Sqh::mCherry using 561 nm light during cellularization to visualize the effects on actomyosin-II rings.

5.4.2. Immunostaining.

Flies were kept in a cage with a removable agar plate supplemented with apple juice and yeast paste at the bottom at 18 °C for 8 h. The agar plate was collected and the yeast paste removed. The embryos were bleached using 100% Sodium hypochlorite for 1 min, rinsed multiple times with ddH_2O and fixed in a mixture of equal amounts of 100% heptane and 4% paraformaldehyde/PBS shaken for 20 min. After phase separation the lower phase was removed, the same amount of methanol was added and shaken vigorously for 30 s. The fixed embryos in the lower methanol phase were collected, washed three times with 100% methanol and kept at -20°C until the immunostaining was done. Methanol was removed, washed with water and PBST and incubated in blocking solution for 1 h. Primary antibody against GFP and against Bottleneck were diluted in blocking solution, the embryos incubated in primary antibody solution for 2 h at room temperature and washed three times in PBT. Next, the embryos were incubated for 1.5 h in fluorescently-labled secondary antibody (mouse-alexa488, rat-alexa647) diluted in blocking solution and washed three times in PBT. To stain the nuclei, the embryos were incubated in DAPI solution (600 nM in PBS) for 15 min and washed three times in PBT. The embryos were mounted on a glass slide by removing the PBT and adding Aqua-Poly/Mount (Polysciences). A cover glass was added, excessive mounting medium re-

moved, the slide dried and sealed with nail polish. The immunostained embryos were imaged using a Zeiss LSM 770 confocal microscope with a Plan Apochromat 63×/NA 1.2 water immersion objective (Carl Zeiss).

5.4.3. Actin staining.

Flies were kept in a cage with a removable agar plate supplemented with apple juice and yeast paste at the bottom at 18 °C overnight. The agar plate was collected and the yeast paste removed. Halocarbon oil was added and embryos of the desired cellularization stage selected. Embryos were bleached using 100% Sodium hypochlorite for 1 min, rinsed three times in ddH_2O and fixed in formaldehyde-saturated heptane for 40 min. The formaldehyde-saturated heptane solution was the upper phase separated from a mixture of equal amounts of 100% heptane with 37% formaldehyde vigorously shaken for 15 min. Fixed embryos were placed onto a two-sided sticky tape and covered with PBS. Using forceps and brushes, the vitelline membrane was removed from the embryos under a standard stereomicroscope and the embryos were collected in PBST in an Eppendorf tube. Devitellinized embryos were washed three times in PBT and incubated in blocking solution for 1 h at room temperature. Afterwards, embryos were incubated in actin staining solution (15 μl of phalloidin-atto647N stock solution (20 μM in methanol, kept at -20°C) in 1 ml of PBST) for 1.5 h at room temperature and washed three times in PBT. Embryos were mounted on a glass slide by removing the PBT solution and adding ProLong Gold Antifade Mountant (Molecular Probes/Thermo Fisher Scientific). A 0.16 - 0.19 mm thick (Thickness 1.5) cover glass cover glass (Glaswarenfabrik Karl Hecht GmbH & Co KG) was placed on top, excessive mounting medium was removed using tissue paper, dried and sealed using nail polish.

5.4.4. STED microscopy

2D-STED microscopy was performed on a Leica SP8 confocal microscope (DMI6000) with a 100x oil HC PL APO CS2 objective (NA 1.40) and type F immersion liquid. The sample was imaged in both, normal confocal mode using only a 633 nm excitation and

STED mode combining 633 nm excitation with the 775 nm STED laser. Photons in a range of 640 nm and 750 nm wavelength were detected using a Leica HyD detector (6 % gain). The image was scanned with a pixel size of 15 nm, an averaging of 16, a dwell time of 1.2 μs and with a pinhole of 0.93AU. The depicted cross sections were imaged using a reduced resolution.

5.5. Methods in data processing and analysis

5.5.1. *In silico* analysis of Bottleneck structure

In silico analysis based on the primary structure of Bottleneck were done using RONN v3.2 (Yang *et al*., 2005) for the per-residue disorder prediction and ProtScale (ExPASy) to generate the Kyte & Doolittle hydrophobicity plot with a window size of 9 (Gasteiger *et al*., 2003). The mRNA structure of Cheerio and Fimbrin was analyzed using Ensembl (Zerbino *et al*., 2018) and the protein domain architecture was analyzed using SMART (Letunic and Bork, 2018).

5.5.2. Image and data analysis

Images were processed and analyzed using Fiji (https://fiji.sc/) and MATLAB-R2017b (MathWorks). Zeiss LSM files were imported and metadata were extracted using the lsmread function provided via GitHub by Chao-Yuan Yeh (https://github.com/joe-of-all-trades/lsmread) and the ImageJ Bio-Formats package. Image preprocessing was done using Fiji.

Regarding analysis of the first part of the thesis (3.1, pp. 55), the cell base was identified by analyzing the apico-basal intensity profile of the reporter signal using a custom-made matlab script. Three to 5 slices centered at the peak of the basal signal (using the *findpeak* function) were summed to produce top view representations of e.g. basal myosin-II.

To measure the ingression depth of the cellularization furrow, the position of the basal myosin-II peak and the cortical fluorescence at the apical surface were used to retrieve cell base and apex, respectively; the distance between them gives the ingression depth. To quantify furrow ingression kinetics for the different mutants, the ingression depth was measured over time and an ingression curve calculated. To account for differences in the start point of image acquisition, the ingression curves were moved along the time axis so that the difference between the curves was minimized to give rise to an average trend line that was zeroed at an ingression depth of 4 μm.

To quantify the size of the contractile units upon optogenetic activation, the basal acto-myosin network was segmented in the photo-activated and non-activated region using a watershed segmentation algorithm (Matlab). The area of the segmented units was measured and averaged for the activated and non-activated region, respectively, over time and normalized to the initial time point. At least three independent experiments were quantified to give rise to the mean curves presented. The initial constriction rate was calculated by measuring the difference in the area within the first two minutes after initial photo-activation. To quantify myosin-II recruitment within the photo-activated region, the basal myosin-II intensity (sum of three slices) was measured over time, background subtracted and normalized to the first time point to reveal the peak fold induction compared to the first time point.

To infer the position of the nuclei from myosin-II recorded in the transversal cross section of the embryo, the image was inverted; the background was estimated from the thresholded and gauss-filtered sum over time and subtracted from the inverted image. To measure the efficiency of the protein knockdown, the YFP signal of control embryos and upon nanobody expression was recorded in image stacks, the apico-basal intensity profile was calculated to identify the peak position of the (retained) signal and the same number of image slices was summed centered around the plane of the highest signal. The integrated signal density for each embryo was measured and normalized to the mean of embryos of the control condition.

Methods and Materials

To analyze geometric parameters characterizing the actomyosin network in different mutant phenotypes, the contractile units were segmented, and the shape of the units quantified. The angularity was defined as the square of the quotient of the convex perimeter over the ellipse perimeter (the convex perimeter is the perimeter of the convex hull and the ellipse perimeter is an ellipse with the same minor and major axis as the analyzed contractile unit). The segmented contractile units were laid over the basal myosin-II signal and color-coded according to the respective angularity values for different ingression depths.

For the second part of the thesis (3.2, pp. 75) image segmentation and cell tracking was done using Embryo Development Geometry Explorer (EDGE) software(Gelbart *et al.*, 2012) provided via GitHub (*https://github.com/mgelbart/embryo-development-geometry-explorer)*. The standard settings used, that were different from default, were bandpass filter thresholds of 2 and 10 μm, minimum cell size of 2 μm and a minimum spatial and/or temporal fractional overlap of 0.4. Vectorized cells were adjusted manually if required. Cells that were correctly and completely segmented and tracked were selected and subject to further analysis. Cell area and anisotropy measurements were extracted from EDGE. Other cell features (A/B ration, cell length, cell volume) were calculated and cell shapes reconstructed based on the processed membranes and centroid information using customized MATLAB scripts. Cells displaying extreme values in the volume parameter were thresholded within a *Coefficient of Variation (C.V)* range of $C.V = 25\%$. Cells were visualized using the MATLAB function *isosurface*.

To quantify basal myosin levels, regions of interest (ROIs) were defined within the activated and the non-activated region, respectively. Each ROI was sub-divided into smaller regions to better account for the uneven morphology of the embryo, the sub-regions processed individually and finally averaged. A line intensity plot along the apico-basal cell axis results in a z-profile of the myosin-II signal. Fitting a Gaussian function to the z-profile using the MATLAB function *findpeaks*, basal myosin peaks were identified. The width of the Gaussian fit was used as a measurement for the extent of signal spreading in the z-dimension. Myosin-II levels result from the mean value (integrated density per

area) of 5 consecutive image frames (5 μm size) centered at the basal peak position. To obtain basal myosin-II images, a window size of 5 frames was centered at the isolated basal myosin-II peak both, in the non-activated and activated region. All frames within the combined frameset were summed to produce a z-projection. The projection was normalized by the total mean value.

In order to measure constriction rates of actomyosin rings in activated vs. non-activated regions (3.2.1 p.76), circles were fitted to basal myosin-II projections of different time points using the *imfindcircles* MATLAB function. Diameters of the fitted circles were used to approximate the actomyosin ring size and normalized to the mean value of the initial time point. A linear function was fitted to the data with the slope being a measure for the constriction speed. Compaction of the activated tissue was analyzed by manually marking the position and automated counting of actomyosin rings. The number of rings was normalized to the analyzed area resulting in the ring density value.

For quantifying apical myosin-II upon basal activation, the myosin-II signal was superimposed to the membrane signal (image stack of 15 μm). Cells were segmented, tracked and myosin-II intensity per cell area measured using EDGE software. The procedure previously described to identify myosin-II peaks was applied correspondingly to find apical myosin-II peaks. For each cell the myosin-II intensities of 3 frames (3 μm) centered at the identified apical peak were integrated. The values were normalized by the mean integrated density per cell of the combined (non-activated and activated region) population.

In order to analyze apical pulsing behavior, apical GAP43::mCherry plasma membrane signal was segmented and tracked using EDGE software and cell area values over time were extracted. Pulses in apical cell area were identified by finding local maxima using the *findpeaks* MATLAB function. The mean temporal distance between identified peaks revealed the mean pulsing period. The mean change in area between consecutive peaks describes the extent of ratchet cell constriction during a single pulse.

5.5.3. Statistical analysis

Statistical analyses were performed in MATLAB (MathWorks). Two sample Student's *t*-test was perform to determine if two sets of data are significantly different from each other and the p-value was calculated. To compare multiple samples and test for significant differences, a one-way analysis of variance (ANOVA) was performed followed by a post hoc Tukey's honestly significant difference procedure. In addition, as the sample size of the present data is high, the effect size was analyzed by calculating Cohen's d:

Eq. 1 $$d = \frac{\sqrt{(\overline{x_1} - \overline{x_2})^2}}{s} = \frac{\sqrt{(\mu_1 - \mu_2)^2}}{s}$$

where $\overline{x_1} - \overline{x_1}$ is the difference between the two means of the compared sample pair and s is the maximal standard deviation of the analysed dataset (comprising multiple sample pairs). Cohen's d values of $d \leq 0.5$ are considered as low effect size, whereas $d \geq 1$ represent a large effect size and thus argue in favor of two significantly different sample populations.

5.6. Methods in fly genetics

5.6.1. Anti-GFP Nanobody-mediated protein knockdown

Female flies homozygous for YFP-insertion in the locus of *cheerio* or *fimbrin* and expressing the myosin-II probe Sqh::mCh were crossed to males heterozygous for the respective YFP-tagged insertion, and expressing the anti GFP-nanobody under the control of the maternal tubulin promoter, to generate flies homozygous for either YFP-*cheerio* or *fimbrin* and co-expressing Sqh::mCh and the anti-GFP nanobody. Heterozygous flies (of the parental crosses) expressing YFP-tagged *cheerio* or *fimbrin* together with the nanobody were kept at 25 °C to reduce the efficiency of protein knockdown and minimize the selective pressure to compensate for the crosslinker depletion. Flies of the final genotype were collected for three days, put in a cage, shifted to 18 °C and after one day of adaptation used for phenotypic characterization over a period of 5 days.

5.6.2. Verification of YFP-Cheerio and YFP-Fimbrin insertion sites

To verify the position of the YFP in the gene locus of *Cheerio* and *Fimbrin*, cDNA was generated from adult flies of the cher[CPTI001399] and Fim[CPTI100066] lines using gene-specific and YFP/Venus-specific primers. The insertion and surrounding genomic regions were cloned into a pCR-Blunt II-TOPO vector using the Zero Blunt™ TOPO™ PCR Cloning Kit (Thermo Fisher Scientific) and sequenced. The precise insertion point in the *Fimbrin* locus was determined here for the first time.

5.6.3. Single embryo genotyping PCR

Fly embryos were picked and smashed in squeezing buffer and incubated for 30 min at 37°C. Primer pairs specific for the *bottleneck* and *cheerio* locus were used in a routine PCR to amplify gene-specific fragments.

5.6.4. Fly Strains and Genetics

5.6.4.1. Phenotypic characterization

To visualize myosin-II upon protein knock down of Cheerio, the following line were generated:

$$\mathrm{w[*]};\frac{\mathrm{P[w+,mat.tub>\,Slimb-GFP-nanobody]}}{\mathrm{P[w+,sqhp>sqh::mCherry]}};\frac{\mathrm{cher[w+,CPTI001399]}}{\mathrm{cher[w+,CPTI001399]}}$$

To visualize myosin-II upon protein knock down of Fimbrin, the following line were generated:

$$\frac{\mathrm{w[*],Fim[w+,CPTI100066]}}{\mathrm{w[*],Fim[w+,CPTI100066]}};\frac{\mathrm{P[w+,mat.tub>\,Slimb-GFP-nanobody]}}{\mathrm{P[w+,sqhp>sqh::mCherry]}};+$$

To visualize Cheerio::YFP and the nuclei in a *bnk -/-* embryo:

$$w[*];\frac{P[w+,His2Av-mRFP]}{+};\frac{cher[w+,CPTI001399]}{Df(3R)Exel6218}$$

To visualize myosin-II upon protein knock down of Cheerio in combination with *bnk -/-*, cher[w+, CPTI001399] and Df(3R)Exel6218 were recombined to generate the following lines:

$$w[*];\frac{P[w+,mat.tub>Slimb-nanobody]}{P[w+,sqhp>sqh::mCherry]};\frac{cher[w+,CPTI001399],Df(3R)Exel6218}{cher[w+,CPTI001399]}$$

To visualize myosin-II upon protein knock down of Fimbrin in combination with the *bnk* deficiency the following lines were generated:

$$\frac{w[*],Fim[w+,CPTI100066]}{w[*],Fim[w+,CPTI100066]};\frac{P[w+,mat.tub>Slimb-nanobody]}{P[w+,sqhp>sqh::mCherry]};\frac{Df(3R)Exel6218}{TM3,P[twi>GAL4],P[UAS>EGFP],Sb,Ser}$$

5.6.4.2. Optogenetic experiments

All fly stocks used for optogenetics experiments were kept at 22°C. Crosses were set up and maintained in the dark to generate flies of the following genotype.

To visualize myosin-II upon activation of the optogenetic module:

$$w[*];\frac{P[w+,UASp>CIBN::pmGFP]}{P[w+,Sqh::mCherry]};\frac{P[w+,UASp>RhoGEF2-CRY2]}{P[w+,Osk>Gal4::VP16]}$$

To visualize RhoGEF2-CRY2 local recruitment:

$$w[*];\frac{P[w+,UASp>CIBN::pmGFP]}{+};\frac{P[w+,UASp>RhoGEF2-CRY2::mCh]}{P[w+,Osk>Gal4::VP16]}$$

To visualize the plasma membrane upon photo-activation of the optogenetic module:

$$\frac{\text{P[w+,sqhp>Gap43::mCherry]}}{\text{w[*]}};\frac{\text{P[w+,UASp>CIBN::pmGFP]}}{+};\frac{\text{P[w+,UASp>RhoGEF2-CRY2]}}{\text{P[w+,Osk>Gal4::VP16]}}$$

Optogenetic basal-specific anchors that resulted in RhoGEF2-CRY2 plasma membrane recruitment but did not show functionality (increased contractility):

$$\text{w[*]};\frac{\text{P[w+,UASp> CIBN::GFP::Bnk]}}{+};\frac{\text{P[w+,UASp>RhoGEF2-CRY2::mCh]}}{\text{P[w+,Osk>Gal4::VP16]}}$$

$$\text{w[*]};\frac{\text{P[w+,UASp> CIBN-Bnk::GFP]}}{+};\frac{\text{P[w+,UASp>RhoGEF2-CRY2::mCh]}}{\text{P[w+,Osk>Gal4::VP16]}}$$

$$\text{w[*]};\frac{\text{P[w+,UASp> GFP::CIBN-Slam]}}{+};\frac{\text{P[w+,UASp>RhoGEF2-CRY2::mCh]}}{\text{P[w+,Osk>Gal4::VP16]}}$$

$$\text{w[*]};\frac{\text{P[w+,UASp> PatJPDZ-CIBN]}}{+};\frac{\text{P[w+,UASp>RhoGEF2-CRY2::mCh]}}{\text{P[w+,Osk>Gal4::VP16]}}$$

$$\text{w[*]};\frac{\text{P[w+,UASp> PatJ-CIBN]}}{+};\frac{\text{P[w+,UASp>RhoGEF2-CRY2::mCh]}}{\text{P[w+,Osk>Gal4::VP16]}}$$

Optogenetic basal-specific anchor that both resulted in RhoGEF2-CRY2 plasma membrane recruitment and increased contractility:

$$\text{w[*]};\frac{\text{P[w+,UASp> PatJ-CIBN::GFP-pm]}}{+};\frac{\text{P[w+,UASp>RhoGEF2-CRY2::mCh]}}{\text{P[w+,Osk>Gal4::VP16]}}$$

To visualize myosin-II upon basal-specific recruitment of RhoGEF2-CRY2:

$$\frac{\text{P[w+,sqhp>Sqh::mCherry]}}{\text{w[*]}};\frac{\text{P[w+,UASp> PatJ-CIBN::GFP-pm]}}{\text{CyO}};\frac{\text{P[w+,UASp>RhoGEF2-CRY2]}}{\text{P[w+,mat.tubulin>Gal4::VP16]}}$$

To visualize the plasma membrane upon basal-specific recruitment of RhoGEF2-CRY2:

$$\frac{\text{P[w+,sqhp>Gap43::mCherry]}}{\text{w[*]}};\frac{\text{P[w+,UASp> PatJ-CIBN::GFP-pm]}}{+};\frac{\text{P[w+,UASp>RhoGEF2-CRY2]}}{\text{P[w+,mat.tubulin>Gal4::VP16]}}$$

5.6.5. Fly Stocks

Transgenic lines generated as part of this work were generated by microinjection and standard procedures. All fly stocks were kept at 22°C or 18°C.

Table 1l Fly stocks. The genotype of the used fly stocks is indicated with the first three chromosomes separated by semicolons. The first chromosome typically has a mutation in the *white* gene (w[*]) resulting in white eyes color, that is restored by transgenic insertion containing a mini-*white* gene (w+). The + symbol indicates a wild type chromosome. The > symbol indicates that a specific promoter (to the left of the symbol) is driving a transgene (to the right of the symbol). Fly lines that were marked by an asterisk in front of the genotype were produced in the course of this study.

	Fly stock	Description
	w[*];+; cher[w+, CPTI001399]	Endogenously YFP-tagged Cheerio generated by Cambridge Protein Trap Insertion (CPTI) project (Kyoto DGGR stock number 115514)
	w[*], fim[w+, CPTI100066]	Endogenously YFP-tagged Cheerio generated by Cambridge Protein Trap Insertion (CPTI) project (Kyoto DGGR stock number 115092)
	w[*]; Df(3R)Exel6218/TM6B,Tb	Deficiency deleting the *Bottleneck* gene (Bloomington stock number 7696)
	w[*]; P[w+, His2Av::mRFP]	mRFP1 tagged Histone 2A version A. (Bloomington stock number 23651.)
*	w[*]; P[w+, mat.tub> Slimb-GFP-nanobody]; MKRS/TM6,Tb	Maternal tubulin promoter-driven anti-GFP nanobody fused to the *Drosophila* F-Box protein Slimb
	w[*];; MKRS/TM3, P[w+, twi>GAL4]2.3, P[w+, UAS-2xEGFP]AH2.3, Sb, Ser	TM3 balancer chromosome combined with transcript expressing Gal4 transcription factor under the control of the *twist* promoter and Gal4-UAS-driven EGFP to mark ventral mesodermal cells after VF. (obtained from: Bloomington stock number 51328)
	w[*]; If/CyO; P[w+, UASp>RhoGEF2-CRY2::mCherry]/TM3, Ser	Gal4-UAS-driven DHPH domain of *Drosophila* RhoGEF2 fused to the photosensitive PHR domain of CRY2 and the fluorescent protein mCherry

	Fly stock	Description
	w[*]; If/CyO; P[w+, UASp>RhoGEF2-CRY2]/TM3, Ser	Gal4-UAS-driven *Drosophila* RhoGEF2 DHPH domain fused to CRY2 PHR domain
	w[*]; P[w+, UASp>CIBN::pmGFP]/Cyo; Sb/TM3, Ser	Gal4-UAS-driven CIB1 N-terminal domain (CIBN) fused to EGFP and CAAX box
	P[w+, sqhp>Gap43::mCherry]/Fm7;; Sb/TM6 Tb	Spaghetti-squash promoter-driven Gap43 membrane marker fused to mCherry
	yw[*];If/CyO;P[w+, Sqh::GFP]	Myosin regulatory light chain (Spaghetti-squash) tagged with the fluorescent protein GFP
	yw[*]; P[w+, sqhp>sqh::mCherry]/CyO; Dr/TM3, Ser, Sb].	Myosin regulatory light chain (Spaghetti-squash) tagged with the fluorescent protein mCherry
	w[*]; If/CyO; P[w+, Oskp>Gal4::VP16]/TM3, Ser	Oskar promoter-driven and maternally deposited Gal4 transcription factor (Bloomington stock number 44242)
*	w[*]; PatJ-CIBN::GFP-pm/CyO;MKRS/TM6,Tb	Gal4-UAS-driven *Drosophila* PatJ (full-length) fused to CIB1 N-terminal domain (CIBN), EGFP and a CAAX box membrane anchor
*	w[*]; PatJ-CIBN/CyO;MKRS/TM6,Tb	Gal4-UAS-driven *Drosophila* PatJ (full-length) fused to CIB1 N-terminal domain (CIBN)
*	w[*]; $PatJ_{PDZ}$-CIBN::GFP/CyO;MKRS/TM6,Tb	Gal4-UAS-driven first two PDZ domains of *Drosophila* PatJ ($PatJ_{1-244}$) fused to CIBN and EGFP
*	w[*]; GFP::CIBN-Slam/CyO;MKRS/TM6,Tb	Gal4-UAS-driven full-length *Drosophila* Slam (Slow as molasses) N-terminally fused to the fluorescent protein EGFP and CIBN
*	w[*]; CIBN::GFP::Bnk/CyO;MKRS/TM6,Tb	Gal4-UAS-driven full-length *Drosophila* Bnk (Bottleneck) N-terminally fused to CIBN and EGFP
*	w[*]; CIBN-Bnk::GFP/CyO;MKRS/TM6,Tb	Gal4-UAS-driven full-length *Drosophila* Bnk (Bottleneck) flanked CIBN and EGFP
	w[*]; P[w+, mat.tubulin>Gal4::VP16]; P[w+, mat.tubulin>Gal4::VP16]	Maternal tubulin promoter-driven and maternally deposited Gal4 transcription factor (Bloomington stock number 7062-7063).

5.7. Materials

Table 2| Kits and reagents. Kits and reagents were purchased from the suppliers indicated below.

Material	Supplier
Phusion Flash High-Fidelity PCR Master Mix	Thermo Scientific
QIAprep Spin Miniprep Kit	Qiagen
Plasmid Midi Kit	Qiagen
QIAquick PCR Purification Kit	Qiagen
QIAquick Gel Extraction Kit	Qiagen
RNeasy Mini Kit	Qiagen
ProtoScript First Strand cDNA Synthesis Kit	New England Biolabs
TOPO TA Cloning Kit	Thermo Fisher Scientific
pENTR/D-TOPO Cloning Kit	Thermo Fisher Scientific
Zero Blunt™ TOPO™ PCR Cloning Kit	Thermo Fisher Scientific
One Shot™ TOP10 Chemically Competent *E. coli*	Thermo Fisher Scientific
Actin Binding Protein Biochem Kit – Non-Muscle Actin (Cat. # BK013)	Cytoskeleton
NuPAGE 4-12% Bis-Tris Gel SDS PAGE	Invitrogen/Thermo Fisher Scientific
NuPAGE™ MOPS SDS Running Buffer (20X)	Invitrogen/Thermo Fisher Scientific
Precision Plus Protein Dual Color Standards	Bio-Rad Laboratories
LB (NuPAGE LDS Sample Buffer, 4X)	Invitrogen/Thermo Fisher Scientific[1]
HisPur Ni-NTA Resin	Thermo Fisher Scientific
Amylose Resin	New England Biolabs
Protease inhibitor cocktail	Sigma

Table 3| Chemicals.

Chemical	Supplier

Chemical	Supplier
Ampicillin	Gerbu (Gaiberg, Germany)
Chloramphinicol	US Biological (Swampscott, USA)
Kanamycin	Gerbu (Gaiberg, Germany)
DAPI (4′,6-diamidino-2-phenylindole)	Thermo Scientific
Phalloidin-atto647N	Sigma-Aldrich
IPTG (Isopropyl-β-D-thiogalactopyranosid)	Carl Roth

Table 4l Antibodies. Antibodies used in immunofluorescence (IF) or western blot (WB). Please note, if not indicated differently, the specified dilution accounts for application in immunofluorescence.

Antibody	Specie	Dilution	Supplier
anti-GFP	mouse	1:1000	Torrey Pines
anti-Bnk	rat	1:200 (IF)	
		1:200 (WB)	
anti-mouse IgG-alexa fluor 488	goat	1:1000	Thermo Scientific
anti-rat IgG-alexa fluor 647	goat	1:1000	Thermo Scientific

Table 5l Standard buffer and solutions. Recipe of buffers and solutions used in cell and molecular biology techniques.

Buffer	Ingredient	Concentration
Coomassie staining solution	Coomassie brilliant blue R250	0.5% (m/v)
	Methanol	45% (v/v)
	Acetic acid	10% (v/v)
LB (Luria-Bertani) medium	Tryptone	10 g/l
	Yeast extract	5 g/l
	NaCl	10 g/l
TB medium (Terrific Broth)	Tryptone	20 g/l
	Yeast extract	24 g/l
	Phosphate buffer	0.017 M KH_2PO_4, 0.072 M K_2HPO_4
TBL medium	TB medium	1x
	Lactose	20% (v/v)
PBS (Phosphate-buffered saline)	Na_2HPO_4/KH_2PO_4	12 mM
	NaCl	137 mM
	KCl	3 mM
PBST	PBS	1X
	Triton-X100	0.1% (v/v)
PBT	PBS	1X

Buffer	Ingredient	Concentration
	BSA	1% (m/v)
	Triton-X100	0.05% (v/v)
Blocking solution	PBS	1X
	BSA	6% (m/v)
	Triton-X100	0.05% (v/v)
TAE (Tris/acetate/EDTA), 50X	Tris-acetate pH 8.0	2 M
	EDTA	50 mM
Transfer buffer	Tris base	20 mM
	Glycine	192 mM
	Methanol	20% (v/v)
Isothermal reaction buffer (5X)	Tris-HCl, pH 7.5	500 mM
	PEG-8000	25% (v/v)
	$MgCl_2$	50 mM
	DTT	50 mM
	NAD	5 mM
Gibson assembly master mix	Isothermal reaction buffer	1X
	T5 exonuclease (New England Biolabs)	10 U/μl
	Phusion DNA polymerase (New England Biolabs)	2 U/μl
	Taq Ligase (Epicentre)	40 U/μl

Buffer	Ingredient	Concentration
Squeezing buffer	Tris-HCl, pH 7.5	10 mM
	NaCl	25 mM
	EDTA	1 mM
	Proteinase K (Thermo Fisher Scientific)	200 μg/ml

Table 6l Buffers used for protein purification.

Buffer	Ingredient	Concentration
Standard lysis buffer (SLB)	Tris-HCl, pH 7.5	20 mM
	NaCl	50-500 mM
	NP40	0.1% (v/v)
	$MgCl_2$	2 mM
	Glycerol	10% (v/v)
	DNaseI	10 μg/ml
	β-Mercaptoethanol	2 mM
	Standard lysis buffer was supplemented protease inhibitor cock-tail, DNaseI and β-Mercaptoethanol directly before use	
(His-)Standard lysis buffer (His-SLB)	SLB	1X, 350 mM NaCl
	Imidazole	20 mM
Wash buffer (WB)	Tris-HCl, pH 7.5	20 mM
	NaCl	350 mM
	Glycerol	10 % (v/v)
	β-Mercaptoethanol	2 mM

Buffer	Ingredient	Concentration
(His-)Wash buffer (His-WB)	WB	1X
	Imidazole	20 mM
Elution buffer (EB)	Tris-HCl, pH 7.5	20 mM
	NaCl	350 mM
	Glycerol	10 % (v/v)
	β-Mercaptoethanol	2 mM
(His-)Elution buffer (His-EB)	EB	1X
	Imidazole	200 mM
(MBP-)Elution buffer (MBP-EB)	EB	1X
	Maltose	50 mM
Bottleneck buffer	Tris-HCl, pH 7.5	20 mM
	NaCl	50 mM
	Glycerol	10 % (v/v)
	β-Mercaptoethanol	2 mM

6. Literature

Acloque, H., Adams, M.S., Fishwick, K., Bronner-Fraser, M., and Nieto, M.A. (2009). Epithelial-mesenchymal transitions: the importance of changing cell state in development and disease. J Clin Invest *119*, 1438–1449.

Aelst, L.V., and Symons, M. (2002). Role of Rho family GTPases in epithelial morphogenesis. Genes Dev. *16*, 1032–1054.

Agarwal, P., and Zaidel-Bar, R. (2018). Principles of Actomyosin Regulation *In vivi*. Trends in Cell Biology.

Amadio, A.H., and Kenny, A.J.P. (2018). Aristotle - Philosophy of mind.

Amemiya, S., Akasaka, K., and Terayama, H. (1982). Scanning electron microscopy of gastrulation in a sea urchin (Anthocidaris crassispina). Development *67*, 27–35.

Banerjee, D.S., Munjal, A., Lecuit, T., and Rao, M. (2017). Actomyosin pulsation and flows in an active elastomer with turnover and network remodeling. Nature Communications *8*, 1121.

Barrett, K., Leptin, M., and Settleman, J. (1997). The Rho GTPase and a putative RhoGEF mediate a signaling pathway for the cell shape changes in *Drosophila* gastrulation. Cell *91*, 905–915.

Baskin, Meekes, Liang, and Sharp (1999). Regulation of growth anisotropy in well-watered and water-stressed maize roots. II. Role Of cortical microtubules and cellulose microfibrils. Plant Physiol. *119*, 681–692.

Belmonte, J.M., Leptin, M., and Nedelec, F. (2017). A theory that predicts behaviors of disordered cytoskeletal networks. Mol Syst Biol *13*, 941.

Bement, W.M., Miller, A.L., and von Dassow, G. (2006). Rho GTPase activity zones and transient contractile arrays. Bioessays *28*, 983–993.

Bishop, A.L., and Hall, A. (2000). Rho GTPases and their effector proteins. Biochemical Journal *348*, 241–255.

Blanchoin, L., Boujemaa-Paterski, R., Sykes, C., and Plastino, J. (2014). Actin Dynamics, Architecture, and Mechanics in Cell Motility. Physiological Reviews *94*, 235–263.

Boulter, E., and Garcia-Mata, R. (2010). RhoGDI. Small GTPases *1*, 65–68.

Boyden, E.S., Zhang, F., Bamberg, E., Nagel, G., and Deisseroth, K. (2005). Millisecond-timescale, genetically targeted optical control of neural activity. Nat Neurosci *8*, 1263–1268.

Buckley, C.E., Moore, R.E., Reade, A., Goldberg, A.R., Weiner, O.D., and Clarke, J.D.W. (2016). Reversible Optogenetic Control of Subcellular Protein Localization in a Live Vertebrate Embryo. Dev Cell *36*, 117–126.

Butler, L.C., Blanchard, G.B., Kabla, A.J., Lawrence, N.J., Welchman, D.P., Mahadevan, L., Adams, R.J., and Sanson, B. (2009). Cell shape changes indicate a role for extrinsic tensile forces in *Drosophila* germ-band extension. Nat. Cell Biol. *11*, 859–864.

Campanale, J.P., Sun, T.Y., and Montell, D.J. (2017). Development and dynamics of cell polarity at a glance. J Cell Sci *130*, 1201–1207.

Chanet, S., Miller, C.J., Vaishnav, E.D., Ermentrout, B., Davidson, L.A., and Martin, A.C. (2017). Actomyosin meshwork mechanosensing enables tissue shape to orient cell force. Nature Communications *8*, 15014.

Chen, Q., and Pollard, T.D. (2011). Actin filament severing by cofilin is more important for assembly than constriction of the cytokinetic contractile ring. J Cell Biol *195*, 485–498.

Chen, Q., Courtemanche, N., and Pollard, T.D. (2015). Aip1 Promotes Actin Filament Severing by Cofilin and Regulates Constriction of the Cytokinetic Contractile Ring. J Biol Chem *290*, 2289–2300.

Chung, M.-I., Nascone-Yoder, N.M., Grover, S.A., Drysdale, T.A., and Wallingford, J.B. (2010). Direct activation of Shroom3 transcription by Pitx proteins drives epithelial morphogenesis in the developing gut. Development *137*, 1339–1349.

Cleaver, O., and Krieg, P.A. (1998). VEGF mediates angioblast migration during development of the dorsal aorta in Xenopus. Development *125*, 3905–3914.

Colas, J.F., and Schoenwolf, G.C. (2001). Towards a cellular and molecular understanding of neurulation. Dev. Dyn. *221*, 117–145.

Collinet, C., Rauzi, M., Lenne, P.-F., and Lecuit, T. (2015). Local and tissue-scale forces drive oriented junction growth during tissue extension. Nat. Cell Biol. *17*, 1247–1258.

Collins, J.E., and Fleming, T.P. (1995). Epithelial differentiation in the mouse preimplantation embryo: making adhesive cell contacts for the first time. Trends Biochem. Sci. *20*, 307–312.

Literature

Conti, M.A., and Adelstein, R.S. (2008). Nonmuscle myosin II moves in new directions. Journal of Cell Science *121*, 11–18.

Costa, M., Wilson, E.T., and Wieschaus, E. (1994). A putative cell signal encoded by the folded gastrulation gene coordinates cell shape changes during *Drosophila* gastrulation. Cell *76*, 1075–1089.

Crawford, J.M., Harden, N., Leung, T., Lim, L., and Kiehart, D.P. (1998). Cellularization in*Drosophila* melanogasterIs Disrupted by the Inhibition of Rho Activity and the Activation of Cdc42 Function. Developmental Biology *204*, 151–164.

Cunningham, D., Xiao, Q., Chatterjee, A., Sulik, K., Juriloff, D., Elder, F., Harrison, W., Schuster, G., Overbeek, P.A., and Herman, G.E. (2002). exma: an X-linked insertional mutation that disrupts forebrain and eye development. Mamm. Genome *13*, 179–185.

Davies, J. (2013). Mechanisms of Morphogenesis (Academic Press).

Davies, J.A. (2008). Synthetic morphology: prospects for engineered, self-constructing anatomies. Journal of Anatomy *212*, 707–719.

Dawes-Hoang, R.E., Parmar, K.M., Christiansen, A.E., Phelps, C.B., Brand, A.H., and Wieschaus, E.F. (2005). folded gastrulation, cell shape change and the control of myosin localization. Development *132*, 4165–4178.

De Renzis, S., Yu, J., Zinzen, R., and Wieschaus, E. (2006). Dorsal-ventral pattern of Delta trafficking is established by a snail-tom-neuralized pathway. Developmental Cell *10*, 257–264.

De Renzis, S., Elemento, O., Tavazoie, S., and Wieschaus, E.F. (2007). Unmasking Activation of the Zygotic Genome Using Chromosomal Deletions in the *Drosophila* Embryo. PLOS Biology *5*, e117.

De Sousa, P.A., Valdimarsson, G., Nicholson, B.J., and Kidder, G.M. (1993). Connexin trafficking and the control of gap junction assembly in mouse preimplantation embryos. Development *117*, 1355–1367.

Detrait, E.R., George, T.M., Etchevers, H.C., Gilbert, J.R., Vekemans, M., and Speer, M.C. (2005). Human neural tube defects: developmental biology, epidemiology, and genetics. Neurotoxicol Teratol *27*, 515–524.

Ding, W.Y., Ong, H.T., Hara, Y., Wongsantichon, J., Toyama, Y., Robinson, R.C., Nedelec, F., and Zaidel-Bar, R. (2017). Plastin increases cortical connectivity to facilitate robust polarization and timely cytokinesis. J Cell Biol *216*, 1371–1386.

Dor-On, E., Raviv, S., Cohen, Y., Adir, O., Padmanabhan, K., and Luxenburg, C. (2017). T-plastin is essential for basement membrane assembly and epidermal morphogenesis. Sci Signal *10*.

Doubrovinski, K., Tchoufag, J., and Mandadapu, K. (2018). A simplified mechanism for anisotropic constriction in *Drosophila* mesoderm. Development *145*, dev167387.

Drechsel, D.N., Hyman, A.A., Hall, A., and Glotzer, M. (1997). A requirement for Rho and Cdc42 during cytokinesis in Xenopus embryos. Curr. Biol. *7*, 12–23.

Ehrlicher, A.J., Nakamura, F., Hartwig, J.H., Weitz, D.A., and Stossel, T.P. (2011). Mechanical strain in actin networks regulates FilGAP and integrin binding to filamin A. Nature *478*, 260–263.

Ennomani, H., Letort, G., Guérin, C., Martiel, J.-L., Cao, W., Nédélec, F., De La Cruz, E.M., Théry, M., and Blanchoin, L. (2016). Architecture and Connectivity Govern Actin Network Contractility. Current Biology *26*, 616–626.

Esue, O., Harris, E.S., Higgs, H.N., and Wirtz, D. (2008). The Filamentous Actin Cross-Linking/Bundling Activity of Mammalian Formins. Journal of Molecular Biology *384*, 324–334.

Esue, O., Tseng, Y., and Wirtz, D. (2009). α-Actinin and Filamin Cooperatively Enhance the Stiffness of Actin Filament Networks. PLOS ONE *4*, e4411.

Etienne-Manneville, S. (2013). Microtubules in Cell Migration. Annual Review of Cell and Developmental Biology *29*, 471–499.

Etienne-Manneville, S., and Hall, A. (2002). Rho GTPases in cell biology. Nature *420*, 629–635.

Fabrowski, P., Necakov, A.S., Mumbauer, S., Loeser, E., Reversi, A., Streichan, S., Briggs, J.A., and De Renzis, S. (2013). Tubular endocytosis drives remodelling of the apical surface during epithelial morphogenesis in *Drosophila*. Nature Communications *4*, 2244.

Falzone, T.T., Lenz, M., Kovar, D.R., and Gardel, M.L. (2012). Assembly kinetics determine the architecture of α-actinin crosslinked F-actin networks. Nature Communications *3*, 861.

Feng, Y., and Walsh, C. a (2004). The many faces of filamin: a versatile molecular scaffold for cell motility and signalling. Nature Cell Biology *6*, 1034–1038.

Figard, L., Wang, M., Zheng, L., Golding, I., and Sokac, A.M. (2016). Membrane supply and demand regulates F-actin in a cell surface reservoir. Dev Cell *37*, 267–278.

Fletcher, D.A., and Mullins, R.D. (2010). Cell mechanics and the cytoskeleton. Nature *463*, 485–492.

Literature

van der Flier, A., and Sonnenberg, A. (2001). Structural and functional aspects of filamins. Biochimica et Biophysica Acta (BBA) - Molecular Cell Research *1538*, 99–117.

Fox, D.T., and Peifer, M. (2007). Abelson kinase (Abl) and RhoGEF2 regulate actin organization during cell constriction in *Drosophila*. Development *134*, 567–578.

Gardel, M.L., Shin, J.H., MacKintosh, F.C., Mahadevan, L., Matsudaira, P., and Weitz, D.A. (2004). Elastic behavior of cross-linked and bundled actin networks. Science (New York, N.Y.) *304*, 1301–1305.

Gasteiger, E., Gattiker, A., Hoogland, C., Ivanyi, I., Appel, R.D., and Bairoch, A. (2003). ExPASy: The proteomics server for in-depth protein knowledge and analysis. Nucleic Acids Res. *31*, 3784–3788.

Gay, O., and Baudier, J. (2011). RefilinsA link between perinuclear actin bundle dynamics and mechanosensing signaling. 245–249.

Gay, O., Nakamura, F., and Baudier, J. (2011a). Refilin holds the cap. Commun Integr Biol *4*, 791–795.

Gay, O., Gilquin, B., Nakamura, F., Jenkins, Z. a, McCartney, R., Krakow, D., Deshiere, A., Assard, N., Hartwig, J.H., Robertson, S.P., *et al*. (2011b). RefilinB (FAM101B) targets FilaminA to organize perinuclear actin networks and regulates nuclear shape. Proceedings of the National Academy of Sciences of the United States of America *108*, 11464–11469.

Gelbart, M.A., He, B., Martin, A.C., Thiberge, S.Y., Wieschaus, E.F., and Kaschube, M. (2012). Volume conservation principle involved in cell lengthening and nucleus movement during tissue morphogenesis. Proc Natl Acad Sci U S A *109*, 19298–19303.

Ghashghaei, H.T., Lai, C., and Anton, E.S. (2007). Neuronal migration in the adult brain: are we there yet? Nature Reviews Neuroscience *8*, 141–151.

Gibson, D.G., Young, L., Chuang, R.Y., Venter, J.C., Hutchison, C.A., 3rd, and Smith, H.O. (2009). Enzymatic assembly of DNA molecules up to several hundred kilobases. Nat Methods *6*, 343–345.

Gilmour, D., Rembold, M., and Leptin, M. (2017). From morphogen to morphogenesis and back. Nature *541*, 311–320.

Gimona, M., Djinovic-Carugo, K., Kranewitter, W.J., and Winder, S.J. (2002). Functional plasticity of CH domains. FEBS Letters *513*, 98–106.

Gittes, F., Mickey, B., Nettleton, J., and Howard, J. (1993). Flexural rigidity of microtubules and actin filaments measured from thermal fluctuations in shape. The Journal of Cell Biology *120*, 923–934.

Goley, E.D., and Welch, M.D. (2006). The ARP2/3 complex: an actin nucleator comes of age. Nature Reviews Molecular Cell Biology *7*, 713–726.

Gómez-Gálvez, P., Vicente-Munuera, P., Tagua, A., Forja, C., Castro, A.M., Letrán, M., Valencia-Expósito, A., Grima, C., Bermúdez-Gallardo, M., Serrano-Pérez-Higueras, Ó., *et al*. (2018). Scutoids are a geometrical solution to three-dimensional packing of epithelia. Nature Communications *9*, 2960.

Gong, L., Puri, M., Ünlü, M., Young, M., Robertson, K., Viswanathan, S., Krishnaswamy, A., Dowd, S.R., and Minden, J.S. (2004). *Drosophila* ventral furrow morphogenesis: a proteomic analysis. Development *131*, 643–656.

Goodwin, K., Ellis, S.J., Lostchuck, E., Zulueta-Coarasa, T., Fernandez-Gonzalez, R., and Tanentzapf, G. (2016). Basal Cell-Extracellular Matrix Adhesion Regulates Force Transmission during Tissue Morphogenesis. Dev. Cell *39*, 611–625.

Grosshans, J., and Wieschaus, E. (2000). A genetic link between morphogenesis and cell division during formation of the ventral furrow in *Drosophila*. Cell *101*, 523–531.

Grosshans, J., Muller, H.A., and Wieschaus, E. (2003). Control of cleavage cycles in *Drosophila* embryos by fruhstart. Dev Cell *5*, 285–294.

Grusch, M., Schelch, K., Riedler, R., Reichhart, E., Differ, C., Berger, W., Inglés-Prieto, Á., and Janovjak, H. (2014). Spatio-temporally precise activation of engineered receptor tyrosine kinases by light. EMBO J *33*, 1713–1726.

Guglielmi, G., Barry, J.D., Huber, W., and De Renzis, S. (2015). An Optogenetic Method to Modulate Cell Contractility during Tissue Morphogenesis. Dev Cell *35*, 646–660.

Guglielmi, G., Falk, H.J., and De Renzis, S. (2016). Optogenetic Control of Protein Function: From Intracellular Processes to Tissue Morphogenesis. Trends in Cell Biology *26*, 864–874.

Guntas, G., Hallett, R.A., Zimmerman, S.P., Williams, T., Yumerefendi, H., Bear, J.E., and Kuhlman, B. (2015). Engineering an improved light-induced dimer (iLID) for controlling the localization and activity of signaling proteins. Proc Natl Acad Sci U S A *112*, 112–117.

Hacker, U., and Perrimon, N. (1998). DRhoGEF2 encodes a member of the Dbl family of oncogenes and controls cell shape changes during gastrulation in *Drosophila*. Genes Dev *12*, 274–284.

Literature

Haigo, S.L., and Bilder, D. (2011). Global Tissue Revolutions in a Morphogenetic Movement Controlling Elongation. Science *331*, 1071–1074.

Hartman, M.A., and Spudich, J.A. (2012). The myosin superfamily at a glance. J Cell Sci *125*, 1627–1632.

Hartsock, A., and Nelson, W.J. (2008). Adherens and Tight Junctions: Structure, Function and Connections to the Actin Cytoskeleton. Biochim Biophys Acta *1778*, 660–669.

Hasley, A., Chavez, S., Danilchik, M., Wühr, M., and Pelegri, F. (2017). Vertebrate Embryonic Cleavage Pattern Determination. Adv. Exp. Med. Biol. *953*, 117–171.

He, B., Doubrovinski, K., Polyakov, O., and Wieschaus, E. (2014). Apical constriction drives tissue-scale hydrodynamic flow to mediate cell elongation. Nature *508*, 392–396.

He, L., Wang, X., Tang, H.L., and Montell, D.J. (2010). Tissue elongation requires oscillating contractions of a basal actomyosin network. Nature Cell Biology *12*, 1133–1142.

Heisenberg, C.P., and Bellaiche, Y. (2013). Forces in tissue morphogenesis and patterning. Cell *153*, 948–962.

Hildebrand, J.D. (2005). Shroom regulates epithelial cell shape via the apical positioning of an actomyosin network. J. Cell. Sci. *118*, 5191–5203.

Huelsmann, S., Ylänne, J., and Brown, N.H. (2013). Filopodia-like Actin Cables Position Nuclei in Association with Perinuclear Actin in *Drosophila* Nurse Cells. Developmental Cell *26*, 604–615.

Hunter, C., and Wieschaus, E. (2000). Regulated expression of nullo is required for the formation of distinct apical and basal adherens junctions in the *Drosophila* blastoderm. J Cell Biol *150*, 391–401.

Hunter, C., Sung, P., Schejter, E.D., and Wieschaus, E. (2002). Conserved domains of the Nullo protein required for cell-surface localization and formation of adherens junctions. Mol Biol Cell *13*, 146–157.

Hyman, A.A., and Karsenti, E. (1996). Morphogenetic Properties of Microtubules and Mitotic Spindle Assembly. Cell *84*, 401–410.

Ibnsouda, S., Schweisguth, F., de Billy, G., and Vincent, A. (1993). Relationship between expression of serendipity alpha and cellularisation of the *Drosophila* embryo as revealed by interspecific transformation. Development *119*, 471–483.

Ito, T., Suzuki, A., and Stossel, T.P. (1992). Regulation of water flow by actin-binding protein-induced actin gelatin. Biophys J *61*, 1301–1305.

Izquierdo, E., Quinkler, T., and De Renzis, S. (2018). Guided morphogenesis through optogenetic activation of Rho signalling during early *Drosophila* embryogenesis. Nat Commun *9*, 2366.

Izumi, Y., Motoishi, M., Furuse, K., and Furuse, M. (2016). A tetraspanin regulates septate junction formation in *Drosophila* midgut. J. Cell. Sci. *129*, 1155–1164.

Johnson, M.H. (2009). From mouse egg to mouse embryo: polarities, axes, and tissues. Annu. Rev. Cell Dev. Biol. *25*, 483–512.

Johnson, H.E., Goyal, Y., Pannucci, N.L., Schüpbach, T., Shvartsman, S.Y., and Toettcher, J.E. (2017). The Spatiotemporal Limits of Developmental Erk Signaling. Developmental Cell *40*, 185–192.

Karunarathne, W.K.A., O'Neill, P.R., and Gautam, N. (2015). Subcellular optogenetics – controlling signaling and single-cell behavior. J Cell Sci *128*, 15–25.

Kasza, K.E., Broedersz, C.P., Koenderink, G.H., Lin, Y.C., Messner, W., Millman, E.A., Nakamura, F., Stossel, T.P., MacKintosh, F.C., and Weitz, D.A. (2010). Actin Filament Length Tunes Elasticity of Flexibly Cross-Linked Actin Networks. Biophys J *99*, 1091–1100.

Kawano, F., Suzuki, H., Furuya, A., and Sato, M. (2015). Engineered pairs of distinct photoswitches for optogenetic control of cellular proteins. Nature Communications *6*, 6256.

Keller, R.E. (1978). Time-lapse cinemicrographic analysis of superficial cell behavior during and prior to gastrulation in Xenopus laevis. Journal of Morphology *157*, 223–247.

Kennedy, M.J., Hughes, R.M., Peteya, L.A., Schwartz, J.W., Ehlers, M.D., and Tucker, C.L. (2010). Rapid blue-light-mediated induction of protein interactions in living cells. Nature Methods *7*, 973–975.

Kerridge, S., Munjal, A., Philippe, J.-M., Jha, A., de las Bayonas, A.G., Saurin, A.J., and Lecuit, T. (2016). Modular activation of Rho1 by GPCR signalling imparts polarized myosin II activation during morphogenesis. Nat. Cell Biol. *18*, 261–270.

Khaliullin, R.N., Green, R.A., Shi, L.Z., Gomez-Cavazos, J.S., Berns, M.W., Desai, A., and Oegema, K. (2018). A positive-feedback-based mechanism for constriction rate acceleration during cytokinesis in Caenorhabditis elegans. ELife *7*, e36073.

Literature

Klein, M.G., Shi, W., Ramagopal, U., Tseng, Y., Wirtz, D., Kovar, D.R., Staiger, C.J., and Almo, S.C. (2004). Structure of the Actin Crosslinking Core of Fimbrin. Structure *12*, 999–1013.

Kolsch, V., Seher, T., Fernandez-Ballester, G.J., Serrano, L., and Leptin, M. (2007). Control of *Drosophila* gastrulation by apical localization of adherens junctions and RhoGEF2. Science *315*, 384–386.

Kono, K., Tamashiro, D.A.A., and Alarcon, V.B. (2014). Inhibition of RHO–ROCK signaling enhances ICM and suppresses TE characteristics through activation of Hippo signaling in the mouse blastocyst. Developmental Biology *394*, 142–155.

Krueger, D., Tardivo, P., Nguyen, C., and De Renzis, S. (2018). Downregulation of basal myosin-II is required for cell shape changes and tissue invagination. EMBO J *37*.

Kuroda, R., Endo, B., Abe, M., and Shimizu, M. (2009). Chiral blastomere arrangement dictates zygotic left–right asymmetry pathway in snails. Nature *462*, 790–794.

Lane, M.C., Koehl, M.A., Wilt, F., and Keller, R. (1993). A role for regulated secretion of apical extracellular matrix during epithelial invagination in the sea urchin. Development *117*, 1049–1060.

Laporte, D., Ojkic, N., Vavylonis, D., and Wu, J.-Q. (2012). α-Actinin and fimbrin cooperate with myosin II to organize actomyosin bundles during contractile-ring assembly. Mol. Biol. Cell *23*, 3094–3110.

Le Lièvre, C.S., and Le Douarin, N.M. (1975). Mesenchymal derivatives of the neural crest: analysis of chimaeric quail and chick embryos. J Embryol Exp Morphol *34*, 125–154.

Lecuit, T., and Wieschaus, E. (2000). Polarized insertion of new membrane from a cytoplasmic reservoir during cleavage of the *Drosophila* embryo. J Cell Biol *150*, 849–860.

Lecuit, T., Samanta, R., and Wieschaus, E. (2002). slam encodes a developmental regulator of polarized membrane growth during cleavage of the Drosphila embryo. Developmental Cell *2*, 425–436.

Lee, J.-Y., and Harland, R.M. (2007). Actomyosin contractility and microtubules drive apical constriction in Xenopus bottle cells. Dev. Biol. *311*, 40–52.

Lennox, J. (2017). Aristotle's Biology. In The Stanford Encyclopedia of Philosophy, E.N. Zalta, ed. (Metaphysics Research Lab, Stanford University), p.

Leptin, M. (1991). twist and snail as positive and negative regulators during *Drosophila* mesoderm development. Genes Dev *5*, 1568–1576.

Leptin, M., and Grunewald, B. (1990). Cell shape changes during gastrulation in *Drosophila*. Development *110*, 73–84.

Letunic, I., and Bork, P. (2018). 20 years of the SMART protein domain annotation resource. Nucleic Acids Research *46*, D493–D496.

Leung, C.Y., Zhu, M., and Zernicka-Goetz, M. (2016). Chapter Six - Polarity in Cell-Fate Acquisition in the Early Mouse Embryo. In Current Topics in Developmental Biology, M.L. DePamphilis, ed. (Academic Press), pp. 203–234.

Levayer, R., and Lecuit, T. (2012). Biomechanical regulation of contractility: spatial control and dynamics. Trends Cell Biol. *22*, 61–81.

Levskaya, A., Weiner, O.D., Lim, W.A., and Voigt, C.A. (2009). Spatiotemporal control of cell signalling using a light-switchable protein interaction. Nature *461*, 997–1001.

Li, M.G., Serr, M., Edwards, K., Ludmann, S., Yamamoto, D., Tilney, L.G., Field, C.M., and Hays, T.S. (1999). Filamin is required for ring canal assembly and actin organization during *Drosophila* oogenesis. J Cell Biol *146*, 1061–1074.

Lieleg, O., Claessens, M.M. a. E., and Bausch, A.R. (2010). Structure and dynamics of cross-linked actin networks. Soft Matter *6*, 218.

Linde-Medina, M., and Marcucio, R. (2018). Living tissues are more than cell clusters: The extracellular matrix as a driving force in morphogenesis. Progress in Biophysics and Molecular Biology *137*, 46–51.

Lomakin, A.J., Lee, K.C., Han, S.J., Bui, D.A., Davidson, M., Mogilner, A., and Danuser, G. (2015). Competition for actin between two distinct F-actin networks defines a bistable switch for cell polarization. Nat Cell Biol *17*, 1435–1445.

Mabuchi, I., Hamaguchi, Y., Fujimoto, H., Morii, N., Mishima, M., and Narumiya, S. (1993). A rho-like protein is involved in the organisation of the contractile ring in dividing sand dollar eggs. Zygote *1*, 325–331.

Maienschein, J. (1991). The Origins of Entwicklungsmechanik. In A Conceptual History of Modern Embryology, S.F. Gilbert, ed. (Boston, MA: Springer US), pp. 43–61.

Manning, A.J., Peters, K.A., Peifer, M., and Rogers, S.L. (2013). Regulation of epithelial morphogenesis by the G protein-coupled receptor mist and its ligand fog. Sci Signal *6*, ra98.

Literature

Margolis, B., and Borg, J.-P. (2005). Apicobasal polarity complexes. Journal of Cell Science *118*, 5157–5159.

Marston, D.J., and Goldstein, B. (2006). Symmetry Breaking in C. elegans: Another Gift from the Sperm. Dev Cell *11*, 273–274.

Martin, A.C., and Goldstein, B. (2014). Apical constriction: themes and variations on a cellular mechanism driving morphogenesis. Development (Cambridge, England) *141*, 1987–1998.

Martin, A.C., Kaschube, M., and Wieschaus, E.F. (2009). Pulsed contractions of an actin-myosin network drive apical constriction. Nature *457*, 495–499.

Martin, A.C., Gelbart, M., Fernandez-Gonzalez, R., Kaschube, M., and Wieschaus, E.F. (2010). Integration of contractile forces during tissue invagination. The Journal of Cell Biology *188*, 735–749.

Mason, F.M., Tworoger, M., and Martin, A.C. (2013). Apical domain polarization localizes actin-myosin activity to drive ratchet-like apical constriction. Nature Cell Biology *15*, 926–936.

Mathew, S.J., Rembold, M., and Leptin, M. (2011). Role for Traf4 in polarizing adherens junctions as a prerequisite for efficient cell shape changes. Mol. Cell. Biol. *31*, 4978–4993.

Mavrakis, M., Rikhy, R., and Lippincott-Schwartz, J. (2009). Plasma membrane polarity and compartmentalization are established before cellularization in the fly embryo. Dev Cell *16*, 93–104.

Mavrakis, M., Azou-Gros, Y., Tsai, F.-C., Alvarado, J., Bertin, A., Iv, F., Kress, A., Brasselet, S., Koenderink, G.H., and Lecuit, T. (2014). Septins promote F-actin ring formation by crosslinking actin filaments into curved bundles. Nature Cell Biology *16*, 322–334.

Mazumdar, A., and Mazumdar, M. (2002). How one becomes many: Blastoderm cellularization in *Drosophila* melanogaster. Bioessays *24*, 1012–1022.

Miller, G. (2006). Optogenetics. Shining new light on neural circuits. Science *314*, 1674–1676.

Morin, X., and Bellaïche, Y. (2011). Mitotic Spindle Orientation in Asymmetric and Symmetric Cell Divisions during Animal Development. Developmental Cell *21*, 102–119.

Morize, P., Christiansen, A.E., Costa, M., Parks, S., and Wieschaus, E. (1998). Hyperactivation of the folded gastrulation pathway induces specific cell shape changes. Development *125*, 589–597.

Morriss-Kay, G., and Tuckett, F. (1985). The role of microfilaments in cranial neurulation in rat embryos: effects of short-term exposure to cytochalasin D. J Embryol Exp Morphol *88*, 333–348.

Mulder, M. (2000). MEMBRANE PREPARATION I Phase Inversion Membranes. In Encyclopedia of Separation Science, I.D. Wilson, ed. (Oxford: Academic Press), pp. 3331–3346.

Müller, H.A., and Wieschaus, E. (1996). armadillo, bazooka, and stardust are critical for early stages in formation of the zonula adherens and maintenance of the polarized blastoderm epithelium in *Drosophila*. J. Cell Biol. *134*, 149–163.

Nakamura, F., Heikkinen, O., Pentikäinen, O.T., Osborn, T.M., Kasza, K.E., Weitz, D.A., Kupiainen, O., Permi, P., Kilpeläinen, I., Ylänne, J., *et al*. (2009). Molecular Basis of Filamin A-FilGAP Interaction and Its Impairment in Congenital Disorders Associated with Filamin A Mutations. PLOS ONE *4*, e4928.

Nakamura, F., Stossel, T.P., and Hartwig, J.H. (2011). The filamins: organizers of cell structure and function. Cell Adh Migr *5*, 160–169.

Nature Cell Biology (2018). An update on organoid research. Nature Cell Biology *20*, 633–633.

Nicolás-Pérez, M., Kuchling, F., Letelier, J., Polvillo, R., Wittbrodt, J., and Martínez-Morales, J.R. (2016). Analysis of cellular behavior and cytoskeletal dynamics reveal a constriction mechanism driving optic cup morphogenesis. ELife *5*, e15797.

Niopek, D., Benzinger, D., Roensch, J., Draebing, T., Wehler, P., Eils, R., and Di Ventura, B. (2014). Engineering light-inducible nuclear localization signals for precise spatiotemporal control of protein dynamics in living cells. Nature Communications *5*, 4404.

Niopek, D., Wehler, P., Roensch, J., Eils, R., and Di Ventura, B. (2016). Optogenetic control of nuclear protein export. Nature Communications *7*, 10624.

Nishimura, T., and Takeichi, M. (2008). Shroom3-mediated recruitment of Rho kinases to the apical cell junctions regulates epithelial and neuroepithelial planar remodeling. Development *135*, 1493–1502.

Noden, D.M. (1983). The role of the neural crest in patterning of avian cranial skeletal, connective, and muscle tissues. Developmental Biology *96*, 144–165.

Nüsslein-Volhard, C., and Wieschaus, E. (1980). Mutations affecting segment number and polarity in *Drosophila*. Nature *287*, 795–801.

Literature

Nüsslein-Volhard, C., Wieschaus, E., and Kluding, H. (1984). Mutations affecting the pattern of the larval cuticle in-*Drosophila* melanogaster. Wilhelm Roux' Archiv *193*, 267–282.

Oakes, P.W., Wagner, E., Brand, C.A., Probst, D., Linke, M., Schwarz, U.S., Glotzer, M., and Gardel, M.L. (2017). Optogenetic control of RhoA reveals zyxin-mediated elasticity of stress fibres. Nat Commun *8*, 15817.

Ohashi, K., Fujiwara, S., and Mizuno, K. (2017). Roles of the cytoskeleton, cell adhesion and rho signalling in mechanosensing and mechanotransduction. J Biochem *161*, 245–254.

Ohi, M., Li, Y., Cheng, Y., and Walz, T. (2004). Negative Staining and Image Classification - Powerful Tools in Modern Electron Microscopy. Biol Proced Online *6*, 23–34.

Ohta, Y., Suzuki, N., Nakamura, S., Hartwig, J.H., and Stossel, T.P. (1999). The small GTPase RalA targets filamin to induce filopodia. Proc. Natl. Acad. Sci. U.S.A. *96*, 2122–2128.

Oppenheimer, J.M. (1991). Curt Herbst's Contributions to the Concept of Embryonic Induction. In A Conceptual History of Modern Embryology, S.F. Gilbert, ed. (Boston, MA: Springer US), pp. 63–89.

Padash Barmchi, M. (2005). DRhoGEF2 regulates actin organization and contractility in the *Drosophila* blastoderm embryo. The Journal of Cell Biology *168*, 575–585.

Panousopoulou, E., Hobbs, C., Mason, I., Green, J.B.A., and Formstone, C.J. (2016). Epiboly generates the epidermal basal monolayer and spreads the nascent mammalian skin to enclose the embryonic body. J Cell Sci *129*, 1915–1927.

Perrimon, N., Pitsouli, C., and Shilo, B.-Z. (2012). Signaling Mechanisms Controlling Cell Fate and Embryonic Patterning. Cold Spring Harb Perspect Biol *4*.

Pinheiro, D., and Bellaïche, Y. (2018). Mechanical Force-Driven Adherens Junction Remodeling and Epithelial Dynamics. Developmental Cell *47*, 3–19.

Pollard, T.D. (2010). Mechanics of cytokinesis in eukaryotes. Current Opinion in Cell Biology *22*, 50–56.

Polyakov, O., He, B., Swan, M., Shaevitz, J., Kaschube, M., and Wieschaus, E. (2014). Passive Mechanical Forces Control Cell-Shape Change during *Drosophila* Ventral Furrow Formation. Biophysical Journal *107*, 998–1010.

Postner, M.A., and Wieschaus, E.F. (1994). The nullo protein is a component of the actin-myosin network that mediates cellularization in *Drosophila* melanogaster embryos. J Cell Sci *107 (Pt 7)*, 1863–1873.

Pudasaini, A., El-Arab, K.K., and Zoltowski, B.D. (2015). LOV-based optogenetic devices: light-driven modules to impart photoregulated control of cellular signaling. Front Mol Biosci *2*, 18.

Pujol, T., du Roure, O., Fermigier, M., and Heuvingh, J. (2012). Impact of branching on the elasticity of actin networks. Proc Natl Acad Sci U S A *109*, 10364–10369.

Qin, X., Park, B.O., Liu, J., Chen, B., Choesmel-Cadamuro, V., Belguise, K., Heo, W.D., and Wang, X. (2017). Cell-matrix adhesion and cell-cell adhesion differentially control basal myosin oscillation and *Drosophila* egg chamber elongation. Nature Communications *8*, 14708.

Rauzi, M., Lenne, P.F., and Lecuit, T. (2010). Planar polarized actomyosin contractile flows control epithelial junction remodelling. Nature *468*, 1110–1114.

Reversi, A., Loeser, E., Subramanian, D., Schultz, C., and De Renzis, S. (2014). Plasma membrane phosphoinositide balance regulates cell shape during *Drosophila* embryo morphogenesis. J Cell Biol *205*, 395–408.

Reymann, A.C., Boujemaa-Paterski, R., Martiel, J.L., Guerin, C., Cao, W., Chin, H.F., De La Cruz, E.M., Thery, M., and Blanchoin, L. (2012). Actin network architecture can determine myosin motor activity. Science *336*, 1310–1314.

Roh, M.H., Makarova, O., Liu, C.-J., Shin, Lee, S., Laurinec, S., Goyal, M., Wiggins, R., and Margolis, B. (2002). The Maguk protein, Pals1, functions as an adapter, linking mammalian homologues of Crumbs and Discs Lost. J Cell Biol *157*, 161–172.

Roh-Johnson, M., Shemer, G., Higgins, C.D., McClellan, J.H., Werts, A.D., Tulu, U.S., Gao, L., Betzig, E., Kiehart, D.P., and Goldstein, B. (2012). Triggering a Cell Shape Change by Exploiting Pre-Existing Actomyosin Contractions. Science *335*, 1232–1235.

Rose, L.S., and Wieschaus, E. (1992). The *Drosophila* cellularization gene nullo produces a blastoderm-specific transcript whose levels respond to the nucleocytoplasmic ratio. Genes Dev *6*, 1255–1268.

Rousso, T., Schejter, E.D., and Shilo, B.-Z. (2016). Orchestrated content release from *Drosophila* glue-protein vesicles by a contractile actomyosin network. Nature Cell Biology *18*, 181–190.

Sawyer, J.K., Harris, N.J., Slep, K.C., Gaul, U., and Peifer, M. (2009). The *Drosophila* afadin homologue Canoe regulates linkage of the actin cytoskeleton to adherens junctions during apical constriction. The Journal of Cell Biology *186*, 57–73.

Literature

Sawyer, J.M., Harrell, J.R., Shemer, G., Sullivan-Brown, J., Roh-Johnson, M., and Goldstein, B. (2010). Apical constriction: A cell shape change that can drive morphogenesis. Developmental Biology *341*, 5–19.

Schejter, E.D., and Wieschaus, E. (1993). bottleneck acts as a regulator of the microfilament network governing cellularization of the *Drosophila* embryo. Cell *75*, 373–385.

Schmoller, K.M., Lieleg, O., and Bausch, A.R. (2009). Structural and Viscoelastic Properties of Actin/Filamin Networks: Cross-Linked versus Bundled Networks. Biophys J *97*, 83–89.

Schwayer, C., Sikora, M., Slováková, J., Kardos, R., and Heisenberg, C.-P. (2016). Actin Rings of Power. Dev. Cell *37*, 493–506.

Schweisguth, F., Lepesant, J.A., and Vincent, A. (1990). The serendipity alpha gene encodes a membrane-associated protein required for the cellularization of the *Drosophila* embryo. Genes & Development *4*, 922–931.

Shekhar, S., Zhu, L., Mazutis, L., Sgro, A.E., Fai, T.G., and Podolski, M. (2014). Quantitative biology: where modern biology meets physical sciences. Mol Biol Cell *25*, 3482–3485.

Sherrard, K., Robin, F., Lemaire, P., and Munro, E. (2010). Sequential activation of apical and basolateral contractility drives ascidian endoderm invagination. Current Biology : CB *20*, 1499–1510.

Siegrist, S.E., and Doe, C.Q. (2007). Microtubule-induced cortical cell polarity. Genes Dev. *21*, 483–496.

Simões, S., Denholm, B., Azevedo, D., Sotillos, S., Martin, P., Skaer, H., Hombría, J.C.-G., and Jacinto, A. (2006). Compartmentalisation of Rho regulators directs cell invagination during tissue morphogenesis. Development *133*, 4257–4267.

Simpson, P. (1983). Maternal-Zygotic Gene Interactions During Formation of the Dorsoventral Pattern in *Drosophila* Embryos. Genetics *105*, 615–632.

Sisson, J.C., Field, C., Ventura, R., Royou, A., and Sullivan, W. (2000). Lava lamp, a novel peripheral golgi protein, is required for *Drosophila* melanogaster cellularization. J Cell Biol *151*, 905–918.

Skau, C.T., Courson, D.S., Bestul, A.J., Winkelman, J.D., Rock, R.S., Sirotkin, V., and Kovar, D.R. (2011). Actin filament bundling by fimbrin is important for endocytosis, cytokinesis, and polarization in fission yeast. J. Biol. Chem. *286*, 26964–26977.

Sokac, A.M., and Wieschaus, E. (2008). Zygotically controlled F-actin establishes cortical compartments to stabilize furrows during *Drosophila* cellularization. Journal of Cell Science *121*, 1815–1824.

Sokol, N.S., and Cooley, L. (1999). *Drosophila* filamin encoded by the cheerio locus is a component of ovarian ring canals. Current Biology : CB *9*, 1221–1230.

Solon, J., Kaya-Copur, A., Colombelli, J., and Brunner, D. (2009). Pulsed forces timed by a ratchet-like mechanism drive directed tissue movement during dorsal closure. Cell *137*, 1331–1342.

Sonavane, P.R., Wang, C., Dzamba, B., Weber, G.F., Periasamy, A., and DeSimone, D.W. (2017). Mechanical and signaling roles for keratin intermediate filaments in the assembly and morphogenesis of Xenopus mesendoderm tissue at gastrulation. Development *144*, 4363–4376.

Sonnen, K.F., Lauschke, V.M., Uraji, J., Falk, H.J., Petersen, Y., Funk, M.C., Beaupeux, M., François, P., Merten, C.A., and Aulehla, A. (2018). Modulation of Phase Shift between Wnt and Notch Signaling Oscillations Controls Mesoderm Segmentation. Cell *172*, 1079-1090.e12.

Stossel, T.P., Condeelis, J., Cooley, L., Hartwig, J.H., Noegel, A., Schleicher, M., and Shapiro, S.S. (2001). Filamins as integrators of cell mechanics and signalling. Nat. Rev. Mol. Cell Biol. *2*, 138–145.

Stutchbury, B., Atherton, P., Tsang, R., Wang, D.-Y., and Ballestrem, C. (2017). Distinct focal adhesion protein modules control different aspects of mechanotransduction. J Cell Sci *130*, 1612–1624.

Subramani, K., and Ahmed, W. (2012). Chapter 13 - Self-Assembly of Proteins and Peptides and Their Applications in Bionanotechnology and Dentistry. In Emerging Nanotechnologies in Dentistry, K. Subramani, and W. Ahmed, eds. (Boston: William Andrew Publishing), pp. 209–224.

Sung, H., Spangenberg, S., Vogt, N., and Großhans, J. (2013). Number of Nuclear Divisions in the *Drosophila* Blastoderm Controlled by Onset of Zygotic Transcription. Current Biology *23*, 133–138.

Sweeton, D., Parks, S., Costa, M., and Wieschaus, E. (1991). Gastrulation in *Drosophila*: the formation of the ventral furrow and posterior midgut invaginations. Development *112*, 775–789.

Tan, P.Y., and Zaidel-Bar, R. (2015). Transient Membrane Localization of SPV-1 Drives Cyclical Actomyosin Contractions in the C. elegans Spermatheca. Current Biology *25*, 141–151.

Taslimi, A., Vrana, J.D., Chen, D., Borinskaya, S., Mayer, B.J., Kennedy, M.J., and Tucker, C.L. (2014). An optimized optogenetic clustering tool for probing protein interaction and function. Nat Commun *5*, 4925–4925.

Teng, X., Qin, L., Borgne, R.L., and Toyama, Y. (2017). Remodeling of adhesion and modulation of mechanical tensile forces during apoptosis in *Drosophila* epithelium. Development *144*, 95–105.

Literature

Tepass, U. (1997). Epithelial differentiation in *Drosophila*. BioEssays *19*, 673–682.

Theurkauf, W.E. (1994). Actin cytoskeleton. Through the bottleneck. Current Biology : CB *4*, 76–78.

Thomas, G.H., and Williams, J.A. (1999). Dynamic rearrangement of the spectrin membrane skeleton during the generation of epithelial polarity in *Drosophila*. J. Cell. Sci. *112 (Pt 17)*, 2843–2852.

Thomas, J.H., and Wieschaus, E. (2004). src64 and tec29 are required for microfilament contraction during *Drosophila* cellularization. Development (Cambridge, England) *131*, 863–71.

Tischer, D., and Weiner, O.D. (2014). Illuminating cell signalling with optogenetic tools. Nature Reviews Molecular Cell Biology *15*, 551–558.

Toettcher, J.E., Voigt, C.A., Weiner, O.D., and Lim, W.A. (2011). The promise of optogenetics in cell biology: interrogating molecular circuits in space and time. Nature Methods *8*, 35–38.

Tseng, Y., An, K.M., Esue, O., and Wirtz, D. (2004). The bimodal role of filamin in controlling the architecture and mechanics of F-actin networks. The Journal of Biological Chemistry *279*, 1819–26.

Vinot, S., Le, T., Ohno, S., Pawson, T., Maro, B., and Louvet-Vallée, S. (2005). Asymmetric distribution of PAR proteins in the mouse embryo begins at the 8-cell stage during compaction. Developmental Biology *282*, 307–319.

Violette, M.I., Madan, P., and Watson, A.J. (2006). Na+/K+ -ATPase regulates tight junction formation and function during mouse preimplantation development. Dev. Biol. *289*, 406–419.

Welnhofer, E.A., Zhao, L., and Cohan, C.S. (1997). Actin dynamics and organization during growth cone morphogenesis in Helisoma neurons. Cell Motility *37*, 54–71.

Welte, M.A., Gross, S.P., Postner, M., Block, S.M., and Wieschaus, E.F. (1998). Developmental regulation of vesicle transport in *Drosophila* embryos: forces and kinetics. Cell *92*, 547–557.

Wenzl, C., Yan, S., Laupsien, P., and Großhans, J. (2010). Localization of RhoGEF2 during *Drosophila* cellularization is developmentally controlled by slam. Mechanisms of Development *127*, 371–384.

West, J.J., Zulueta-Coarasa, T., Maier, J.A., Lee, D.M., Bruce, A.E.E., Fernandez-Gonzalez, R., and Harris, T.J.C. (2017). An Actomyosin-Arf-GEF Negative Feedback Loop for Tissue Elongation under Stress. Curr. Biol. *27*, 2260-2270.e5.

Wieschaus, E., and Nüsslein-Volhard, C. (2016). The Heidelberg Screen for Pattern Mutants of *Drosophila*: A Personal Account. Annu. Rev. Cell Dev. Biol. *32*, 1–46.

Wirshing, A.C.E., and Cram, E.J. (2017). Myosin activity drives actomyosin bundle formation and organization in contractile cells of the Caenorhabditis elegans spermatheca. Mol. Biol. Cell *28*, 1937–1949.

Wu, Y.I., Frey, D., Lungu, O.I., Jaehrig, A., Schlichting, I., Kuhlman, B., and Hahn, K.M. (2009). A genetically encoded photoactivatable Rac controls the motility of living cells. Nature *461*, 104–108.

Wu, Y.I., Wang, X., He, L., Montell, D., and Hahn, K.M. (2011). Spatiotemporal control of small GTPases with light using the LOV domain. Meth. Enzymol. *497*, 393–407.

Xie, S., and Martin, A.C. (2015). Intracellular signalling and intercellular coupling coordinate heterogeneous contractile events to facilitate tissue folding. Nat Commun *6*, 7161.

Xue, Z., and Sokac, A.M. (2016). -Back-to-back mechanisms drive actomyosin ring closure during *Drosophila* embryo cleavage. J Cell Biol *215*, 335–344.

Yang, Z.R., Thomson, R., McNeil, P., and Esnouf, R.M. (2005). RONN: the bio-basis function neural network technique applied to the detection of natively disordered regions in proteins. Bioinformatics *21*, 3369–3376.

Zemelman, B.V., Lee, G.A., Ng, M., and Miesenböck, G. (2002). Selective photostimulation of genetically chARGed neurons. Neuron *33*, 15–22.

Zerbino, D.R., Achuthan, P., Akanni, W., Amode, M.R., Barrell, D., Bhai, J., Billis, K., Cummins, C., Gall, A., Girón, C.G., *et al*. (2018). Ensembl 2018. Nucleic Acids Research *46*, D754–D761.

Zhang, K., and Cui, B. (2015). Optogenetic control of intracellular signaling pathways. Trends Biotechnol *33*, 92–100.

Zhou, A.X., Hartwig, J.H., and Akyurek, L.M. (2010). Filamins in cell signaling, transcription and organ development. Trends Cell Biol *20*, 113–123.

7. Appendix

7.1. Supplementary Figures

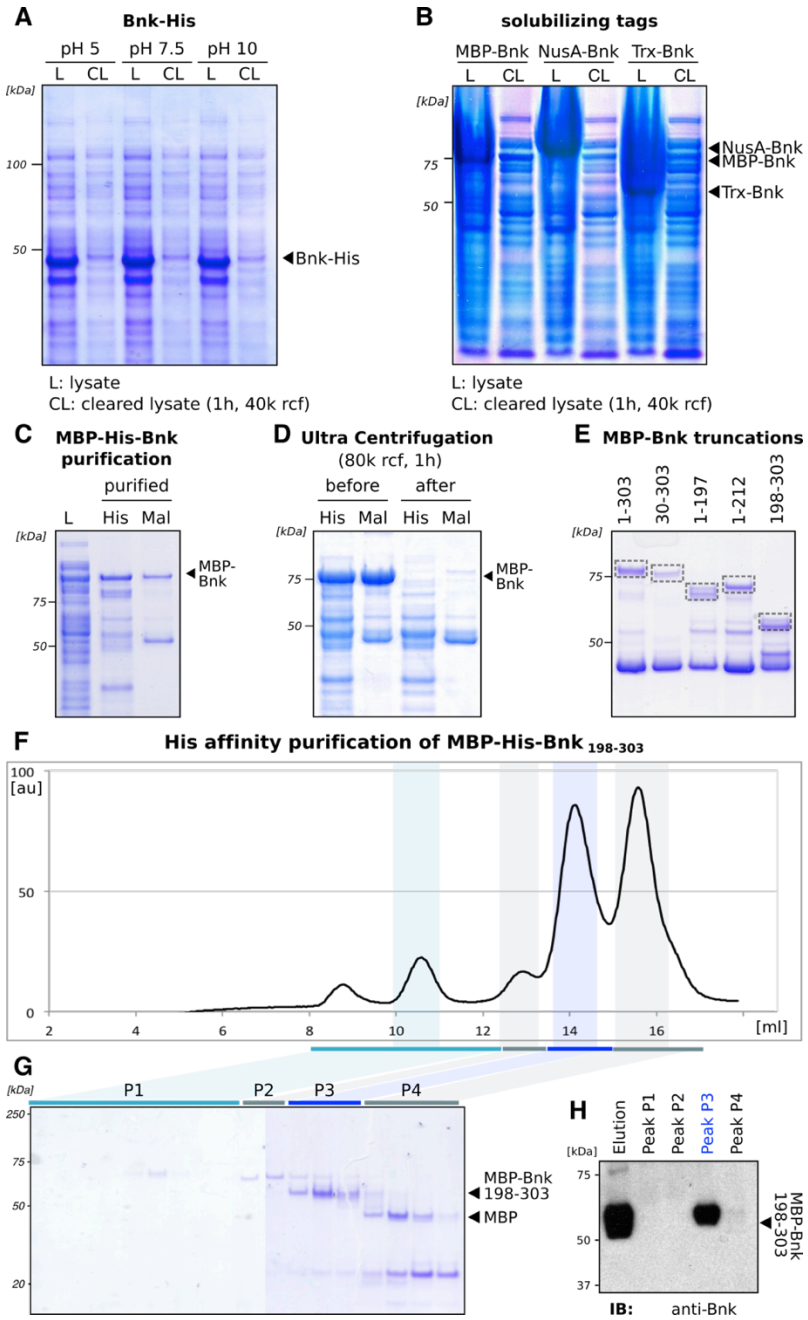

Appendix 1. Steps in purifying recombinant Bottleneck protein. (A) Coomassie stained gel showing the result of a solubility test of His-tagged Bottleneck expressed in *E. coli* lysed in buffer with different pH (5, 7.5, 10).

Appendix

The lysate (L) before and cleared lysate (CL) after 40k rcf centrifugation is shown. Equal volumes were loaded in all lanes Full-length Bottleneck-His is insoluble independent of the pH of the lysis buffer. **(B)** Coomassie stained gel showing the results of a solubility test of bottleneck expressed as maltose binding protein (MBP)-, N-utilization substance (NusA)-, or thioredoxin (Trx)-fusion protein. The lysate (L) before and cleared lysate (CL) after 40k rcf centrifugation is shown. Equal volumes were loaded in all lanes. A fraction of MBP-Bottleneck remained soluble, while the other fusion proteins aggregated upon centrifugation. **(C)** Coomassie gel showing the cleared lysate (L) of an *E. coli* culture expressing MBP-His-Bottleneck. MBP-His-Bottleneck could be purified from bacteria immobilizing either the His- or the MBP-tag. **(D)** Coomassie stained gel showing NiNTA-purified (His) and amylose-purified (MBP) MBP-His-Bottleneck before and after ultracentrifugation (80k rcf). MBP-His-Bottleneck aggregated upon ultracentrifugation. **(E)** Coomassie stained gel showing different truncations of Bottleneck (Bnk_{1-303}, Bnk_{30-303}, Bnk_{1-197}, Bnk_{1-212}, $Bnk_{198-303}$, $Bnk_{198-303}$) expressed and purified as MBP-His fusion proteins. The dashed box indicates the fusion protein of the respective size **(F)** SEC elution profile (Superdex 200 Increase 10/300 G) of MBP-His-$Bnk_{198-303}$ revealed a void peak at ~9 ml, and four other peaks (colored in shades of blue) at ~11 ml (P1), 13 ml (P2), 14 ml (P3) and 15.5 ml (P4), respectively. **(G)** Cooomassie stained gel showing the fractions corresponding to peaks P1-P4 of the SEC elution as indicated by the matching colors in (F). **(H)** Western blot against Bottleneck of the total purified protein elution (Lane 1), peaks P1-p4 of the SEC elution. MBP-His-$Bnk_{198-303}$ eluted as a single peak in the size of a monomer.

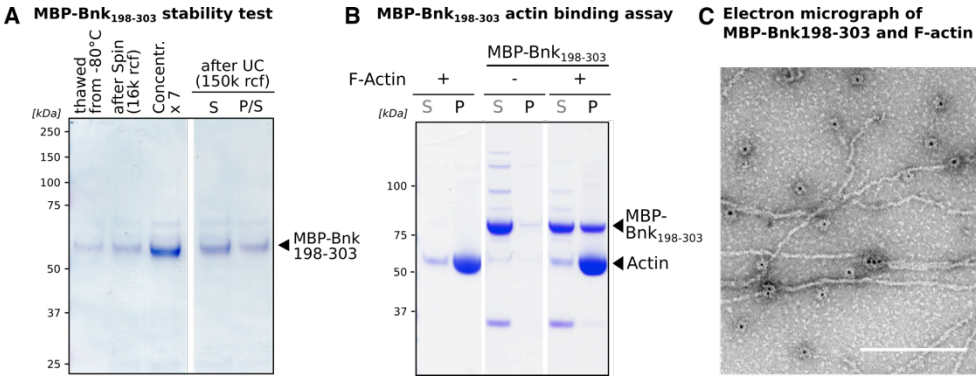

Appendix 2. MBP-His-Bnk198-303 was stable but did not efficiently bind actin fibers. **(A)** Coomassie stained gel showing the protein stability upon freeze-thawing (lane 1), subsequent tabletop centrifugation (lane 2) and 7-fold concentration using an Amicon filter column (lane 3). After ultracentrifugation the majority of MBP-His-$Bnk_{198-303}$ remains in the supernatant (S), while a smaller amount of protein pellets (P/S). **(B)** Coomassie gel showing the result of an actin-binding assay with MBP-His-$Bnk_{198-303}$. In absence of F-actin (-) MBP-His-$Bnk_{198-303}$ remained in the supernatant faction (S), whereas a fraction of the protein shifted to the pellet faction (P) in presence of F-actin (+) upon ultracentrifugation suggesting that actin-binding activity for MBP-His-$Bnk_{198-303}$ **(C)** Electron micrograph of MBP-His-$Bnk_{198-303}$ labeled with nanogold in presence of F-actin. Although some MBP-His-$Bnk_{198-303}$ molecules aligned with actin filaments, the majority of the protein was present in monomers and did not co-localize with actin fibers suggesting low actin-binding activity.

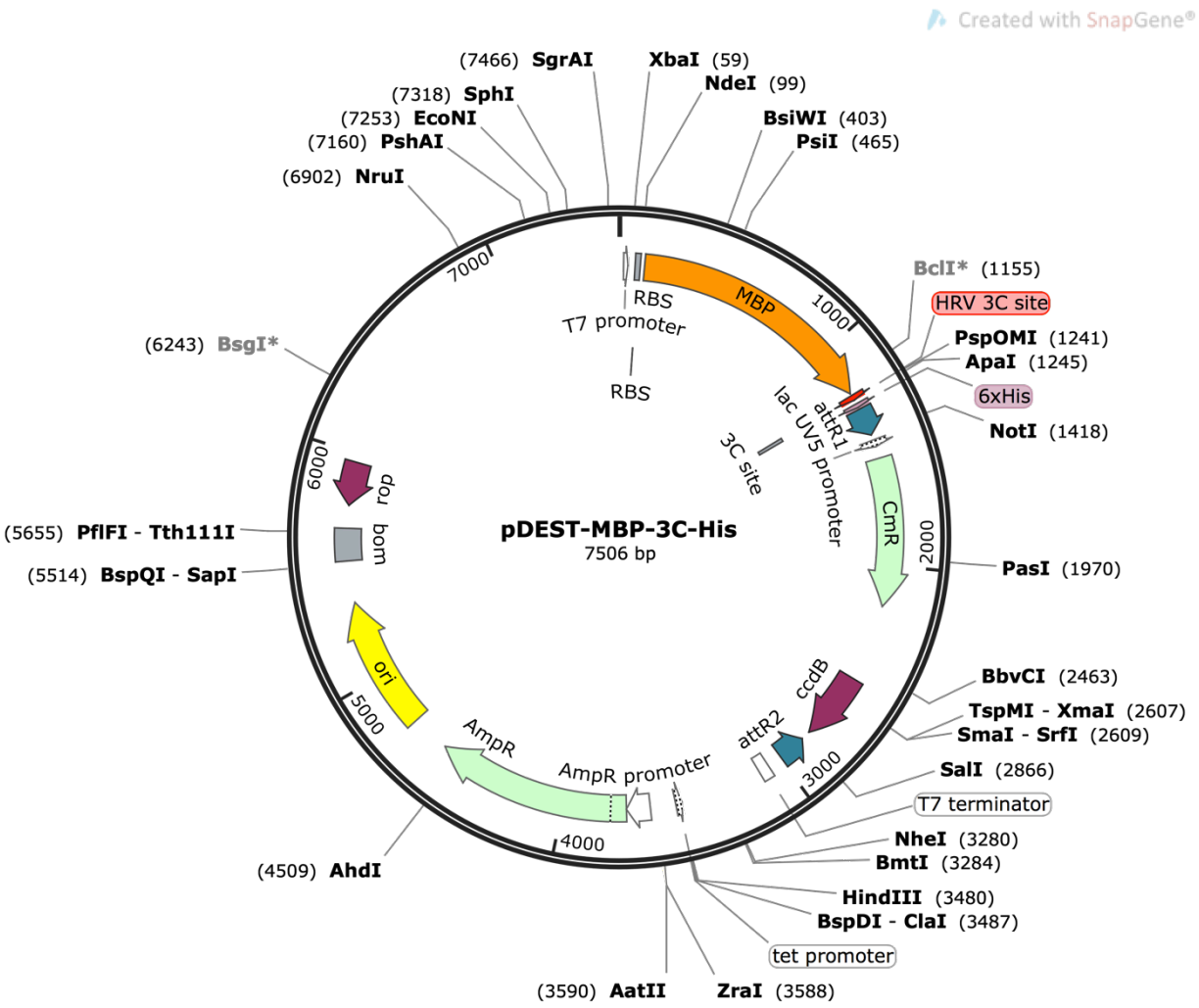

Appendix 3. Plasmid map of the customized vector pDEST-MBP-3C-His. A Gateway destination vector for *E. coli* expression (T7 promoter) of MBP-(6x)His-fusion proteins. A HRV 3C cutting site is located between MBP-and His-tag to cleave of the MBP but keep the His-tag fused to the protein of interest. The chloramphenicol and ccdB death cassette is flanked by attR sites and can be replaced by a gene of interest.

Appendix

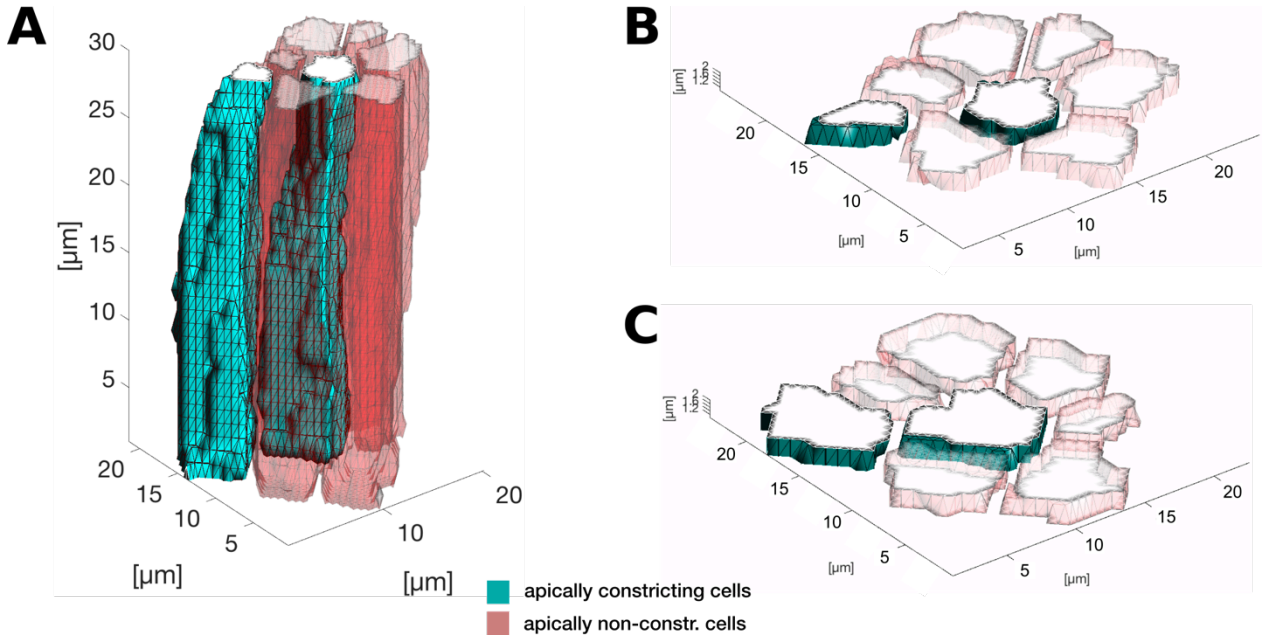

Appendix 4: Cell shapes in the photo-activated area after minutes of photo-activation. (A) Upon photo-activation of the cell base, the majority of cells does not constrict their apical surface and expand the base, while a fraction of cells constrict apically and expand their basal surface. The 3D cell reconstructions show the shape of cells in the photo-activated region 10 min after initial photoactivation. **(B)** A projection of the apical cell surface shows a cell in the center with constricted apical surface (green) and six neighbors that did not constrict. **(C)** A projection of the basal cell surface reveals that the center cell expanded the cell base, while the red-colored cells did not. Note that the same center cell contacts six cells at the apical surface (red), whereas seven cells at the basal surface (red and another green cell).

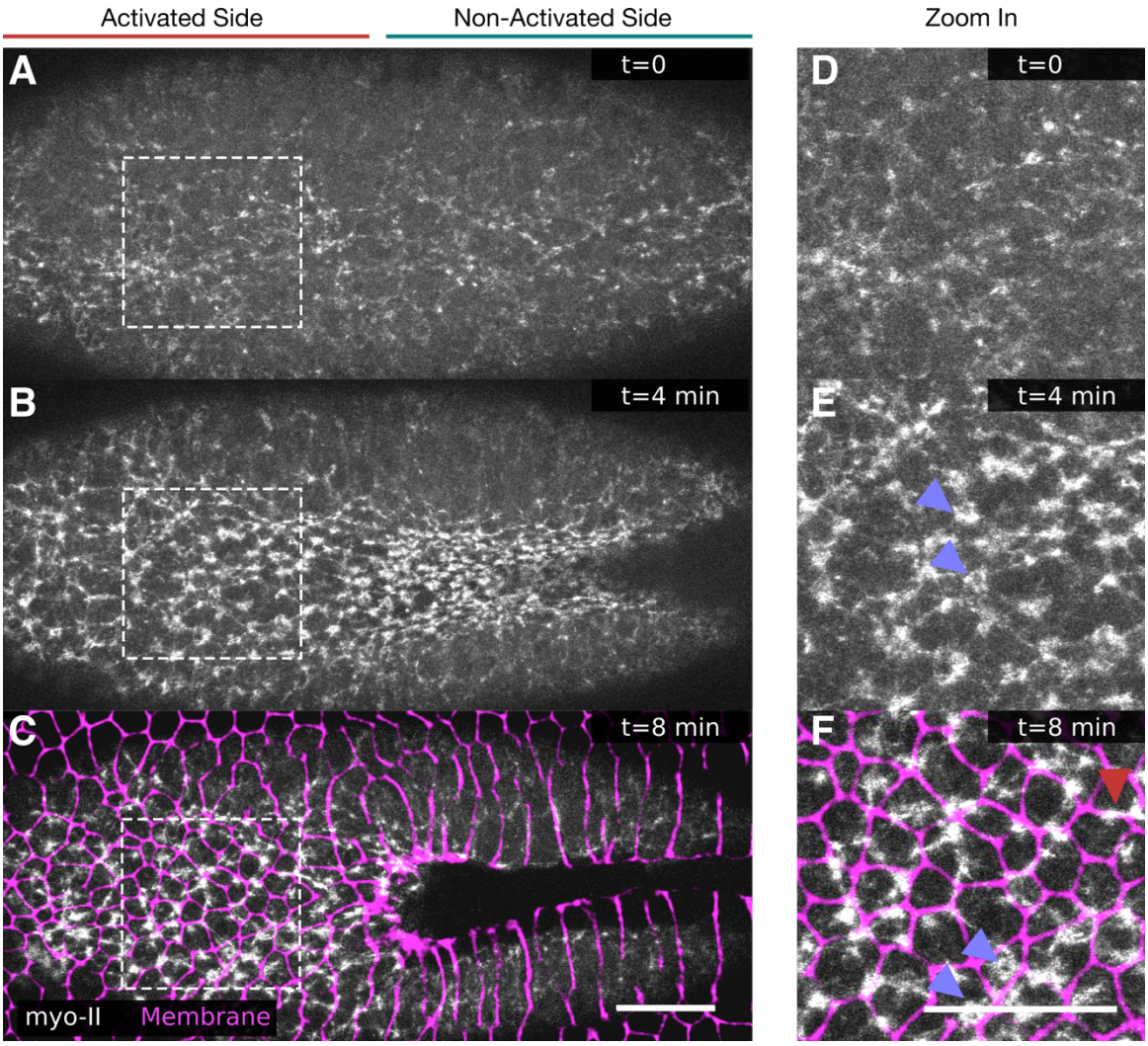

Appendix 5. Apical myosin-II accumulation is not affected upon optogenetic stabilization of basal myosin-II. (A-F) Confocal images of the apical surface of an embryo co-expressing RhoGEF2-CRY2/CIBN::pmGFP, and the myosin-II marker Sqh::mCherry. In an alternating fashion, the base was photo-activated and in the anterior (left) half of the embryo and myosin-II was recorded in a 5 μm-sized image stack at the apical surface in the whole embryo. Top views show apical myosin before photo-activation (A, D), 4 min (B, E) and 8 min (C,F) after initial photo-activation. (A,B,C) White dashed box in the photo-activated region is shown in high magnification in (D,E,F). (D-F) In the activated region myosin-II accumulated in the center of the cells, in stable ring-like structures (blue arrowheads), or to cell junctions (red arrowhead). (C,F) Directly after the final Sqh::mCherry recording the membrane signal (magenta) derived from CIBN::pmGFP was acquired and superimposed on the myosin-II signal (grayscale). Scale bars, 25 μm. Figure and legend adapted from (Krueger *et al.*, 2018).

Appendix

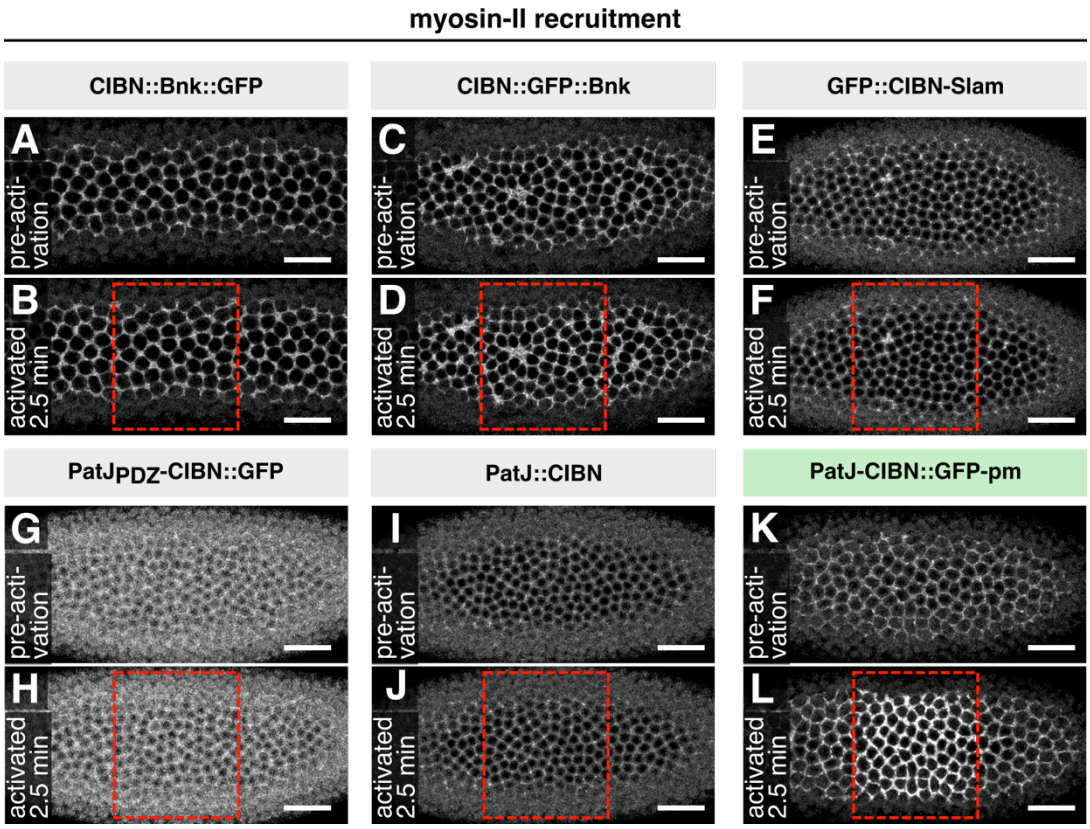

Appendix 6. Among the tested basal-specific optogenetic anchors, only CIBN-PatJ::GFPpm is effective in inducing myosin-II activity. (A–L) Confocal images showing the myosin-II probe Sqh:mCherry co-expressed in embryos together with RhoGEF2-CRY2, and one of the basal-specific anchors (A,B: CIBN::Bnk::GFP; C, D: CIBN::GFP::Bnk; E, F: GFP-CIBN-Slam; G, H: PatJPDZ-CIBN::GFP; I, J: PatJ-CIBN; K, L: PatJ-CIBN::GFP-pm). The embryos were photo-activated using one photon illumination (488 nm) within a region of interest (red dashed box) early during cellularization when the actomyosin network is close to the objective. Top views show the myosin-II signal prior to (A, C, E, G, I and K) and 2.5 min (B, D, F, H, J and L) after photo-activation. Scale bars, 20 µm. Figure and legend adapted from (Krueger *et al.*, 2018).

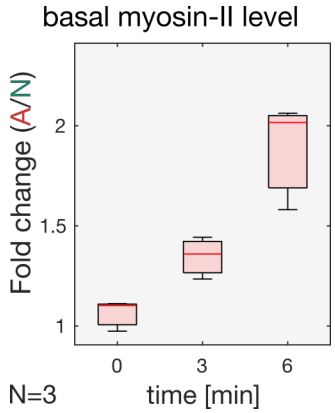

Appendix 7. The CIBN-PatJ::GFPpm anchor co-expressed with RhoGEF2-CRY2 facilitates 2-fold increase of basal myosin-II upon light activation. Quantification of the basal myosin-II levels in the photo-activated region in the ventral tissue of embryos expressing CIBN-PatJ::GFPpm/ RhoGEF2-CRY2 and the myosin-II marker Sqh:mCh. Embryos were photo-activated after the first phase of VF, when cells constricted apically. Photo-activation and myo-II acquisition was done alternatingly. Basal myosin-II was measured within and outside the photo-activated region. FC of the myosin-II in the photo-activated region compared to the non-activated region was plotted. The central mark, bottom and top edges of each box indicate the median, 25th and 75th percentile, respectively. Whiskers extent to the most extreme data point. Figure and legend adapted from (Krueger *et al.*, 2018).

7.2. Usage permissions for figures

This Agreement between Daniel Krüger ("You") and Springer Nature ("Springer Nature") consists of your license details and the terms and conditions provided by Springer Nature and Copyright Clearance Center.

License Number	4491010203481
License date	Dec 16, 2018
Licensed Content Publisher	Springer Nature
Licensed Content Publication	Nature Communications
Licensed Content Title	Assembly kinetics determine the architecture of α-actinin crosslinked F-actin networks
Licensed Content Author	Tobias T. Falzone, Martin Lenz, David R. Kovar, Margaret L. Gardel
Licensed Content Date	May 29, 2012
Licensed Content Volume	3
Type of Use	Thesis/Dissertation
Requestor type	academic/university or research institute
Format	print and electronic
Portion	figures/tables/illustrations
Number of figures/tables /illustrations	2
High-res required	no
Will you be translating?	no
Circulation/distribution	<501
Author of this Springer Nature content	no
Title	Regulation of Actomyosin Contraction during Tissue Morphogenesis: Genes and Mechanics
Institution name	n/a
Expected presentation date	Dec 2018
Portions	Figure 1 and Figure 6
Requestor Location	Daniel Krüger Meyerhofstr 1 Heidelberg, BW 69117 Germany Attn: Daniel Krüger
Billing Type	Invoice
Billing Address	Daniel Krüger Meyerhofstr 1 Heidelberg, Germany 69117 Attn: Daniel Krüger
Total	0.00 EUR

This Agreement between Daniel Krüger ("You") and Elsevier ("Elsevier") consists of your license details and the terms and conditions provided by Elsevier and Copyright Clearance Center.

License Number	4491000191195
License date	Dec 16, 2018
Licensed Content Publisher	Elsevier
Licensed Content Publication	Current Biology
Licensed Content Title	Architecture and Connectivity Govern Actin Network Contractility
Licensed Content Author	Hajer Ennomani,Gaëlle Letort,Christophe Guérin,Jean-Louis Martiel,Wenxiang Cao,François Nédélec,Enrique M. De La Cruz,Manuel Théry,Laurent Blanchoin
Licensed Content Date	Mar 7, 2016
Licensed Content Volume	26
Licensed Content Issue	5
Licensed Content Pages	11
Start Page	616
End Page	626
Type of Use	reuse in a thesis/dissertation
Portion	figures/tables/illustrations
Number of figures/tables /illustrations	1
Format	both print and electronic
Are you the author of this Elsevier article?	No
Will you be translating?	No
Original figure numbers	Figure 1
Title of your thesis/dissertation	Regulation of Actomyosin Contraction during Tissue Morphogenesis: Genes and Mechanics
Expected completion date	Dec 2018
Estimated size (number of pages)	150
Requestor Location	Daniel Krüger Meyerhofstr 1 Heidelberg, BW 69117 Germany Attn: Daniel Krüger
Publisher Tax ID	GB 494 6272 12
Total	0.00 EUR

Development

Order detail ID: 71715771
Order License Id: 4487850778388
ISSN: 1477-9129
Publication Type: e-Journal
Volume:
Issue:
Start page:
Publisher: COMPANY OF BIOLOGISTS,
Author/Editor: Company of Biologists

Permission Status: Granted
Permission type: Republish or display content
Type of use: Republish in a thesis/dissertation

Requestor type	Academic institution
Format	Print, Electronic
Portion	image/photo
Number of images/photos requested	1
The requesting person/organization	Daniel Krueger
Title or numeric reference of the portion(s)	Figure 8 and 9
Title of the article or chapter the portion is from	Scanning electron microscopy of gastrulation in a sea urchin (Anthocidaris crassispina)
Editor of portion(s)	N/A
Author of portion(s)	SHONAN AMEMIY A, KOJI MASAKA AND 2 HIROSHI

Note: This item will be invoiced or charged separately through CCC's **RightsLink** service. More info **$ 0.00**

Development

Order detail ID: 71715761
Order License Id: 4487840615851
ISSN: 1477-9129
Publication Type: e-Journal
Volume:
Issue:
Start page:
Publisher: COMPANY OF BIOLOGISTS,
Author/Editor: Company of Biologists

Permission Status: Granted
Permission type: Republish or display content
Type of use: Republish in a thesis/dissertation

Requestor type	Academic institution
Format	Print, Electronic
Portion	image/photo
Number of images/photos requested	1
The requesting person/organization	Daniel Krueger
Title or numeric reference of the portion(s)	Figure 3
Title of the article or chapter the portion is from	Gastrulation in Drosophila:the formation of the ventral furrow and posterior midgut invaginations
Editor of portion(s)	N/A

Note: This item will be invoiced or charged separately through CCC's **RightsLink** service. More info **$ 0.00**

Appendix

This Agreement between Daniel Krüger ("You") and John Wiley and Sons ("John Wiley and Sons") consists of your license details and the terms and conditions provided by John Wiley and Sons and Copyright Clearance Center.

License Number	4487861474741
License date	Dec 14, 2018
Licensed Content Publisher	John Wiley and Sons
Licensed Content Publication	Developmental Dynamics
Licensed Content Title	Towards a cellular and molecular understanding of neurulation
Licensed Content Author	Jean-François Colas, Gary C. Schoenwolf
Licensed Content Date	May 2, 2001
Licensed Content Volume	221
Licensed Content Issue	2
Licensed Content Pages	29
Type of use	Dissertation/Thesis
Requestor type	University/Academic
Format	Print and electronic
Portion	Figure/table
Number of figures/tables	1
Original Wiley figure/table number(s)	Figure 2
Will you be translating?	No
Title of your thesis / dissertation	Regulation of Actomyosin Contraction during Tissue Morphogenesis: Genes and Mechanics
Expected completion date	Dec 2018
Expected size (number of pages)	150
Requestor Location	Daniel Krüger Meyerhofstr 1 Heidelberg, BW 69117 Germany Attn: Daniel Krüger
Publisher Tax ID	EU826007151
Total	0.00 EUR

This Agreement between Daniel Krüger ("You") and Elsevier ("Elsevier") consists of your license details and the terms and conditions provided by Elsevier and Copyright Clearance Center.

License Number	4490320544051
License date	Dec 15, 2018
Licensed Content Publisher	Elsevier
Licensed Content Publication	Biophysical Journal
Licensed Content Title	Passive Mechanical Forces Control Cell-Shape Change during Drosophila Ventral Furrow Formation
Licensed Content Author	Oleg Polyakov,Bing He,Michael Swan,Joshua W. Shaevitz,Matthias Kaschube,Eric Wieschaus
Licensed Content Date	Aug 19, 2014
Licensed Content Volume	107
Licensed Content Issue	4
Licensed Content Pages	13
Start Page	998
End Page	1010
Type of Use	reuse in a thesis/dissertation
Portion	figures/tables/illustrations
Number of figures/tables /illustrations	2
Format	both print and electronic
Are you the author of this Elsevier article?	No
Will you be translating?	No
Original figure numbers	Figure 1 and Figure 4
Title of your thesis/dissertation	Regulation of Actomyosin Contraction during Tissue Morphogenesis: Genes and Mechanics
Expected completion date	Dec 2018
Estimated size (number of pages)	150
Requestor Location	Daniel Krüger Meyerhofstr 1 Heidelberg, BW 69117 Germany Attn: Daniel Krüger
Publisher Tax ID	GB 494 6272 12
Total	0.00 EUR

Order detail ID: 71723576
ISSN: 1477-9129
Publication Type: e-Journal
Volume:
Issue:
Start page:
Publisher: COMPANY OF BIOLOGISTS,
Author/Editor: Company of Biologists

Permission Status: Granted
Permission type: Republish or display content
Type of use: Republish in a thesis/dissertation
Order License Id: 4491290049372

Hide details

Requestor type	Academic institution
Format	Print, Electronic
Portion	image/photo
Number of images/photos requested	1
The requesting person/organization	Daniel Krueger
Title or numeric reference of the portion(s)	Figure 7
Title of the article or chapter the portion is from	Apical constriction: themes and variations on a cellular mechanism driving morphogenesis
Editor of portion(s)	N/A
Author of portion(s)	Adam C. Martin, Bob Goldstein
Volume of serial or monograph	Development 2014 141
Issue, if republishing an article from a serial	N/A
Page range of portion	1994
Publication date of portion	2014
Rights for	Main product
Duration of use	Life of current edition
Creation of copies for the disabled	no
With minor editing privileges	yes
For distribution to	Worldwide
In the following language(s)	Original language of publication
With incidental promotional use	no
Lifetime unit quantity of new product	Up to 499
Title	Regulation of Actomyosin Contraction during Tissue Morphogenesis: Genes and Mechanics
Institution name	n/a
Expected presentation date	Dec 2018

Order detail ID: 71723580
ISSN: 1540-8140
Publication Type: e-Journal
Volume:
Issue:
Start page:
Publisher: ROCKEFELLER UNIVERSITY PRESS

Permission Status: Granted
Permission type: Republish or display content
Type of use: Thesis/Dissertation
Order License Id: 4491290714768

Hide details

Requestor type	Academic institution
Format	Print, Electronic
Portion	image/photo
Number of images/photos requested	1
The requesting person/organization	Daniel Krueger
Title or numeric reference of the portion(s)	Figure 1
Title of the article or chapter the portion is from	Integration of contractile forces during tissue invagination
Editor of portion(s)	N/A
Author of portion(s)	Adam C. Martin, Michael Gelbart, Rodrigo Fernandez-Gonzalez, Matthias Kaschube, Eric F. Wieschaus
Volume of serial or monograph	jcb 2010 8 March » 188 (5): 735
Issue, if republishing an article from a serial	N/A
Page range of portion	736
Publication date of portion	2010
Rights for	Main product
Duration of use	Life of current edition
Creation of copies for the disabled	no
With minor editing privileges	no
For distribution to	Worldwide
In the following language(s)	Original language of publication
With incidental promotional use	no
Lifetime unit quantity of new product	Up to 499
Title	Regulation of Actomyosin Contraction during Tissue Morphogenesis: Genes and Mechanics
Institution name	n/a
Expected presentation date	Dec 2018

Appendix

This Agreement between Daniel Krüger ("You") and Elsevier ("Elsevier") consists of your license details and the terms and conditions provided by Elsevier and Copyright Clearance Center.

License Number	4491240343849
License date	Dec 17, 2018
Licensed Content Publisher	Elsevier
Licensed Content Publication	Cell
Licensed Content Title	bottleneck acts as a regulator of the microfilament network governing cellularization of the Drosophila embryo
Licensed Content Author	Eyal D. Schejter,Eric Wieschaus
Licensed Content Date	Oct 22, 1993
Licensed Content Volume	75
Licensed Content Issue	2
Licensed Content Pages	13
Start Page	373
End Page	385
Type of Use	reuse in a thesis/dissertation
Portion	figures/tables/illustrations
Number of figures/tables /illustrations	2
Format	both print and electronic
Are you the author of this Elsevier article?	No
Will you be translating?	No
Original figure numbers	Figure 2, Figure 8
Title of your thesis/dissertation	Regulation of Actomyosin Contraction during Tissue Morphogenesis: Genes and Mechanics
Expected completion date	Dec 2018
Estimated size (number of pages)	150
Requestor Location	Daniel Krüger Meyerhofstr 1 Heidelberg, BW 69117 Germany Attn: Daniel Krüger
Publisher Tax ID	GB 494 6272 12
Total	0.00 EUR

This Agreement between Daniel Krüger ("You") and Elsevier ("Elsevier") consists of your license details and the terms and conditions provided by Elsevier and Copyright Clearance Center.

License Number	4491240846799
License date	Dec 17, 2018
Licensed Content Publisher	Elsevier
Licensed Content Publication	Current Biology
Licensed Content Title	Actin Cytoskeleton: Through the bottleneck
Licensed Content Author	William E. Theurkauf
Licensed Content Date	Jan 1, 1994
Licensed Content Volume	4
Licensed Content Issue	1
Licensed Content Pages	3
Start Page	76
End Page	78
Type of Use	reuse in a thesis/dissertation
Intended publisher of new work	other
Portion	figures/tables/illustrations
Number of figures/tables /illustrations	1
Format	both print and electronic
Are you the author of this Elsevier article?	No
Will you be translating?	No
Original figure numbers	Figure 2
Title of your thesis/dissertation	Regulation of Actomyosin Contraction during Tissue Morphogenesis: Genes and Mechanics
Expected completion date	Dec 2018
Estimated size (number of pages)	150
Requestor Location	Daniel Krüger Meyerhofstr 1 Heidelberg, BW 69117 Germany Attn: Daniel Krüger
Publisher Tax ID	GB 494 6272 12
Total	0.00 EUR

Acknowledgement

When I think back today and try to remember what happened during the last four years, I am overwhelmed by memories in all colors that will hopefully stay with me for the rest of my life. I constantly felt that time was just flying. However, trying to only grasp the essences of these memories, I realize how much I have learned, experienced and gained – in terms of education, in terms of science and in personal circumstances. I realize that I have achieved something significant and that there are many things I can be tremendously happy about.

I am happy to have worked in the lab of Stefano De Renzis. I thank you, Stefano, for your supervision, for your mentoring, for critically reading my thesis, for guiding me during my PhD, for delegating responsibility to me regarding my own projects, training of others and important lab instruments, for the invitation to your home town Napoli, for challenging the boundaries of political correctness, for letting me understand that I can be happy without pet cats, for letting me go to South America before starting the PhD project, for paying Döner lunch even though it was definitely my turn to pay upon my delayed recognition of soluble Bottleneck. Talking about Bottleneck, I am suspicious why I wasn't more skeptical when you proposed 'the *Bottleneck(!) project'* to me that goes back to a publication in the early 90s by a first author called Schejter – the German imperative of (to) fail (!). Despite the many failures I indeed experienced in trying to produce recombinant Bottleneck, today I am even happier to see that I did not *scheiter* (fail) but together with Theresa succeeded in characterizing the molecular function of Bottleneck. Thank you, Theresa, for helping me during the longest time of my PhD also in various other occasions, for the vibe and craziness you brought to the lab, for the fun we had and for the appreciation and promotion of 'Musikalischer Mittwoch'. I am happy to have worked together with Pietro, Justin and Thijs. Probably, by supervising you I have learned more than you. I am really grateful for the cool project I could pursue together with my friends Pietro, Justin and Stefano; it was a very positive experience and a great example of excellent teamwork. Many thanks to Giorgia, Emiliano, Ranjith, Cristina,

Acknowledgement

Sasha, Ale and Rohit for making my time in the lab more enjoyable. Thanks also to Victoria, who although she was only in the lab for a few weeks, left lasting positive memories.

Furthermore, I thank the members of my thesis advisory committee (TAC), Anne Ephrussi, Ulrich Schwarz and Carsten Sachse for guiding and supporting me over the entire course of my PhD. Thanks, Anne, for keeping the DB unit in a good shape and creating a very welcoming and supportive working environment. Thanks, Ulrich, for the important feedback on my first first author publication. Thanks, Carsten and Simon Mortensen, for helping me to characterize the protein function of Bottleneck by EM and for the very straightforward and productive collaboration. I also thank Martin Jechlinger and Steffen Lemke for being part of my defense committee.

I am glad for the civilization project of European Integration and the translation of the abstract idea of international understanding into lived reality in form of EMBL. I am glad to be part of the EMBL community – it coined my understanding of how scientific exchange, collaboration and research should be.

I am happy to have worked together with Richard Grandison to establish an eLearning course on optogenetics. It was a great experience, thank you, Richard.

I am also grateful for the unquestionable support by the Pepcore facility, especially Kim, Jacob and Ines for helping us to produce Bottleneck protein again and again and the ALMF for helping out whenever there was a problem with the microscope. Thanks also to all people that keep EMBL running so smoothly (like Andreas – you'll rarely see walls painted so accurately like at EMBL). And to all the people that I got to know during my time at the institute. Special thanks to Sourabh for inviting us to his wedding in India – it was a very special experience that I will hopefully remember forever.

Acknowledgement

Ich danke den vielen Menschen, die direkt oder indirekt an den Ergebnissen dieser Arbeit beteiligt sind. Gleichzeitig will ich aber von Herzen auch den Menschen danken, die nicht hinter dieser Arbeit sondern allein hinter mir standen und stehen. Ich danke Dir, Mutti, für die bedingungslose Unterstützung nicht nur während meiner Doktorandenzeit, sondern für die lebenslange Sorge, Fürsorge und Hingabe, die mich bis zu diesem Punkt getragen haben. Ich danke auch meinen Tanten Conny, Ake und Ati dafür, dass sie mich wie drei weitere Mütter begleiten. Damit denke ich auch an meine Cousinen und Cousins und meine Onkels und bedanke mich dafür, dass ihr mir Anker und Rückhalt seid. Ich danke meinen guten Freundinnen und Freunde aus meiner Pasewalker Heimat, besonders meinen Lebensfreunden Robin und Philipp – das Glück auch nach dieser langen Zeit euch als Freunde zu haben ließe sich durch nichts aufwiegen. Ich danke aber besonders auch meinen Heidelberger Freunden, die Heidelberg während der letzten 10 Jahre zu einer neuen Heimat gemacht haben. Danke, dass ihr es immer geschafft habt einen Ausgleich zur manchmal frustrierenden Laborarbeit zu schaffen, danke für die Freude, den Spaß, die Kultur, die Subkultur, die Trinkkultur. Danke an die vielen wechselnden Teilnehmer und besonders an den Kern unseres Pubquiz-Teams. Der ein oder andere Sieg am Montag Abend hat mich zwar wahrscheinlich den ein oder anderen produktiven Dienstag Morgen gekostet, aber dieser wöchentliche Fixpunkt lieferte ansonsten einen super Vorschub in beinahe jede neue Doktorarbeitswoche. Danke an den Mohr und das Eckstein für die Betreuung.

Wohin mich auch das Leben zukünftig bewegt. Mein Herz, das habe ich in Heidelberg vergeben. Nicht verloren, sondern einem Menschen geschenkt. Dir, Anna, möchte ich für alles danken, was du für mich getan hast und was wir zusammen erlebt haben. Vielen Dank für deine Liebe und für deine Unterstützung. Ich freue mich auf unsere gemeinsame Zukunft.